

Sources, sinks, and transport of energetic particles within Saturn's magnetosphere

Von der Fakultät für Elektrotechnik, Informationstechnik, Physik
der Technischen Universität Carolo-Wilhelmina
zu Braunschweig
zur Erlangung des Grades eines
Doktors der Naturwissenschaften
(Dr. rer. nat.)
genehmigte
Dissertation

von Peter Kollmann
aus Karlsruhe

Bibliografische Information der Deutschen Nationalbibliothek

Die Deutsche Nationalbibliothek verzeichnet diese Publikation in der Deutschen Nationalbibliografie; detaillierte bibliografische Daten sind im Internet über <http://dnb.d-nb.de> abrufbar.

1. Referentin oder Referent: Prof. Dr. Karl-Heinz Glaßmeier
 2. Referentin oder Referent: Prof. Dr. Sascha Kempf
- eingereicht am: 22. Dezember 2011
mündliche Prüfung (Disputation) am: 26. März 2012

ISBN 978-3-942171-66-3

uni-edition GmbH 2012
<http://www.uni-edition.de>
© Peter Kollmann



This work is distributed under a
Creative Commons Attribution 3.0 License

Printed in Germany

Cover figure: Saturn and its radiation belts.

Saturn is in the center. The yellow dashed arrows indicate its magnetic field lines. The intensity of 27 MeV protons in the radiation belts is color coded. White lines show the orbits of the moons Mimas, Enceladus, and Tethys, which separate the belts from each other.

Red=0.1 protons/(cm² s str keV), yellow=red/10, cyan=red/100, blue=red/1000.

Data: E. Roussos. Art: S. E. Nelson. (2011)

Vorveröffentlichungen der Dissertation

Teilergebnisse aus dieser Arbeit wurden mit Genehmigung der Fakultät für Elektrotechnik, Informationstechnik, Physik, vertreten durch die Mentorin oder den Mentor/die Beitreuerin oder den Betreuer der Arbeit, in folgenden Beiträgen vorab veröffentlicht:

Publikationen

- **Kollmann, P.**, Roussos, E., Paranicas, C., Krupp, N., Jackman, C., Kirsch, E. & Glassmeier, K.-H.: *Energetic particle phase space densities at Saturn: Cassini observations and interpretations.* J. Geophys. Res., 116, A05222, doi:10.1029/2010JA016221 (2011).
- **Kollmann, P.**, Roussos, E., Paranicas, C., Krupp, N. & Haggerty, D. K.: *Processes forming and sustaining Saturn's proton radiation belts.* Icarus, submitted (2011).
- Roussos, E., Krupp, N., Paranicas, C., Mitchell, D. G., Müller, A. L., **Kollmann, P.**, Bebesi, Z., Krimigis, S. M. & Coates, A. J.: *Energetic electron microsignatures as tracers of radial flows and dynamics in Saturn's innermost magnetosphere.* J. Geophys. Res., 115, A03202, doi:10.1029/2009JA014808 (2010).
- Paranicas, C., Mitchell, D. G., Roussos, E., **Kollmann, P.**, Krupp, N., Müller, A. L., Krimigis, S. M., Turner, F. S., Brandt, P. C., Rymer, A. M., & Johnson, R. E.: *Transport of energetic electrons into Saturn's inner magnetosphere.* J. Geophys. Res., 115, A09214, doi:10.1029/2010JA015853 (2010).
- Roussos, E., Krupp, N., Paranicas, C., **Kollmann, P.**, Mitchell, D. G., Krimigis, S. M., Armstrong, T. P., Went, D. R., Dougherty, M. K. & Jones, G. H.: *Long-and short-term variability of Saturn's ionic radiation belts.* J. Geophys. Res., 116, A02217, doi:10.1029/2010JA015954 (2011).
- Paranicas, C., Roussos, E., Krupp, N., **Kollmann, P.**, Hendrix, A. R., Cassidy, T., Johnson, R. E., Schenk, P., Jones, G., Carberry, J., Mitchell, D. G. & Dialyn.as, K.: *Energetic charged particle weathering of Saturn's inner satellites.* Planet. Space Sci., 61, 60-65, doi:10.1016/j.pss.2011.02.012, (2011).
- Hendrix, A. R., Cassidy, T. A., Buratti, B. J., Paranicas, C., Hansen, C. J., Teolis, B., Roussos, E., Bradley, E. T., **Kollmann, P.** & Johnson, R. E.: *The Albedo Pattern of Mimas as measured by Cassini UVIS.* Submitted to Icarus (2011).

-
- Krupp, N., Roussos, E., **Kollmann, P.**, Paranicas, C., Mitchell, D. G. Krimigis, S. M., Rymer, A., Jones, G. H., Arridge, C. S., Armstrong, T. P. & Khurana, K. K.: *The Cassini Enceladus encounters 2005-2010 in the view of energetic electron measurements*. Icarus, 218, 33-447, doi:10.1016/j.icarus.2011.12.018, (2011).

Tagungsbeiträge

- **Kollmann, P.**, Krupp, N., Glassmeier, K.-H., Roussos, E. & Krimigis, S. M.: *Sources and sinks of energetic protons in Saturn's magnetosphere* (Oral). Solar System School seminar, Katlenburg-Lindau, Germany (3 October 2010).
- **Kollmann, P.**, Krupp, N., Glassmeier, K.-H. , Roussos, E. & Krimigis, S. M.: *Energetische Teilchen in der Saturn-Magnetosphäre und ihre Wechselwirkung mit dem Neutraltorus* (Oral). IGEP Oberseminar, Braunschweig, Germany (17 November 2009).
- **Kollmann, P.**, Krupp, N., Glassmeier, K.-H., Roussos, E. & Krimigis, S. M.: *Saturns neutral torus density as inferred from energetic particle diffusion observed by Cassini/ LEMMS* (Poster). MPS Fachbeirat, Katlenburg-Lindau, Germany (3 November 2009).
- **Kollmann, P.**, Krupp, N., Glassmeier, K.-H. , Roussos, E., Paranicas, C. & Krimigis, S. M.: *Energetic particles in Saturn's dipolar region from MIMI/ LEMMS* (Oral). Cassini MAPS Workshop, Meudon, France (6-9 April 2010).
- **Kollmann, P.**, Roussos, E., Paranicas, C., Krupp, N., Glassmeier, K.-H. & Krimigis, S. M.: *Interaction of energetic particles with the E-ring* (Oral). Cassini PSG meeting, Munich, Germany (7-11 June 2010).
- **Kollmann, P.**, Roussos, E., Paranicas, C., Krupp, N., Glassmeier, K.-H. & Krimigis, S. M.: *Long-term average of energetic particle phase space densities in Saturn's magnetosphere* (Oral). Cassini PSG meeting, Munich, Germany (24-28 June 2010).
- **Kollmann, P.**, Roussos, E., Paranicas, C., Krupp, N., Glassmeier, K.-H. & Krimigis, S. M.: *Long-term average of energetic particle phase space densities in Saturn's magnetosphere* (Oral). European Planetary Science Congress 2010, Rome, Italy (19-24 September 2010).
- **Kollmann, P.**, Krupp, N., Glassmeier, K.-H., Roussos, E. & Krimigis, S. M.: *Energetic particles at Saturn* (Oral). Solar System School seminar, Katlenburg-Lindau, Germany (3 November 2011).
- **Kollmann, P.**, Roussos, E., Paranicas, C., Krupp, N. & Glassmeier, K.-H.: *Effects acting on energetic particles in Saturn's magnetosphere* (Oral). Cassini MAPS workshop, Annapolis, MD, USA (27-29 April 2011).

-
- **Kollmann, P.**, Roussos, E., Paranicas, C., Krupp, N. & Glassmeier, K.-H.: *Effects acting on energetic particles in Saturn's magnetosphere* (Oral). APL seminar, Laurel, MD, USA (21 April 2011).
 - **Kollmann, P.**, Roussos, E., Paranicas, C., Krupp, N. & K. Glassmeier: *Modeling of Energetic Proton Profiles at Saturn* (Poster). Magnetospheres of the Outer Planets 2011, Boston University, Boston, MA, USA (11-15 July 2011).
 - **Kollmann, P.**, Roussos, E., Paranicas, C., Krupp, N., Haggerty, D. K. & Glassmeier, K.-H.: *Effects acting on energetic particles in Saturn's magnetosphere* (Poster). European Planetary Science Congress 2011, Nantes, France (2-7 October 2-7 2011).
 - **Kollmann, P.**, Roussos, E., Paranicas, C., Krupp, N., and Haggerty, D. K.: *Saturn's radiation belts* (Oral). Solar System School seminar, Katlenburg-Lindau, Germany (29 June 2011).
 - Krupp, N., Roussos, E., **Kollmann, P.**, Jones, G. H., Mitchell, D. G., Paranicas, C., Krimigis, S. M., Khurana, K. K., Bebesi, Z., Srama, R., Rymer, A., Kempf, S., Lagg, A. & Müller, A. L.: *The Cassini Enceladus encounters in the view of energetic particle measurements* (Oral). Magnetospheres of the outer planets, Cologne, Germany (27-31 July 2009).
 - Krupp, N., Roussos, E., Jones, G. H., Mitchell, D. G., Krimigis, S. M., Khurana, K. K., **Kollmann, P.**, Srama, R., Kempf, S., Rymer, A., Arridge, C. & Lagg, A.: *The Cassini Enceladus encounters in the view of energetic particles* (Poster). MPS Fachbeirat, Katlenburg-Lindau, Germany (3 November 2009).
 - Roussos, E., Krupp, N., Andriopoulou, M., **Kollmann, P.** & Paranicas, C., *Moon-magnetosphere interaction signatures as tools for studying the magnetospheres of outer planets* (Oral). European Geosciences Union General Assembly, Vienna, Austria (3-8 April 2011).
 - Thomsen, M. F., Tokar, R. L., Roussos E., Andriopoulou, M., Paranicas, C., **Kollmann, P.** & Arridge C. S.: *Evidence at Saturn for an Inner Magnetospheric Convection Pattern, Fixed in Local Time* (Oral). Magnetospheres of the outer planets, Boston, MA, USA (11-15 July 2011).
 - Roussos, E., Krupp, N., **Kollmann, P.**, Paranicas, C., Mitchell, D. G., and Krimigis, S. M., *Energetic electron observations of Rhea's magnetospheric interaction* (Oral). European Planetary Science Congress 2011, Nantes, France (2-7 October 2011).
 - Krupp, N., Roussos, E., **Kollmann, P.**, Andriopoulou, M. & Bebesi, Z.: *Recent MIMI/LEMMS studies* (Oral). Cassini PSG meeting, Pasadena, CA, USA (24-28 October 2011).

Contents

Publication list	5
Abstract	17
Preface	19
This thesis	21
1 Introduction	25
1.1 Structure of planetary magnetospheres	25
1.2 Saturn and its environment	30
1.2.1 Overview	30
1.2.2 Neutral particles and grains	32
1.2.3 Charged particles	35
2 Physical processes in Saturn's magnetosphere	39
2.1 Interactions of charged particles and fields	39
2.1.1 Plasma	39
2.1.2 Energetic particles	42
2.2 Transport	46
2.2.1 Diffusion	47
2.2.2 Injection events from dipolarization	54
2.2.3 Injection events from interchange	60
2.3 Sinks	62
2.3.1 Influence of sinks on particle profiles	62
2.3.2 Charge exchange	63
2.3.3 Energy loss in grains	66
2.3.4 Energy loss in gas	70
2.3.5 Scattering into the loss cone	71
2.3.6 Losses at moon orbits	72
2.4 Sources	75
2.4.1 Non-diffusive transport	75
2.4.2 CRAND	75
2.4.3 ENA stripping	78

3 Cassini and its particle instrumentation	81
3.1 The Cassini mission	81
3.2 The energetic particle detector LEMMS	81
3.2.1 Operation principle	81
3.2.2 Technical details	83
3.3 The magnetometer MAG	85
3.3.1 Flux-gate magnetometer	85
3.3.2 Helium magnetometer	86
3.4 Other instruments	86
4 Data set and the average magnetosphere	89
4.1 Data set	89
4.2 Intensities	91
4.2.1 Computation	91
4.2.2 Radial profiles	92
4.2.3 Energy spectra	97
4.2.4 Pitch angle distributions	100
4.3 Phase space densities	101
4.3.1 Computation	101
4.3.2 Radial profiles	103
4.4 Real space densities	107
5 Processes in the proton radiation belts	109
5.1 Introduction	109
5.2 Proton belts model	110
5.2.1 The model	110
5.2.2 Model results	116
5.3 Origin of the belts	125
5.3.1 CRAND	126
5.3.2 Stripped ENAs	131
5.3.3 Radial diffusion	134
5.3.4 Injection events	134
5.3.5 Discussion	135
6 Processes in the middle magnetosphere	137
6.1 Introduction	137
6.2 Studies at $7R_S$	137
6.2.1 Charge exchange	138
6.2.2 Energy loss in grains	139
6.2.3 Energy loss in gas	144
6.2.4 Radial diffusion	144
6.2.5 Pitch angle and energy diffusion	145
6.2.6 Discussion	146
6.2.7 Further sources and losses	147
6.3 Global studies	149
6.3.1 Radial profiles	149

6.3.2 Local time asymmetries	160
Summary	163
Outlook	165
A Used LEMMS channels	167
B Nomenclature	169
Bibliography	173
Acknowledgements	191
Curriculum vitae	193

List of Figures

1.1	Earth's magnetosphere	26
1.2	Jupiter's magnetosphere	26
1.3	Saturn's magnetosphere	28
1.4	Enceladus	32
1.5	Saturn's rings	33
1.6	Neutral Torus density	34
1.7	Electron spectrum down to thermal energies	36
1.8	Plasma density	37
2.1	Gradient-curvature drifts versus corotation	46
2.2	Adiabatic heating	47
2.3	Diffusion coefficients from previous LEMMS measurements	53
2.4	Injection events detected in-situ	55
2.5	Injection event inferred from ENA emissions	56
2.6	Reconnection	57
2.7	Dungey cycle	59
2.8	Vasyliūnas cycle	60
2.9	Particles encountering a loss region	63
2.10	Charge exchange cross sections of protons	65
2.11	Differential energy loss in water	68
2.12	Lifetimes at Mimas	74
2.13	Secondary particles from protons on water	76
2.14	Neutron spectrum at Earth	77
2.15	Stripping cross sections of hydrogen	78
3.1	Cassini and LEMMS pictures	82
3.2	LEMMS' mechanical configuration	83
4.1	Intensities during various orbits	93
4.2	Intensities averaged over the mission, overview	94
4.3	Intensities averaged over the mission, radiation belts	95
4.4	Energy spectra throughout the magnetosphere	98
4.5	Energy spectra of protons and water group ions	99
4.6	Pitch angle distributions	100
4.7	Dipole model vs. average magnetic field	103
4.8	Phase space densities of the magnetosphere, field-aligned	104
4.9	Phase space densities of the magnetosphere, equatorial	105

4.10 Real space density of the magnetosphere	107
5.1 Energy spectra within the radiation belts	112
5.2 Neutral Torus model	114
5.3 Loss rates in gas from energy loss and charge exchange	115
5.4 Best fit of radiation belt model and comparison with measurements	117
5.5 Deviation of model and measurements for different parameters	119
5.6 Best fit of a radiation belt model that includes moon losses	121
5.7 Radiation belt models assuming lower source and denser torus	121
5.8 Phase space densities between Mimas and Enceladus	123
5.9 Diffusion coefficients from literature and this work	124
5.10 Rates within the radiation belts	125
5.11 Long-term variability of the radiation belts	126
5.12 Simulated neutron spectra for CRAND of the Main Rings	128
5.13 ENA production of Saturn’s magnetosphere	132
5.14 Rates of charge exchange and stripping	133
6.1 Regions of Saturn’s magnetosphere	138
6.2 Lifetimes of various processes at $L = 7$	140
6.3 Encounters with ice grains necessary to enter or leave an energy interval .	142
6.4 Encounters with ice grains under different conditions	143
6.5 Calculation of the diffusion lifetime	145
6.6 Source rate at $L = 7$	149
6.7 Sensitivity of a PSD profile on boundary conditions	151
6.8 PSD measurements and theoretical profiles assuming only diffusion . .	153
6.9 PSD measurements in the loss region and theoretical profiles	154
6.10 Modeled PSDs around Rhea	157
6.11 Local time asymmetry in intensity	159
6.12 Local time asymmetry in phase space density	160

List of Tables

1.1	Physical quantities at or of different planets	29
2.1	Size and orbit of Saturn’s moons	72
5.1	Optimal parameters of the radiation belt model	118
6.1	Source and loss mechanisms at $L = 7$	147
A.1	Used LEMMS channels	168
B.1	Variables	171
B.2	Abbreviations	171
B.3	Special terms	172

Abstract

Saturn's magnetosphere has been studied extensively by the Cassini spacecraft during the last seven years. We present for the first time long-term averaged energetic proton and electron measurements obtained by the MIMI/LEMMS instrument onboard the Cassini spacecraft. This is the largest compilation of data in this energy range to date and includes by far more information and better statistics than studies on single orbits or previous flyby missions. The data set covers dipole L -shells equivalent to an equatorial distance up to 20 Saturn radii (R_S) from Saturn's center and an energy range from several 10 keV to several 10 MeV. The averages are displayed at specific energies and equatorial pitch angles, and also at constant first and second adiabatic invariants. The standard deviation of the averages is also calculated. It can extend over two orders of magnitude at large distances to Saturn.

The studied particles are subject to a variety of processes. These are: radial and pitch angle diffusion, energy loss in matter, charge exchange and stripping, beta decay following CRAND, dipolarization of the frozen-in magnetic field, flux-tube interchange. As part of these processes the particles are first produced from other species, transported in space to the observed position, and/or transported in energy to the observed energy. After this, the particles might be further transported and ultimately become lost. Since the average state of the magnetosphere only changes on long time scales, all processes cancel out on average, giving rise to a quasi-steady state. In contrast to previous works that often treat the various processes separately, many of them are in this thesis considered simultaneously and consistently. The relative importance of the various processes is mostly unknown. The strength of the processes can be determined by several parameters, as diffusion coefficients or densities of neutral material, but also many of these parameters are not known with certainty. These issues are partly answered in this thesis.

Using a radial diffusion equation that was generalized to account for most processes, Saturn's proton radiation belts are modeled. The model has free parameters, as a diffusion coefficient, a source rate, and neutral gas densities, which are optimized. It is found that radial diffusion, a source process, and losses at the neighboring moons can reproduce the belts. Further losses due to the gas and grain environment are not important. Several mechanisms that could account for the source process are discussed and mostly excluded. Previous studies proposed that the high-energy fraction of the protons originates from the cosmic ray albedo of Saturn's rings. We find that the most promising candidate to supply all energies is the cosmic ray albedo of Saturn's atmosphere (CRAND process).

The relative importance of different processes is estimated based on published parameters that describe these processes. This is done for a region located at an equatorial distance of $7R_S$. It is found for example that protons are mainly lost due to charge exchange in the neutral gas that is present there. The protons are not significantly affected

Abstract

by ice grains of the E ring that is extending to this region. In order to reach a steady state, it is argued that an additional source has to provide protons, which could be provided by interchange or dipolarization events. The rate at which these events provide particles is estimated.

It is also discussed why the particles distribute in space as they do. It is obvious and well-known that moons located within the proton radiation belts severely deplete the population and separate the belts. The data set of this work reveals that while moons outside of the belts do not significantly deplete the particles, they change the radial gradient of their population. This is clearly visible for electrons around Rhea and there are signatures that this occurs at other moons and also applies to protons. It is shown that within the gas of the Neutral Torus only protons below 100 keV are significantly depleted by charge exchange. Since the torus density peaks at $4R_S$, these protons become increasingly depleted towards this distance.

Preface

The interplanetary space is filled with a variety of charged particles. They originate from the Sun, in the form of solar wind and coronal mass ejections, and from the rest of the universe, mainly in the form of galactic cosmic rays. The particles are mainly protons and electrons. Since they can have energies up to gigaelectron volts, the particles can be referred to as radiation. They give rise to space weather which is harmful for both manned and unmanned spacecraft.

If a planet produces its own magnetic field, it mostly protects the planet, but also enhances the radiation in some regions. The region around a planet that is dominated by its magnetic field is called the magnetosphere and will be the topic of this thesis.

Space weather and space weathering have an impact on the life of a technically advanced civilization. A harmless but well-known result from space weather is the aurora. This is caused by electrons that follow the Earth's magnetic field lines into the atmosphere, where they excite atoms and ions, which then emit light of typical colors. Less well-known is the fact that space weathering is causing damage and temporary failures on satellites. This happens for example because the satellites can charge up until a strong electrical discharge occurs. Energetic particles can flip bits in the memory and cause errors. Over time, the radiation destroys electronic components. Space weather influences the regular weather since cosmic rays ionize the stratosphere and by this produce condensation cores for clouds. It influences the ionosphere, so that the links to communication- and GPS-satellites are disrupted. Especially near the poles, signals from Earth might not be properly reflected back to Earth. Since planes are required to have effective communications for all portions of the flight, their routes might be redirected from the poles during solar events.

An extreme result of space weathering and the absence of a planetary magnetic field over long time is the planet Venus. The fact that its atmosphere is bare of water is today attributed to the solar wind. An example where a planetary magnetic field is of disadvantage is radiation belts. There, radiation is accumulating. During the Apollo missions it was important to know about their presence so that they could be avoided as much as possible.

The magnetosphere and space weathering are therefore important for our life on Earth. Besides this, its exploration is fundamental research that broadens the understanding and awareness of our environment.

Therefore, Earth's magnetosphere has been studied for a long time, starting with precise measurements of the magnetic field on the surface and nowadays additionally by in-situ measurements of spacecraft. While Saturn, and not Earth, will be the focus of this thesis this does not necessarily mean that it would be impossible to draw conclusions from this about Earth. Studying processes that are similar but different to the one of major interest

is a common approach. It is one justification for experiments in microgravity. Under these conditions, processes can be studied that on Earth are obscured by gravity. The equivalent to gravity in magnetospheric science is the solar wind as the driver of dynamics. Effects following from internal processes, as from Earth's rotation, might be important but are obscured. This is different for other planets as Jupiter and partly also Saturn. Since they are fast rotators, they follow the other extreme and their magnetospheres are dominated by internal processes.

In order to study Saturn and its magnetosphere, it has been visited by four spacecraft so far: Pioneer 11, Voyager 1, Voyager 2, and Cassini. The first three missions already provided a wealth of in-situ and remote data. They were flyby-type missions and occurred during a time where it was possible to visit all giant planets in a row with the same spacecraft. Their particle instruments, however, could only provide snapshots of the present magnetospheric configurations. Therefore, the results were limited to the narrow spatial coverage of the trajectory, current solar wind conditions, and the current local season. The Pioneer 11 flyby for example occurred during a period when the magnetosphere was severely compressed and disturbed by one of the largest solar particle events during this solar cycle ([Simpson et al. 1980](#)). Consequently, it has been challenging to distinguish between spatial asymmetries and temporal variability. An example for this is the fact that it was doubted after the flybys if Saturn possesses a magnetodisk as Jupiter. It was found with Cassini, that this disk does exist but can be suppressed during periods of strong solar wind kinetic pressure ([Arridge et al. 2008b](#)).

As an orbiting spacecraft, Cassini completed 159 orbits around Saturn between 2004 and the end of 2011. During this time it sampled in-situ a wide range of radial distances, latitudes, and longitudes. In addition to the observation of dynamic events, this allowed for the very first time to conduct a study of the global magnetospheric configuration. Its mission is planned to continue until 2017. A time period as long as this allows to study effects of the seasonal effects over half a Saturn year (=29/2 Earth years) and the dependence on solar cycle (11 Earth years).

One essential aspect of any magnetosphere are the charged particles at keV and MeV energies, which are referred to as energetic particles. They are the focus of this thesis. These particles have been sampled by the instrumentation onboard every mission to this planet in order to answer some major questions:

How do energetic particles distribute around Saturn? Why are they doing this? Where do they come from in the first place? Which processes govern their evolution?

Many facts are known and we will state them in the following and throughout this thesis. However, complete and certain answers are not available even today.

To the aspects that are known belongs the fact that the MeV energy fraction of protons within Saturn's magnetosphere is originating from cosmic ray albedo neutron decay (CRAND). This can be concluded from energy spectra taken in this region ([Krimigis and Armstrong 1982](#), [Armstrong et al. 2009](#)). The origin of the low-energy fraction and electrons in this region is, however, still under debate ([Roussos et al. 2011](#), [Kollmann et al. 2011a](#)). The particles outside of the radiation belts, at distances larger than about five Saturn radii (R_S) away from Saturn's center, do neither originate from this process, nor the solar wind. This can be concluded from their composition (large amount of oxygen and water ions, [Sittler et al. \(2006\)](#), [DiFabio et al. \(2011\)](#)). Their source was thought for a long time to be neutral material that was sputtered from the rings and moons of Saturn.

A major finding of Cassini was that it is erupted from the moon Enceladus instead (Porco et al. 2006, Waite et al. 2006).

This material is partly ionized afterwards, but how it is accelerated up and beyond MeV energies, is not known with certainty yet. At Jupiter, there exist several theories as recirculation (Nishida 1976), and turbulent heating (Saur 2004), but it is unclear if they apply to Saturn.

There can be a close relationship between heating in energy and radial transport in space. While Sittler et al. (2006) found a mostly outward flow of eV and keV particles, later studies showed flows in both directions (Wilson et al. 2008). This transport occurs partly adiabatically, which can be determined from pitch angle distributions (Rymer et al. 2008). Adiabatic transport means that the energy of the particles changes during motion. The transport time scale can be estimated from the temperature equilibration of different species (Rymer et al. 2007) or the refilling of moon microsignatures (Van Allen et al. 1980b). However, there are several possible mechanisms how transport with such velocities and time scales could be achieved.

The study of energetic particles not only provides information about their phenomenology and underlying physics. It can also reveal information beyond that. Energetic particles can act as a probe for matter that they pass, because they interact with it and ultimately get lost there. At Earth, there is not much matter outside the atmosphere that could do so. Saturn, on the other hand, is surrounded by rings, moons, and a relative large density of neutral gas. The interaction of energetic particles with matter allowed Hedman et al. (2007) to support the discovery of an arc within the G ring and Roussos et al. (2008a) to suggest the existence of another arc near Methone.

However, this interaction was for a long time not used in a quantitative way in order to determine parameters of the interacting matter. In case of the Neutral Torus and the E ring it was not even proven which of them causes by which process the observed depletion of energetic particles. Also, the effect of energy loss occurring in dilute, macroscopic ice grains (in contrast to a distributed gas) on the spectrum of energetic particles was to our knowledge not treated in theory before Kollmann et al. (2011b). While the work of this thesis was ongoing, knowledge of the Neutral Torus and E ring was significantly improving due to ongoing measurements and careful analysis (Perry et al. 2010, Kempf et al. 2011, Hartogh et al. 2011). Nevertheless, energetic particles still provide not only an independent method to explore these objects but also have other advantages. For example, the interaction between energetic charged particles and neutral gas produces energetic neutral atoms (ENAs). Since they can be detected remotely, more data is available compared to in-situ measurements. This allowed Dialynas et al. (2012) to determine the density profile of the Neutral Torus.

This thesis

The three major questions given above have been the driver of this thesis.

To answer them, first background knowledge about the structure of magnetospheres in general is provided in Sec. 1. This includes the magnetosphere of Saturn and compares it with the ones of Earth, and Jupiter. Also Saturn's neutral environment is described. Since they will be of relevance in the following studies, the E ring and Neutral Torus are

discussed in detail.

Sec. 2 then describes the theory of the various processes that are thought to occur in Saturn's magnetosphere. A mathematical description for most processes is given. This is not done to extend the explanations, but because most formulas are of relevance or are directly applied later.

The utilized instruments are described in Sec. 3. The focus is on the low energy magnetospheric measurement system (LEMMS) that measures protons and electrons from several 10 keV to several 10 MeV. Its physical operation principle and technical specifications are provided in this section. Additionally, the Cassini spacecraft that carries LEMMS is described, together with several other instruments that are used or of interest for this thesis.

All these instruments provide a wealth of data. This wealth is necessary in order to understand a magnetosphere. If its configuration was steady, it would be easy to explore: Even a single spacecraft, which can measure in-situ only at one point per time, could accumulate information about the entire structure. However, a magnetosphere is a highly dynamic structure, a fact that makes it difficult to explore. To approach this, a mission average of all data is produced. This average represents the typical state of Saturn's magnetosphere. The deviations from the average show the presence of dynamic processes. Details of the averaging, the used dataset, and how it is organized are given in Sec. 4. Also, an overview on energetic particle data from large parts of the magnetosphere is given. The data are displayed for example as radial profiles, and energy spectra. A detailed discussion about these profiles and spectra, and the processes responsible for them is topic of the following sections.

Although the average state derived for the magnetosphere is, per definition, steady within the time period of averaging, this does not imply that it is static, i.e. that dynamic processes do not play a role. Dynamic processes can be either continuous (as diffusive processes), or sporadic (as massive reconfigurations of the magnetic field). In both cases, they do not average out but are necessary to reproduce even the average state.

Throughout this thesis, we will split the magnetosphere in several regions. These are the radiation belts at distances smaller than $\approx 5R_S$, and the middle and outer magnetosphere. A clear definition is part of Sec. 4 and an overview is given in Fig. 6.1.

Sec. 5 focuses on the proton radiation belts. The shape of the belts is reproduced with a model in Sec. 5.2. This model includes radial diffusion, and a phenomenological source. The physical origin of the source discussed directly afterwards in Sec. 5.3.

Sec. 6 studies the middle magnetosphere for both protons and electrons. First, a narrow region located at $7R_S$ is studied in detail. Estimates of the relative importance of the processes that were introduced in the theory section are calculated in Sec. 6.2. After this, the entire middle magnetosphere is qualitatively discussed in Sec. 6.3. The aim of this discussion is to find the relative importance of processes outside the $7R_S$ -region and to understand the overall particle distribution.

A useful tool for the reader might be Appendix B that compiles explanations of many variables and abbreviations used throughout this thesis. The reader should also be aware that all equations throughout the thesis are given in the SI system. A slightly updated version of Sec. 2.4.2 and 5 will be available in Kollmann et al. (2011a), as soon as it is published. References to the literature as to sections, equations, and figures of this thesis are links that can be clicked on in the PDF version.

Throughout the thesis, light is shed on a large number of aspects concerning Saturn's magnetosphere. Answers to the initial questions given here in the preface are compiled in the summary.

1 Introduction

1.1 Structure of planetary magnetospheres

A magnetosphere is forming when the solar wind encounters an obstacle that is either magnetized and/or is enclosed by gas, ionized in the upper layers. Depending if the obstacle is strongly or not magnetized, one distinguishes between an intrinsic and an induced magnetosphere.

The term *magnetosphere* refers in the general case to a region where the magnetic field of the solar wind is highly perturbed due to the presence of an obstacle. In the case of an intrinsic magnetosphere, the field is not just perturbed but dominated by the field of the obstacle itself. Beside magnetic fields, the magnetosphere is also filled with charged and neutral matter, i.e. electrons, ions, grains, and gas. The charged population plays a special role since it can both react to and modify the magnetic field if it flows in electric currents. The details of this are subject of this section.

Most of the following discussion is on magnetized planets that have a strong quasi-dipolar field with an axis that is close to the rotation axis and approximately perpendicular to the ecliptic. In other words: Earth, Jupiter, and Saturn. We show sketches of the respective magnetospheres in Figures 1.1, 1.2, and 1.3. Since the topic of this thesis is the average state of Saturn's magnetosphere, we focus here more on typical magnetospheric configurations than on their dynamics.

Magnetospheres interact with the solar wind. This emanates from the Sun and consists mainly of a plasma of protons and electrons with $\approx 2\%$ of He and traces of heavier elements. The plasma moves with supersonic velocities. Since all particles share the same velocity, their energies differ depending on their mass. At 1 AU, the mean energies are on the order of 1 keV for protons and 1 eV for electrons. The magnetic Reynolds number of the solar wind (see Eq. (2.6) for details) is larger than one, so that the solar magnetic field is frozen into the plasma and carried along with it, forming the interplanetary magnetic field (IMF). At Earth's orbit it has an average strength of 4 nT and at Saturn of 0.5 nT (Gombosi et al. 2009).

Many planets in our Solar System have a dynamo process acting within their interior. Dynamos can be very different from each other, using for example different conducting materials as iron, metallic hydrogen, or water-ammonia "ice" and acting in different layers of the planet. Despite these differences, they all create a magnetic field and many of them are well described as dipoles outside the planetary surface.

Also charged particles, as they are found in the vicinity of planets, can create magnetic fields. Because of this, the field around a magnetized planet is not just a superposition of the field produced by the dynamo and IMF but a self-consistent configuration of charged

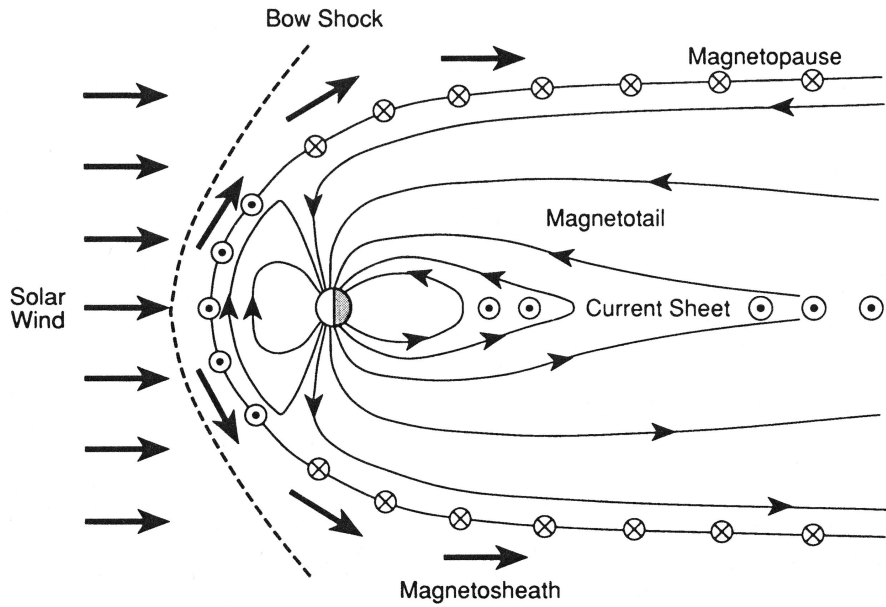


Figure 1.1: Sketch of Earth's magnetosphere. Thin lines with arrows indicate the magnetic field, thick arrows the plasma flow, and encircled crosses and dots electric currents perpendicular to the figure plane. Figure adapted from Kivelson and Russell (1995).

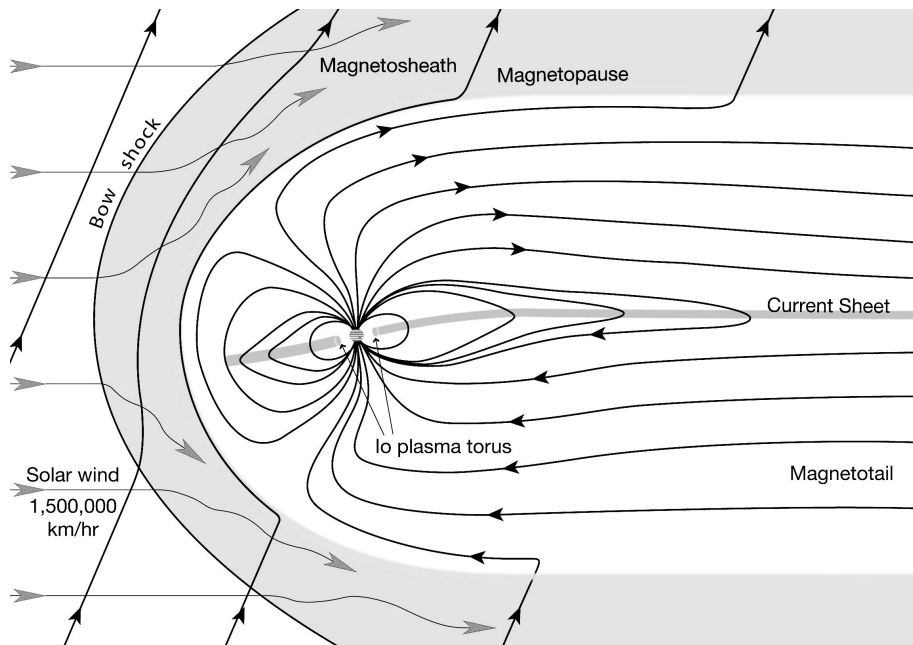


Figure 1.2: Sketch of Jupiter's magnetosphere. Black arrows indicate the magnetic field, gray arrows the plasma flow. Figure adapted from Bartlett (2011).

particle currents and fields. The particles involved in this originate from various sources. These include the solar wind, and secondary particles from cosmic rays (CRAND process, see Sec. 2.4.2). Also neutral material, as from the atmosphere, can contribute after it was ionized by UV light or particle impacts.

The magnetic field at Earth is sketched within Fig. 1.1. The solar wind arrives from the left side of the figure. At the *bow shock*, it is decelerated to subsonic velocities. The subsonic plasma is flowing around the obstacle imposed by the planetary magnetic field. In this process, the dayside field is compressed until a pressure balance is reached. (The pressure includes thermal, kinetic, and magnetic pressure. For the latter see Sec. 2.1.1.3.) This modification in the field configuration requires the *magnetopause* current to flow. The magnetic field created by it enforces the compression of the planetary field on the planetward side, and cancels it out on the sunward side. The magnetopause is therefore the boundary between the IMF and the planetary field. The region contained by it is equal to the magnetosphere.

The solar wind plasma passing the planet modifies also the magnetic field on the night-side of the planet and creates the *magnetotail*. In this region, oppositely directed fields can be found next to each other and are separated by a current sheet. Additionally, the planetary field is modified by the *ring current*, created by charged particles. They move around the planet with a direction depending on the sign of their charge. This motion component results from the inhomogeneity of the magnetic dipole field (gradient- and curvature-drift, Sec. 2.1.2.4). There is also a variety of current systems that flow in parts parallel to the magnetic field lines, then radially near the magnetic equator, back along the field lines, and finally close in the ionosphere. At Jupiter, these currents are so strong that they add an azimuthal component to the magnetic field. As a result the field lines are mostly lagging behind the planetary rotation (Khurana 2001). This occurs also at Saturn, but much weaker (Goldreich and Farmer 2007).

If the planet has an atmosphere, its upper layers are ionized mainly by UV light from the Sun and form the *ionosphere*, which consists mainly of particles with thermal energies in the eV range. Due to drag, ionosphere and atmosphere rotate together with the planet. As the ionosphere is highly conducting, the embedded planetary magnetic field can be considered as frozen-in (see Sec. 2.1.1.2), which means that it would become twisted if the plasma outside the ionosphere did not follow the plasma in the ionosphere. Since the plasmas *do* follow each other (due to their high conductivity, leading to Ferraro's law of isorotation, Alfvén and Fälthammar (1963)), this does not happen. Therefore, plasma motion and magnetic field give rise to the radially directed corotational electric field. This combination of magnetic and electric field can accelerate charged particles, which are freshly ionized and do not follow the plasma motion yet, until the corotation velocity is reached. The corotation velocity is independent of charge and energy. The velocities of the various drifts around the planet are additive.

In the case of Earth, corotation with the planet is limited to the so-called *plasmasphere*. Outside this region, the particles flow frequently from the tail side towards the Sun (a process, which is called substorm, see Sec. 2.2.2). This is triggered by the conditions in the solar wind and therefore Earth's magnetosphere can be categorized as solar-wind driven. This is the opposite to rotationally-driven magnetospheres, as the one of Jupiter. In this case, the particles are roughly moving around the planet until the magnetopause. The entire dynamics is mainly determined by internal processes. The reason for the difference

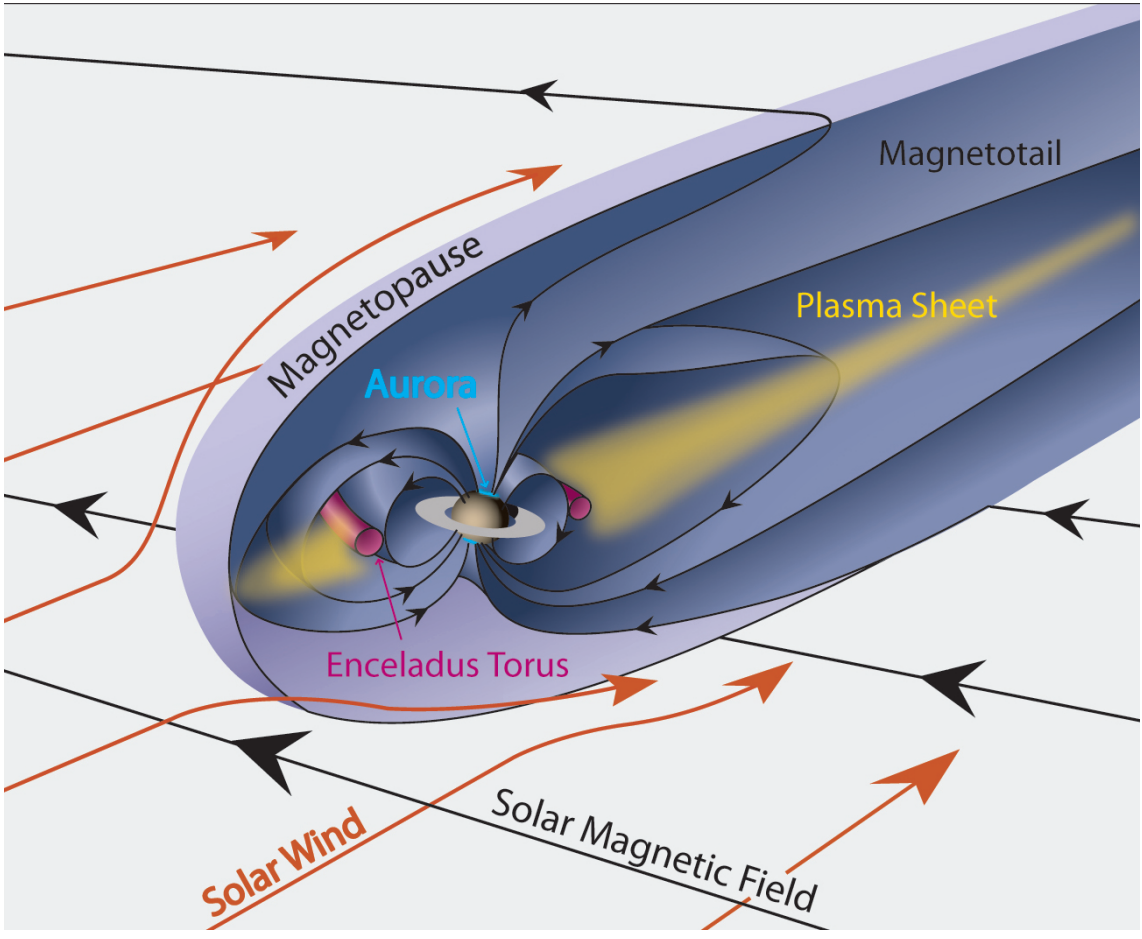


Figure 1.3: Sketch of Saturn’s magnetosphere. Black arrows indicate the magnetic field, orange arrows the plasma flow. Figure from [Bartlett \(2011\)](#).

in categories is that Jupiter’s rotation rate is higher than at Earth. Saturn lies between the two cases in all these aspects ([Mauk et al. 2009](#)).

Another difference of Earth with respect to Saturn, and Jupiter is the strong internal plasma source provided by the moons Enceladus (Sec. 1.2) and Io, respectively. Enceladus ejects water gas and ice grains from fractures at its south pole. Io shows strong volcanic activity and expels silicate dust and sulfur compounds. This material orbits the respective planets with approximately Keplerian velocities. After ionization, the material is accelerated by the corotational electric field towards corotation velocity. Since this increased velocity would require a centripetal force larger than gravity, the plasma moves radially outward. Because the magnetic field is frozen-in, this additionally stretches the magnetic field lines and creates the so-called *magnetodisk*. It can be easily identified in the figures when comparing Fig. 1.2 (with disk) to Fig. 1.1 (without disk). On the nightside the magnetodisk extends to the magnetotail, which aligns itself with the solar wind flow. In the case of Saturn, also the dayside magnetodisk aligns with the solar wind, forcing Saturn’s disk into a bowl-shape configuration, except at equinox ([Arridge et al. 2008a](#)). This does not occur at Jupiter, which has a rotation axis that is less inclined towards the ecliptic and the solar wind flow (see Tab. 1.1). On the other hand, Jupiter’s rotation axis

	Earth	Jupiter	Saturn
semimajor axis [AU]	1	5.2	9.5
equatorial radius	$6371 \text{ km} = 1R_E$	$71492 \text{ km} = 1R_J$	$60268 \text{ km} = 1R_S$
equatorial rotation period [h]	23.934	9.925	≈ 11
equatorial magnetic field [μT]	30	424	21
magnetic moment [Tm^{-3}]	$7.75 \cdot 10^{15}$	$1.55 \cdot 10^{20}$	$4.6 \cdot 10^{18}$
dipole tilt [$^\circ$]	10.5	10	< 1
axial tilt [$^\circ$]	23.4	3.1	26.7
typical magnetopause distance	$10R_E$	$50R_J$	$22R_S$
typical bow shock distance	$13R_E$	$70R_J$	$27R_S$
average IMF strength [nT]	4	1	0.5
internal mass source [kg/s]	1	10^3	10^2
internal plasma source [kg/s]	1	10^3	1
ion lifetime	hours - days	10 - 100 days	months - years

Table 1.1: Comparison of physical quantities at or of different planets. ([Dougherty et al. 2005](#), [Gombosi et al. 2009](#), [Williams 2010](#), [de Pater and Lissauer 2011](#)).

is not aligned with the magnetic axis. This causes the axis of the magnetodisk to precess with every planetary rotation.

Beside the described particle motions that have been mostly perpendicular to the planetary magnetic field, charged particles can also move parallel to the field. Typically this does not yield an electric current since the particles are periodically reflected each time when they reach into regions of sufficiently enhanced magnetic field. (This is called bounce motion, Sec. 2.1.2.) This latitudinal motion adds to the azimuthal drift. Close to the planet, the magnetic field is strong enough that it - and therefore also the particle motion - is not perturbed by any dynamic effect within the magnetosphere. There, a large intensity of charged particles can accumulate. This region is called the *radiation belts* ([Van Allen and Frank 1959](#)). They can coincide with the region of the ring current. While the outer edge of the belts is limited by the strength of the magnetic field, their inner boundary and latitudinal extent are determined by the atmosphere (or surface, or dense rings) of the planet, which decelerates and finally absorbs precipitating particles. In the case of Earth, the electron belts are differentiated into an outer and an inner radiation belt, separated by a slot region. This region is depleted by waves that scatter electrons to the atmosphere where they are lost ([Beutier and Boscher 1995](#), [Abel and Thorne 1998](#)). In contrast, Saturn's radiation belts are split along the orbits of several of its inner moons that sweep out energetic particles along their orbit. This feature is unique in the Solar System. More information about radiation belts is given in Sec. 5.1.

Whenever charged particles follow the magnetic field so far that they approach the magnetic poles and precipitate into the polar atmosphere, they cause *auroras*. During this process, they excite various atmospheric constituents in their electronic or vibrational state. The following deexcitation yields the emission of light ranging from infrared to UV. Light of wavelengths different to that is produced by other processes: X-ray emissions derive from electron bremsstrahlung losses ([Bhardwaj et al. 2007](#)), and radio emissions are caused by the cyclotron maser instability ([Wu and Lee 1979](#)).

The discussion so far dealt with typical or average configurations of magnetospheres.

Magnetospheres, however, are very dynamic objects and there is a large variety of dynamic processes. For example, the magnetopause can change its distance to the planet, depending on the solar wind pressure. Also magnetodisks can be suppressed on the day-side in case that strong solar wind pressure compresses the magnetosphere. This occurs at Saturn but not at Jupiter (Arridge et al. 2008b). Depending on the orientation of the IMF with respect to the planetary field, reconnection can occur (Sec. 2.2.2) that results in a significant chance in the magnetic configuration, setting large amounts of plasma in motion. A similar process, but triggered by the planetary rotation, also occurs at Jupiter and Saturn. Another dynamical process is interchange (Sec. 2.2.3), where plasma from two different radial distances is exchanged. Some of the dynamic processes are periodic or quasi-periodic. A large variety of periodicities can be observed in charged particle and ENA intensities or densities, in the magnetic field, and in plasma waves. These periodicities can derive from the planetary rotation, periodicities in the solar wind conditions, or represent eigenmodes of the magnetosphere. At Earth, substorms often occur with periods of 3 h (Borovsky et al. 1993). At Jupiter and Saturn, especially periodicities near the planetary rotation period are observed (Krupp et al. 2004, Mitchell et al. 2009).

There exist also magnetospheres different to the ones discussed. Mercury has a magnetic field that is so weak that the magnetopause is only about one Mercury radius away from its surface. Uranus and Neptune have strong quadrupole fields that are not aligned with the rotation axis. Jupiter's moon Ganymede also has an intrinsic field. The situation there differs from the described one because Ganymede is not immersed in the supersonic solar wind but in the subsonic Jovian plasma. The Sun generates a magnetic field that forms the heliosphere, which is governed by the solar wind pressure from the inside and the pressure exerted by the interstellar medium from the outside. Neutron stars have magnetic fields and rotation periods that are so extreme, that the corotating particles emit synchrotron radiation.

In case a body does not have an intrinsic magnetic field, an induced magnetosphere can be formed if the body is surrounded by gas as an atmosphere or the coma of a comet. The gas is photoionized by light from the Sun and the resulting plasma interacts with the solar wind. This situation is fulfilled for Venus and Mars. The latter additionally has a partly magnetized crust. If there is no gas around the body and it is not conducting (as Earth's moon) the solar wind particles are absorbed by the obstacle, but the IMF passes it.

1.2 Saturn and its environment

1.2.1 Overview

Saturn is the sixth planet within our solar system, counted from the Sun. It is orbiting at heliocentric distances between 9 and 10 AU (with 1 AU being an astronomical unit). After Jupiter, it is the second largest planet in the system. Since it is a gas planet, its extent is a matter of definition and usually taken to be at the one bar level, leading to an equatorial radius of 60268 km (this will be referred to as $1R_S$). Saturn is relatively oblate due to its fast rotation, which results in a polar radius that is only 90.2 % of the equatorial one.

Saturn's atmosphere consists mainly of molecular hydrogen. Compared to the other gas planets, its hydrogen fraction is the largest. Helium is the next abundant element but has a

number fraction of only $< 6\%$. Its precise value is still under debate. Other species found in the atmosphere are for example H_2O , CH_4 and NH_3 . (A review on Saturn's atmosphere is given in [Fouchet et al. \(2009\)](#).)

In the deep interior of Saturn, pressure and temperature are high enough that the electrons of the hydrogen degenerate, so that hydrogen becomes metallic. Due to the resulting conductivity, a dynamo process can operate which creates Saturn's intrinsic magnetic field. This field is aligned to the rotation axis by less than 1° ([Ness et al. 1981](#)). A solid core is expected in Saturn's center. This consists of rock and/or ice and has a mass of 15 to 20 Earth masses ([Hubbard et al. 2009](#)).

Saturn has at least 62 moons but only 11 with a mean diameter of more than 100 km. These moons are referred to as *icy moons* since they consist out of a mantle of water ice around a rocky core. A special case is the largest moon of Saturn, Titan, which has an atmosphere of mainly nitrogen, and traces of hydrocarbons.

The moon Enceladus plays a special role. At first glance, it does not fundamentally differ from the other icy moons. It has a diameter of 504 km and a semi-major axis of $3.95R_S$. In contrast to the other moons, its south polar region releases plumes of gas and grains. This was originally detected due to the interaction of this material with the surrounding plasma and magnetic field ([Dougherty et al. 2006](#)). Close to the moon, the plumes can be seen optically ([Porco et al. 2006](#)).

Part of the ejected material does not fall back on the moon ([Kempf et al. 2010](#), [Smith et al. 2010](#)), but populates the vicinity of Saturn and forms the *E ring* (consisting of grains) and the *Neutral Torus* (consisting of gas), sometimes called Enceladus Torus. However, one should point out that the size distribution of the ejected, and the escaping and further processed grains significantly differs.

The escaping grains and gas particles are subject to sputtering, dissociation, ionization, and acceleration ([Bagenal and Delamere 2011](#), [Cravens et al. 2011](#)). By this, they supply a population of plasma and energetic particles, which is detailed in Sec. 1.2.3. This plasma, in combination with the magnetic field of Saturn's dynamo, and with fields and plasma of the solar wind, creates Saturn's magnetosphere, as it was introduced in Sec. 1.1.

Saturn is famous for its striking rings, as they are shown in Fig. 1.5. Contrary to the tenuous rings D, E, and G, the *Main Rings* A, B, C, and F have a large optical depth of > 0.1 . They extend from Saturn's center over the range between 1.2 to $2.3R_S$ and feature complex permanent as well as transient structures. The rings mainly consist of water ice grains with sizes on the order of cm and above, and have a combined mass similar to the moon Mimas. They lie within the Roche zone where tidal forces keep the grains from coagulating to moonlets. (A review on the dense rings is given in [Cuzzi et al. \(2009\)](#).)

While the tenuous rings are (or are potentially) fed from sputtered or ejected moon material, the origin of the Main Rings is still an open question. They probably do not derive from a destroyed moon or remnants from Saturn's accretion disc since there is no mechanism that would only remove the silicates, which would be unavoidable for a moon, but not the ice. If they derived from a comet (as they were highly abundant during the late heavy bombardment) they might have aged significantly up to now by spreading out and incorporating much meteoroid material. (A review on the origin of Saturn's rings is given in [Charnoz et al. \(2009\)](#).)

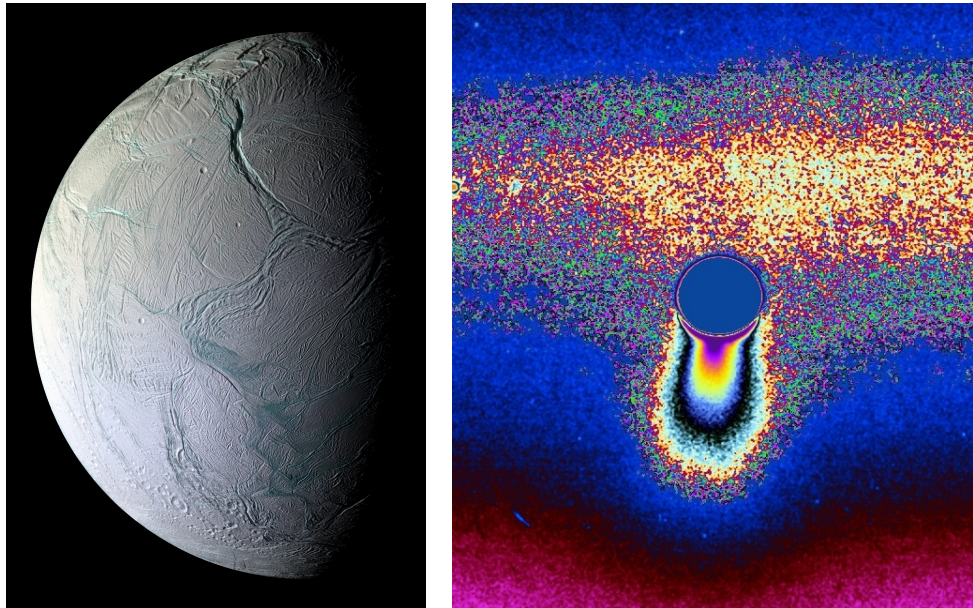


Figure 1.4: *Left panel:* Mosaic of composite images showing the south pole of Enceladus. The images were taken by the ISS instrument during a close flyby, colors are derived from images taken in different filters ranging from ultraviolet to infrared. *Right panel:* Processed image showing Enceladus (circle), its plumes (below) and the E ring (bright background). The image was taken in visible light during a distant flyby. Image courtesies of NASA/JPL/SSI.

1.2.2 Neutral particles and grains

The neutral material in Saturn's environment originates to a large fraction from the plumes of Enceladus. Cassini's ion and neutral mass spectrometer (INMS) determined in-situ the ejected gas species. 91 % of the gas is H_2O , with contributions of CO_2 , and CO (Waite et al. 2006, Perry et al. 2010). Most ejected grains mostly consist of water ice (Hillier et al. 2007), although there exist two other populations: one incorporates siliceous and/or organic compounds, the other sodium salts (Postberg et al. 2009).

These μm -sized ice grains (Kempf et al. 2008) have been detected and analyzed in-situ by the Cassini dust analyzer (CDA). They can also be detected by other instruments of Cassini, although they have not been designed to do this. The Cassini plasma spectrometer (CAPS) detected charged nm grains (Jones et al. 2009). Also INMS (Teolis et al. 2010), LEMMS (Krupp et al. 2012), and the ion and neutral camera (INCA) (Jones et al. 2008) detected signatures of dust. The presence of dust can also be inferred indirectly via the dust's charge using the radio and plasma wave science instrument (RPWS) (Yaroshenko et al. 2009).

The already mentioned *E ring* fed by Enceladus is one of Saturn's diffuse and tenuous rings. Its density peaks near the orbit of Enceladus. Even with cameras in the orbit of Saturn it cannot be seen easily. A rare occasion where both the Main Rings and the E ring are visible is shown in Fig. 1.5. The E ring was originally discovered by Feibelman (1967). Since then, it has been studied by observation of scattered light (Nicholson et al. 1996, de Pater et al. 2004), and by means of numerical simulations that evolve grains

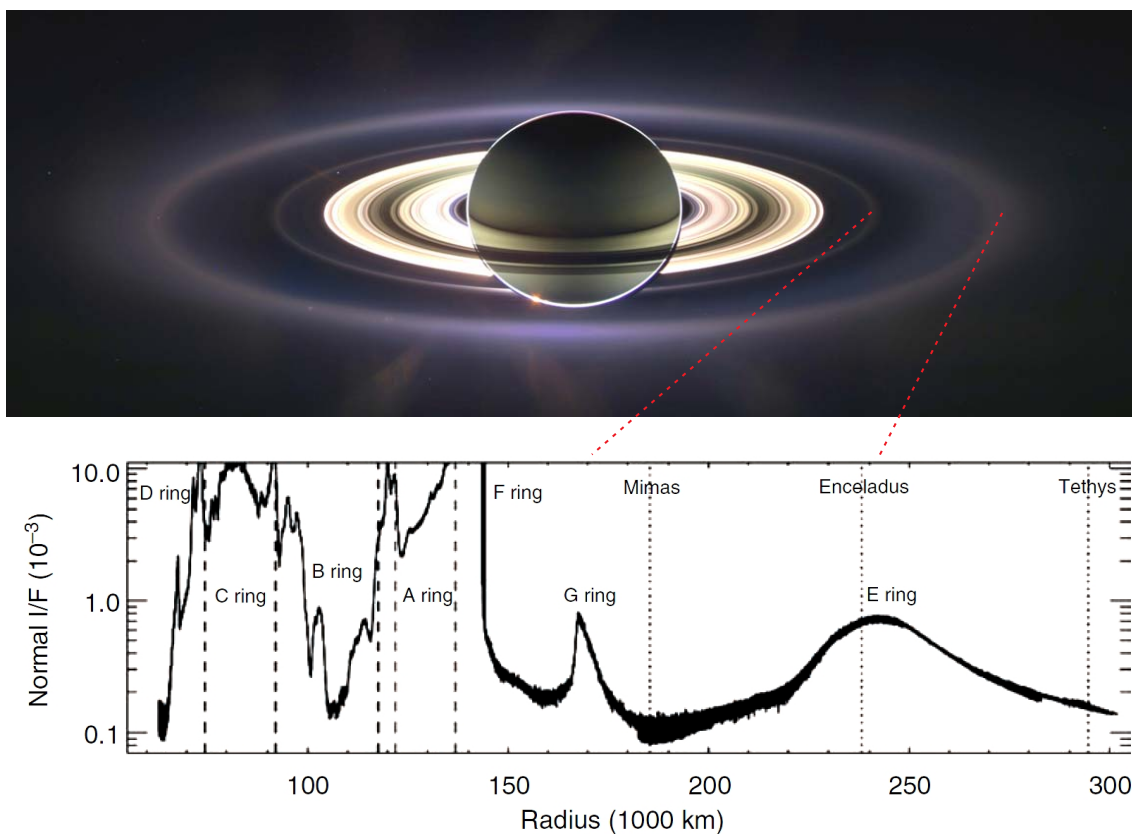


Figure 1.5: *Upper panel:* Mosaic of composite images taken by the ISS instrument while Cassini was in the shadow of Saturn. Colors are derived from images taken in different filters ranging from ultraviolet to infrared. Image courtesy of NASA/JPL/SSI. *Lower panel:* Brightness of Saturn's rings as a function of radial distance. It was measured around 635 nm at constant phase angle. Figure adapted from Horányi et al. (2009).

emitted from Enceladus (Horányi et al. 2008, Beckmann 2008). Additionally, it was explored in-situ by CDA. They found that the density of $> 0.9 \mu\text{m}$ -grains lies within $(1 - 2) \cdot 10^{-1} \text{ m}^{-3}$ at $4R_S$. There, the vertical FWHM (full width at half maximum) of their distribution has its minimum and is approximately $0.07R_S$ (Kempf et al. 2008).

The full size distribution of E ring grains is not known with certainty. The ring's optical spectrum and phase function can be reproduced by a narrow function centered around $1 \mu\text{m}$ (Showalter et al. 1991, Nicholson et al. 1996). However, this is not consistent with in-situ observations and modeling: Cassini's Cosmic Dust Analyzer (CDA) measured a power law size distribution for particles with a radius larger than $\approx 1 \mu\text{m}$ (Kempf et al. 2008). This distribution should extend to smaller sizes since any grain will be eroded due to sputtering. Nevertheless, such small grains should be transient and the power law not applicable below several 10 nm. This is because the grains are positively charged outside $7R_S$ (Kempf et al. 2006) and therefore are accelerated by the corotational electric field (Sec. 1.1) and leave the Saturnian System, possibly within dust streams (Kempf et al. 2005, Hsu et al. 2011). Based on these considerations, we estimate the maximum of the diameter distribution here to be on the order of $0.1 \mu\text{m}$.

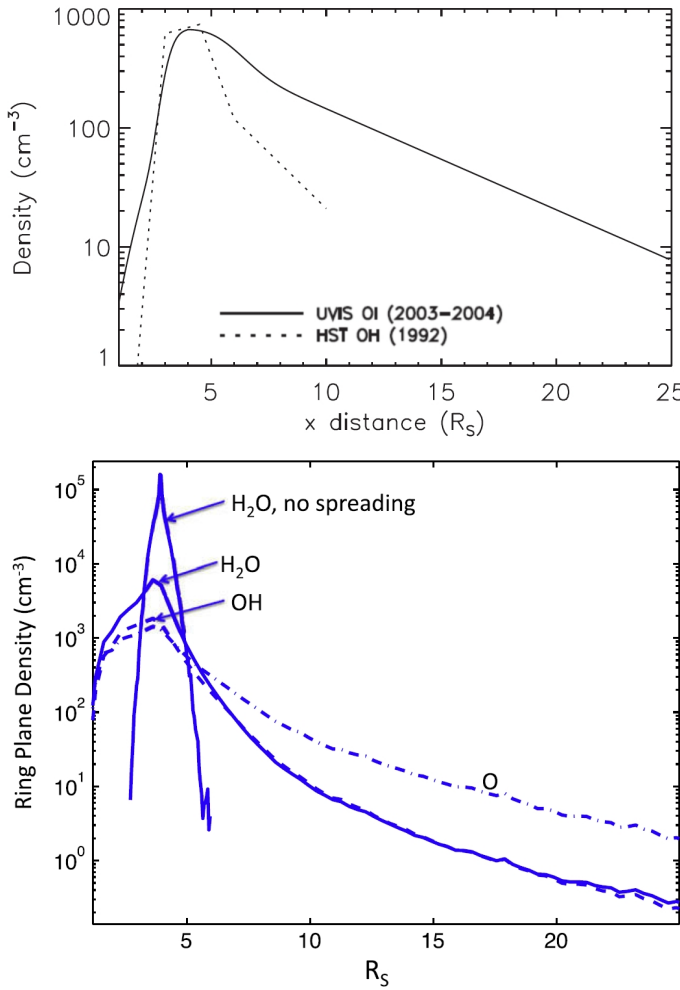


Figure 1.6: *Left panel:* Equatorial density of O and OH derived from optical observations. Figure adapted from Melin et al. (2009). *Right panel:* Equatorial density of OH , O , and H_2O from modeling. Figure from Cassidy and Johnson (2010). Remember that $1 \text{ cm}^{-3} = 10^6 \text{ m}^{-3}$.

Partly coinciding with the E ring is the *Neutral Torus*, first detected by Shemansky et al. (1993). As the E ring derives from the grains of the plumes, the torus mainly derives from their gas (Burger et al. 2007) and has its highest density at the orbit of Enceladus. Sputtering from rings (Jurac et al. 2001a) or surfaces of the icy moons (Jurac et al. 2001b) also contributes to the neutral production and mainly provides H_2O . This is partly dissociated so that also significant amounts of O , H , and OH are present.

Observations of light from atomic or molecular transitions can be used to observe the constituents of the torus. Recently, Hartogh et al. (2011) showed for the first time sub-mm measurements of H_2O at Enceladus consistent with an equatorial density of $8 \cdot 10^9 \text{ m}^{-3}$. Melin et al. (2009) presents measurements of O based on UV observations that yield a density of $0.7 \cdot 10^9 \text{ m}^{-3}$. Another tool to measure the gas is the observation of ENAs that are emitted when the gas interacts with energetic particles. Dialynas et al. (2012) uses this method and reconstructs densities partly at lower values: $1 \cdot 10^9 \text{ m}^{-3}$ for H_2O and $0.7 \cdot 10^9 \text{ m}^{-3}$ for O . Finally, the Neutral Torus can be measured in-situ using INMS. Perry et al. (2010) found that close to Enceladus, but still outside the plumes, the H_2O density is with $85 \cdot 10^9 \text{ m}^{-3}$ very high. 180° away from the moon, on the other side of the planet, the density is only $19 \cdot 10^9 \text{ m}^{-3}$.

Although these gas densities are much larger than the grain densities, this does not mean

that the grains carry a negligible mass. The grains might be rare but they are much more massive than an isolated gas particle.

The gas densities decrease with radial distance from Enceladus' orbit. Recent models (Cassidy and Johnson 2010, Smith et al. 2010) and the observations of Dialynas et al. (2012) show that while H_2O is dominant near $4R_S$, its density decays relatively fast with distance. Several R_S outward of Enceladus, the density of O starts to dominate. Due to Cassidy and Johnson (2010) this occurs at $6R_S$ distance from Saturn. Inward of Enceladus' orbit, the density decays fast because the neutral particles are absorbed at the Main Rings. We consider the distance $3R_S$ here as a proxy of the decay. Dialynas et al. (2012) finds that the H_2O density decays to 70% of the peak value there, but their reconstruction is not sensitive to the density in that region. Other species than H_2O are known with more certainty and decay faster: O to 30% (Melin et al. 2009) and OH to 10% (Richardson et al. 1998). We show several radial density profiles in Fig. 1.6.

Beside the radial changes of the density, also the changes perpendicular to the equatorial plane can be of interest. Hartogh et al. (2011) derived a constant scale height (half width at one over e) of $0.4R_S$. The modeled densities and column densities of Cassidy and Johnson (2010) can also be used to derive this height. If we assume a Gaussian distribution in vertical direction, this yields a scale height of $0.47R_S$ of H_2O at $4R_S$. Models additionally show an increasing scale height with increasing distance outward of Enceladus (Jurac and Richardson 2005). They do not agree how the scale height evolves inward of Enceladus' orbit, which might be because they do not properly account for the losses at the Main Rings so far. INMS is not able to measure the scale height of H_2O and therefore cannot falsify this. Nevertheless, it measured the scale height of CO_2 to be $0.1R_S$.

Finally, the dependence on time is of interest. The source rate of the plumes can vary over one order of magnitude within 20 days (Saur et al. 2008, Smith et al. 2010). At least the density of (27-220) keV ions, which derives from the neutral density, is stable within the time frame of Cassini's mission (DiFabio et al. 2011). Melin et al. (2009) observed the total number of neutral O -atoms over 5 months and also found no significant changes. It can therefore be suspected that the Neutral Torus reacts on much longer time scales than the variability of the plumes and that its density only depends on the average rate at which the plumes eject material.

1.2.3 Charged particles

Besides neutral particles, the environment of Saturn is also filled with charged particles in the *plasma* state (Sec. 2.1.1.1). These particles are important for a magnetosphere since they do not simply move according to the background magnetic field but modify this field in case that they flow in currents.

An extraordinary property of Saturn's environment that is unique within the Solar System is the fact that the plasma density is smaller compared to the density of the neutral material.

Particles in thermal equilibrium have a Maxwell-Boltzmann energy distribution, which is defined by a temperature. It can occur in a plasma that different species have different temperatures since the collision rate amongst particles of the same species can be different to the collision rate between different species.

Although space plasmas can be in stable or quasistable states, their distributions can be

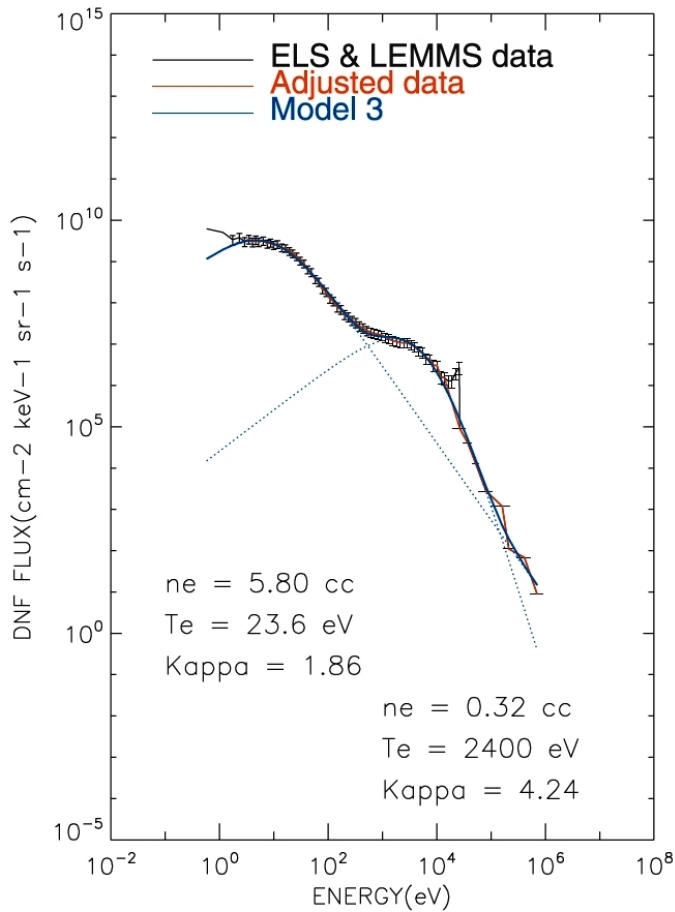


Figure 1.7: Electron spectrum at Saturn taken during a single orbit of Cassini at $9R_S$ radial distance from Saturn’s center. *Black points:* Data from CAPS and LEMMS. *Blue lines:* Fit with two kappa distributions. From [Schipper et al. \(2008\)](#).

far away from thermal equilibrium. A common non-equilibrium distribution is the kappa distribution, which deforms the Maxwellian by adding a high-energy tail. This distribution was originally introduced as a phenomenological fit ([Vasyliunas 1968](#)) and occurs in several modified versions. However, it can also be derived in the framework of statistical mechanics: Systems with long-range correlations can be described meaningfully by the Tsallis entropy ([Milovanov and Zelenyi 2000, Tsallis 2009](#)). From this naturally arises an energy distribution function equal to the kappa function ([Milovanov and Zelenyi 2000, Livadiotis and McComas 2009](#)). It is possible that the energy distribution is described by several kappa functions. Fig. 1.7 shows that this is for example observed for electrons in Saturn’s magnetosphere.

The high-energy tail of a kappa distribution is well approximated by a power law. We will take advantage of this in the following sections. High energies are the regime of *energetic particles* that will be dealt with in this thesis.

The maximum of a plasma’s energy distribution gives the order of magnitude of the thermal energies within the plasma. At Saturn, this lies below 100 eV for both protons ([Thomsen et al. 2010](#)) and electrons ([Sittler et al. 2006](#)). Energetic particles are considered as being well above these energies. In this thesis, we will analyze measurements at energies > 10 keV.

There are several methods to determine the plasma density. With a charged particle detector that is capable of detecting energies near the maximum of the energy spectrum it is possible to infer the total plasma density at all energies. This can be done with CAPS

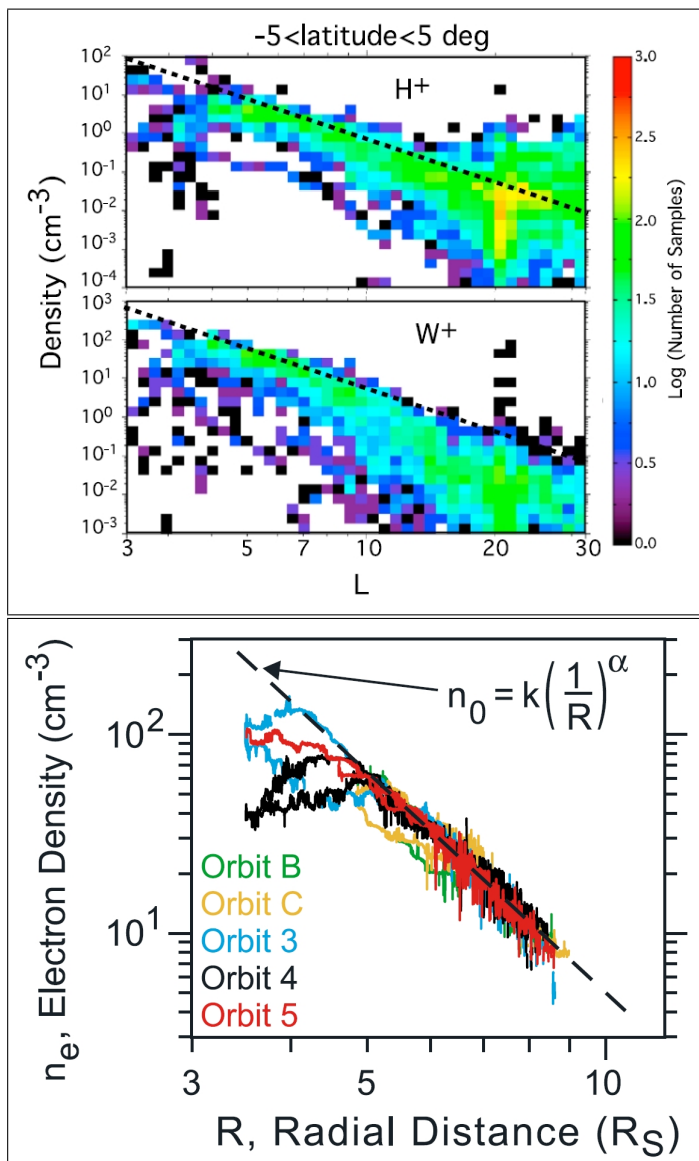


Figure 1.8: *Left panel:* Equatorial density of water group ions (W^+) and protons (H^+) from CAPS. Figure adapted from Thomsen et al. (2010). *Right panel:* Equatorial density of electrons from RWPS. Figure from Persoon et al. (2005).

(Sittler et al. 2006, Thomsen et al. 2010). These results should not be confused with the density of a population within a narrow energy interval, as it will be shown in Figures 4.5 and 4.10. Another method makes use of the electron upper hybrid emission (Persoon et al. 2005), which peaks at a frequency that depends on the electron density, or uses other emission lines as they can be detected by RPWS. Instead of passively detecting electric field fluctuations, characteristic resonances can be triggered actively by RPWS (Wahlund et al. 2005). Also the spacecraft potential can be used to determine the electron density (Morooka et al. 2009). Models can be used to determine the densities of all species (plasma and potentially also neutral) from a subset of densities (as only OH and ion plasma (Jurac and Richardson 2005), or electron density and temperature and ion anisotropies (Persoon et al. 2009).)

Fig. 1.8 shows measured equatorial plasma densities, which are relatively consistent throughout the literature. The density of water group ions and electrons is on the order of 10^8 m^{-3} around $L = 4$ and a magnitude smaller at $L = 7$. (*Water group* refers to water

ions and derivative products, namely O^+ , OH^+ , H_2O^+ , H_3O^+ .) The density of protons is always below that.

2 Physical processes in Saturn's magnetosphere

The entire Sec. 2 is describing processes that are important for energetic particles with keV energies or above.

The plasma and its constituents, which have in magnetospheres typically eV energies, are rich in processes. As long as they do not affect the energetic particles, they are not of interest here, beside one exception. Since plasma is much more abundant than energetic particles, it carries much more charge. This is relevant since charges can flow in currents that produce magnetic fields and by this modify the magnetospheric configuration. Some basic plasma concepts will therefore be introduced in Sec. 2.1.1.

2.1 Interactions of charged particles and fields

2.1.1 Plasma

2.1.1.1 Definition

Plasma is a state of matter. It is a quasineutral gas of charged and neutral particles which exhibits collective behavior. This is different to the other states of matter where only neighboring or colliding particles exert forces on each other.

The charged particles of a plasma are typically ions and electrons, but can in general be all kinds of particles (including quarks, and gluons) or quasiparticles (as holes). Charged dust particles are usually treated separately since their interaction with the environment is complex and poorly understood. Their presence gives rise to the class of dusty plasmas that will not be discussed here.

The term *quasineutral* given above does not simply mean that the total charge of the plasma is zero but that any charge is collectively shielded by the others. If we assume an excess charge within the plasma, then its electric potential will cause the surrounding charges to rearrange. This modifies the potential. The distance where it falls to $1/e$ of the value in vacuum is the Debye length λ_D (Chen 1984, Baumjohann and Treumann 1996)

$$\lambda_D = \sqrt{\frac{\epsilon_0 k_B T_e}{e^2 n_e}} \quad (2.1)$$

with the free space permittivity ϵ_0 , the Boltzmann constant k_B , the elementary charge e , the electron temperature T_e and electron number density n_e .

In a plasma, this shielding occurs on length scales much smaller than the typical extent X of the plasma ($X \gg \lambda_D$). The shielding can only work if there are a significant number

of particles within a sphere with the radius of one Debye length ($S \ll \lambda_D$, with S the average particle distance). The latter is equivalent to the condition that the kinetic and thermal energy of the particles has to be greater than their potential energy in the Coulomb potential of the neighboring charges.

The term *collective* in the plasma definition refers to the possibility of plasma oscillations. If we assume a situation in which all negative charges are displaced relative to the positive ones, this results in an electric potential in which the plasma oscillates with the plasma angular frequency

$$\omega_p = \sqrt{\frac{e^2}{\epsilon_0 m_e} n_e} \quad (2.2)$$

where m_e is the electron rest mass.

Collisions with neutral material damp the oscillations, reducing the plasma's behavior to the one of a mere gas. Therefore, another condition for a plasma state is that the oscillations occur with a higher frequency than the collisions ($\omega_p \gg \omega_c$, with ω_c the collision angular frequency).

2.1.1.2 Diffusing and frozen-in fields

Since plasma consists of charged particles, it modifies electric \vec{E} and magnetic \vec{B} fields. To describe this, we use a form of Ohm's law (Baumjohann and Treumann 1996, Chen 1984)

$$\vec{j} = \sigma_0(\vec{E} + \vec{v}_{\text{mass}} \times \vec{B}) \quad (2.3)$$

with the current density $\vec{j} = ne(\vec{v}_i - \vec{v}_e)$, the conductivity $\sigma_0 = 2\pi e^2 n / (m_e \omega_c)$ parallel to \vec{E} , and the velocity $\vec{v}_{\text{mass}} = (m_i \vec{v}_i + m_e \vec{v}_e) / (m_i + m_e)$ of the mass flow. These equations are valid for a steady state, if $\vec{j} \times \vec{B}$ is small, no pressure or non-electromagnetic forces act, only singly charged ions are present (i.e. $q_i = +e$) and their density is equal to the electrons (i.e. $n = n_i = n_e$). It can be derived from the generalized Lorentz force $\vec{F}_{i,e} = q_{i,e}(\vec{E} + \vec{v}_{i,e} \times \vec{B}) - m_e(\vec{v}_{i,e} - \vec{v}_{e,i})\omega_c/(2\pi)$.

Eq. (2.3) can by the use of Maxwell's equations be converted into the general induction equation (also called dynamo equation)

$$\frac{\partial \vec{B}}{\partial t} = \text{curl}(\vec{v}_{\text{mass}} \times \vec{B}) + \frac{1}{\sigma_0 \mu_0} \nabla^2 \vec{B} \quad (2.4)$$

where μ_0 is the vacuum permeability.

We distinguish between two extreme cases where either the left or the right term on the right-hand side of (2.4) dominates.

In the first case, we assume that the right term dominates. $\vec{v}_{\text{mass}} = 0$ is a sufficient condition for this. In this case, (2.4) has the form of a diffusion equation for \vec{B} , which means that an initial magnetic field distribution will diffuse within the plasma.

In the second case, the left term dominates, which is fulfilled if σ_0 is very large. The motion of the plasma then leads to a change in the magnetic field in a way that can be imagined as if the magnetic field lines would be *frozen* into the plasma which would drag them with it.

Using the Maxwell equations and the frozen-in condition, both (2.3) and (2.4) can be equated into

$$\vec{E} = \vec{B} \times \vec{v}_{\text{mass}} \quad (2.5)$$

This expression implies that plasma moving within a magnetic field creates an electric field.

A measure on which of the two extreme cases is fulfilled is the magnetic Reynolds number R_m

$$R_m = \mu_0 \sigma_0 X u_{\text{mass}} \quad (2.6)$$

R_m is an estimate of the ratio of the left to the right term in (2.4). X is the length scale over which \vec{B} varies. u_{mass} is the typical mass velocity. For $R_m \gg 1$, the magnetic field can be considered frozen-in. This is a common property of space plasmas (that have large X) and fulfilled in most cases relevant for this thesis.

2.1.1.3 Magnetic pressure and tension

The force density exerted on a plasma is described by the momentum equation

$$m_i n \frac{\partial \vec{v}_{\text{mass}}}{\partial t} + m_i n (\vec{v}_{\text{mass}} \vec{\nabla}) \vec{v}_{\text{mass}} = -\vec{\nabla} \tilde{p} + n_q \vec{E} + \vec{j} \times \vec{B} + n \vec{F} \quad (2.7)$$

$n = (m_i n_i + m_e n_e)/(m_i + m_e)$ is the mean number density and n_q the charge density, which is $n_q = e(n_i - n_e) = 0$ considering the assumptions used above. A careful derivation can be found for example in Baumjohann and Treumann (1996). \tilde{p} is the plasma's thermal pressure, and \vec{F} is any non-electromagnetic force as gravity. Scalar products are throughout this thesis written as $\vec{x} \cdot \vec{y}$ without any sign between the vectors.

Using Maxwell's equations we can express the $\vec{j} \times \vec{B}$ -term in (2.7) as

$$\vec{j} \times \vec{B} = -\vec{\nabla} \left(\frac{B^2}{2\mu_0} \right) + \frac{1}{\mu_0} (\vec{B} \vec{\nabla}) \vec{B} \quad (2.8)$$

The first term is of the same form as the $\vec{\nabla} \tilde{p}$ -term in (2.7). Therefore, the expression

$$\tilde{p}_B = \frac{B^2}{2\mu_0} \quad (2.9)$$

is called *magnetic pressure*. It only acts perpendicularly to the magnetic field gradient, since the other component cancels out with part of the second term in (2.8). The remaining part of the second term is (Kivelson and Russell 1995)

$$n \vec{F}_t = -\frac{B^2}{\mu_0 r_c^2} \vec{r}_c \quad (2.10)$$

Since this depends on \vec{r}_c , which is the radius of magnetic curvature, (2.10) is commonly referred to as *magnetic tension*.

2.1.2 Energetic particles

As we have seen in the previous section, the presence of a plasma severely modifies electromagnetic fields compared to the vacuum case. This is different for energetic particles. Since they represent only the tail of the plasma's energy spectrum, they do not represent strong charge- or current-densities. This statement applies not only to the general case but also to the particles analyzed in this thesis, see Fig. 4.10. Therefore, they act similarly as test charges that move within fields without changing them significantly. Also, energetic particles that have velocities much higher than the root-mean-square velocity of the plasma electrons, are not subject of Debeye shielding. Their potential at large distances decays with r^{-3} instead (Neufeld and Ritchie 1955).

In the following, we will discuss the motion that energetic particles undergo under the influence of electromagnetic fields, especially a magnetic dipole field. Scattering with other particles and collective behavior are neglected.

2.1.2.1 Magnetic dipole

The inner part of a magnetosphere is well described as a magnetic dipole field, despite all modifications that were discussed in Sec. 1.1. The dipole field strength is given by

$$B(L, \lambda) = B_S \left(\frac{R_S}{LR_S} \right)^3 \frac{\sqrt{1 + 3 \sin^2(\lambda)}}{\cos^6(\lambda)} \quad (2.11)$$

where λ is the magnetic latitude (with $\lambda = 0$ at the equator) and L the dipole *L-shell*. The latter is a dimensionless quantity. At the equatorial plane it is equal to the radial distance divided by the planetary radius $1R_S$. For higher latitudes, the *L-shell* follows the magnetic field lines.

B_S is the equatorial magnetic field at Saturn's surface. B_S is related to the magnetic moment of Saturn. Depending on the used definition of the magnetic moment, the relation is either $B_S = \tilde{\mu}_S/R_S^3$ (with $\tilde{\mu}_S = 4.6 \cdot 10^{18} \text{ Tm}^3$, Gombosi et al. (2009)) or $B_S = \mu_0/(4\pi) \cdot \mu_S/R_S^3$.

A useful expression that will be needed later is the infinitesimal path element ds along a magnetic dipole field line

$$ds = L \cos(\lambda) \sqrt{1 + 3 \sin^2(\lambda)} d\lambda \quad (2.12)$$

2.1.2.2 Gyration

A particle with charge q that moves with velocity v within a magnetic field \vec{B} experiences the Lorentz force $\vec{F}_L = q(\vec{v} \times \vec{B})$. If the particle moves perpendicular to the field, \vec{F}_L forces the particle on a circular *gyro* motion. In case the particle has a velocity component parallel to the field, the net motion follows a spiral shape. Equating \vec{F}_L with the centrifugal force $\vec{F}_c = \gamma mv_\perp^2 \vec{e}_r/r$ leads to the the gyro radius r_g

$$r_g = \frac{m\gamma v_\perp}{qB} \quad (2.13)$$

with velocity $v_\perp = v \sin(\alpha)$ perpendicular to the magnetic field, local *pitch angle* α between \vec{v} and \vec{B} , Lorentz factor $\gamma = (1 - v^2/c^2)^{-1/2}$, rest mass m , radius r , and unity vector \vec{e}_r .

The relation $v_\perp = 2\pi r_g/T_g$ immediately leads to the gyro period T_g

$$T_g = \frac{2\pi}{q} \frac{\gamma m}{B} \quad (2.14)$$

which is equivalent to the gyro angular frequency $\omega_g = 2\pi/T_g$.

Moving charges are equivalent to a current. Since the gyration is equivalent to a current $I = q/T_g$ around an area $A = \pi r_g^2$, it gives rise to the magnetic moment $\vec{\mu} = I\vec{A} = p^2 \sin^2(\alpha) \vec{B}/(2\gamma m B^2)$, with the momentum $p = m\gamma v$ and \vec{A} a vector of size A that points perpendicular to this area.

For every motion that is periodic in the momentum \vec{p} during the motion \vec{s} , the adiabatic invariant J is conserved (Walt 1994).

$$J = \oint (\vec{p} + q\vec{\mathcal{A}}) d\vec{s} \quad (2.15)$$

$\vec{\mathcal{A}}$ is the magnetic vector potential. This conservation is even fulfilled in case of perturbations that occur on time scales much larger than the integration. Since the gyro motion is periodic, there is an adiabatic invariant associated with it. From (2.15) follows $J_1 = \int_0^{2\pi} p \sin(\alpha) r_g d\phi + \int \vec{B} d\vec{A}$, where ϕ is the gyro phase and the second integral describes the magnetic flux enclosed during the gyration. Simplifying this yields $J_1 = 2\pi m\mu/q$, which is proportional to $\mu = p^2 \sin^2(\alpha)/(2mB)$.

$$\mu = \frac{E(E + 2mc^2)}{2mc^2 B} \sin^2(\alpha) \approx \frac{E \sin^2(\alpha)}{B} \quad (2.16)$$

$E = E_{\text{tot}} - mc^2$ is the kinetic energy, E_{tot} the total energy, and c is the speed of light. The approximation on the right-hand side of (2.16) is valid for non-relativistic kinetic energies E , as it is the case for protons within this thesis.

μ is usually referred to as the *magnetic moment*, although it is only equal to $\tilde{\mu}$ in the non-relativistic limit (Roederer 1970). If the magnetic field varies on scales larger than r_g and T_g , μ is conserved, a fact that will become useful, for example when treating transport processes (Sec. 2.2).

2.1.2.3 Bounce motion

A magnetic dipole field is inhomogeneous. If we consider a charged particle that starts at the equator with a velocity component parallel to the field, its motion will not be a simple spiral since \vec{B} will change in magnitude and direction. In case the particle energy is low enough that the changes occur on scales larger than r_g and T_g , the magnetic moment μ is conserved. It experiences a force $\vec{F} = \vec{\mu} \operatorname{div}(\vec{B})$. Because of this, the particle will lose its parallel velocity, turn around at the *mirror* latitude λ_m , and oscillate along the magnetic field line - a motion that commonly is referred to as *bouncing*.

We calculate λ_m in the absence of electric field components parallel to the magnetic field. In this case both μ and E are conserved for a bounce from λ_1 to λ_2 . From (2.16) then follows

$$\frac{\sin^2 \alpha(\lambda_1)}{B(\lambda_1)} = \frac{\sin^2 \alpha(\lambda_2)}{B(\lambda_2)} \quad (2.17)$$

Due to (2.11), B increases with λ , so that α converges towards 90° . If we set λ_1 to the equator, λ_2 to the mirror point, use (2.11), then (2.17) turns into a transcendent equation for λ_m that only depends on the equatorial pitch angle α_0 :

$$\frac{\cos^6(\lambda_m)}{\sqrt{1 + 3 \sin^2(\lambda_m)}} = \sin^2(\alpha_0) \quad (2.18)$$

The adiabatic invariant associated with the bounce motion can be derived from (2.15). In this case, $\vec{\mathcal{A}}$ does not contribute since the gyro-averaged bounce motion does not enclose magnetic flux.

$$J_2 = 4p \int_0^{\lambda_m} \cos(\alpha) ds \quad (2.19)$$

More convenient than J_2 is the *second adiabatic invariant* $K = J_2 / \sqrt{8\mu m}$ since it is independent of the particle's energy and momentum. If we use $\cos(\alpha) = \sqrt{1 - B/B_m}$ (which follows from (2.17) if we define $B(\lambda_m) = B_m$), K can be written as

$$K = \int_{-\lambda_m}^{+\lambda_m} \sqrt{B_m - B} ds \quad (2.20)$$

2.1.2.4 Drifts

On time scales larger than the gyro and bounce periods, charged particles drift around a planet. These drifts are driven by several forces: The corotational electric field (Sec. 1.1) exerts a force

$$\vec{F}_{\text{corot}} = q\vec{E} \quad (2.21)$$

The gradient of the magnetic field exerts a force

$$\vec{F}_{\text{grad}} = \text{grad}(\vec{\mu}\vec{B}) \quad (2.22)$$

In order to bounce along a curved dipole field line, the particles have to be supported by a centripetal force

$$\vec{F}_{\text{curv}} = \frac{mv_{\parallel}^2}{r_c^2} \vec{r}_c \quad (2.23)$$

where $v_{\parallel} = v \cos(\alpha)$ is the velocity parallel to the magnetic field.

If one adds any arbitrary force F to the Lorentz force and solves the resulting equation of motion, one finds that the particles drift with a velocity (Chen 1984, Baumjohann and Treumann 1996)

$$\vec{v}_F = \frac{\vec{F} \times \vec{B}}{qB} \quad (2.24)$$

This velocity is azimuthal for all forces given above. The direction of motion depends on the charge, except the corotational drift. Keep in mind that such velocities can be converted to angular velocities $\omega = v/r$.

If one calculates the gradient and curvature forces in a dipole field, adds them, and averages their drifts over a bounce period, the combined gradient-curvature drift velocity is

$$v_{\text{grcu}} = \frac{3m\gamma v^2 L^2}{2qB_S R_S} \frac{F}{G} = \frac{3}{qR_S \gamma L} \frac{\mu}{\sin^2(\alpha)} \frac{F}{G} \quad (2.25)$$

$F(\lambda_m)$ and $G(\lambda_m)$ are integrals over a bounce period. They can be found in Lew (1961) together with analytic approximations of them.

The corotation velocity can be estimated from the mean rotation period T_{day} of Saturn, which is difficult to define and to determine for a gas planet. Also, the corotational electric field does not necessarily enforce rigid corotation with the planet. Depending on L -shell, there is subcorotation with up to 70 % of the rigid value (Mauk et al. 2005, Wilson et al. 2008, Müller et al. 2010). We express this with a function $C(L)$.

$$v_{\text{corot}} = C(L) \frac{2\pi L R_S}{T_{\text{day}}} \quad (2.26)$$

The gradient and curvature drifts depend on energy, pitch angle, and L , while the corotational drift only depends on L . For electrons, the gradient-curvature drift is in the opposite direction as the corotation, so that they can cancel out. The relative importance of gradient and curvature drifts relative to the corotation are plotted in Fig. 2.1.

The adiabatic invariant associated with the sum of all drifts is (Walt 1994)

$$J_3 = q\Phi = q \frac{2\pi B_S R_S^2}{L} \quad (2.27)$$

where Φ is the magnetic flux enclosed during the drift around a dipole. It derives from $\vec{\mathcal{A}}$ in (2.15). Since all drifts are relatively slow, \vec{p} was neglected here. Usually Φ is referred to as the third adiabatic invariant. Eq. (2.27) is used as definition of the L -shell and applies also to non-dipolar fields.

2.1.2.5 Rigidity

In the previous sections, we have decoupled the particle motion into three distinct motions that act on different time scales. The particles are trapped in the magnetic field. The total motion, however, is not cyclic in general. In case of a sufficiently high particle energy, this treatment is not valid anymore. For example, if the particle's energy is so high that the particle accesses regions of significantly different fields within a time on the order of the local gyroperiods, there is no gyromotion anymore. In contrast to particles at solar wind energies, such particles might not be sufficiently deflected at the magnetopause and enter the magnetosphere. An estimate for the threshold at which the energy is large enough to achieve that is the vertical *Störmer* cutoff rigidity R_c (Sauer 1980)

$$R_c = \frac{Mc}{4r^2} \cos^4(\lambda) = \frac{Mc}{4L^2 R_S^2} \quad (2.28)$$

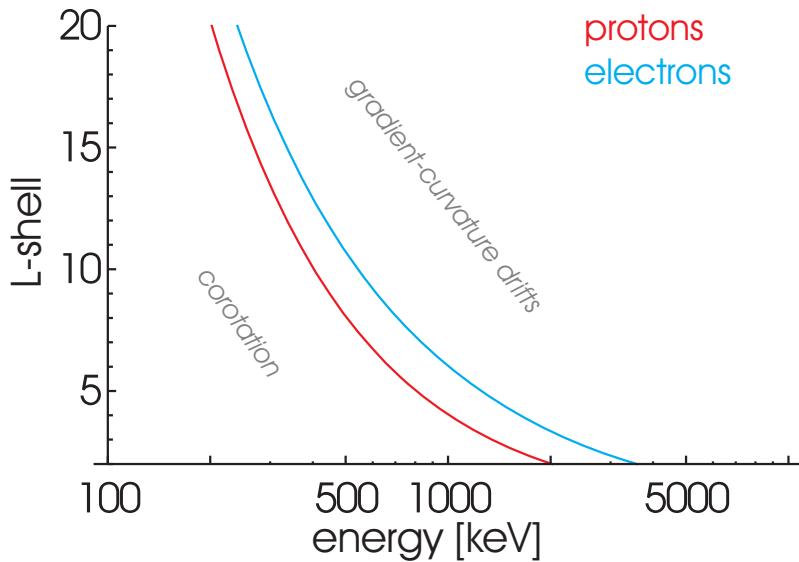


Figure 2.1: Lines show L -shells and energies at which $|v_{\text{grcul}}| = |v_{\text{corot}}|$ is true for equatorially mirroring particles. *Red* describes protons, *blue* electrons. For electrons the two velocities cancel out, due to their signs. For both species corotation dominates at small L -shells and energies. For the calculation, the corotation was estimated to be rigid and with a period of 11 h.

where the rigidity is related to the momentum p (and therefore the kinetic energy E) via

$$R = \frac{pc}{q} \quad (2.29)$$

2.2 Transport

In this section, we will discuss the transport of energetic particles in any direction that should *not* happen according to the previous section. If all assumptions used before were true (static electromagnetic fields, no collisions), the energetic particles would follow the described motions under conservation of the adiabatic invariants μ , K , and Φ and no transport along E , α_0 , or L would occur. Nevertheless, various effects can cause changes in L and other quantities.

The radial transport resulting from this is crucial for magnetospheres with a strong internal plasma source (such as Jupiter and Saturn). In order not to accumulate plasma indefinitely, it has to be removed. Since plasma recombination is negligible in most cases and the planet is too small compared to the magnetosphere to be a sink of large significance ([Vasyliūnas 2009](#)), the plasma has to be transported outward.

One possible mechanism are changes in the present fields. These changes can be either small, stochastic fluctuations, or large-scale changes in the configuration. Fluctuations change the particle motions in a way that the evolution of their distribution can be described in terms of radial diffusion (Sec. 2.2.1). Large-scale changes can for example be transitions from a magnetodisk to a more dipolar magnetic field. In this case, the inward-moving field takes the particles with it (Sec. 2.2.2). Other possibilities for radial transport

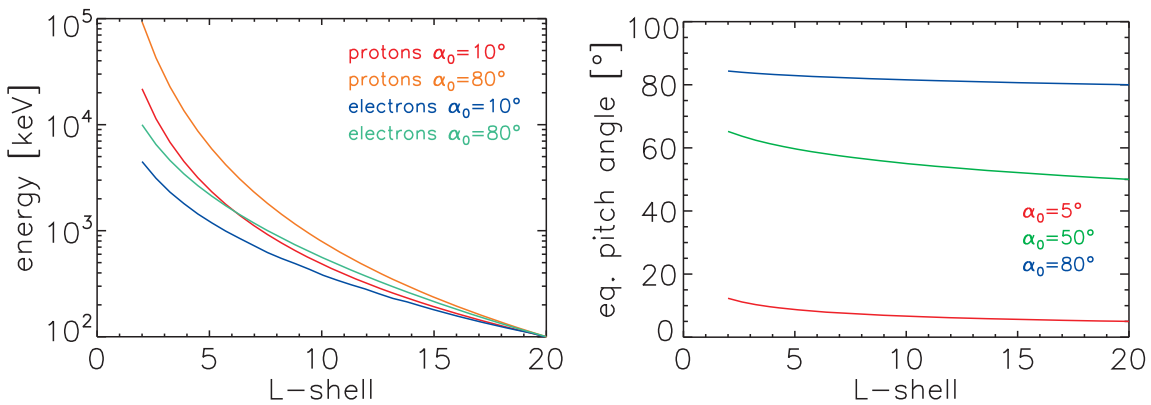


Figure 2.2: Effects of adiabatic transport. *Left panel*: Evolution of energy with L , shown for protons and electrons with different equatorial pitch angles. All particles start at $L = 20$ with 100 keV. *Right panel*: Evolution of equatorial pitch angle with L . This is independent of species and energy.

can be plasma instabilities (Sec. 2.2.3) or collisions with matter (Sec. 2.2.1, 2.3.3, 2.3.4).

All processes, beside the collisions with matter, typically act on time scales that still conserve the first two adiabatic invariants. Interestingly, this not only allows for changes in L , but also changes E and α_0 . This is illustrated first for the special case where the energetic particles start with $\alpha_0 = 90^\circ$ at a given L -shell and energy. Then the adiabatic invariants are $\mu \approx E/B$ and $K = 0$. Since μ is conserved E needs to change with L since B does the same. Moving towards the planet, therefore, increases E , a process that is called *adiabatic heating*. For the general case of $\alpha_0 \neq 90^\circ$ the heating is more complicated to calculate since the conservation of μ and K forms a system of equations that cannot be solved analytically. The method employed here will be addressed in Sec. 4.3. The result is, that α_0 also changes with L and that the change in E becomes larger for $\alpha_0 \rightarrow 90^\circ$. This is illustrated in Fig. 2.2.

2.2.1 Diffusion

Fluctuations of the electromagnetic fields and collisions with matter disturb the energetic particle motions. The resulting change in their distribution can be treated in terms of diffusion. We will focus here on radial diffusion between different L -shells but also introduce pitch angle and energy diffusion.

2.2.1.1 Phase space density

In order to explain transport, first the coordinates have to be explained along which the transport can act. These coordinates are the ones of phase space, which is the combination of real and momentum space. The phase space allows a complete description of the motions of charged particles in electromagnetic fields as they were described in Sec. 2.1.2.

If a large number of particles is considered, it is useful to consider only a density of particles, instead of all single particles. If the particles are evenly distributed in the phases of their motions, the density in phase space is also independent of the phases. (The "phase" of the motion has nothing to do with the "phase" space.) The phase space density (PSD)

then only depends on three independent variables and not anymore on all six dimensions of phase space. These three independent variables can be chosen to be for example the kinetic energy E , the equatorial pitch angle α_0 , and the L -shell, or the adiabatic invariants μ , K , and the L -shell.

An important property for transport in phase space is given by *Liouville's theorem* (Landau and Lifschitz 1975, Walt 1994). It is valid not only for diffusive transport, but as long as the particle motion can be described with a Hamiltonian.

$$\frac{df(\vec{x}(t), \vec{p}(t))}{dt} = \frac{\partial f}{\partial t} + \sum_{i=1}^3 \left(\frac{\partial f}{\partial x_i} \frac{dx_i}{dt} + \frac{\partial f}{\partial p_i} \frac{dp_i}{dt} \right) = 0 \quad (2.30)$$

f is the phase space density and i labels the three dimensions in real and momentum space, respectively. The first equality is an expansion of the total time derivative along a trajectory in phase space. The second equality carries the main information: The phase space density f is constant along a trajectory $(\vec{x}(t), \vec{p}(t))$ for all points in time, in case that no sources or losses occur ($\partial f / \partial t = 0$).

This theorem will be necessary in the derivation of the diffusion formalism.

2.2.1.2 Mathematical description of diffusion

It is assumed now that some process disturbs the initial phase space density f and that the probability to move particles can be described with the function Ψ . More precisely, $\Psi(\vec{x} - \Delta\vec{x}, \Delta\vec{x}, \Delta t)$ is the probability to move particles within the time Δt over a distance $\Delta\vec{x}$ in phase space towards a point \vec{x} . In this case, the PSD evolves in time as (Walt 1994)

$$f(\vec{x}, t + \Delta t) = \int f(\vec{x} - \Delta\vec{x}, t) \Psi(\vec{x} - \Delta\vec{x}, \Delta\vec{x}, \Delta t) d(\Delta\vec{x}) \quad (2.31)$$

Using the Taylor expansion this can be converted to a form of the Fokker-Planck equation

$$\frac{\partial f}{\partial t} = \sum_{i,j} \left(-\frac{\partial}{\partial x_i} \langle \Delta x_i \rangle f + \frac{1}{2} \frac{\partial^2}{\partial x_i \partial x_j} \langle \Delta x_i \Delta x_j \rangle f \right) \quad (2.32)$$

The angular brackets denote an average of the form

$$\begin{aligned} \langle \Delta x_i \rangle &= \frac{1}{\Delta t} \int \Delta x_i \Psi d(\Delta\vec{x}) \\ \langle \Delta x_i \Delta x_j \rangle &= \frac{1}{\Delta t} \int \Delta x_i \Delta x_j \Psi d(\Delta\vec{x}) \end{aligned} \quad (2.33)$$

Using Liouville's theorem (2.30), the Fokker-Planck equation (2.32) transforms to a diffusion equation

$$\frac{\partial f(\vec{x})}{\partial t} = \sum_{i,j} \frac{\partial}{\partial x_i} \left(D_{ij} \frac{\partial f}{\partial x_j} \right) \quad (2.34)$$

where the diffusion matrix D_{ij} was introduced

$$D_{ij} = \frac{1}{2} \langle \Delta x_i \Delta x_j \rangle \quad (2.35)$$

If one wants to change from phase space coordinates \vec{x} to any other coordinates \vec{y} , the diffusion equation (2.34) takes the form

$$\frac{\partial f}{\partial t} = \frac{1}{\mathcal{J}} \sum_{i,j} \frac{\partial}{\partial x_i} \left(\mathcal{J} D_{ij} \frac{\partial f}{\partial x_j} \right) \quad (2.36)$$

with the Jacobian determinant \mathcal{J} . This expression is useful since usually L is used instead of Φ . The Jacobian for this case is $\mathcal{J} = \partial\Phi/\partial L$. If we use this and additionally assume that all diffusion coefficients but D_{LL} are zero, we get the radial diffusion equation ([Schulz and Lanzerotti 1974](#))

$$\frac{\partial f(\mu, K, L)}{\partial t} = L^2 \frac{\partial}{\partial L} \left(\frac{D_{LL}}{L^2} \frac{\partial f}{\partial L} \right) \quad (2.37)$$

In case that the diffusion coefficient follows a power law $D_{LL} = \tilde{D}_0 L^n$, the differential equation in (2.37) is easily solved for most n by a power law ansatz

$$\begin{aligned} f(L) &= AL^{3-n} + B && \text{for } n \neq 3 \\ f(L) &= A \ln(L) + B && \text{for } n = 3 \end{aligned} \quad (2.38)$$

where A and B are parameters that depend on the boundary conditions.

If the coordinates E , $x = \cos(\alpha)$, and L are used instead of the ones above and it is assumed that all diffusion coefficients but D_{EE} and D_{xx} are zero, we get the equation for energy and pitch angle diffusion

$$\frac{\partial f(E, x, L)}{\partial t} = \frac{1}{xT} \frac{\partial}{\partial x} \left(xT D_{xx} \frac{\partial f}{\partial x} \right) + \frac{1}{\gamma p} \frac{\partial}{\partial E} \left(\gamma p D_{EE} \frac{\partial f}{\partial E} \right) \quad (2.39)$$

with $T = T_B p / (LR_S)$ and the bounce time T_B .

2.2.1.3 Magnetic fluctuations

After discussing the mathematical description of diffusion, the next sections treat the physics that can cause it.

Mechanisms driving radial diffusion can be fluctuations of the magnetic or electric fields. If these fluctuations occur on time scales larger than the bounce period, the first two adiabatic invariants will be conserved but not the third and therefore also not L . This leads to *radial* diffusion.

We described the drift velocities in magnetic and electric fields in equations (2.21) - (2.24). While these velocities are purely azimuthal in a magnetic dipole plus radial electric field, they can have a radial component v_r in case of arbitrary fields. Based on the definition of a diffusion coefficient (2.35) the radial coefficient D_{LL} is

$$D_{LL} = \frac{\langle \Delta L \rangle^2}{2} = \frac{\left(\int v_r dt \right)^2}{2R_S^2 t} \quad (2.40)$$

Its dimension is 1/time. In case the L -shell would be a length and not a dimensionless quantity, the dimension would be length-squared per time, which might be expressed in units of R_S^2/s .

Magnetic fluctuations can for example be caused by magnetospheric boundary currents. If these are weak, the magnetic disturbances can be approximated by lower-order spherical harmonics. We therefore assume the magnetic disturbance \vec{b} to be (Walt 1994)

$$\vec{b} = \left(-b_S \cos(\vartheta) - b_A r \sin(2\vartheta) \cos(\varphi) \right) \vec{e}_r + \left(b_S \sin(\vartheta) - b_A r \cos(2\vartheta) \cos(\varphi) \right) \vec{e}_\vartheta + \left(b_A r \cos(\vartheta) \sin(\varphi) \right) \vec{e}_\varphi \quad (2.41)$$

where \vec{e}_i are the unity vectors of the spherical coordinate system (remember that $\vartheta = \pi/2 - \lambda$), and b_A and b_S are time-dependent coefficients. With this it can be shown that

$$D_{LL}^m = \frac{25R_S^2}{329B_S^2} L^{10} \omega_{tot}^2 P_{bA}(\omega_{tot}) \Gamma(\alpha_0) \quad (2.42)$$

ω_{tot} is the angular frequency of all drifts (gradient, curvature, and corotation). At small energies and L -shells, it is dominated by corotation (Fig. 2.1) and therefore energy independent. In the opposite case it is dominated by gradient-curvature drifts (Eq. (2.25)) and scales with $\omega_{grcu} \propto \mu/(\gamma L^2)$, so that $D_{LL}^m \propto L^8$.

P_{bA} is the power spectral density of the autocorrelation of the fluctuation b_A .

$$P_{bA}(\omega) = 4 \int_0^\infty \ll b_A(t) \gg \cos(\omega t) dt \quad (2.43)$$

We used the definition $\ll X(t) \gg = t^{-1} \int_0^t X(t') X(t' + t) dt'$. If X is periodic, $\ll X(t) \gg$ is periodic with the same frequency. A common assumption for the power spectral density is $P \propto \omega^{-2}$. In this case, ω_{tot} cancels out in (2.42) and the diffusion coefficient stays $D_{LL} \propto L^{10}$.

Γ is a function of pitch angle with $\Gamma(\alpha_0 = 90^\circ) = 1$ and $\Gamma(\alpha_0 \leq 30^\circ) \approx 0.1$. A plot of Γ can be found in Walt (1971).

2.2.1.4 Electric fluctuations

Beside magnetic fields, there are also electric fields present in a magnetosphere. This can be the corotational field from the planetary rotation (Sec. 1.1), or a dawn-dusk or noon-midnight field. As long as these fields are static, they only modify the drift paths of the particles. If they fluctuate randomly, this causes diffusion.

A field parallel to the dawn-dusk direction can be produced by processes as the Dungey circle or ionospheric winds. During the Dungey circle (Sec. 2.2.2) frozen-in plasma moves sunward from the magnetotail and by this creates an electric field. Alternatively, strong winds in the ionosphere can modify the usual corotational electric field. Since due to the winds the ionosphere does not strictly follow the planetary rotation anymore, the plasma outside the ionosphere will not do this either. A global wind pattern with high-latitude flows from noon to midnight will impose a dawn-dusk field on the radial one (Brice and McDonough 1973). We will find evidence for a noon-midnight electric field at Saturn in Sec. 6.3.2. Its origin remains a puzzle.

We assume the existence of a electric disturbance \vec{e} that is perpendicular to the dipole field. Only its azimuthal component will cause a radial motion of the particles and is

therefore considered here. It can be expressed via a Fourier series in longitude φ

$$e_\varphi(r, \varphi, t) = \sum_{n=1}^{n_{\max}} e_n(r, t) \cos(n\varphi + \varphi_0) \quad (2.44)$$

e_φ can for example be used to express a dawn-dusk electric field. Setting $n_{\max} = 1$ causes the field to be strongest only in one direction. It will change its sign in the center of the coordinate system. An appropriate choice of the phase φ_0 can align the field along the dawn-dusk or noon-midnight direction.

In case that the particles mainly experience gradient and curvature drift but are not relativistic, the radial diffusion coefficient is (Walt 1994, Schulz 1979)

$$D_{LL}^e = \frac{L^6}{8R_S^2 B_S^2} \sum_n P_{en}(L, n\omega_{grcu}) \quad (2.45)$$

with P_{en} being analog to P_{bA} given in (2.43). In case that $P_{en} \propto L^0 \omega^{-2}$, the diffusion coefficient changes to $D_{LL}^e \propto L^{10} \gamma^4 / \mu^2$. This expression is appropriate for Earth's magnetosphere, and commonly (Beutier and Boscher 1995, Beutier et al. 1995) linearly combined with the expression for diffusion from magnetic fluctuations (2.42).

In the case of Jupiter, such an approach is not adequate since particles corotate instead (with a period T_c) over a wide range in L and energy. Brice and McDonough (1973) derived the diffusion coefficient for corotating, equatorially mirroring particles as $D_{LL}^e \propto L^4 / (T_c R_S^2) \Delta U^2$. ΔU are the average fluctuations of the electric potential during the time the particles need to encircle the planet. If the electric field is caused by winds in the ionosphere (that are strongest at high latitudes), the relation of magnetospheric and ionospheric potential can be assumed to be $\Delta U^2 = \Delta U_0^2 / L$. Substituting this yields

$$D_{LL}^e \propto \frac{L^3}{T_c R_S^2} \Delta U_0^2 \quad (2.46)$$

The expression from Brice and McDonough (1973) for non-relativistic, gradient and curvature drifting particles can be equated to the form $D_{LL}^e \propto L^6 / (B_S^2 R_S^2 \mu) \Delta U^2$. This depends on μ , which contradicts the equivalent equation (2.45) given above.

2.2.1.5 Waves

If field fluctuations occur on time scales similar or faster than the bounce motion, also the first two adiabatic invariants are not conserved anymore. Then, particle energy and equatorial pitch angle as well diffuse, which is quantified by D_{EE} and $D_{\alpha\alpha}$. Additionally mixed types of diffusion occur.

Field fluctuations with sufficiently high frequencies can be a signature of plasma waves. There exists a large variety of waves and different approaches to describe them (Chen 1984, Baumjohann and Treumann 1996) and their interaction with plasma and energetic particles (Walt 1994, Thorne 2010). A detailed discussion is beyond the scope of this thesis, so that we will only discuss one example here.

We consider the interaction between a non-relativistic electron of total velocity v and a wave (with ω and k) that propagates along the magnetic field (oriented along the z -axis) with the group velocity v_G and the phase velocity v_P . The wave causes a magnetic

perturbation

$$\vec{b} = b(\cos(\omega t + kz)\vec{e}_x - \sin(\omega t + kz)\vec{e}_y) \quad (2.47)$$

which induces an electric field. The wave-particle interaction causes pitch angle diffusion which can be approximated with the diffusion coefficient (Walt 1994)

$$D_{\alpha\alpha} = \frac{e^2}{2m^2} \left(1 - \frac{v_p \cos(\alpha)}{v}\right)^2 \frac{v_g}{v_g + v \sin(\alpha)} P_b(\bar{\omega}) \quad (2.48)$$

where P_b is equivalent to (2.43). $\bar{\omega} = \omega_g - kv \sin(\alpha)$ is the resonant frequency of wave and electron. The diffusion in pitch angle is proportional to the diffusion in energy: $\Delta E = (dE/dt)(dt/d\alpha)\Delta\alpha$.

2.2.1.6 Scattering

A completely different reason for the adiabatic invariants not being conserved are collisions with other particles. These can change the energy of the incident particle and deflect it. While the change in energy will be discussed in Sec. 2.3.3 and 2.3.4, the focus here is on deflection. This is most important for electrons encountering ions or nuclei of atoms. Since electrons are 3 - 5 orders of magnitude lighter than nuclei, they can easily be deflected. Nuclei, on the other hand, are barely deflected and only lose energy in such encounters.

The most simple case of deflection is described by Coulomb scattering of two point-like particles with charge q_i . The differential cross section for scattering the projectile to an angle θ relative to its incident direction in the center-of-mass system is (Rutherford 1911)

$$\frac{d\sigma}{d\Omega} = \left(\frac{q_1 q_2}{8\pi\epsilon_0 E}\right)^2 \sin^{-4}\left(\frac{\theta}{2}\right) \quad (2.49)$$

This relation has to be modified if involved particles have an inner structure or because additional particles and forces are present. Even in such cases, the relation holds as a first approximation over a wide range in E and θ . Since $d\sigma/d\Omega$ is largest for small scattering angles, most projectiles are only weakly deflected. The divergence of the Rutherford cross section (2.49) for $\theta \rightarrow 0$ typically does not occur in reality since the involved charges are screened at some distance.

Energetic protons can lose energy to bound electrons but are barely deflected by them due to momentum considerations. Therefore, protons are mainly scattered by nuclei. The bound electrons screen this nucleus but do not further contribute to this process. Electrons are typically scattered more than protons because they have similar masses as the bound electrons. This is even true at the relativistic energies considered here (Jackson 1998).

The mean square angle of the scattering after one encounter is

$$\langle\theta^2\rangle = \frac{\int \theta^2 \left(\frac{d\sigma}{d\Omega}\right) d\Omega}{\int \left(\frac{d\sigma}{d\Omega}\right) d\Omega} \quad (2.50)$$

with the infinitesimal solid angle $d\Omega = \sin(\theta) d\theta d\phi$. If n multiple successive collisions occur, the distribution of the total square angle of scattering will be a Gaussian centered around $\langle\Theta^2\rangle = n\langle\theta^2\rangle$ (Jackson 1998).

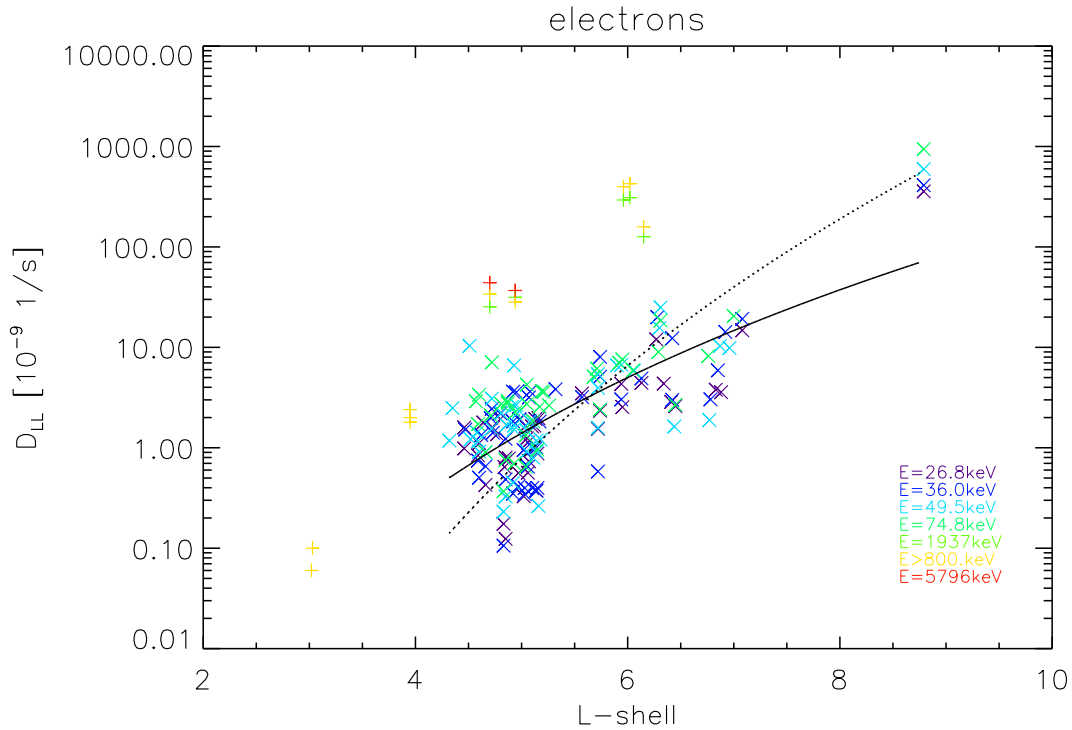


Figure 2.3: Radial diffusion coefficients derived from electron microsignatures of Tethys, Dione, and Rhea. This is the full data set of [Roussos et al. \(2007\)](#). Different *colors* represent different energies, where *x-symbols* represent LEMMS C channels and *+-symbols* E channels. *Black solid line*: power law fit to C channels (they measure low energies within a relatively small interval). *Black dashed line*: power law fit to *L*-bins of the data.

In external fields (as they are present in a magnetosphere), the same relations for scattering can be used. Prerequisite for this is that the particle motions in the external fields occur on such large spatial scales that the angle θ is still well defined. Nevertheless, in our case we are more interested in the change $\langle \Delta\alpha^2 \rangle$ in local pitch angle than the change $\langle \Theta^2 \rangle$ relative to the incidence direction. The pitch angle changes if the encounter modifies the particle's velocity component parallel to the magnetic field. Introducing the resulting $\langle \Delta\alpha^2 \rangle$ into the definition of the diffusion coefficient (2.35) yields $D_{\alpha\alpha}$ from scattering. If scattering only modifies the direction of the perpendicular velocity component, this will only change the gyro phase but not the pitch angle.

2.2.1.7 Measurement

As we have shown now, the diffusion coefficients might be derived from theory if (1) the theory is complete and (2) sufficient experimental data about field fluctuations (over a sufficient frequency range) and material densities were available. This is currently tried by [Lorenzato et al. \(2011\)](#). However, it would be unclear if the used data and theory can reproduce the actual coefficients, so that there is a need for confirmation by experimental

measurements anyway. Such analysis will be either used or carried out here.

One method to experimentally measure the radial diffusion coefficient, independent of its cause, is the observation of electron microsignatures. Electrons can be lost if they encounter a moon during their drift (Sec. 2.3.6). Due to this, the electron intensity measured in the "drift-shadow" of the moon is depleted relative to the environment. This depletion is called a *microsignature*. The depletion refills in time because of diffusion. With knowledge or assumptions of the age of the microsignature and its initial shape it is then possible to derive the diffusion coefficient (Van Allen et al. 1980b). Roussos et al. (2007) applied this method to a large set of microsignatures observed by LEMMS. The resulting coefficients are shown in Fig. 2.3.

The data scatter along L since the microsignatures are often displaced from the orbit of the moon. This, together with the energy width of the used channels and uncertainties of the corotational electric field, causes uncertainties in the age of the signature, which can contribute to the scattering of the D_{LL} values. Further uncertainties are caused by the general variability of the magnetosphere and a deviation of the real initial shape of the depletion with the assumed (square-shaped) one.

A linear fit to the diffusion coefficients, done on a double-logarithmic plot, yields a power law dependence of the diffusion coefficient following $D_{LL} = 0.12 \cdot 10^{-9} \text{ s}^{-1} (L/3.5)^{7.0}$.

The data set only includes one microsignature from Rhea. This is consistent with a positive exponent of the power law i.e. diffusion becoming stronger with L and therefore filling up Rhea's microsignatures faster than the ones of the inner moons. If one assumes that the single D_{LL} value at Rhea is representative and therefore increases its weight in the fit, this can easily change the exponent of the diffusion coefficient to $n \approx 12$.

Another method to determine the diffusion coefficient uses the large-scale distribution of energetic particles, which is partly determined by radial diffusion. This is the approach of this thesis. It is used it in Sections 5.2 and 6.3 and compared to previous works.

2.2.2 Injection events from dipolarization

2.2.2.1 Introduction

Though the term *injection event* is widely used in magnetospheric science, there is a lack of agreement about its precise meaning. We therefore clearly define the term here, accepting that it contradicts some other definitions.

An injection is an intensity enhancement of energetic particles that drifts around the planet and disperses depending on particle energy.

In case that the particle intensity is measured in-situ, the dispersion has the effect that different particle energies are detected as enhanced at different times. Exemplary LEMMS measurements showing this behavior are displayed in Fig. 2.4.

Injects can also be detected indirectly if the intensity enhancement occurs in a region with significant neutral gas densities. In this case, energetic singly charged ions can charge exchange with the gas (Sec. 2.3.2) and produce ENAs that can then be detected remotely. One example for a remotely detected injection is shown in Fig. 2.5. Since ENA images usually show ENAs within a narrow energy, only the drift of the particles is apparent, not the energy dispersion.

Injection events can be explained by a fast radial transport of energetic particles, which

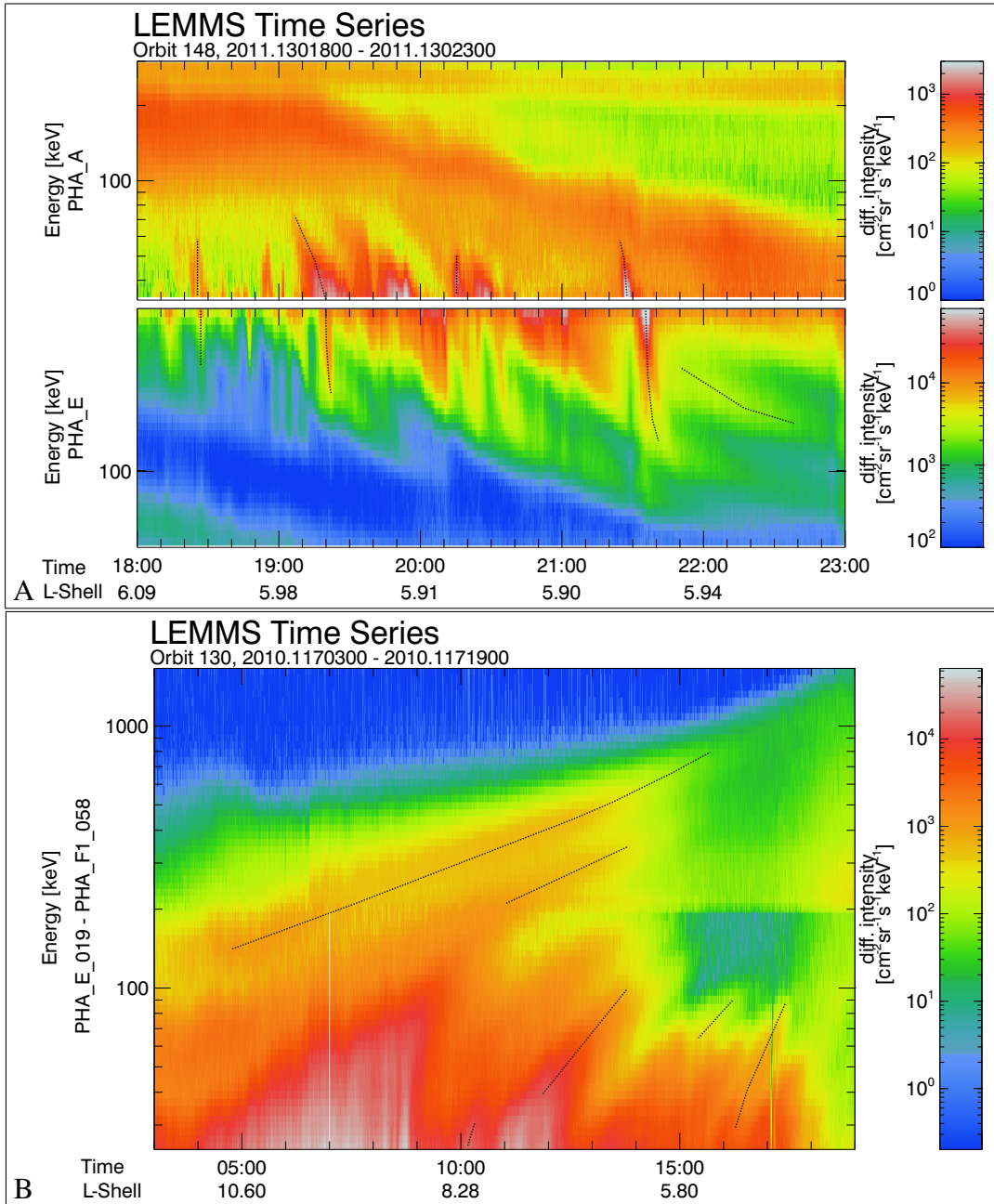


Figure 2.4: Examples of injection events measured by LEMMS. All panels show the evolution of energetic particle intensity (color coded) at different energies in time. Some representative injections are marked with dotted lines to guide the eye. *Panel a* shows both protons (upper panel) and electrons (lower panel). The energy axis of electrons shows the smallest energies at the top. The injections are relatively young so that the lower energies barely drifted. Higher energies drift faster with increasing energy, and in opposite directions for protons and electrons. *Panel b* shows only electrons. The injections at lower energies cover a small spatial scale, while injections at large energies often are large-scale.

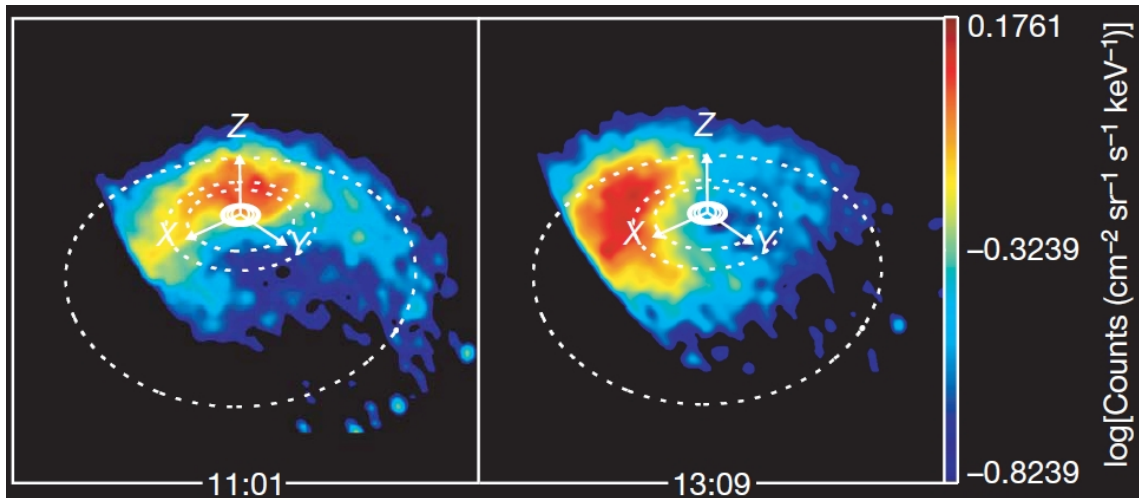


Figure 2.5: Example of an injection event detected remotely by an enhanced ENA emission. The two images were taken by INCA, about 2 h apart from each other. They show the differential intensity of energetic hydrogen atoms with energies between 20 and 50 keV. Saturn is at the center, the z-axis is pointing along Saturn's spin axis, x approximately points towards the Sun, and y completes the set, pointing towards dusk. The dotted lines mark the orbits of Dione ($6.3R_S$), Rhea ($8.7R_S$), and Titan ($20.2R_S$). Figure from [Krimigis et al. \(2007\)](#).

deposits them within an azimuthally confined region. After this, the particles drift (Sec. 2.1.2) around the planet, which is visible in the ENA images. Since most drifts are energy dependent, the injected particles disperse, which can be inferred from the in-situ measurements ([Müller et al. 2010](#)).

In the following, we will discuss two common mechanisms to drive the radial transport resulting in an injection. One mechanism is *interchange* and will be discussed in the following Section 2.2.3. The other mechanism is *dipolarization* of the magnetospheric magnetic field and is discussed here.

To understand dipolarization, one first should point out that magnetospheres are dynamic objects and that the Figures 1.1, 1.2, and 1.3 only sketched typical cases. Especially in their outer part, field configurations and particle populations are varying. One example of a dynamic process is dipolarization.

The magnetic field on the nightside of the planet is typically not dipolar but extended into a tail. Following *reconnection*, this configuration can change back to a more dipolar case. This is dipolarization. Due to the frozen-in condition, plasma and energetic particles are transported towards the planet. These particles then form an injection event.

2.2.2.2 Reconnection

Reconnection occurs if the direction of the magnetic field changes its sign within a small length, as sketched in Fig. 2.6, Panel a. This is the case for example within magnetotails and -disks. In order to sustain this magnetic configuration, a current sheet is required ($j = \text{curl} \vec{B}/\mu_0$, due to Maxwell's equations). If there exists a large but finite conductivity, an initial abrupt change in the magnetic field is smoothed out via magnetic diffusion.

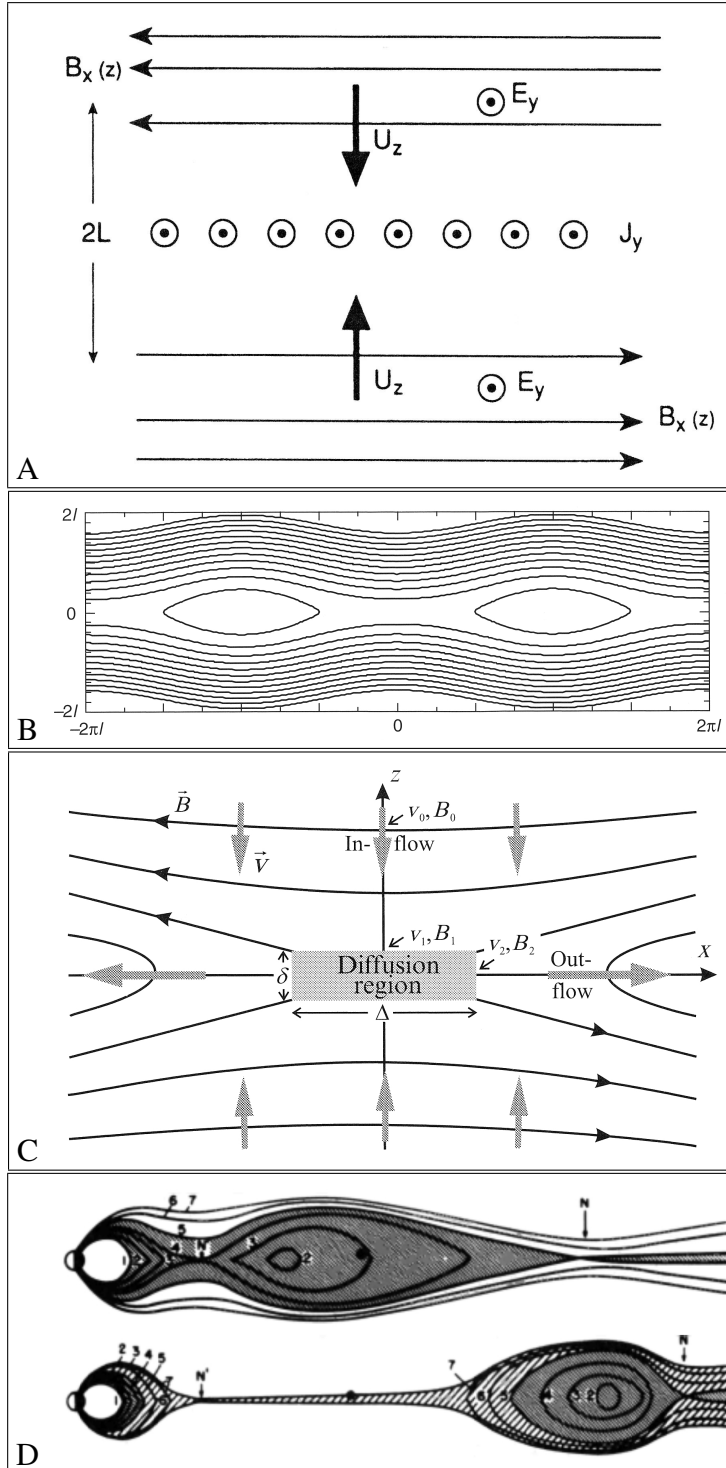


Figure 2.6: *Panel a:* Undisturbed current sheet. (B magnetic field, E electric field, J electric current, u plasma mass velocity. Encircled points indicate vectors out of the plane. From Kivelson and Russell (1995)). *Panel b:* Current sheet after the growth of the Tearing instability. (Lines are magnetic. From Schindler (2006).) *Panel c:* As Panel b but only for $|x| \leq \pi l$ (B magnetic field, v plasma velocity, x is along the current sheet. From Birn and Priest (2007).) *Panel d:* Time evolution after reconnection for the case of Earth's magnetosphere. The field in the vicinity of the planet becomes more dipolar while at the tail side a plasmoid is released. (Lines are magnetic. The small half-black, half-white sphere on the left-hand side is Earth. N refers to reconnection sites. From Hones (1977).)

To drive the current of the sheet, it needs an electric field ($\vec{E} = \vec{j}/\sigma_0$, due to (2.3) with $B = 0$ in the current sheet). A steady state can be achieved if this field is constant in space (due to $\text{curl } \vec{E} = -\partial \vec{B}/\partial t = 0$). In the described \vec{E} - and \vec{B} -fields, the plasma will move towards the current sheet (as described by $\vec{E} = \vec{B} \times \vec{v}_{\text{mass}}$. This follows from (2.3) with $\vec{j} = 0$ outside the current sheet). In the sheet, opposite charges do not move anymore parallel to each other with v_{mass} , but separate there. This produces the current \vec{j} to sustain the current sheet (Kivelson and Russell 1995).

This steady configuration is not stable if the current sheet is thinner than the extent (measured parallel to the sheet) of a perturbation. For an infinite current sheet and a periodic perturbation with wave number k along a current sheet of thickness l , the sheet is unstable for $kl < 1$. This is called the Tearing instability (Furth et al. 1963). Its result is sketched in Fig. 2.6, Panel b. It can be seen there, that the configuration of the magnetic field changed. *Reconnection* occurred at multiples of $2\pi l$. In between, *plasmoids* formed, which are magnetic structures with closed magnetic field lines.

A single reconnection site is sketched in Fig. 2.6, Panel c. As before, plasma moves towards the current sheet, dragging the frozen-in magnetic field with it. At the reconnection site, the plasma changes its direction and moves parallel to the current sheet, dragging the magnetic field with it. At the reconnection site itself, the frozen-in condition is not fulfilled. The magnetic field lines that reach into it can be imagined as torn apart and then reconnected with field lines that reached the site from the other direction.

Again, this situation might be constructed as steady, but usually it is not. Magnetic tension (2.10) tears the two halves of the initial current sheet apart, see Fig. 2.6, Panel d. If the current sheet is part of a magnetotail or magnetodisk, one half will move towards the planet, restoring a more dipolar magnetic configuration (dipolarization). The other half of the magnetic field might be closed to a plasmoid (as in Fig. 2.6, Panel d) or connected to the IMF (as in Fig. 2.7). In any case, it will be released downtail into the interplanetary space.

2.2.2.3 Dungey cycle

The processes that lead to reconnection within a magnetosphere can be different. In case of a solar-wind dominated magnetosphere, as the one of Earth, it is the Dungey cycle (Dungey 1961), which is sketched in Fig. 2.7. It starts when the IMF is directed oppositely to the planetary field (for Earth this means a southward IMF). Then reconnection first occurs on the dayside and merges planetary and IMF field lines. These lines are dragged with the solar wind towards the night side, where they reconnect within the magnetotail. The following dipolarization is called substorm. It partly occurs as soon as the field lines reach the tail. This case is sketched in Fig. 2.7. Partly the tail current sheet stays steady for times on the order of an hour and only after that time reconnection occurs and releases the energy stored in the sheet. This is shown by sketches without IMF. (A more detailed description can for example be found in Baumjohann and Treumann (1996).)

If the IMF is directed differently, reconnection also occurs, but at different positions and without driving the Dungey cycle. Sketches of these cases can for example be found in Dungey (1963) or Birn and Priest (2007).

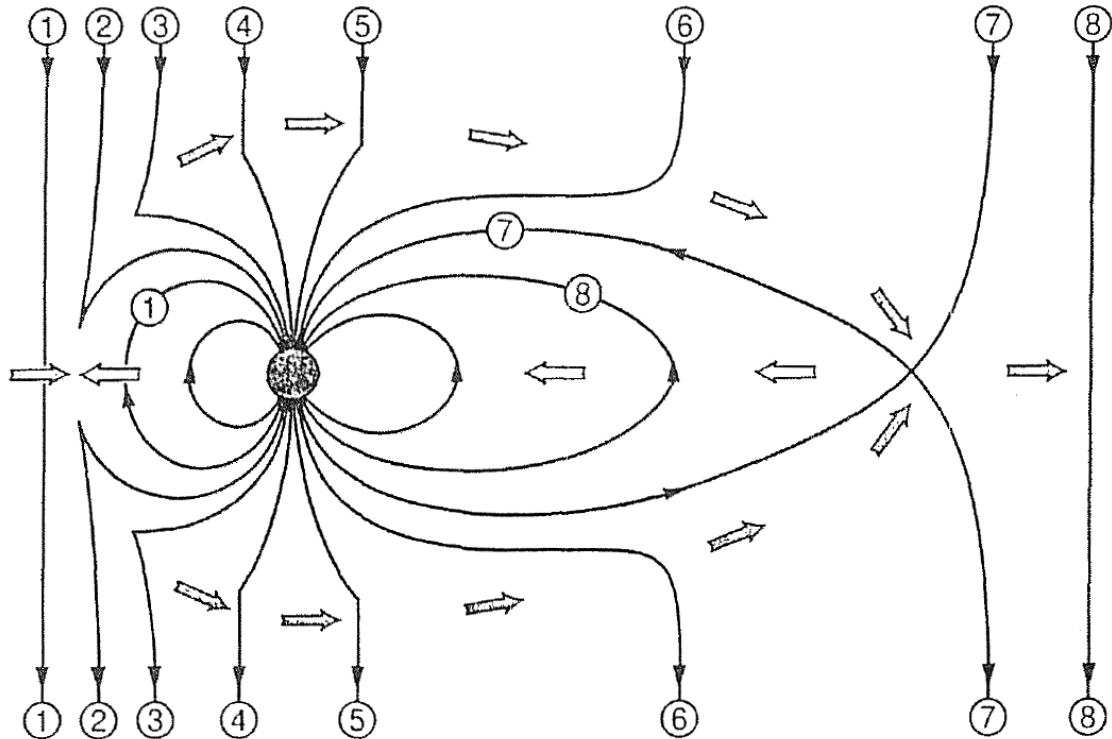


Figure 2.7: Sketch of the Dungey cycle. Lines with arrows show magnetic fields, thick arrows depict plasma flow. A southward directed IMF reconnects on the dayside with the planetary field (line 2), is dragged towards the nightside, and reconnects within the tail (line 7). After this, dipolarization occurs. From [Baumjohann and Treumann \(1996\)](#).

2.2.2.4 Vasyliūnas cycle

In rotationally dominated magnetospheres as the one of Jupiter, the Vasyliūnas cycle is thought to act ([Vasyliūnas 1983](#)). The combination of a fast planetary rotation and a strong internal plasma source creates a magnetodisk. The plasma moves both azimuthally around the planet and radially away from it, in a way that is sketched in Fig. 2.8. This stretches the magnetodisk especially on the nightside until reconnection occurs. Different to Earth, the reconnection is therefore not triggered by the IMF and its orientation. The result, however, is the same: Dipolarization occurs.

2.2.2.5 Reconnection at Saturn

In the case of Saturn, both Dungey- and Vasyliūnas-cycle are thought to exist in parallel ([Cowley et al. 2004](#)) and to be of similar importance ([Badman and Cowley 2007](#)). Signatures of both dipolarization ([Jackman et al. 2008](#)) and released plasmoids ([Jackman et al. 2007](#)) have been identified in the magnetic field data.

Reconnection occurs on spatial scales that are as large as the enhanced ENA emissions shown in Fig. 2.5. It is therefore widely accepted that ENA images show signatures of reconnection, not of interchange events (Sec. 2.2.3).

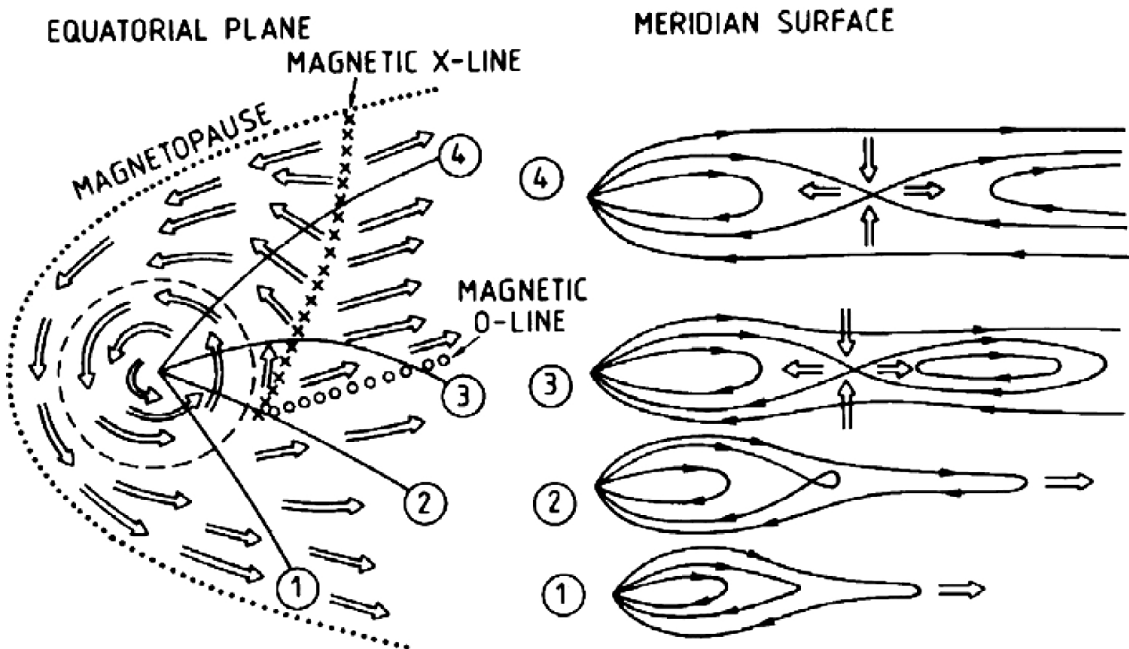


Figure 2.8: Sketch of the Vasyliūnas cycle. Lines with arrows show magnetic fields, thick arrows depict plasma flow. The panels on the right side are cuts along the solid lines shown on the left side. Plasma motion is both azimuthal and radially outward. The outward motion stretches the magnetic field (cuts 1 to 2) until reconnection occurs (cut 3). Then a plasmoid is released and dipolarization occurs (cut 4). From [Vasyliūnas \(1983\)](#).

2.2.3 Injection events from interchange

Another transport mechanism is interchange of flux tubes. A flux tube describes plasma and fields contained in a volume that is aligned with the magnetic field lines. The special case of the *centrifugally-driven* interchange instability is analogous to the Rayleigh-Taylor instability of a dense fluid that is placed in a gravity field on top of a less dense fluid. The situation is unstable since the exchange of the two fluids releases energy. This occurs already after a small perturbation. In the case of a magnetosphere, flux tubes play the role of the fluid and the force is not purely gravitational but includes the centrifugal force. The energy of the flux tubes is gravitational, centrifugal, and thermal.

If the thermal energy is neglected it can be shown ([Southwood and Kivelson 1987](#)) that the configuration is stable against centrifugally-driven interchange for

$$\frac{\partial \eta}{\partial L} > 0 \quad (2.51)$$

$\eta = \int n/B ds$ is the flux tube content. The condition is fulfilled at Saturn for $L > 6$ ([Sittler et al. 2006](#)).

If the thermal energy dominates, there is stability against *pressure-driven* interchange in case that

$$\frac{\partial(pV^{\bar{\gamma}})}{\partial L} > 0 \quad (2.52)$$

$\bar{\gamma}$ is the adiabatic index, which is the ratio of the heat capacity at constant pressure to

the heat capacity at constant volume. Saturn's magnetosphere is stable against pressure-driven interchange ([Bagenal and Delamere 2011](#)).

The plasma temperature at Saturn changes with distance over about two orders of magnitude, being lowest close to the planet ([Sittler et al. 2006](#), [Thomsen et al. 2010](#)). Therefore, the inward-moving plasma is initially hot. Since the interchange is thought to occur on time scales larger than the bounce and gyro motion, the transport is adiabatic, so that the particles further increase their energy when moving into the stronger magnetic field close to the planet. The opposite is true for the outward-moving plasma.

Also the PSD of energetic particles is changing with distance (Fig. 4.8). The average PSD of protons for example increases from $L = 5$ to $L = 10$ by about three orders of magnitude. A flux tube from $L \approx 10$ can therefore transport a significant PSD inward, which then will be observed as an injection event. Indeed, most injections are observed around $L \approx 7.5$, in the region where the PSD is steep ([Chen and Hill 2008](#), [Chen et al. 2010](#)).

Although the occurrence rate of injections is decreasing outward of $L \approx 7.5$, energetic particle injection events can be observed even at larger distances. This is because the magnetosphere is usually not in the average state so that interchange in this region still causes a change in the observed intensities or PSDs. Additionally, observations in the cold < 0.1 keV plasma show the presence of "detached plasma blobs". These can be interpreted as caused by centrifugal interchange ([Goertz 1983](#)).

Interchange typically transports particles only within a spatial region that is small compared to dipolarization. Therefore, such events are probably not visible in ENA images. It can also be safely assumed that the small-scale injections, as we show them in Fig. 2.4, Panel b originate in interchange, not dipolarization. It is difficult to distinguish interchange and dipolarization for large-scale injections if they are detected in-situ. This is because they can be large due to two reasons: First, because they are caused by reconnection, which is a large-scale reconfiguration. Second, because they are energetic. In this case, they are less affected by losses in matter (as they will be discussed in Sec. 2.3), therefore decay slower in intensity, have more time to disperse, and ultimately cover a large range.

Injection events following interchange are not expected to have a preference in local time, contrary to injections from dipolarization that should occur on the night and morning side of the planet. (*Local time* refers to an azimuthal position with 0 h being the angle aligned with the meridian along midnight and 12 h the meridian at noon.) Since most injections originate from the night and morning quadrant of the planet it can be concluded that most observed injections actually follow from dipolarization ([Müller et al. 2010](#)). It is interesting to mention that there appears also to be a local time dependence in the properties of injections. [Müller \(2011\)](#) found a difference in energy integrated intensity and spectral index between two halves of the magnetosphere: injections on the evening side (12 h to 24 h local time), which have a larger contribution from interchange than the morning side (0 h to 12 h local time), are found to be less intense and less energetic.

2.3 Sinks

2.3.1 Influence of sinks on particle profiles

One of the goals of this thesis is to reproduce measured radial particle profiles. Before the different mechanisms that cause losses are discussed (starting from Sec. 2.3.2), we first explain how losses in general modify the spatial particle distributions.

2.3.1.1 Loss within a small azimuthal range

This case is sketched in Fig. 2.9, Panel a. While drifting and bouncing around the planet, the particles encounter a region where they are lost. We assume that this loss can be described with a lifetime τ that is constant (over the full bounce time) and that the loss is much faster than any other process (as sources or diffusion). The phase space density f of the particles then changes over time t as

$$\frac{\partial f}{\partial t} = -\frac{f}{\tau} \quad (2.53)$$

This relation will be thoroughly derived in Sec. 2.3.2. It can be used to determine the time evolution of the phase space density itself, which is

$$f(t) = f_0 \exp\left(-\frac{t}{\tau}\right) \quad (2.54)$$

f_0 is the initial PSD before entering the loss region.

If a flux of particles enters the loss region, one can transform the time dependence in a space dependence by substituting $t = \varphi/(\partial\varphi/\partial t)$, where φ is the azimuth angle within spherical coordinates, equivalent to the local time. With this substitution (2.54) is

$$f(t) = f_0 \exp\left(-\frac{\varphi}{\frac{\partial\varphi}{\partial t}\tau}\right) \quad (2.55)$$

After one revolution around the planet the PSD behind the loss region will become the PSD f_0 *before* it, which can be treated iteratively. If only the loss acts, then f_0 will converge in time to zero. On the other hand, if other processes occur and counter for the losses, it is possible that a steady state is reached.

2.3.1.2 Loss at all local times

Now a different case is considered, where the loss extends within a region in L over all local times. This is sketched in Fig. 2.9, Panel b. The particle motion is now determined by radial diffusion instead of drifts. It is not possible simply to substitute φ with L in Eq. (2.55). This is because the radial particle velocity $\partial L/\partial t$ is not constant (as the azimuthal one is) but coupled to the particle profile which is modified by the losses. We therefore go back to the differential equation of the losses (2.53) and add (2.53) as an additional term to the radial diffusion equation (2.37). The result written in a general form is

$$\begin{aligned} \frac{\partial f}{\partial t} &= L^2 \frac{\partial}{\partial L} \left(\frac{D_{LL}}{L^2} \frac{\partial f}{\partial L} \right) + \left. \frac{\delta f}{\delta t} \right|_S - \left. \frac{\delta f}{\delta t} \right|_L = \\ &= \widehat{D}f + \frac{\delta f}{\delta t} \end{aligned} \quad (2.56)$$

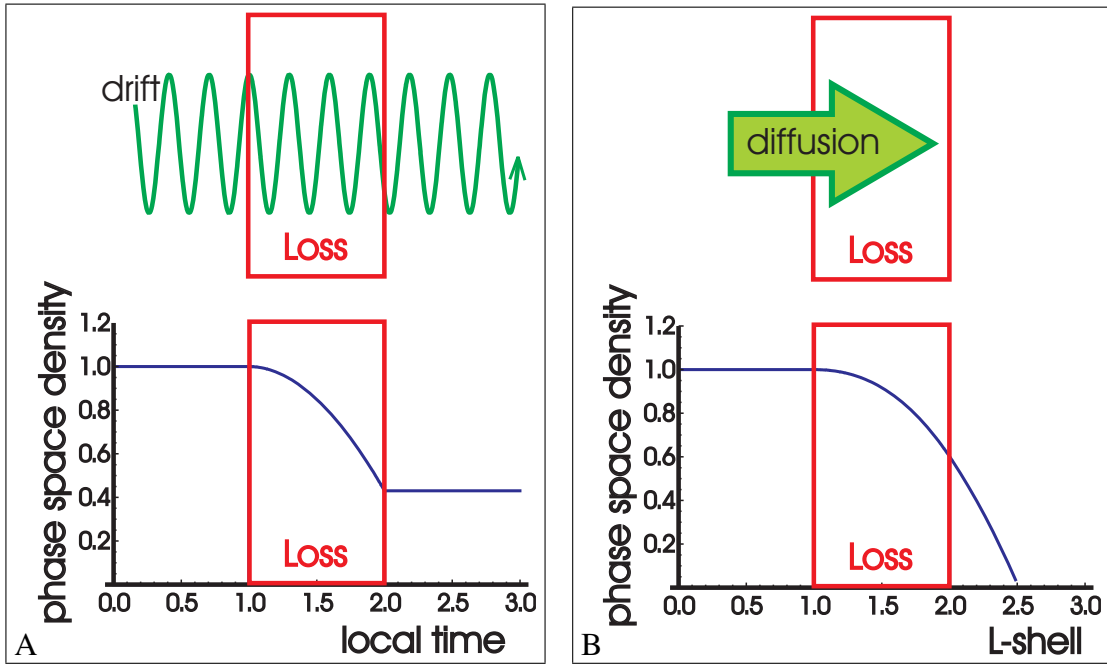


Figure 2.9: Sketch of particles encountering a region with losses. *Panel a:* The particles drift and bounce. Their PSD decays as given by (2.54). *Panel b:* The particles diffuse in L . This decay is given by (2.57). Outside the loss region, the intensity follows (2.38) (using $n = 0$) and therefore changes even far away from the loss region.

We defined here the diffusion operator \widehat{D} for simplicity. $\delta f / \delta t$ describes any changes of f per time that are not included in $\widehat{D}f$. It might be a sum of different processes that can, beside losses $\delta f / \delta t|_L$, also account for sources $\delta f / \delta t|_S$. One example for $\delta f / \delta t|_L$ are the losses we used in (2.53).

In case of a steady state, the PSD does not change over time. Then the rates of all processes on the right-hand side of (2.56) cancel out and the left-hand side is $\partial f / \partial t = 0$.

Such a simplified case can be solved analytically for special cases. One typical case uses the assumption of a constant lifetime τ (as in Eq. (2.53)) and a diffusion coefficient following a power law $D = \bar{D}_0 L^n$. Under these assumptions, it is (Thomsen et al. 1977)

$$\begin{aligned} f(L) &= AL^{(3-n)/2} I_\nu(x) + BL^{(3-n)/2} K_\nu(x) && \text{for } n \neq 2 \\ f(L) &= AL^{1/2+q} + BL^{1/2-q} && \text{for } n = 2 \end{aligned} \quad (2.57)$$

with $\nu = |n - 3|/|2 - n|$, $x = 2L^{(2-n)/2}/(|2 - n| \sqrt{D_0 \tau})$, $q = \sqrt{1/4 + 1/(D_0 \tau)}$, and the modified Bessel functions I_ν and K_ν of order ν . It should be pointed out that this solution only depends on the product of D_0 and τ .

In other cases as for $\delta f / \delta t = S(L)$ (Cooper 1983) or $\delta f / \delta t = f / \tau + S(L)$ (Randall 1994), f can be given at least as an explicit integral. For general cases, (2.56) can be solved numerically.

2.3.2 Charge exchange

Energetic singly charged ions interact with neutral particles essentially via charge exchange (CE). During this process, an electron is transferred from the neutral particle to

the ion. The energies of both particles are changed little. The created neutral particle is, because of its neutrality and high velocity, neither bound to the magnetic nor the gravity field. Therefore, it escapes as an ENA, if it is not stripped again during its exit. Since the created charged particle is below energies that LEMMS detects, we consider charge exchange being a loss process.

The probability that two particles charge exchange can be expressed with the total cross section of this process, which can be measured experimentally. Values for the charge exchange cross section σ can be found in literature for species as H , O , and H_2O but not OH , since this molecule is highly reactive and cannot be studied easily in the laboratory. Theoretical work has been done in calculating cross sections that could also be applied to OH in the future (Houamer et al. 2009). All of the mentioned cross sections exhibit strong energy dependence: between 10 keV and 100 keV, σ decreases by about one order of magnitude, between 100 keV and 1 MeV about four orders. Although σ depends on the species, the differences between them are usually smaller than 1 order of magnitude. Values for the cross section of energetic protons encountering O are based within this thesis on the fit of McEntire and Mitchell (1989). For protons on H_2O we use our own fit to data of various sources (Toburen et al. 1968, Dagnac et al. 1970, Gobet et al. 2001, Luna et al. 2007). The phenomenological function of the fit and the data are displayed in Fig. 2.10. To our knowledge, experimental measurements of these gas species never extend above 1 MeV. If values at these energies are required, we estimate them by extending the fits until there. Since we will find that other effects dominate at these energies, this is not critical.

To calculate the loss rate from CE, we assume that N projectiles (energetic ions) are incident on an area A and pass a medium of targets (neutral particles). This medium has a space-dependent target density $n_g(\vec{x})$. We parametrize the path \vec{x} traversed by the projectiles with the time t , which yields $n_g(t)$. With this, we formally do not have to distinguish anymore if the projectiles travel on a straight line or the complex combination of gyro, bounce, and drift motion.

On average, the N projectiles travel the time T and the distance S until the first one encounters a target. The volume AS is filled with N_g targets. We assume that the target medium is sufficiently dilute, so that the projection of the targets on an assumed plane would not cause overlap. We also assume that a target covers an area σ that we set equal to the charge exchange cross section. Then the total area covered by the targets is $N_g\sigma$ and the probability of hitting a target is $N_g\sigma/A$. This yields the loss ΔN of projectiles per time t (equivalent to distance s) to be

$$\frac{\Delta N}{t} = -\frac{N_g\sigma}{A} \frac{N}{t} \quad (2.58)$$

We conduct a transition from macroscopic to infinitesimal quantities which yields $\delta N/\delta t = -n_g v \sigma N$. For this, we used the velocity $v = s/t$ and the density $n_g = N_g/(A \cdot s)$.

The number of projectiles N can be related to their phase space density f , which is the number of projectiles per volume in phase space: $f = N/(As \cdot \Delta p^3)$. It is then

$$\frac{\delta f}{\delta t} = -n_g v \sigma f \quad (2.59)$$

$\delta f/\delta t$ depends on the (bounce)phase of the projectile motion if n_g does the same. We assume here that the projectiles are evenly distributed in phase so that we will be in any

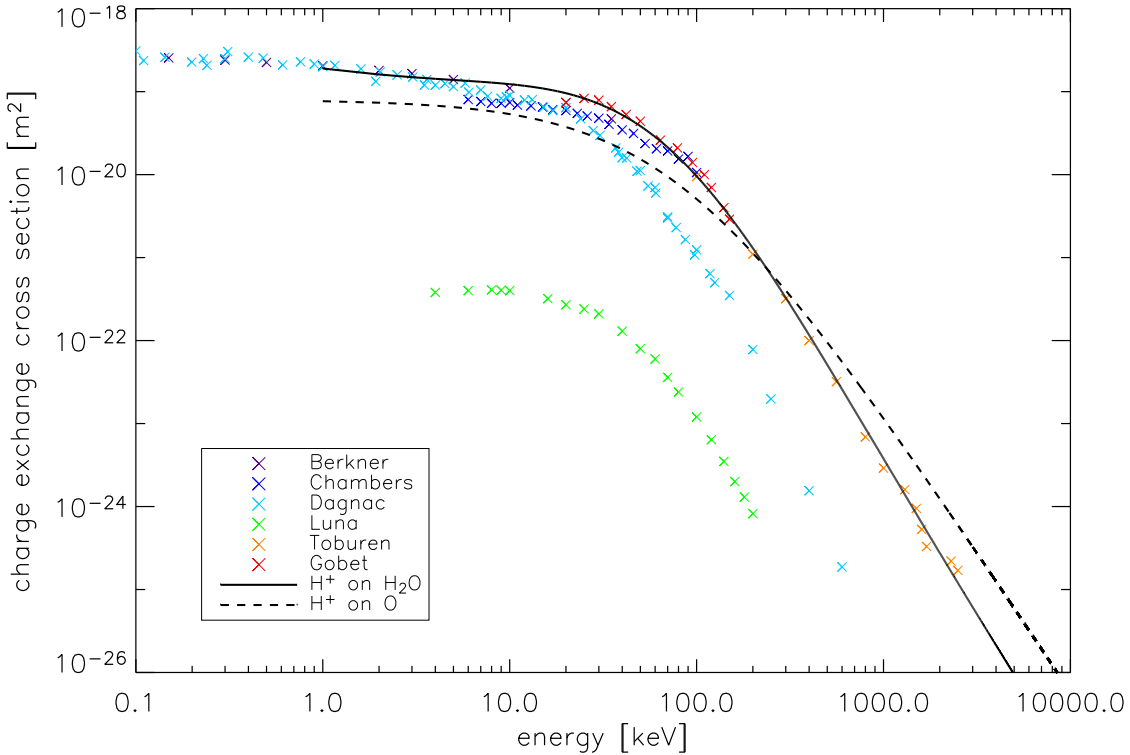


Figure 2.10: Charge exchange cross sections. *Crosses*: Measurements of energetic protons encountering H_2O -molecules from the references given in the legend. *Solid black line*: Fit to these measurements. *Dashed black line*: Fit from [McEntire and Mitchell \(1989\)](#) for energetic protons encountering O -atoms.

case more interested in an phase averaged value of $\delta f / \delta t$. To derive an expression for this, we integrate the diffusion equation (2.56) over a full bounce period:

$$\int_0^{T_B} \frac{\partial f}{\partial t} dt' = \int_0^{T_B} \widehat{D}f dt' + \int_0^{T_B} \frac{\delta f}{\delta t} dt' \quad (2.60)$$

To further evaluate this equation, we have to find the time dependencies of f and n_g . Since we assume a steady state for f and a static density n_g , these quantities do not have a dependence on the time t themselves. Nevertheless will an observer moving in space experience a change of these quantities in time. In order not to confuse these two types of time dependence, we parametrized the spatial coordinates here with the time t' instead of t . To derive the t' -dependence of f and n_g we discuss their spatial distribution first.

We assume the Neutral Torus and n_g to be axisymmetric and therefore constant for all local times. f depends on its phase space coordinates that we express here as $(\mu, K, L, \phi, \lambda, \varphi)$, where ϕ , λ and φ are the phase of gyro, bounce, and drift motion. Due to Liouville's the-

orem (Sec. 2.2.1.1), f can be factorized as

$$\begin{aligned} f(\mu, K, L, g, \varphi, \lambda; t) &= \Theta(\lambda + \lambda_m(L)) \Theta(-\lambda + \lambda_m(L)) \tilde{f}(\mu, K, L; t) \\ &\approx \Theta(\lambda + \tilde{\lambda}_m) \Theta(-\lambda + \tilde{\lambda}_m) \tilde{f}(\mu, K, L; t) \end{aligned} \quad (2.61)$$

where Θ is the Heaviside function, also referred to as step function. The approximation can be used if α_0 is varying slowly with L so that the mirror latitude approximately stays $\tilde{\lambda}_m$. This is valid in the L -range considered here: Particles with $\alpha_0 = 10^\circ$ at $L = 2$ for example change their pitch angle only to $\alpha_0 = 4^\circ$ if they are moved adiabatically to $L = 20$.

Due to the particle motion, all spatial coordinates are time dependent. The gyration causes L and φ to be t' -dependent, but only by a negligible amount. The bounce motion changes λ , which will be the main effect that changes n_g with t' . The drift changes φ but this neither affects f or n_g . Radial diffusion changes L , but on time scales larger than T_B , so that this can be neglected. Therefore, we assume that $\lambda = \lambda(t')$ while all other coordinates stay constant. Equating (2.61) and (2.59) into (2.60) yields the path-averaged diffusion equation

$$\frac{\partial \tilde{f}}{\partial t} \approx \tilde{D}\tilde{f} + \frac{1}{T_B} v \sigma \tilde{f} \int_0^{T_B} n_g dt' \quad (2.62)$$

This expression can be simplified by the definition of the path-averaged target density \tilde{n}_g .

$$\tilde{n}_g = \frac{1}{T_B} \int_0^{T_B} n_g(L, \lambda(t), \varphi) dt \quad (2.63)$$

Keep in mind that the path average over t' is not equivalent to the bounce average over λ . The integration over time weights the latitudes differently. This is important since the particle's parallel speed maximizes at the magnetic equator, so that it experiences the (usually high) density there for only a short time.

Combining (2.62) and (2.63) finally yields the loss term of charge exchange and its lifetime τ_{CE} .

$$\frac{\delta \tilde{f}}{\delta t} = -\sigma v \tilde{n}_g \tilde{f} = \frac{\tilde{f}}{\tau_{CE}} \quad (2.64)$$

2.3.3 Energy loss in grains

This section studies the losses that follow if energetic particles encounter grains, as they can be found in the rings of Saturn. These mostly consist of water ice. If the particles pass through a grain, they lose a macroscopic amount of energy. This is different to the process that occurs within a gas (as in an atmosphere or the Neutral Torus), where the energy loss can be considered as continuous. Although interactions with grains are important at Saturn, they were to our knowledge never treated properly. This was first done in Kollmann et al. (2011b).

The main interaction of energetic particles in our energy range with matter is energy loss due to impact ionization. At the lower and upper end of our energy range, other processes are important. Protons well below our detection limit (< 1 keV) significantly

scatter with the nuclei and transfer parts of their energy to them (Berger et al. 2005). Protons at the lower end of our energy range ($< 100 \text{ keV}$) capture electrons during the passage, which is called neutralization (Kreussler and Sizmann 1982, Mauk et al. 1998). For electrons at the upper end of our energy range ($> 10 \text{ MeV}$), radiative bremsstrahlung losses start significantly contributing to the loss (Berger et al. 2005). Also interaction with photons becomes important i.e. inverse Compton scattering and e^-/e^+ -pair production occur. Protons at these energies lose energy due to inelastic nuclear collisions including pion production (Schlickeiser 2002).

Every energy loss in matter can be expressed by the differential energy loss per distance dE/dx , which is usually referred to as *stopping power* or, more confusing, stopping cross section. Tabulated values of it are commonly normalized to the mass density of the target material. A derivation of the differential energy loss was first given by Bethe (1930). While starting with single atoms and wave functions of all their electrons, it is shown that this complex problem at the end only depends on the density n_e of bound electrons within the medium and the mean ionization energy I necessary to excite them to the vacuum. Generalized to its relativistic form it is (Bethge et al. 2001)

$$\frac{dE}{dx} = -\frac{z^2 e^4}{4\pi\epsilon_0^2 m_e} \frac{n_e}{v^2} \left(\ln\left(2m_e \frac{v^2}{I}\right) - \ln(1 - \beta^2) - \beta^2 \right) \quad (2.65)$$

z is the charge number and v the velocity of the projectile. Although Bethe's formula is commonly used to derive the differential energy loss within solid matter (as ice grains), it can therefore also be applied to very dilute gases (as the Neutral Torus), a fact that will be used in the upcoming Sec. 2.3.4. The only difference between these two cases is a slight difference in I . This is because the electrons of different molecules are not overlapping at all with the neighboring molecules in case of a dilute gas. For a liquid or solid body they do so, which changes the mean ionization energy. For dilute water-gas, it is $I = 70.2 \text{ eV}$, for liquid water, $I = 75.0 \text{ eV}$.

The values of differential energy loss used in this thesis are taken from Berger et al. (2005) and are shown in Fig. 2.11. They account for nuclear, electronic, and bremsstrahlung losses by using theory and experimental values of I . Effects at high energies are not included. We show examples for the differential energy loss in Fig. 2.11. An alternative compilation, but only for protons, may be found in Ziegler (2008).

What makes any energy loss difficult to implement is the fact that a loss in energy is not directly equivalent to a loss of particles. This interaction is therefore a very different from processes as charge exchange or neutralization. To derive the relation between a loss in energy and a loss within a particle population, one first has to define this population. If defined only by the species and the fact that the particles are moving freely, it is necessary for them to lose all of their kinetic energy to be considered as lost. We call the typical time for this to happen *global lifetime* τ^{glob} . This case was usually treated in literature (Thomsen and Van Allen 1979, Van Allen 1983).

The global lifetime is important to characterize the evolution of energetic particles but is not appropriate to explain the decrease of particles with a given energy. The use of an instrument that distinguishes between energies or energy intervals implicitly defines the population not only by species but also by energy. Most instruments do not determine the precise energy of the incident particles but measure the particle intensity within multiple

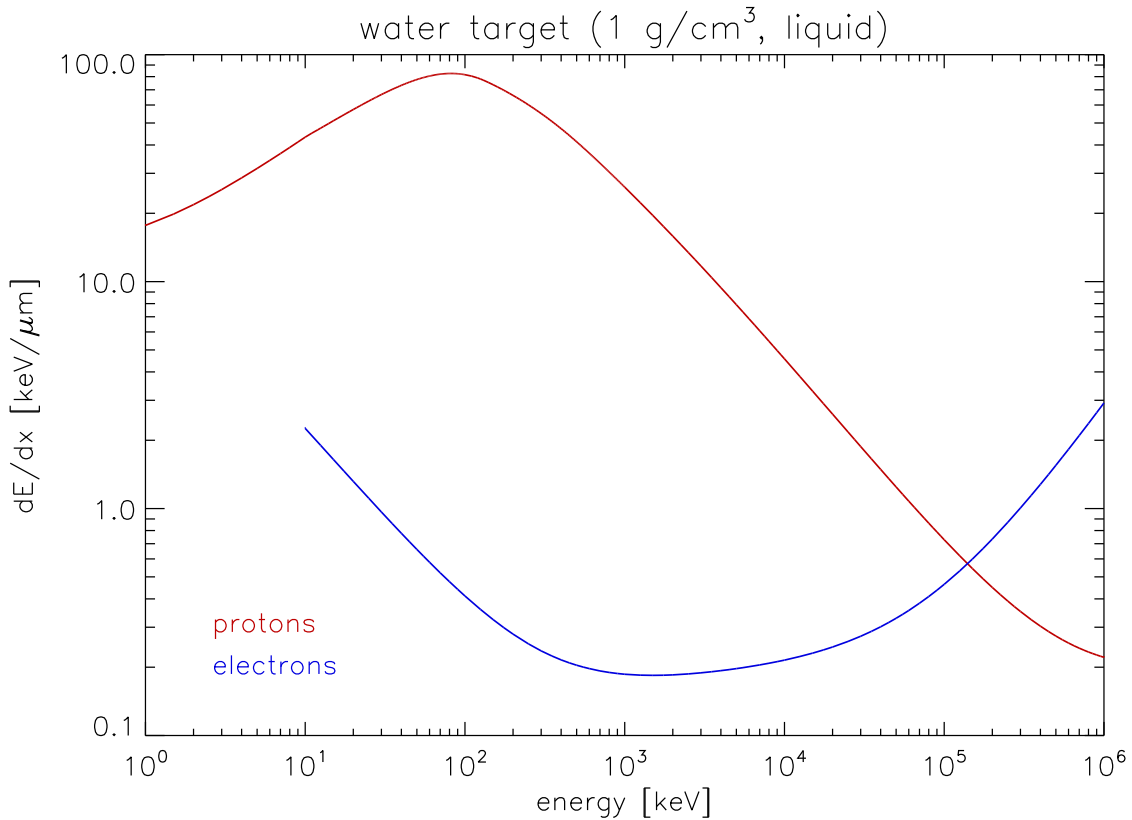


Figure 2.11: Differential energy loss per distance of energetic protons (red) and electrons (blue) in liquid water. Values from Berger et al. (2005).

predefined energy intervals, called *channels*. If a particle loses enough energy to leave such an energy interval, the intensity measured by the channel decreases.

Contrary to the loss it is also possible that particles with initially higher energies than the channel lose energy and reach its energy interval. This increases the intensity. (An exception is the case where the particles overshoot because they lost too much energy within a grain.) Depending on the energy spectrum, energy loss can therefore act as a loss or source process for a given channel. We call the typical time to enter or leave a channel the *channel lifetime* τ .

The loss and source rates of the phase space density of a given channel are derived now. For this, we use the results of charge exchange (Sec. 2.3.2), where one encounter with a target was enough to lose the projectile. In contrast to this, the interaction with ice grains can require several encounters until the projectile has lost enough energy to leave the range of the channel used to measure it. Therefore, we generalize our equations to the case where M encounters are necessary to lose a projectile.

A sink term can often be expressed as phase space density multiplied with a factor of the dimension 1/time. This time is usually defined as the lifetime τ .

$$\frac{\delta f}{\delta t} = -\frac{f}{\tau} \quad (2.66)$$

Since this is a definition it can hold also for phase space densities with definitions different to f , like \tilde{f} .

The expression and derivation for the charge exchange lifetime given in (2.64) also works for the average time for a single encounter with an ice grain of radius r_r . The only thing that has to be changed is that the charge exchange cross section σ has to be replaced by the geometric cross section σ of the ice grains. The time for M encounters to happen is then

$$\tau = \sum_{k=1}^M \frac{1}{v_k \sigma \tilde{n}_r} = \frac{M}{\tilde{v} \sigma \tilde{n}_r} \quad (2.67)$$

v_k is the projectile velocity before the k^{th} encounter. \tilde{v} is the effective velocity during all M encounters. In this thesis, we consider only the contribution of *typical* grains. We define these as grains of cross section σ , where τ is minimum and therefore affects the particle profile most. Equation (2.67) could be generalized for a distribution of grain sizes by integrating over σ .

To calculate $M_{L,S}$ the following expression is used

$$\Delta E = \int_0^X \frac{dE}{dx} dx \quad (2.68)$$

X is the distance that the projectile would have to traverse within an ice block until it has lost the energy ΔE and leaves the channel. The value of M is calculated from this by

$$M = \text{rnd}\left(\frac{X}{\varnothing}\right) \quad (2.69)$$

$\varnothing = 2r_r \cdot 2/3$ is the average diameter of a grain. The factor $2/3$ takes into account that not every grain is hit centrally. Since we only consider grains of one size here, we use the function `rnd` that rounds its argument up.

Equation (2.67) calculates the *energy lifetime* τ for projectiles with a precise energy. It does not describe a population of particles measured by a detector channel. A channel measures the average phase space density $\langle f \rangle$ of a population within an energy range from E_i to E_o (with $E_i < E_o$). The population within this channel has an average channel lifetime $\langle \tau \rangle$. The channel-averaged phase space density calculates as

$$\langle f \rangle = \frac{\int_{E_i}^{E_o} f dE}{\int_{E_i}^{E_o} dE} \quad (2.70)$$

The loss of $\langle f \rangle$ per time is the channel average of the loss of f per time

$$\frac{\delta \langle f \rangle}{\delta t} = -\left\langle \frac{f}{\tau} \right\rangle = \frac{\int_{E_i}^{E_o} (f/\tau) dE}{\int_{E_i}^{E_o} dE} \quad (2.71)$$

Up to now only particles were considered that are lost from an energy interval after encountering grains. Now particles are included that enter this interval. The source rate of this calculates similar as the loss rate. The PSD of particles entering the channel per time

is $\int_{E_i}^{\infty} (f/\tau_s) dE$, where $\tau_s(E)$ is the time to reach the channel from E on. (An important detail is that the energy loss within a single grain might be in a way that the channel cannot be reached from any energy E .) To get the channel-averaged source rate from this, we have to divide the previous expression by the width of the channel, which is $\int_{E_i}^{E_o} dE$.

The source competes with the loss. To get the *net* channel-averaged lifetime $\langle\tau\rangle$ of particles within a channel, we have to sum over both effects.

$$\begin{aligned}\frac{\delta\langle f \rangle}{\delta t} &= \left(- \int_{E_i}^{E_o} \frac{f}{\tau_L} dE + \int_{E_o}^{\infty} \frac{f}{\tau_s} dE \right) \Big/ \int_{E_i}^{E_o} dE = \\ &= \frac{n\sigma}{E_o - E_i} \left(- \int_{E_i}^{E_o} \frac{v f}{M_L} dE + \int_{E_o}^{\infty} \frac{v f}{M_S} dE \right) = -\frac{\langle f \rangle}{\langle \tau \rangle}\end{aligned}\quad (2.72)$$

The first term of the sum is the channel loss rate. We renamed τ given in (2.71) to τ_L , because this equation described only the pure loss. The second term is channel source rate. The net rate is given by the complete sum.

The net rate is related to the net channel lifetime. This is written as $\langle\tau\rangle$ to make clear that it describes the whole channel. Nevertheless, it is not a channel-averaged value as $\langle f \rangle$ that could be derived formally the same as within (2.70).

The higher the initial energy of a particle, the larger the number M_S of encounters necessary to enter a specific channel. Also, high-energy particles are typically less abundant due to the spectral shape. Both decreases the contribution of high energies to the source process. Because of this, the integration to determine the channel lifetime in (2.72) does not have to extend until $E \rightarrow \infty$ to achieve convergence. This is useful, since we have measured intensities only until finite energies.

2.3.4 Energy loss in gas

Now we consider the case that the energy loss acts continuously within a gas. For this, we consider that the energetic particles have a momentum \vec{p} and a number density n . One can express this via the phase space density f with

$$n = f d^3 p \quad (2.73)$$

If the particles along their trajectory continuously change their energy but not their direction, as it is approximately fulfilled for energy loss in a gas, n will be constant, but the infinitesimal volume $d^3 p$ at \vec{p} in momentum space will move and change in size. We can describe this by using spherical coordinates $d^3 p = p^2 dp d\Omega$ and replacing the interval dp in momentum by an interval in time $dp = dt dp/dt$. Since we are free to consider the intervals dt and $d\Omega$ in time and space angle as constant, a fixed density is equivalent to the expression

$$\frac{d}{dt} \left(f p^2 \frac{dp}{dt} \right) = 0 \quad (2.74)$$

This expression is related to the energy loss per distance dE/dx via

$$\frac{dp}{dt} = \frac{dE}{dx} \quad (2.75)$$

due to $dp/dt = dp/dE \cdot dE/dt$, $dp/dE = 1/v$ (which is true for the non- as the relativistic case), and $dE/dt = v dE/dx$.

If we insert (2.75) into (2.74) and expand the total time derivative there, we find (Kollmann et al. 2011a)

$$\frac{\partial f}{\partial t} = -\frac{v}{p^2} \frac{\partial}{\partial E} \left(p^2 f \frac{dE}{dx} \right) = \frac{f}{\tau_{\text{Ex}}} \quad (2.76)$$

where τ_{Ex} is a mere definition. An equivalent expression without derivation can be found in Schulz and Lanzerotti (1974).

The energy loss of particles moving through a plasma can be calculated to first order in the same manner. Since the energies considered here are much larger than the mean ionization energy I (going into the calculation of dE/dx), the fact that an electron is bound becomes a second-order effect. Also, the electric field of particles with energies much larger than the thermal energy of a plasma is not screened by this plasma (Neufeld and Ritchie 1955). This means that the plasma represents itself to the energetic particles as a mere gas.

2.3.5 Scattering into the loss cone

Pitch angle diffusion due to any process redistributes particles in pitch angle. If one considers only a pitch angle interval, some intervals might experience a net gain or net loss in particles. This is equivalent to the energy channels that were discussed in Sec. 2.3.3. In this section, particles lost energy until they approached $E \rightarrow 0$, where they became lost to the population of freely moving charges. The equivalent in pitch angle diffusion is $\alpha_0 \rightarrow 0$. If the pitch angle becomes smaller, the mirror point is shifting towards higher latitudes and lower altitudes. For very field-aligned particles the mirror point lies within the dense atmosphere. In the atmosphere, the particles experience the same processes as described in Sections 2.3.2 and 2.3.4 but with much higher neutral densities, generating a very efficient loss.

If we define that the loss occurs exactly when the particles mirror at an altitude of $1R_s$ (equivalent to a magnetic field equal B_s) all particles with equatorial pitch angles smaller α_L are lost. This angle defines the *loss cone* and can be calculated with (2.16).

$$\alpha_L = \text{ArcSin} \left(L^{-3/2} \right) \quad (2.77)$$

Assuming that the pitch angle diffusion is so strong that an arbitrary PAD would become isotropic latest within half a bounce period, then during every half-bounce a fraction of particles would be lost. This fraction is equal to the ratio of solid angle $2\pi(1 - \cos(\alpha_L))$ of the loss cone to the solid angle 2π of the particles incident to the planet. Since this process occurs during $T_B/2$, the lifetime due to *strong pitch angle diffusion* loss is (Schulz and Lanzerotti 1974, Gombosi et al. 2009)

$$\tau_{\text{PA}} = \frac{T_B}{2(1 - \cos(\alpha_L))} \quad (2.78)$$

This expression is a factor 2 larger for small α_L than the one given by (Kennel and Petschek 1966).

A mechanism that can cause scattering to the loss cone is given at the end of the following Section 2.3.6.

	mean radius [km]	semi-major axis [R_S]	eccentricity
Janus	95.0	2.51	0.0068
Epimetheus	58.1	2.51	0.0098
Mimas	198.2	3.08	0.0196
Enceladus	252.1	3.95	0.0047
Tethys	533.0	4.89	0.0001
Dione	561.7	6.26	0.0022
Rhea	764.3	8.75	0.0010

Table 2.1: Comparison of size and orbit of different Saturnian moons. Values from [Matson et al. \(2009\)](#) and [Thomas \(2010\)](#).

2.3.6 Losses at moon orbits

A moon can also cause losses of energetic particles. In case that the moon is non-conducting and atmosphereless, the particles are simply absorbed if they encounter the body of the moon. This absorption can be treated by considering the moon as a large grain in which the incident particles lose energy until they are completely stopped. The probability to encounter a moon has to be calculated differently from in case of homogeneously distributed grains. We will discuss absorption and its probability in this section. Moons that relevant for this thesis (because they are large enough and orbit in the region of interest) are listed together with some characteristics in Tab. 2.1.

The mean period τ_{enc} of a particle coming at least close to the moon is determined by the particle's total azimuthal motion ω_{tot} (usually separated in gradient-curvature drift ω_{grcu} and (sub)corotation ω_{corot} , see Sec. 2.1.2.4), and the moon's Keplerian motion ω_{kepler} .

$$\tau_{\text{enc}} = \frac{2\pi}{\omega_{\text{grcu}} + \omega_{\text{corot}} - \omega_{\text{kepler}}} \quad (2.79)$$

The mean time τ_{mo} until the particle is actually lost is larger than τ_{enc} since it can escape for different reasons that one can account for by introducing several absorption efficiencies a_i

$$\tau_{\text{mo}} = \frac{\tau_{\text{enc}}}{a_D a_G a_R a_L} \quad (2.80)$$

For all these factors it is $0 \leq a_i \leq 1$.

If the particle is bouncing and the bounce length Λ_D that it covers during half a bounce period in the equatorial plane is approximately larger than the moon's effective size \mathcal{O}_{eff} , it *leapfrogs* over the moon and escapes absorption. The effective size of the moon is larger than its diameter $\mathcal{O}_{\text{mo}} = 2r_{\text{mo}}$. This is because the particle is already absorbed when reaching a distance to the moon's center that is smaller than $\mathcal{O}_{\text{eff}} = 2(r_{\text{mo}} + r_g)$. The absorption efficiency a_D despite leapfrogging is ([Thomsen et al. 1977](#))

$$a_D = \begin{cases} \frac{\pi}{4} \frac{\mathcal{O}_{\text{eff}}}{\Lambda_D} & \text{for } \Lambda_D \geq \mathcal{O}_{\text{eff}} \\ \frac{1}{2} \left(\sqrt{1 - \frac{\Lambda_D^2}{\mathcal{O}_{\text{eff}}^2}} + \frac{\mathcal{O}_{\text{eff}}}{\Lambda_D} \arcsin \left(\frac{\Lambda_D}{\mathcal{O}_{\text{eff}}} \right) \right) & \text{for } \Lambda_D < \mathcal{O}_{\text{eff}} \end{cases} \quad (2.81)$$

with the bounce length $\Lambda_D = v_{\text{azi}} T_B / 2$, and the bounce-averaged azimuthal velocity $v_{\text{azi}} = L_M R_S (\omega_{\text{grcu}} + \omega_{\text{corot}})$.

Even if the particle's gyro center enters \mathcal{O}_{eff} , the particle itself can still evade the moon due to its gyro motion. If the particle is equatorial, it will encircle the moon if the distance $\Lambda_{G,e}$ that it traverses during half a gyro period in the equatorial plane is larger than the moon. If the particle has a mirror latitude λ_m above the latitudinal extent λ_{mo} of the moon, it can *corkscrew* around it when the distance $\lambda_{G,f}$ that the particle travels in latitudinal direction during a full gyro period is larger than the moon (Hood 1983).

$$\begin{aligned} a_G &= \frac{\mathcal{O}_{\text{mo}}}{\Lambda_{G,e}} \quad \text{for } \lambda_m < \lambda_{\text{mo}} \\ a_G &= \frac{\mathcal{O}_{\text{mo}}}{\Lambda_{G,f}} \quad \text{for } \lambda_m \geq \lambda_{\text{mo}} \end{aligned} \quad (2.82)$$

with $\Lambda_{G,e} = v_{\text{azi}} T_g / 2$, $\Lambda_{G,f} = v_{\parallel} T_g$, $v_{\parallel} = v \cos(\alpha_0)$.

In case that the moon's orbit is eccentric or the magnetic field azimuthally asymmetric, the moon will sweep a corridor in L that is even larger than \mathcal{O}_{eff} . If the particles move within this corridor for a time τ_{enc} they will come close to the moon but are only absorbed with a probability (Paonessa and Cheng 1985)

$$a_R = \frac{\Delta L_{\text{mo}} R_S}{\mathcal{O}_{\text{eff}}} \quad (2.83)$$

Since Saturn's magnetic field is dipolar and therefore very symmetric within the radiation belts (Smith et al. 1980), ΔL is only determined by the moon's eccentricity as given

$$\Delta L_{\text{mo}} = 2r_M + 2e_M L_M R_S + 4r_g \quad (2.84)$$

Thomsen et al. (1977) gives another expression than (2.83) but it yields similar results.

At planets like Jupiter with a magnetic equator not parallel to the orbital plane of the moons, another factor a_L has to be considered. It is attributed to this that equatorially mirroring particles in a setup of this kind have the longest lifetimes. At Saturn, equatorially mirroring particles behave oppositely: they have short lifetimes since they have less options to escape a moon. We therefore set $a_L = 1$.

Paonessa and Cheng (1985) calculated lifetimes for protons by the use of Monte Carlo simulations instead the analytic expressions above. Their values typically deviate (in both directions) by less than a factor of 2. Even in extreme cases, the difference is less than an order of magnitude and will therefore not significantly affect the results in the upcoming Sec. 5.2.

Electrons at the energies and in the regions considered here have gyro radii and bounce lengths that typically are much smaller than the moons (Roussos 2007). Therefore, they cannot escape by the means described above, as ions do. This can make their absorption relatively efficient. Nevertheless, they can escape due to their azimuthal velocity. The gradient and curvature drifts of electrons at Saturn are in the opposite direction than the corotation direction. This is because the drift depends on the particle charge and the direction of the planet's magnetic axis to the rotation axis, see Sec. 2.1.2.4. For electrons, there exist combinations of (L, E, α_0) where the total azimuthal velocity is zero or equal to the velocity of the moon. In the latter case, (2.79) diverges and the electrons keep a constant distance to the moon.

A comparison of proton and electron lifetimes against moon absorption is given in Fig. 2.12.

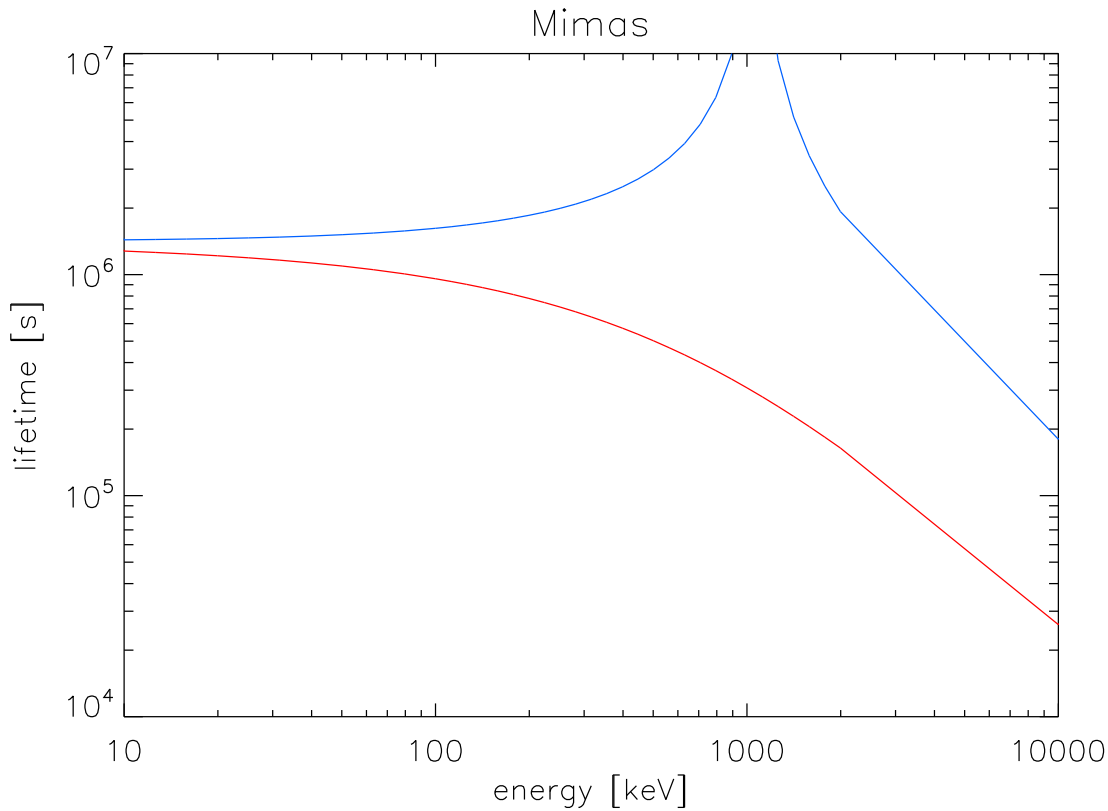


Figure 2.12: Lifetimes of equatorially mirroring protons (*red*) and electrons (*blue*) against absorption along Mimas' orbit. The calculation is based on the assumption of rigid corotation. Electrons are resonant with Mimas at $E \approx 1$ MeV.

Although absorption is the process usually considered as the relevant loss process at moons (see references above), it is not the only one possible. As a result of the particle absorption at a moon, the pitch angle distribution will be anisotropic along field lines connected with the moon: there exist particles bouncing into the direction of the moon, but since they are absorbed, there are no particles coming back. This anisotropy can cause whistler-mode waves that in the following cause pitch angle scattering. It is therefore a mechanism for the process described in Sec. 2.3.5, where particles are driven into the loss cone and are lost. Since whistler waves do not necessarily move parallel to the field, this loss can even act on particles outside the close vicinity of the moon. Indeed, whistler waves and beams of < 1 keV field-aligned electrons have been recently observed near the moon Rhea (Santolík et al. 2011).

Another type of waves that can be excited by conducting moons are Alfvén waves. These can carry field-aligned currents, which then cause auroral features that are referred to as *moon footprints*. This is probably best known for Jupiter's moon Io (Clarke et al. 2004) but was also recently observed at Enceladus (Pryor et al. 2011). In the Enceladus case, beams of electrons (< 1 keV) and ions (≈ 70 keV) causing the observed footprint were detected in-situ. Both for Enceladus and for Rhea it was not studied so far if the

intensity of particles following the field lines is significant i.e. that this interaction causes a *strong* loss. Additionally, since no beams above 100 keV have been observed so far, the losses following from them can be assumed to be unimportant for the LEMMS energy range, which is analyzed in this thesis.

2.4 Sources

2.4.1 Non-diffusive transport

In order to reproduce radial particle profiles with a model, this model needs to account for all relevant effects acting on the energetic particles. In the previous sections we provided expressions to describe the rate of PSD change due to diffusion (Sec. 2.2.1), and various losses (Sec. 2.3). Using the radial diffusion equation (2.56), these rates could be used to derive radial profiles if only these effects would occur. Nevertheless, there are two classes missing: the non-diffusive transport, and real source processes.

Diffusive transport causes a diffusive flux j_D that scales as (van Milligen et al. 2005)

$$j_D = \frac{\partial(D_{LL}f)}{\partial L} \quad (2.85)$$

The transport flux from dipolarization (Sec. 2.2.2), however, does not depend on $\partial f / \partial L$ at all. Interchange occurs if the flux tube content or pressure profiles show a certain L -dependence (Sec. 2.2.3). We are not aware of an expression that would relate the size and frequency of interchange events to the gradient of such profiles. It is therefore doubtful that D_{LL} could be constructed in a way that it reproduces the transport flux from injections.

Also, radial diffusion refills moon microsignatures. It is not clear that injections can do the same. They might displace the signatures instead (Roussos et al. 2010). Even if they do not: the observed refilling of microsignatures is consistent with a steady process. Since injections occur sporadically, they can not account for this.

Instead of including injections somehow in the diffusion coefficient, we will treat them throughout this thesis as a source process instead. To reproduce the radial profiles it is not important how exactly the non-diffusive processes work. For this it only matters at which rate the processes change the PSD per time i.e. how many particles they deposit at one L per time. Since we will not study instantaneous particle profiles (which could not be measured with one spacecraft anyway) but long-time averages, it even does not matter if the deposition is continuous or sporadic. Knowledge about average rates is enough.

Although this is the right approach, we are not aware of a method to derive such rates for injection events from theory. We will derive them therefore experimentally, based on measurements and several assumptions concerning the other processes (Sec. 5.2 and 6.2).

2.4.2 CRAND

Beside the possibility to transport particles to a given L -shell, particles can also be created there by conversion from another particle type. Mechanisms for this are given here and in the following sections.

One mechanism to create energetic protons is by cosmic ray albedo neutron decay (CRAND) (Singer 1958). This process is fed by galactic cosmic rays with energies of

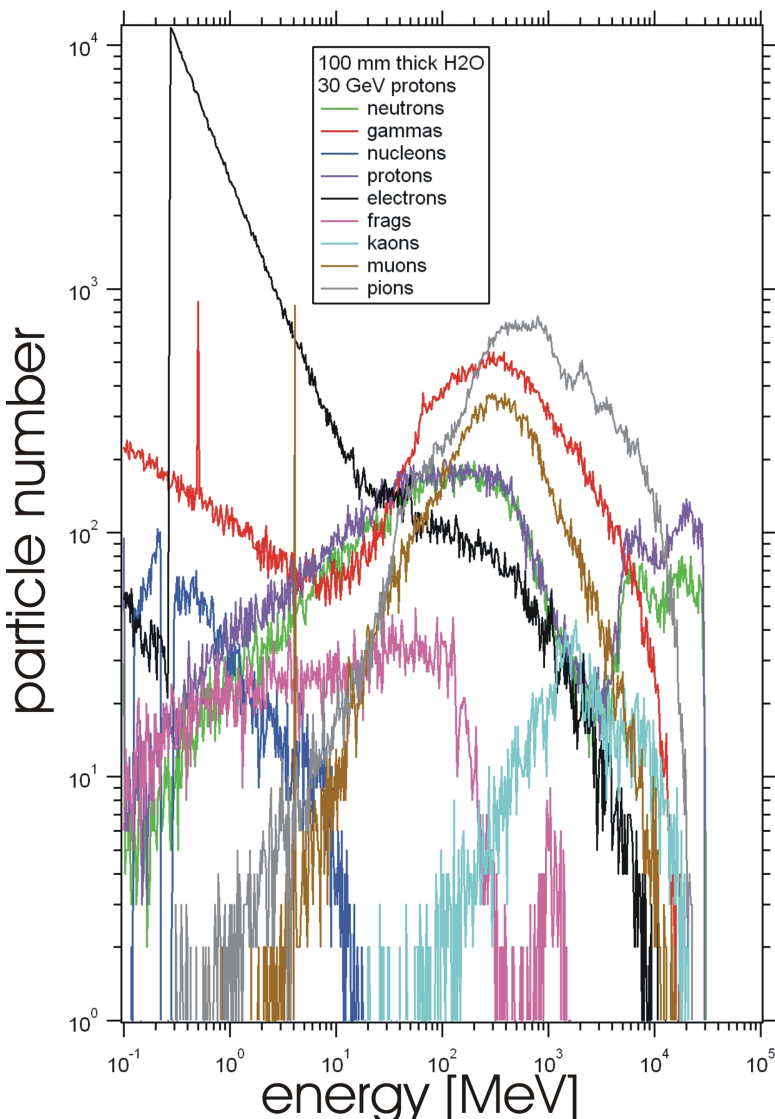


Figure 2.13: Spectra of particles produced by 30 GeV protons passing through a 10 cm thick slab of water. This GEANT-4 simulation was provided by D. K. Haggerty (2011).

several 10 GeV. This is large enough to enter the magnetosphere (Sec. 2.1.2.5), where the particles can impact into material of and around Saturn. This creates a large variety of secondary particles, partly at much lower energies. These particles include neutrons, protons and other particles such as photons, electrons, pions, and various antiparticles, see Fig. 2.13.

The charged protons bounce and are bound to the magnetic field lines. The bounce motion causes periodic reencounters with the material that produced them. During every encounter, they lose energy or undergo charge exchange (Sec. 2.3) until they are ultimately lost again. This is different for the neutrons that are moving freely. Most of them simply escape the vicinity of Saturn but due to their lifetime of $\tau_n \approx 881.5$ s (Nakamura and the Particle Data Group 2010), some of them also β^- -decay within the magnetosphere and create a population of tertiary protons. The latter is known as the CRAND process.

CRAND is a common process within the Solar System. It is for example known from cosmic rays impacting Earth's atmosphere (Hess et al. 1959, Goldhagen et al. 2002), Earth's moon (McKinney et al. 2006, Ota et al. 2011), and Saturn's rings (Cooper 1983,

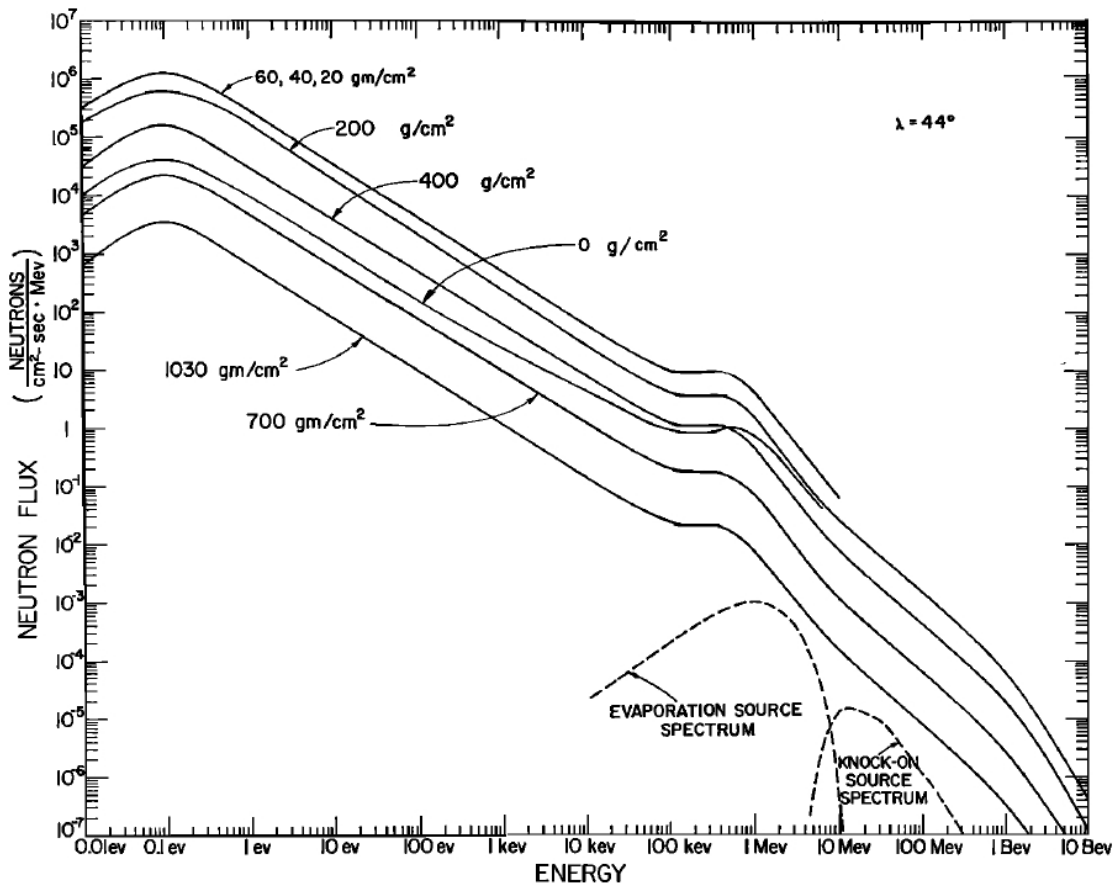


Figure 2.14: Neutron energy spectrum in Earth’s atmosphere complied by [Hess et al. \(1961\)](#). Different solid lines show intensities at different heights expressed in terms of column density. Dashed lines sketch the two source process of the neutrons.

[Blake et al. 1983](#)). Neutrons produced in Saturn’s atmosphere have been discussed ([Cooper and Simpson 1980](#)) but their intensities have not been calculated so far.

The neutrons are created from cosmic rays via two processes ([Serber 1947, Roesler et al. 1998](#)). The cosmic ray first knocks off nucleons from the target nucleus. This excites the remaining core that relaxes by emitting more nucleons. (The latter process is also referred to as *evaporation* of nucleons from a heated core.) The two processes act at slightly different energies around 1 MeV, as displayed in Fig. 2.14.

After production, the neutrons interact with the surrounding material. This decelerates them so fast to lower energies that most of the neutrons are not observed at their initial energy but within a wide range of lower energies. The resulting spectrum is a power law $j_n \propto E^{-\gamma_n}$, with j_n the neutron differential intensity. It scales exactly with $\gamma_n = 1$ when the neutron deceleration is energy independent and no losses occur ([Oldekop 1975](#)). This is approximately fulfilled in many cases as Earth’s atmosphere ($\gamma_n \approx 0.9$), the lunar surface, or nuclear reactors ([Goldhagen et al. 2003, McKinney et al. 2006, Hess et al. 1959](#)).

At energies on the order of eV, the neutrons are captured again, causing their intensity to drop. Only a few neutrons are produced at 100 MeV energies, but since the atmosphere becomes transparent for neutrons there, another peak forms at these energies ([Roesler](#)

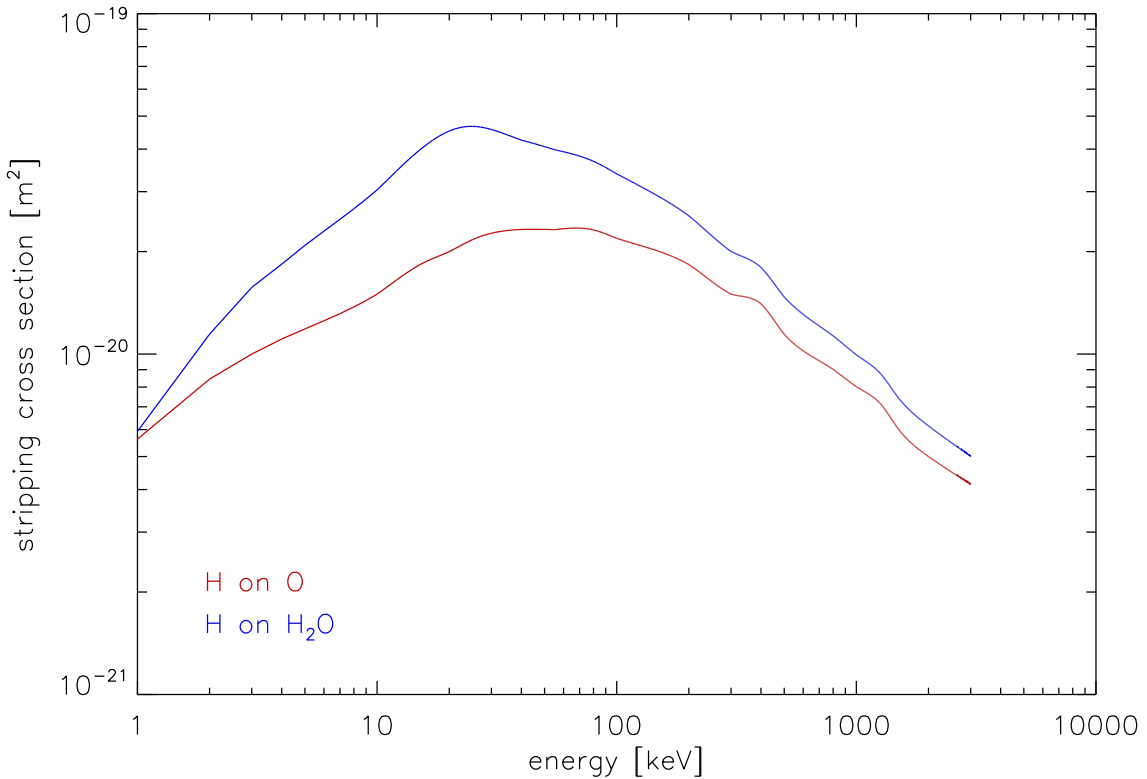


Figure 2.15: Stripping cross sections of H impacting O and H_2O . See Sec. 2.4.3 for details.

et al. 1998).

2.4.3 ENA stripping

The feature that made the CRAND process a source is the fact that its neutrons are not charged, which allows them to move freely within the magnetosphere. Another relevant neutral species within a magnetosphere is ENAs. They are produced during the charge exchange process where an electron of a neutral gas particle is transferred to an energetic singly charged ion. Most of the ENAs escape the magnetosphere, which is why charge exchange is usually considered as a loss for energetic ions (Sec. 2.3.2). Nevertheless, if an ENA encounters another gas particle, this can strip off the electron again and retrap the ion.

Above 10 keV, the stripping cross section typically becomes larger than the charge exchange cross section (see Johnson (1990) or Bishop (1996), or compare Figures 2.10 and 2.15.) If an ENA passes through a gas cloud, it will therefore be stripped faster than the resulting ion will experience charge exchange again. This process will provide energetic ions to regions where gas is present. At Earth, this might supply the secondary proton radiation belt between the classic belts and the atmosphere (Moritz 1972, Gusev et al.

2003).

To derive the source rate of ions from stripping first the rate $\tilde{\mathcal{P}}$ is calculated at which ENAs that are produced in the entire magnetosphere reach to the an L -interval at L_{rb} , where we want to consider stripping.

$$\tilde{\mathcal{P}} = \int_{\text{all}} \epsilon \frac{\delta f}{\delta t} \Big|_{\text{CE}} dV \quad (2.86)$$

The loss rate from charge exchange $\delta f / \delta t|_{\text{CE}}$ was given in (2.64). The integration is a volume integral with $dV = R_s^3 L^2 dL \sin(\lambda) d\lambda d\varphi$. The index *all* indicates that it goes over the entire magnetosphere. ϵ is the fraction of ENAs that reach the belt. We constrain ourselves to equatorial mirroring particles here. In that case, the produced ENAs are only emitted in the equatorial plane. The considered interval ΔL at L_{rb} covers an angle of $\Xi = \arctan((L_{rb}/2)/(L - L_{rb}))$ of all possible directions so that $\epsilon = \Xi/(2\pi)$.

The ENAs need time to traverse the L -interval. During this, they might be stripped, which is a loss of ENAs. Its rate can formally calculated the same as CE losses. For this, the CE cross section in (2.64) has to be replaced with the stripping-cross section and the ion PSD with the one of ENAs. Since the loss of ENAs is equal to the source of ions, it is found for both

$$\left\langle \frac{\delta f}{\delta t} \right\rangle_{\text{str}} = + \int_{rb} n_g \sigma_{\text{str}} v \tilde{\mathcal{P}} dt \Bigg/ \int_{rb} dV \quad (2.87)$$

σ_{str} is the stripping cross section. The integral $\int_{rb} dt$ ranges over the time interval that the ENAs spend within the L -interval, that we call *rb*. During this time, the ENAs pass through a gas of number density $n(L(t))$. Equation (2.87) can be understood when the average phase space density of ENAs is identified as $\langle f \rangle_{\text{ENA}} = \tilde{\mathcal{P}} \int_{rb} dt / \int_{rb} dV$.

Stripping cross sections of H_2O , and O are required in this thesis. They are estimated by linearly combining cross sections of H and O_2 taken from Barnett et al. (1990). The result is given in Fig. 2.15. This approximation is good since the considered energies are much higher than the binding energies. Corrections only occur because the constituents of a molecule can geometrically shield others. The error when applying this to oxygen is < 5% (Riessellmann et al. 1991).

3 Cassini and its particle instrumentation

3.1 The Cassini mission

Cassini-Huygens is a joint NASA/ESA/ASI mission to Saturn and its moon Titan. It was launched in October 1997 and had its Saturn orbit insertion (SOI) in July 2004. The Cassini spacecraft is the fourth that visits Saturn and the first one that stayed within orbit. The Huygens probe was carried by Cassini on its way and then dropped on Titan, where it landed safely in January 2005. Cassini is planned to continue its mission until 2017. At its end, Cassini will descend into Saturn.

Cassini's science objectives deal with the planet itself, its rings, moons, especially Titan, and its magnetosphere. For this, it carries a wide variety of scientific instruments that will in part be discussed in the following sections.

By the end of 2011 Cassini completed 159 orbits, each with a duration of one to several weeks. This allowed the sampling of a wide range of radial distances, latitudes, longitudes, and time. The orbital coverage up to July 2008 is described in detail in [Krupp et al. \(2009\)](#). Cassini reached its minimal distance of $L = 1.3$ to Saturn's center during SOI. Usually Cassini does not reach much closer than $L \approx 3$. Its orbits can be divided in periods close to the equatorial plane and periods of high inclination, where latitudes up to $\lambda \approx 60^\circ$ are reached. The change in inclination is achieved by flybys at Titan, which is not only massive but also far ($20R_S$) away from Saturn.

3.2 The energetic particle detector LEMMS

3.2.1 Operation principle

This thesis is based on measurements taken by the Low Energy Magnetospheric Measurement System (LEMMS), which is part of the Magnetosphere Imaging System (MIMI) on board of Cassini. LEMMS can detect ions and electrons. Despite its name it measures at the *highest* energies covered by MIMI, which roughly is between several 10 keV and several 10 MeV.

In general, many instruments commonly used to detect charged particles use detectors as micro-channel plates (MCPs) or channeltrons. In order to distinguish well between different particle energies, masses, and charges, the particles are first deflected by electric and/or magnetic fields before they either reach the detector or are filtered out. For the energies that we want to measure, it is difficult to achieve the necessary field strengths

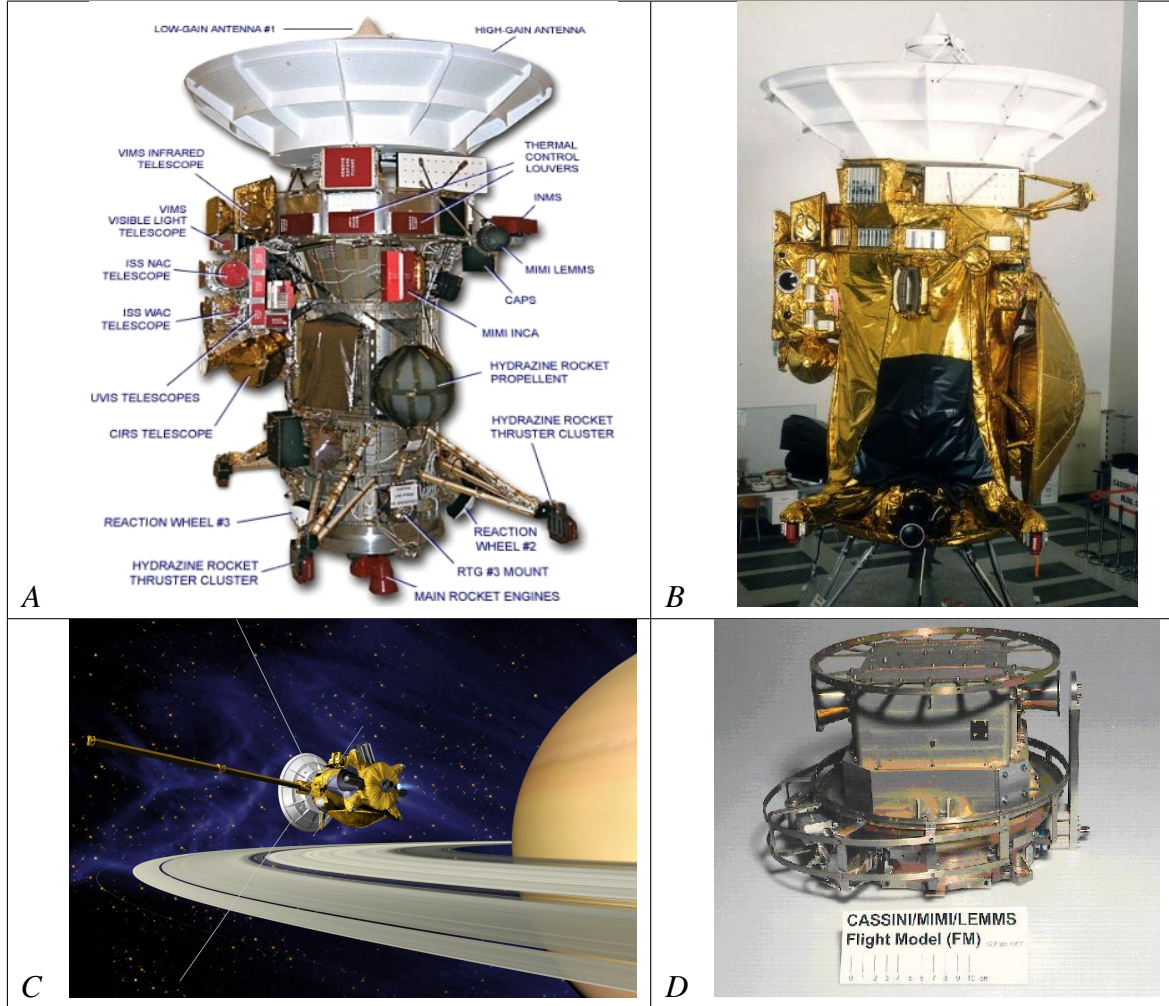


Figure 3.1: The Cassini spacecraft. *Panel a*: Cassini without thermal insulation foil, which allows a good view on its different instruments. *Panel b*: Cassini with insulation. The magnetometer boom and the electric antennas of RPWS are not mounted yet. *Panel c*: Rendered graphic of Cassini in the fully equipped state. *Panel d*: Photography of the LEMMS flight model.

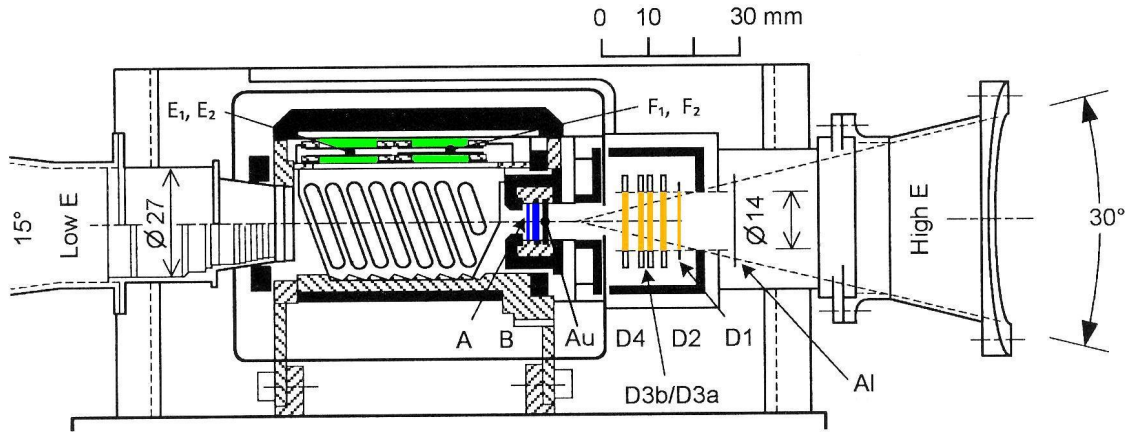


Figure 3.2: Configuration of LEMMS. The low-energy end is to the left, the high-energy end to the right. The detectors are shown in color.

within a small and light space instrument. Therefore a detector is required that can measure the particle's energy by itself. This is possible with a *solid state detector* (SSD), also referred to as a semiconductor diode detector (Knoll 2000). Such detectors are used in LEMMS.

A SSD is manufactured out of a semiconductor, silicon in the case of LEMMS. Incident energetic particles lose energy in this material, as discussed in Sec. 2.3.3. Ionization within a semiconductor usually transfers an electron from the valence to the conduction band, which creates an electron/hole pair. The energy consumed by one pair production caused by light ions within silicon is about 3.6 eV, which is about three times the band gap (Knoll 2000). The number of pairs produced by energetic particles is proportional to the particle energy.

The pairs would recombine if they were not separated before by an electric field. Such a field forms by itself at a junction between p- and n-doped semiconductors. Applying a reverse voltage to it (negative potential on p-doped side) not only increases the field strength but also extends the field from the close vicinity of the junction to the bulk material. In case of a *fully depleted* detector, as LEMMS (S. Livi, priv. comm., 2011), the region of the electric field extends over the whole detector so that pairs created anywhere in it are separated.

The separated pairs produce a charge Q at the contacted edges of the detector, which is, depending on the capacity C of the detector, equivalent to a voltage $U = Q/C$. This voltage is in LEMMS not measured directly but after a charge sensitive amplifier, as described for example in Dearnaley (1966).

3.2.2 Technical details

A sketch of LEMMS is shown in Fig. 3.2. It consists of two telescopes: the low-energy and the high-energy end. The low-energy telescope includes 5 distinct detectors, partly stacked together. It includes a permanent magnet that is strong enough to bend incoming energetic electrons to the detectors referred to as E1, F1, and E2F2. Incoming ions are barely deflected and impact on the detectors A, and B. The high-energy end has a stack

of 4 detectors that are called D1, D2, D3ab, and D4. Low and high-energy telescope have collimators in front with apertures of 15° respectively 30° and are divided in 7 respectively 19 hexagonal-shaped entrance channels to avoid particles entering from larger angles. An Aluminum foil in front of the high-energy end prevents low-energy particles to enter. Both telescopes are separated by an absorber, which is a gold-coin.

The measurements are taken with two different methods that produce the data of the pulse height analyzer (PHA) channels and the rate channels. Considering the previous discussion, the most straightforward way to derive particle energies is to use a pulse height analyzer and relate the amplified voltage to the energy of the particle that initially caused it. The disadvantage of this is that the measured particle not necessarily entered the detector in a defined way through the collimator. It is also possible that it penetrated through the shielding (and lost energy there) or produced secondary particles that also can be detected. Also, if the particle had such a high energy that it did not stop within the detector, its energy cannot be determined.

Both issues are improved by the use of the rate channels. These combine the output of several stacked detectors. If for example the detectors D1, D2, and D3 detect a pulse simultaneously, but D4 detects nothing, this means that the responsible particle entered along the line from D1 to D3. This reduces the contamination from particles that entered by other means. Also, since the stack is thicker than a single detector, this approach allows for the measurement of higher energies. The disadvantage of the rate channels is that they do not use the full information of the pulse but only measure if the voltage passes different threshold values. This reduces their energy resolution.

The available PHA channels are PHA_A, PHA_E1, and PHA_F1, depending on which detector they use. Since the sensitivity of the PHA channels with low and high energies are so low that they sample barely particles and have a poor statistics, we only use the PHA channels in between. All used PHA channels are listed in Appendix A. The PHA channels have a energy resolution between 2 keV and 90 keV, equivalent to an excellent ratio of mean energy to energy width of 4 % and 8 %.

The rate channels measuring protons are numbered as A0 to A7 (using both the A and the B detector) and P2 to P8 (using the D detectors). The electron rate channels are C0 to C7 (using the E and F detectors) and E0 to E7 (using the D detectors, for clarity). All channels deliver reliable data beside some exceptions. The A0 channel occasionally shows erratic behavior. The mean energy of P4 is still under debate in the instrument team. P1 and P9 are sensitive to both protons and electrons. E5 does not have a closed sensitivity interval but measures all particles above a given energy. With these justifications we decided not consider these channels. The C and most A channels are not used here because we prefer the equivalent PHA channels because they have a higher energy resolution. We list the rate channels used in this thesis also in Appendix A. We should point out that the energy calibration changed between Krimigis et al. (2004) and Krupp et al. (2009) and might change again in the future. The used rate channels have a energy resolution between 21 keV and 47 MeV, equivalent to a ratio of mean energy to energy width of 16 % and 175 %. There exist also other channels but they are not considered here.

LEMMS cannot distinguish properly between ion species, since most channels are sensitive to all ions with proton number $Z \geq 1$. An exception are for example the Z channels. They are only sensitive to heavy elements with $Z > 6$. These channels use the

fact that heavier elements have stronger energy loss in matter (2.65). Because of this, only high-Z projectiles become stopped in the SSD stack, while other projectiles pass through it and trigger signals in every detector, which are then excluded by the coincidence logic. The disadvantage of the Z channels is that they only measure at higher energies than we do it here (> 55 MeV for O-ions). Therefore, they are not included in the analysis.

Since Cassini is a three-axis stabilized spacecraft and therefore usually does not rotate, LEMMS was originally designed to rotate itself in order to sample different pitch angles. Unfortunately, the turntable stopped its operations early in the mission (beginning of 2005). Since then, only two pitch angles (because of the two telescopes) are sampled at a time. Pitch angle distributions can since then only be measured when the spacecraft is spinning (for example during downlinks) or compiled from various orbits passing similar positions while pointing into different directions. The advantage of the lack of rotation is the increased time resolution (by a factor of 16) at the current pitch angle that allows the detection of very short events.

LEMMS weighs 6.72 kg and consumes 5.2 W. A full description can be found in [Krimigis et al. \(2004\)](#). How the LEMMS data is processed will be issue of Sec. 4.

3.3 The magnetometer MAG

Knowledge of the ambient magnetic field is crucial for the understanding of the behavior of charged particles. We use magnetic field measurements in this thesis to determine the local pitch angle of the detected particles and to estimate their drift paths.

The Cassini magnetometer (MAG) consists of a flux-gate magnetometer (FGM) and a helium magnetometer (HM), which are both mounted along a boom with 11 m length. A full description of MAG is given by [Dougherty et al. \(2004\)](#).

3.3.1 Flux-gate magnetometer

An FGM consists of a drive coil and a sense coil, both wound around the same core, which has a large magnetic permeability. A periodic current is driven through the drive coil. The resulting periodic magnetic field in combination with the present external field (that is to be measured and should vary slower than the current) acts on the core. Its magnetization changes nonlinearly with the magnetic field and shows hysteresis. The sense coil is exposed to the resulting magnetic field. Its variations induce a voltage in the sense coil. The second harmonic of this voltage is proportional to the external field. (See for example [Dougherty et al. \(2004\)](#).)

The latter can be understood by a simple exercise. We assume that B_{ex} is the external field, $B_{\text{dr}} \exp(i\omega t)$ is the one from the drive coil (without core), and that their sum is B_0 . We make the oversimplified assumption that B_0 applied to the core produces a magnetic field as $B = B_0 - B_0^3$. Equating this into the equation for the induction voltage $U = NA \partial B / \partial t$ (with the cross section A and winding number N of the sense coil) yields $U \propto B_{\text{ex}} \exp(i2\omega t) + \xi$, which was to be shown. ξ represents terms oscillating with multiples of ω , except 2ω .

The second harmonic can be filtered out from the full voltage. In case of MAG, this is done by a narrow band amplifier.

In order to measure the vector of the external magnetic field and not just its component aligned with the magnetic core, MAG is equipped with three orthogonally mounted FGMs.

3.3.2 Helium magnetometer

The other component of MAG is a HM. This instrument utilizes the Zeeman effect, in which a weak magnetic field can linearly modify the eigenenergies of electrons within an atom ([Haken and Wolf 2004](#)). Helium is excited from its ground state $|L = 0, S = 0\rangle$ (with the electron quantum numbers L for the total angular momentum and S for the total spin) to the metastable state $|L = 0, S = 1\rangle$. Polarized infrared light from a lamp drives a further excitation towards $|L = 1, S = 0\rangle$. In the presence of an external magnetic field, the metastable $|L = 0, S = 1\rangle$ state is split into three. The excitation therefore becomes off-resonant and only depopulates one of the metastable $|L = 1, S = 0\rangle$ states.

If MAG operates in the vector mode, it applies additional (known) magnetic fields until the external field is canceled and the light absorption becomes maximum ([Balogh et al. 1992](#)). In the scalar mode, radio waves drive transitions within the split metastable $|L = 0, S = 1\rangle$ states. The radio frequency is tuned to resonance ($\propto B$), so that the depopulated state is refilled and more light can be absorbed ([Smith et al. 2001](#)).

Unfortunately, the HM of MAG stopped operating early in the mission.

3.4 Other instruments

Cassini also carries instruments to detect charged particles at lower energies than LEMMS and that allow the detection of neutral particles or dust.

Apart from LEMMS, MIMI also includes the Charge-Energy-Mass Spectrometer (CHEMS) and the Ion and Neutral Camera (INCA). CHEMS uses an electrostatic analyzer, followed by a time-of-flight system (TOF), and a SSD. With this, it can detect ions up to iron in a range from 10 to 200 keV/charge and can distinguish particle masses and charges/mass.

INCA is designed to detect ENAs but also can sense ions. To achieve this, the charged ions are deflected away and the remaining neutral atoms are indirectly detected by secondary electrons that they produce while passing foils. INCA measures the incident energy with the TOF method in the range between 7 keV and 3 MeV/nucleon and can distinguish between a few species ([Krimigis et al. 2004](#)).

The other charged particle detector is the Cassini Plasma Spectrometer (CAPS). It includes the Ion Mass Spectrometer (IMS) to determine the composition of < 50 keV ions, the Ion Beam Spectrometer (IBS) to measure the velocity distribution of the same ions, and the Electron Spectrometer (ELS) for < 28 keV electrons ([Young et al. 2004](#)).

The radio and plasma wave science (RPWS) instrument consists of three nearly orthogonal electric field antennas, three orthogonal magnetic search coil antennas, and a Langmuir probe. The antennas are connected to receivers that cover a frequency range between 1 Hz and ≈ 10 MHz. A sounder transmitter can be used to drive one electric antenna. The antennas allow the detection electromagnetic fields associated with plasma

waves, the Langmuir probe is used to measure the electron density and temperature of the surrounding plasma ([Gurnett et al. 2004](#)).

The Ion and Neutral Mass Spectrometer (INMS) measures masses and number density of neutral particles and low-energy ions ([Waite et al. 2004](#)). It is sensitive enough to measure at Titan's high atmosphere or Enceladus' plumes. Measuring the Neutral Torus is difficult and only succeeded recently since its densities are very low and it is centered in a region of large radiation contamination.

Of importance for this thesis is also the E ring and the ice grains emitted by Enceladus. The Cosmic Dust Analyzer (CDA) can detect some populations of these grains directly. It consists of the Dust Analyzer (DA) and the High Rate Detector (HRD). The DA detects charge and velocity of the incident dust grain when it passes through charged grids at the front end. The impact of the grain inside of the detector destroys it and creates fragments, gas, and plasma. An electric field separates the charges, which are then collected and detected. If the grains hit the integrated chemical analyzer, their ions produce secondary electrons used to measure their TOF and therefore mass. The HRD detects if grains impact on polyvinylidene fluoride (PVDF) sensors ([Srama et al. 2004](#)).

4 Data set and the average magnetosphere

The seven years that LEMMS was measuring energetic particles in the orbit of Saturn provide data with an unprecedentedly good statistics. We will describe the accumulated data set in this section and explain how it is processed and organized. It is the most comprehensive compilation of energetic particle profiles at Saturn to date. Earlier publications usually considered only single orbits (Krimigis et al. 2005) or provided averages only of single channels and without quantifying the fluctuations (Carbary et al. 2009, Krupp et al. 2009).

The averaged data allow for a description of the average state of Saturn's magnetosphere in the view of energetic protons, and electrons. Also the magnetic field configuration and plasma population are discussed briefly. The aim of this section is, however, only to provide an overview over Saturn's magnetosphere. Features in the particle profiles and spectra are pointed out and interpretations are sketched. A detailed analysis will follow in Sec. 5 and 6.

4.1 Data set

The used data set utilizes the LEMMS channels that are listed in Tab. A.1. For studies outside the radiation belts, we PHA channels are used for all energies, where they are available. Rate channels are used above their energy range. In the radiation belts many of the channels that measure at relatively low energies are contaminated. Therefore, only rate channels measuring high energies are used in that region,

We will assume throughout this thesis that the ions are mainly protons. Earlier measurements, as done with the low energy charged particle instrument (LECP) on board of Voyager 2, claimed the opposite, namely that most ions are heavy (Krimigis et al. 1983). We do not follow this since nowadays there is evidence that LECP ion measurements close to Saturn were contaminated by electrons (T. P. Armstrong, priv. comm., 2010). Also, the LEMMS measurements can be compared with other Cassini instruments that have an overlapping energy range. A comparison with CHEMS and INCA was for example done by Dialynas et al. (2009). They show that at least at $L \leq 15.7$ and $E < 1$ MeV most particles are indeed protons. For larger L , the values are comparable. A similar comparison is given below, in Fig. 4.5.

The value of the local pitch angle α_{loc} between the the local magnetic field and the detected particles is inferred from the magnetic field measured by MAG, which is described in Sec. 3.3. From this and the spatial position of the spacecraft, the equatorial pitch

angle α_0 is calculated assuming conservation of the first adiabatic invariant and a model magnetic field. In this work, we use a simple dipole model with a northward offset of $0.038 R_S$ between the center of the planet and the center of the magnetic field (Dougherty et al. 2005). Latitudes λ and L -shells will be given with respect to this. They are purely derived from the position of the spacecraft and are related via $L = r/\cos^2(\lambda)$ with the distance r to the center of the offset dipole.

The used data start with SOI in July 2004. Two data sets are used here, one going until June 2010 (for figures as identically published in Kollmann et al. (2011b)), the other going until August 2011 (for most other figures). This is because the different studies were undertaken during different points in time with the complete data set that was available to date. Since the sets differ only marginally, they are not labeled in the Figures. The data set until August 2011 includes 145 orbits. Although the closest approach to Saturn is different for every orbit still about 80 orbits reached as deep as $L < 5$. The more inner radiation belts are less covered, in case of the innermost belt at $L = 2.4$ only twice.

Several time periods were excluded for the study. This includes orbits where due to enhanced solar activity a significantly increased particle intensity is present outside the orbit of Tethys ($L \approx 5$). These events are atypical and are easy to recognize in data from channels measuring > 1 MeV protons. While the measurements with these channels taken at $L > 5$ are usually at background levels, the aforementioned events cause a clear foreground signal. This occurred in February 2005 and August 2005 (as reported in Roussos et al. (2008b)) and again from May 2011 on.

Additionally, short periods are excluded where direct or reflected sunlight falls into one of the LEMMS heads. During these periods, many channels can abruptly saturate. Although SSD detectors can be sensitive to light, the instrument as a whole was designed to minimize this and indeed this behavior did not occur during prelaunch tests. A hypothesis to explain it is that the detectors became coated during flight with a layer that conducts if illuminated. This not only creates a signal in the instrument but even short-circuits the detectors' power supplies. We remove this automatically by excluding intervals where LEMMS directly points to the sun or where the spectrum has a unrealistic slope.

Occasionally, the MAG instrument is calibrating, or off. Even during these intervals, the raw data provide valid values. The standard way to remove these intervals (and avoid wrong pitch angles derived from them) uses a manually created exclusion list.

While LEMMS technically covers a large energy range, not every channel yields a sufficient signal-to-noise ratio at every position in the magnetosphere. There are two mechanisms that can create noise. Within the radiation belts ($L < 5$), mainly energetic electrons cause a strong contamination. We will refer to this as *radiation belt background*. Because of this we usually prefer rate channels in the radiation belts. However, the use of rate channels does not help in case of *dominating* contamination. There is no way so far to compensate for this. Therefore, we simply do not consider measurements from channels that show such contamination. This mostly applies to channels measuring at low energies. The precise positions at which the various channels are background dominated are a matter of ongoing investigation.

The other type of noise is relevant at much larger distances to the planet. It is attributed for example to instrumental electronic noise, radiation of the spacecraft's RTG power supply, and transient cosmic radiation. We will refer to this as *instrumental background*. All measurements presented here compensate for this. The standard method to approxi-

mate the present background uses measurements where Cassini is in regions $L \gg 20$ and where LEMMS measures intensities that are constant exclusive of random fluctuations. Since also these regions should be dynamic and differentiated, we interpret the constant measurements as a signature that they are background dominated. The retrieved values are then subtracted from the data. This reduces the intensity values at large L but does not null them completely. This is because the subtracted value is an average one while the background can fluctuate up to intensities larger than the average so that a finite value is left even after subtraction.

Until early 2005, LEMMS was rotating to sample data from different pitch angles. For this period, the full time resolution of the data is used within this thesis. Currently, LEMMS is not rotating, measuring only two opposite directions with its two detector heads. This increases the time resolution at the respective pitch angles. Since this resolution is not needed for the current studies, data for the non-rotating period are averaged over the time interval that one rotation would have taken (86 s).

Level 1a data is provided to us by JHU/APL in Laurel, Maryland. The data include for example LEMMS counts per time interval, low-resolution MAG data, and Cassini ephemeris information. This data is first processed by an IDL program ([ITT Visual Information Solutions 2011](#)), provided and supported by A. Lagg. The program calculates for example differential intensities, and local pitch angles and associates them with the current location in space. Its output is the input to further IDL routines that for example average the data and convert them to phase space densities, as it will be described in the following sections.

4.2 Intensities

4.2.1 Computation

The density of energetic particles in phase space can be used to describe their distribution (Sec. [2.2.1.1](#)). The standard quantity in which particle measurements are presented is, however, not phase space density but *differential intensity* j . This is the number d^6N of particles per time dt , area d^2A , solid angle $d^2\Omega$, and energy range dE of the channel.

$$j = \frac{d^6N}{dt d^2A d^2\Omega dE} \quad (4.1)$$

Differential intensity and phase space density can be converted into each other, which will be described in Sec. [4.3.1](#). Both quantities can therefore be used equivalently to represent the distribution function of energetic particles.

Assuming that the particles are evenly distributed over the phases of their motion, and that the sources and losses discussed in Sec. [2.3 - 2.4](#) occur on time scales longer than the periods of the motions, the particle distribution can be expressed as a function of (L, E, α_0) .

Although the particle motions include bouncing over a range of latitudes and drifting over all local times, the distribution function is independent λ (as long as $\lambda \leq \lambda_m$) and φ . This is a result of Liouville's theorem (Sec. [2.2.1.1](#)), which states that the PSD is constant at all points covered by the particle motion. The density in real space, however, differs

along the bounce path. Since the bouncing particles are fastest when passing the equator, they barely spend time there, resulting in a lower density at the equator, compared to higher latitudes.

Because of this, the data set described above is usually filtered only for L -shell and equatorial pitch angle, while λ and φ are ignored. A filtering in energy is already implicit in the measurements since they are taken with instrument channels that measure in discrete energy intervals.

Liouville's theorem, however, is only applicable in case that the values of (L, E, α_0) are precisely and correctly determined. Since this is not fully true, there are exceptions throughout this thesis, where filtering for λ or φ is applied:

(1) LEMMS does not measure a precise local pitch angle, but a range of angles, which is mainly determined by the opening angle of the instrument. This range translates to a range of equatorial pitch angles, which depends on latitude. Because of this, the rate of particles entering LEMMS changes with latitude. (This would be even true if the *equatorial* pitch angle distribution was the same everywhere and if the center of the LEMMS aperture always pointed to the same equatorial pitch angle while Cassini moves in latitude.) Although the number of particles is normalized to the space angle of incidence, this latitude dependence is currently not accounted for in the standard treatment of the data. This is problematic in regions as the radiation belts, where the error of the calculated intensity is smaller than its variability over time. Sec. 5 deals with the radiation belts in detail. Only measurements within magnetic latitudes of $|\lambda| \leq 10^\circ$ are considered there. All other cases use the full latitudinal range.

(2) The dipole L -shell, as it is used here, only approximates the drift path around Saturn. In case that non-azimuthal magnetic or non-radial electric fields occur, the particle drift deviates from the dipole- L . Additionally, it is possible that sources and losses occur on time scales shorter than the drift period. In this case, the statement that the PSD is constant for all φ is not valid anymore. We therefore will apply a filtering in local time in Sec. 6.3.2 and discuss the results.

After the filtering, the data are averaged on a logarithmic scale. If not stated otherwise also the 1σ logarithmic standard deviation is calculated. This method of averaging is also known as performing the geometric mean. We use this type of averaging because the data are also presented on a logarithmic scale. Also, this averaging is not dominated by the highest values, in contrast to linear averaging (arithmetic mean). This would also apply to the median. We do not use the median because there is no well-defined measure of its error.

4.2.2 Radial profiles

Figure 4.1 shows an example of both averaged and original data, as a function of L at constant energy and equatorial pitch angle. This comparison reveals that Saturn's magnetosphere is a highly dynamic system. In the left panel, the mission average is compared to measurements taken during a single orbit. The right panel compares the mission average to all accumulated data points. It can be seen that the single measurements can deviate significantly from the average. Intensities at the same position but different times can differ significantly. Instead of being continuously above or below the average, the intensity fluctuates around the average. Same is true for the entire magnetosphere that fluctuates

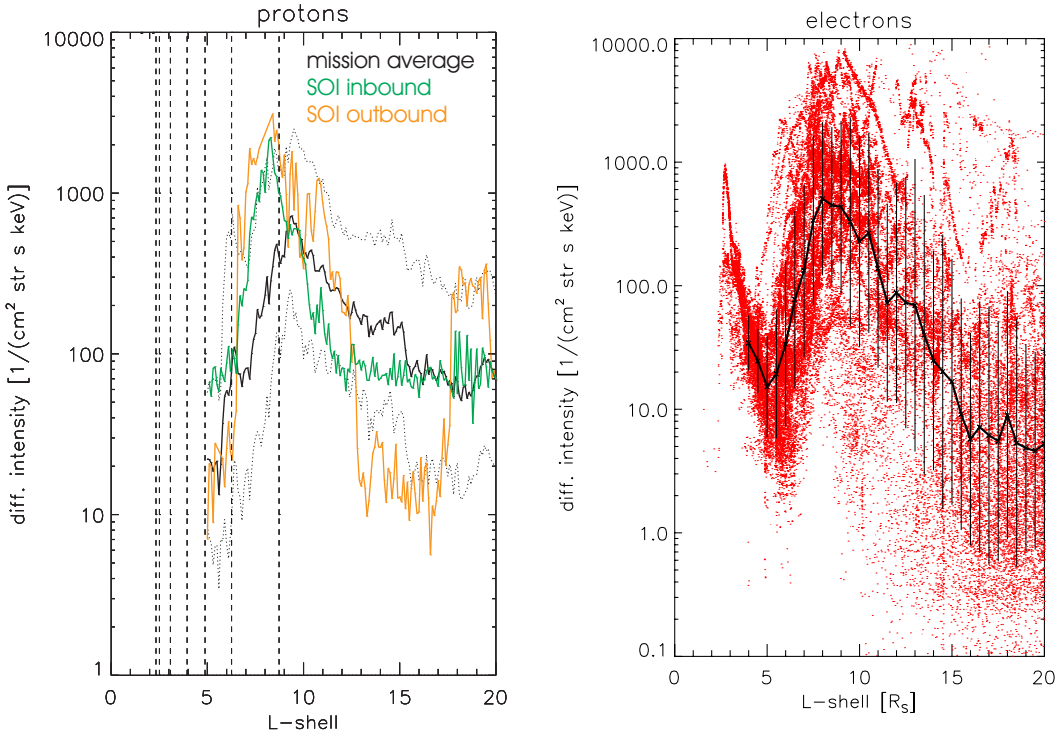


Figure 4.1: Differential intensities during various orbits. *Left panel:* Protons with $E = 37 \text{ keV}$ mean energy and $\alpha_0 = 50^\circ \pm 10^\circ$ equatorial pitch angle. The black solid line represents the mission average, the black dotted lines mark the variability within the 1σ standard deviation. The colored lines show measurements during a single orbit, split for inbound and outbound part. *Right panel:* Electrons with $E = 91 \text{ keV}$ and $\alpha_0 = 10^\circ \pm 10^\circ$. Black lines show the mission average and its 1σ standard deviation as error bars. The red points represent single measurements taken during all orbits within the data set. The increase of intensity for $L < 5$ is caused by radiation belt background and does *not* represent electrons at the stated energy.

around its average state but usually does not reside in this state. Nevertheless, even the data of single orbits roughly follow the average profile. The mission average is therefore meaningful.

Outside $L \approx 10$, the 1σ standard deviation can extend over up to two orders of magnitude. The 2σ error bars can even range over three and four orders in case of protons and electrons, respectively. The error bars decrease for smaller L and larger energies. Close to Saturn, the intensities are usually very stable.

In Figure 4.2, averaged intensities are shown as a function of L , without the single measurements, but for several channels. These profiles show a variety of features:

Close to the planet but still outside the Main Rings reside the *radiation belts*, which will be studied in Sec. 5. In contrast to the rest of the magnetosphere, they exhibit large intensities of energetic particles with energies above 1 MeV. For protons the radiation belts usually extend until $L < 5$. Electrons also have high fluxes in this area but the boundary of the belts is not as sharp as for the protons.

The stable intensities of the radiation belts can be attributed to the general isolation from

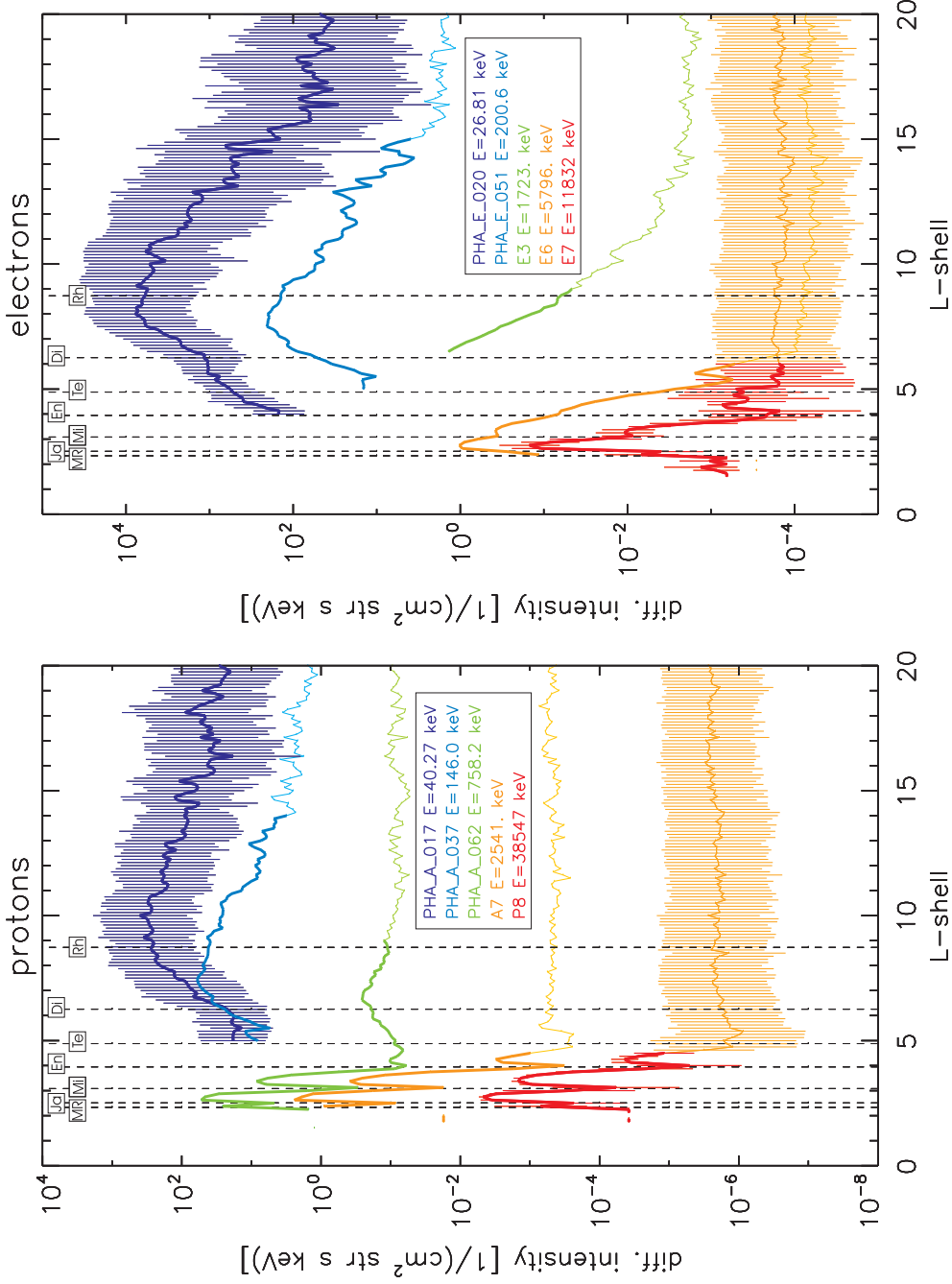


Figure 4.2: Mission-averaged differential intensities of protons (*left*) and electrons (*right*). Representative LEMMS channels are displayed in different colors, their names and mean energies are explained in the legends. All curves are for equatorial pitch angles of $\alpha_0 = 10^\circ \pm 10^\circ$. If the profiles are shown as *thinner lines with modified color*, this marks regions where the average intensity is dominated by instrumental background. The profiles in regions dominated by radiation belt background are not shown. *Dashed lines* mark the outer edge of the Main Rings (MR), and the semimajor axis of Janus (Ja), Mimas (Mi), Enceladus (En), Tethys (Te), Dione (Di), and Rhea (Rh).

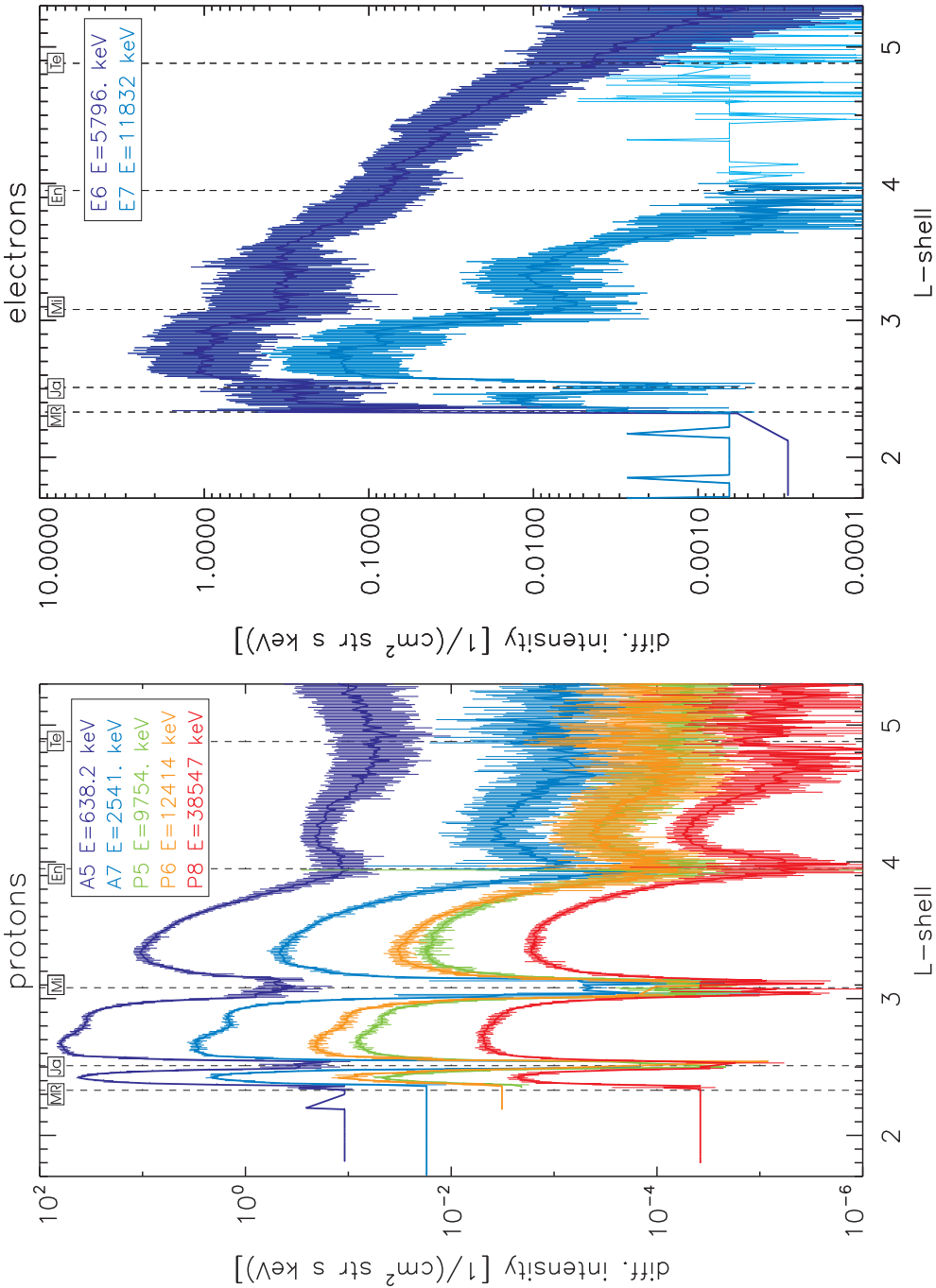


Figure 4.3: Mission-averaged differential intensities of protons (*left*) and electrons (*right*) within the radiation belts. Only latitudes $|\lambda| \leq 10^\circ$ are considered here. The figure is otherwise identical to Fig. 4.2.

the rest of the magnetosphere (Roussos et al. 2008b), the absence of dynamic events as injections, the stability of the involved source and loss processes (Roussos et al. 2011), and the local time symmetry (Paranicas et al. 2010).

The shape of the proton belts is well understood. Energetic particles are swept from the orbits of Saturn's moons (Sec. 2.3.6). This is very efficient for energetic protons and causes the sharp intensity dropouts close to the L -shells of the moon orbits, all around the planet. The belts will be reproduced with a model in Sec. 5.2. Electrons at the observed energies have small azimuthal velocities relative to the moons in the radiation belts (Fig. 2.12) and experience therefore only weak losses. It is therefore not surprising that not all electron energies show the same clear separation into distinct belts as the protons do.

Outside the belts extends the *middle magnetosphere*. It will be discussed in detail throughout Sec. 6. We define this as the region radially outward of the radiation belts. It is governed by a magnetic field that is relatively dipolar and therefore local time symmetric, despite the distance to Saturn.

Outside of this region, the *outer magnetosphere* is extending. This is a region that is close to the magnetopause on the dayside and extends into the magnetotail on the nightside. Because the magnetopause position varies depending on the solar wind, the tail is dynamic, and the planetary magnetic field is weak at large distances, the outer magnetosphere is highly fluctuating. Assuming local time symmetry is not a good assumption there: While the dayside is compressed, the nightside is extended.

Averaging intensities over local time and calculating equatorial values of pitch angles using a dipole, as we practice it here, is only valid in the middle magnetosphere. However, there exists no clearly defined boundary between the outer and middle magnetosphere. We therefore decided to use the assumption of a dipole and local time symmetry for a large L -range but to warn the reader to consider the data provided at large L -shells with caution. As the outermost distance we used $20R_S$. This is close to the dayside magnetopause distance and therefore for sure a position where the assumption of local time symmetry breaks down.

The middle and outer magnetosphere are populated mainly by particles with lower energies than in the radiation belts. The maximum of their intensity is located outside $L > 5$. The maximum's position moves outward with decreasing energy. In contrast to the maxima of the radiation belts that are centered between two moon orbits this does not seem to apply to the intensity maximum of the middle magnetosphere.

At increasing distance from the planet, the average intensities become constant. The onset of this depends mostly on energy and not on pitch angle. The measurements of single orbits can nevertheless feature foreground intensity. It is not clear if the constant profiles are dominated by the averaged foreground, which might be constant, or by instrumental background that, despite being constant on average, was not completely removed since it is fluctuating. We therefore marked regions in the figures by the use of thinner lines with lightly different color. To be on the safe side, we will consider them as indeed dominated by instrumental background. This will become relevant when calculating phase space densities in Sec. 4.3. The PSD profiles are not flat (and therefore not obviously suspicious) in regions where the intensity is flat. Treating the such regions separately is therefore important.

Computing L -shells in a dipole model can be a source of imprecision in the averaged intensities and their standard deviations. Advanced magnetic field models (like the one of

Khurana (Khurana et al. 2006, Carbary et al. 2010), which is a *Tsyganenko*-type model) became available to us only recently. Such models have degrees of freedom that are for example determined by the solar wind conditions. If these values are not chosen correctly, such models would also be imprecise, but in a more obscure way. We therefore used the dipole as a first approach.

We do not consider this approach as a major source of imprecision. A dipole field line intersects at every latitude another real field line. When using the *Khurana*-model at $L_{\text{Khurana}} = 10$, these intersections map to equatorial distances between 10 and 14 R_S , depending on latitude. When averaging intensities of different latitudes to derive the intensity at $L_{\text{dipole}} = 10$ (as presented here), this creates an error. This error decreases if the data is filtered to a decreasing latitudinal range. In the present data set, such a filtering neither causes a significant nor systematic change in the standard deviation. Apparently, the intensity between different field lines is changing slow enough in the region where the dipole model is imprecise, that the error due to the field model is smaller than the time-dependent scattering.

4.2.3 Energy spectra

The previous section provided a cut through the particle distribution along L i.e. was showing radial profiles. The missing coordinates for a complete set are energy and equatorial pitch angle. Cuts of the particle distribution function along E and α_0 will complete its visualization. In this section we therefore shows cuts along E i.e. energy spectra.

Fig. 4.4 displays such spectra at different L -shells for $\alpha_0 = 90^\circ \pm 10^\circ$. It can be seen in the figure that the spectra mostly decrease with increasing energy.

A common function to fit spectra is a power law

$$j = \zeta E^{-\gamma_j} \quad (4.2)$$

As already a visible inspection of Fig. 4.4 shows, this only works well for limited intervals in E and best for protons. The exponent γ_j for protons between several 10 keV and several 1 MeV ranges roughly between 2 and 3.

Figure 4.4 compares measurements of LEMMS with some of CHEMS. The latter instrument can distinguish between ion species. Here, protons and water group ions are shown. Water group ions are expected to be the most abundant heavy-ion species since there are various water sources in Saturn's magnetosphere (Sec. 1). However, the water group within our energy range turns out to be either of comparable or smaller intensity.

The shown CHEMS data are a linear averages and were provided by R. D. DiFabio (2011) Since at high latitudes no equatorially mirroring particles can be measured, only times are taken into account where Cassini was within 1 R_S distance to the equator, equivalent to latitudes $|\lambda| \leq 10^\circ$. The CHEMS data in the two panels of Figure 4.4 differ: the left one uses data until the end of 2010 and the current calibration, the right one includes only data until 2009 with an older calibration.

It is apparent from Fig. 4.4 that protons are depleted approximately at $L < 8$ and $E < 100$ keV. At $L = 6$ this even gives rise to a peak around that energy. Water group ions are more affected than protons (Fig. 4.5). This behavior is also observed by INCA (Dialynas et al. 2009).

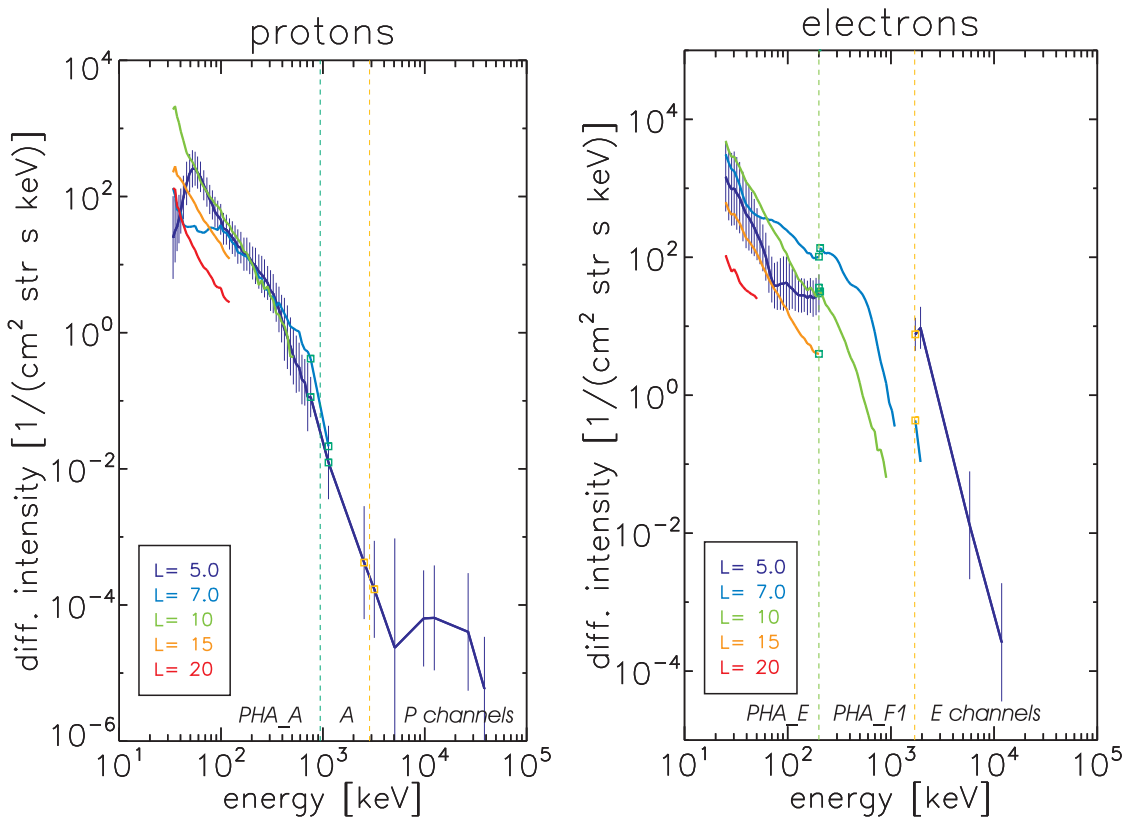


Figure 4.4: Spectra of long-term averaged differential intensities of protons (*left*) and electrons (*right*) with equatorial pitch angle $\alpha_0 = 90^\circ \pm 10^\circ$ for different values of $L \pm 0.5$ (*colors*). The intensity-points are given at the mean energies of the used channels. Several types of channels are used, which differ in energy range and resolution. Every transition from one channel type to the next is marked with *squares*. The standard deviation of the shown averages is shown exemplary for one L -shell. Regions in L and E that are considered as contaminated by any background are not shown.

Such a depletion is consistent with distributed losses from interaction of the protons with the Neutral Torus and the E ring: Both objects become increasingly dense towards $L = 4$, which explains the L -dependence. Charge exchange and energy loss of electrons is most efficient at low energies, which explains the E -dependence. Both processes are also more efficient for oxygen ions than for protons, which explains the difference in species. (O^+ is a component of the water group shown in Fig. 4.4. CE cross sections of H^+ and O^+ are for example compared in McEntire and Mitchell (1989), and Paranicas et al. (2008). Due to (2.65), energy loss in matter scales with the nuclear charge of the projectile.) In Sec. 6.2 it will be found that the proton losses are dominated by charge exchange, not energy loss.

The broad peak in the proton spectrum around 10 MeV is caused by the CRAND process that is producing protons, and electrons, but no other ions. The contribution from CRAND is expected to extend to even higher energies (Blake et al. 1983) and also to lower energies in the MeV range (Sec. 5.3).

In the region of $L \leq 7$, electrons have a flattened energy spectrum in the energy range

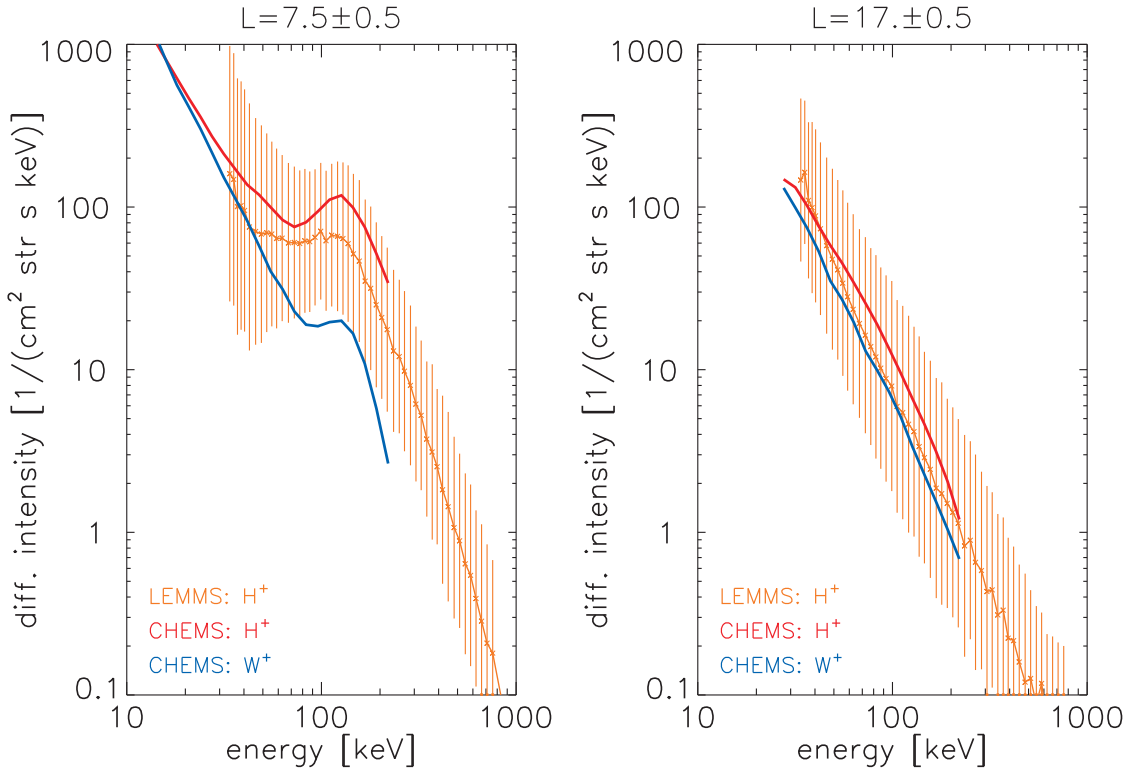


Figure 4.5: Spectra of long-term averaged differential intensities of protons (H^+) and water group ions (W^+) measured by CHEMS and LEMMS at $L = 7.5 \pm 0.5$ (left) and $L = 17.5 \pm 0.5$ (right). Both measurements average over all pitch angles. They were taken within $1R_S$ from the equator, which allows for a good averaging of all equatorial pitch angles. The averaged CHEMS data were provided by R. D. DiFabio (2011).

from several 10 keV to several 100 keV than outside this range. This coincides with the transition from the PHA_E1 to PHA_F1 channels and could therefore be only an instrumental effect. Since the flattening also been observed by Voyager's LECP (Krimigis et al. 1983), we consider it as a real, physical effect and propose several theories to explain it.

The flattening could arise from a depletion of electrons due to distributed losses, as proposed for the protons. The problem with this theory is that it alone cannot explain the relatively large abundance of electrons at the lower end of the spectra.

Instead from distributed losses in the neutral material, the flattening could also be explained due to localized losses along the orbit of Rhea. The absorption of electrons at moons is very energy dependent (Sec. 2.3.6). It can influence radial PSD profiles, and therefore energy spectra, even far inward of Rhea's orbit. This theory will be discussed in detail throughout Sec. 6.3.1.3.

Alternatively, the flattening could be an enhancement of electron intensity, instead of a depletion. The additional electrons might be produced by the neutron decay during the CRAND process. In that case, they are expected at energies less or equal to the mass defect between a neutron and its decay products, which is approximately 800 keV. This approximately fits the high-energy end of the flattening. The total number of protons and electrons produced by CRAND should be equal. This criterium can be used to falsify this theory. However, this would involve more analysis regarding the full electron and proton

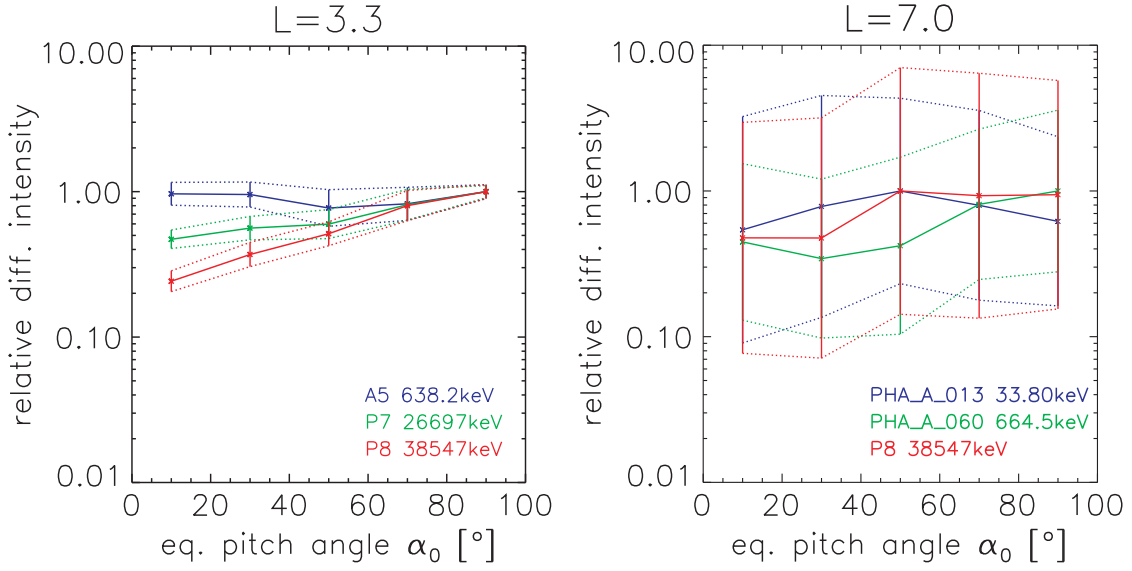


Figure 4.6: Pitch angle distributions in the mission-averaged data set. Protons at different, representative energies are shown. Their differential intensities were normalized to the maximum value. *Left:* PAD at $L = 3.3 \pm 0.1$, within the radiation belt between Mimas and Enceladus. *Right:* PAD at $L = 7 \pm 0.5$, within the middle magnetosphere.

spectra and is beyond the scope of this thesis.

An alternative hypothesis was advanced in [Paranicas et al. \(2010\)](#). They argued that electron injections, which have energies only up to hundreds keV, reach to minimum distances of about $L = 5$. This could lead to a flux pile-up close to this L -shell, consistent with the spectra.

4.2.4 Pitch angle distributions

In this section, we cut the particle distribution along α_0 , i.e. we provide pitch angle distributions (PADs).

Exemplary PADs are shown in Fig. 4.6. It can be seen there that high-energy protons within the radiation belts are mainly equatorially mirroring. Protons with lower energies appear as isotropic in the mission average although they have been found to be weakly field-aligned in single orbits ([Armstrong et al. 2009](#)). The reason why this does not appear in the average data set is that the anisotropy is of the same magnitude as the long-term variability of the radiation belts. As it will be discussed in Sec. 5.3, the belts change their intensity with the solar cycle. If the data are not averaged over the entire mission but within intervals, the PAD becomes visible again ([Roussos et al. 2011](#)).

Pitch angle distributions usually show changes in intensity less than an order of magnitude. This is below the level of the fluctuations in the middle magnetosphere. The PAD therefore vanishes in the mission average of the middle magnetosphere. This can be seen in the right panel of Fig. 4.6 where the changes of the average intensity are smaller than the size of the standard deviation. To derive PADs throughout the magnetosphere, other methods would be necessary. This was done by [Carbary et al. \(2011\)](#). They compiled

PADs for 200 keV electrons from every orbit separately and found that they are equatorially mirroring within $L < 10$ and change to more field-aligned outside this region. For lower energies, this transition occurs at smaller L (Schippers et al. 2008).

The use of the dipole model also causes imprecisions in the calculated equatorial pitch angle α_0 . We compare the pitch angles calculated from our model with some calculated by the *Khurana*-model. Particles with a local pitch angle α in a way that the equatorial one is $\alpha_0 = 10^\circ$ when the dipole model is used, typically have with the *Khurana*-model equatorial pitch angles between 6° and 11° . This error is smaller than the α_0 -bin size used here and therefore negligible.

4.3 Phase space densities

4.3.1 Computation

Energetic particles can move radially within a magnetosphere by adiabatic processes as it was explained in Sec. 2.2. The energy of the particles changes significantly during such processes. Radial intensity profiles at constant particle energy are therefore not helpful to understand the radial dynamics of the particles. To approach this it is useful to compensate for the adiabatic heating i.e. to consider different energies for different L -shells. Also, we ultimately want to apply the diffusion equation (2.56) to the measurements. This equation also does not require phase space densities at constant E and α_0 but at constant invariants μ and K . Therefore, we now do a coordinate transformation from (E, α_0, L) to (μ, K, L) and showing cuts of the distribution function orthogonal to the new axes.

The distribution function expressed in the coordinates (E, α_0, L) was given throughout Sec. 4.2 in terms of differential intensity j . Although the transformation to (μ, K, L) does not require this, we will express the distribution function now in terms of the phase space density f .

The phase space density is, as indicated by the name, the number d^6N of particles per volume d^3V_x in real space, and per volume d^3V_p in momentum space.

$$f = \frac{d^6N}{d^3V_x d^3V_p} \quad (4.3)$$

The differential intensity j is related to the phase space density f by (Walt 1994)

$$f = \frac{j}{p^2} \quad (4.4)$$

This relation is valid independent on the coordinate system in that f and j are given and applies both to relativistic and non-relativistic energies. It can be easily shown that (4.4) is true by equating $dp/dE = 1/v$, $d^3V_x = d^2A v dt$, and $d^3p = p^2 dp d^2\Omega$ into (4.1) and (4.3), and comparing the results.

Throughout Sec. 4.3.1 and for the sake of precision, we will label the differential intensity measured at a precise energy and pitch angle as j , and the one within intervals of these quantities as \bar{j} . Energetic particle detectors measure the latter. We therefore cannot derive f but a quantity \bar{f} that is approximately the same.

The PSD $\bar{f}(\mu, K, L)$ at constant adiabatic invariants is related to the differential intensity $\bar{j}(E, \alpha_0, L)$ at constant energy and pitch angle via

$$\bar{f}(\mu, K, L) = \frac{\bar{j}(E(\mu, K, L), \alpha_0(\mu, K, L), L)}{p^2(E(\mu, K, L))} \quad (4.5)$$

To calculate this, first $E(\mu, K, L)$ and $\alpha_0(\mu, K, L)$ are computed numerically. We have two codes available for this and use both of them. The first one is precise but slow and uses the following algorithm. Both invariants μ and J_2 can analytically be solved for the energy. This provides two functions $E_1(\mu, \alpha_0, L)$ and $E_2(J_2, \alpha_0, L)$, where the second involves a numeric integration. The integration is implemented by the rectangle rule where the size of the intervals is refined until the result converges. Then $E_1 - E_2$ (at fixed values μ, J_2, L) is evaluated for different α_0 (with an initial set of α_0 , which is then refined if and where necessary) until it falls below a threshold. The α_0 and E where this is fulfilled are at the chosen L equivalent to the chosen values of μ and J_2 . After this, J_2 is converted to K by (2.20).

The precision of any code calculating adiabatic heating can be tested by transforming (E, α_0) at a given L to (μ, K) and then back to (E, α_0) at the *same* L . Additionally, (E, α_0) can be calculated at a *different* L . This then can be converted back to (μ, K) to check if there really were conserved. The described code does this check continuously and warns in case of large imprecisions. The typical imprecision is $< 0.1\%$, even in extreme cases it is never above several percent.

The second code used here was provided by E. Roussos (2010) and is faster. Its imprecision is typically $\approx 1\%$, which is larger than the other model but still well enough.

After calculating $E(\mu, K, L)$ and $\alpha_0(\mu, K, L)$, \bar{j} is retrieved at these energies and pitch angles from the data. Since LEMMS does not provide intensities for arbitrary E and α_0 , we use interpolation and binning for this. Due to the extent of LEMMS' apertures, the intensities measured at a given (central) pitch angle also include contributions from the neighboring angles. Therefore, and in order to reach better statistics, the intensities are binned in α_0 . The energy spectrum that can be derived from these bins is then linearly interpolated on a double-logarithmic scale. This interpolation implies the assumption of a power law to fit in between the channels.

Usage of the dipole model causes, again, imprecision, this time in phase space density. We estimate the imprecision for equatorial, non-relativistic particles. A deviation ΔB between the assumed dipole magnetic field and the real field causes a deviation $\Delta E = \mu \Delta B$ in energy, if the energy $E = \mu B$ is calculated from the conservation of μ . Assuming that the phase space density follows a power law

$$f = \zeta E^{-\gamma_f} \quad (4.6)$$

then its deviation due to an imprecise energy is

$$|\Delta f| = \gamma_f \frac{\Delta E}{E} f = \gamma_f \frac{\Delta B}{B} f \quad (4.7)$$

Fig. 4.7 compares the total value of the measured magnetic field with the used dipole model. It can be seen there that it is $\Delta B/B < 1$ for the entire L -range covered here.

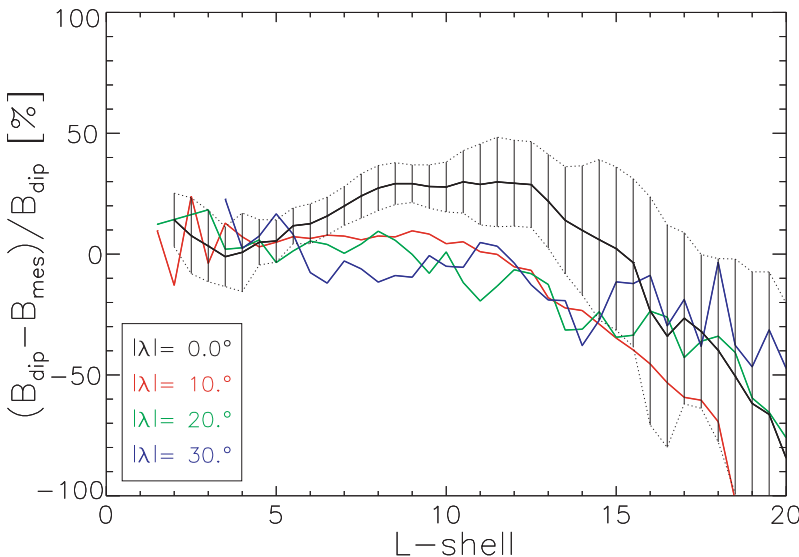


Figure 4.7: Comparison of the total magnetic field derived from the dipole model B_{dip} with the long-term averaged values B_{mes} . The magnetic measurements were linearly averaged within latitudinal bins of 10° .

As already stated in Sec. 4.2.3, it is $\gamma_j \leq 3$. The exponents of j and f are in the non-relativistic case related as $\gamma_f = \gamma_j + 1$ (due to (4.4), and $p^2 \propto E^1$ for the non-relativistic case). From this follows $\Delta f < 4f$ outside the radiation belts, which is well below the standard deviation of the mission average there.

4.3.2 Radial profiles

Figures 4.8 and 4.9 present PSDs as based on the LEMMS mission average. These values are derived by the method described above from differential intensities as they were shown in Fig. 4.2. The data extend over the full range of adiabatic invariants covered by LEMMS. The equatorial pitch angle of the particles shown in the upper panels is approximately $4^\circ \leq \alpha_0 \leq 10^\circ$ (relatively field-aligned) and $83^\circ \leq \alpha_0 \leq 77^\circ$ (almost equatorially mirroring) for the lower ones.

In Figures 4.8 and 4.9, the proton radiation belts are visible for $L < 5$ as regions of locally increased phase space density. We do not provide PSDs of the electron radiation belts because most of the electron channels are contaminated by radiation belt background and the remaining channels do not provide sufficient spectral information for a reliable energy interpolation.

For $L > 5$, all profiles show a general decrease towards small L . The profiles of equatorial particles are generally steeper than field-aligned ones. The latter tendency was neither apparent nor studied in previous works that analyzed data from the flyby missions. Most profiles showed equatorial particles (McDonald et al. 1980, Van Allen et al. 1980a, Hood 1983), or focused on other pitch angles (as $\approx 30^\circ$, Armstrong et al. (1983).) Most profiles were similarly flat as we observe it for field-aligned particles. We discuss this difference at the end of the current section. The origin of the PSD gradient in L , and its dependence on pitch angle will be the topic of Sec. 6.3.1.2.

The electron profiles additionally show a sharp change in gradient at $L \approx 9$, which is the orbit of Saturn's moon Rhea. The magnitude of the gradient-change depends on energy. A profile of this kind is consistent with electrons that are absorbed by Rhea if they have energies to encounter it frequently. This will be further explained and reproduced in Sec.

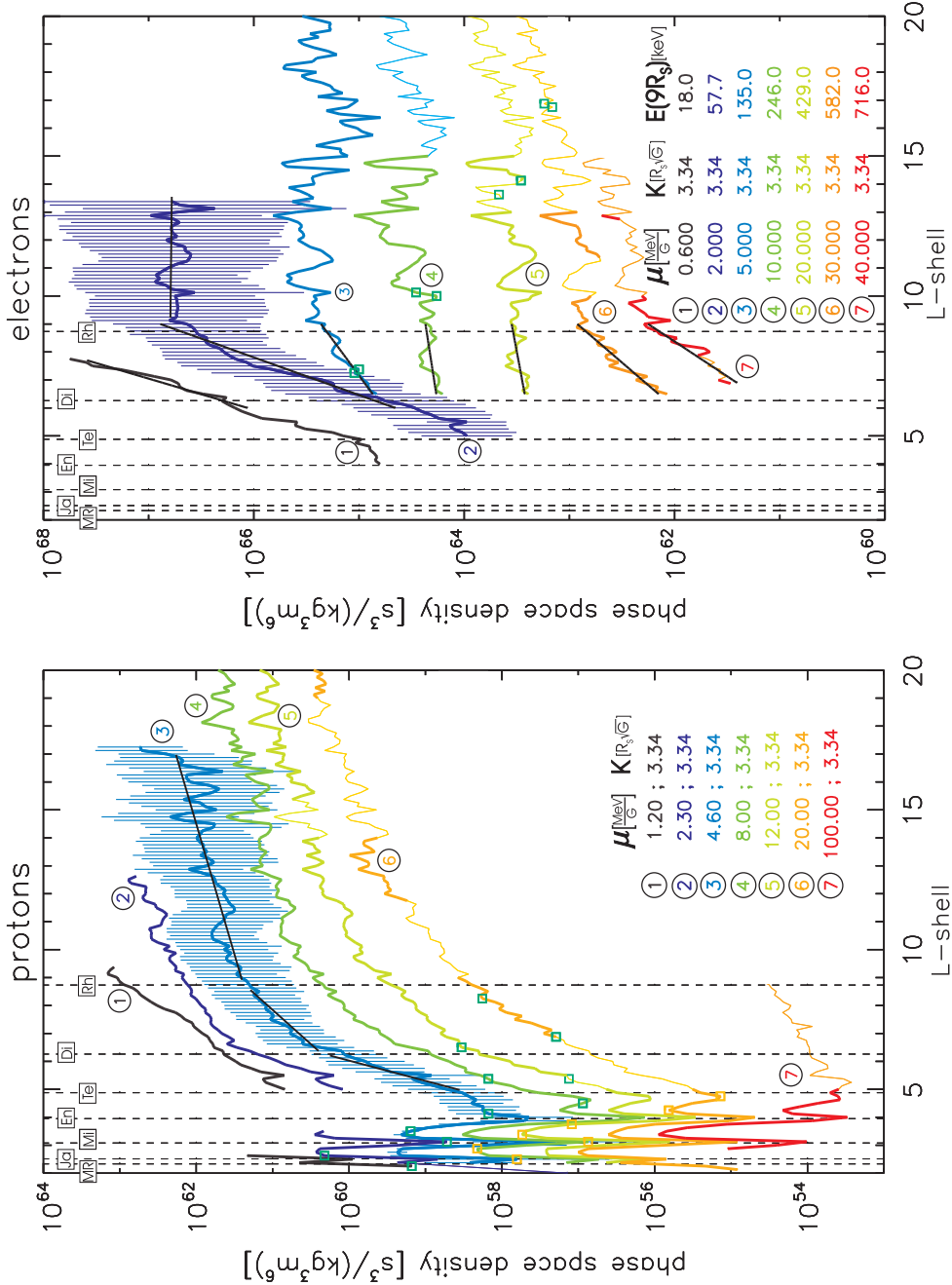


Figure 4.8: Long-term averaged phase space densities of protons (*left*) and electrons (*right*) with constant first and second adiabatic invariants (*colors*). Pitch angles are binned to $\alpha_0 = 10^\circ \pm 10^\circ$. The *squares* mark the transition between different channel types, as in Fig. 4.4. The gradients of the profiles change near moon orbits, which is illustrated by *black, straight lines* to guide the eye.

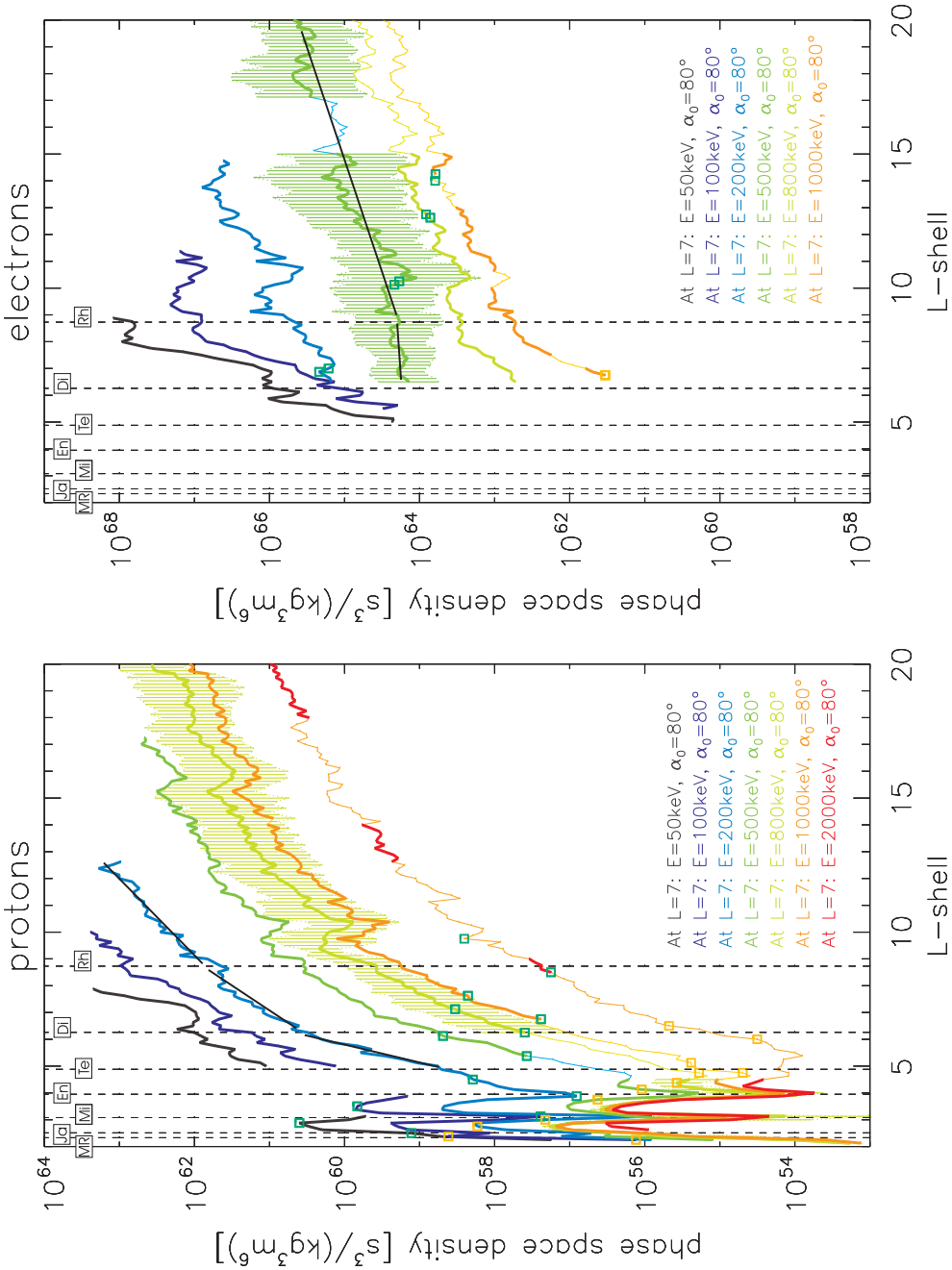


Figure 4.9: Long-term averaged phase space densities of protons (*left*) and electrons (*right*) with constant first and second adiabatic invariants (*colors*). The pitch angle is binned to $\alpha_0 = 80^\circ \pm 10^\circ$. Otherwise as Fig. 4.8

6.3.1.3.

It is interesting to mention that Van Allen et al. (1980a) observed a similar gradient-change of electron PSDs, but at $L \approx 10$. However, this is probably the same feature because the large energy range of their channels transforms to a imprecision in L , they assumed a constant γ_j for computing the PSDs, the PSDs generally scatter a lot, and moon signatures are commonly displaced from their expected L -shell (Roussos et al. 2005, Andriopoulou et al. 2012).

Rymer et al. (2007) analyzed electrons at lower energies than LEMMS with CAPS. They show that electron PSDs with a different behavior: not the PSD gradient changes with energy, but the L -shell where the gradient-change occurs moves outward with rising energy. Since this behavior does not show up in the other orbit they analyzed, we interpret it as an atypical configuration that is not apparent in the mission average. Such a configuration can arise from recent interchange events (Sec. 2.2.3). During such events, a flux tube is moving towards smaller L . High-energy particles drift faster out of this flux tube than the low-energy particles. The PSD profile of high-energy particles therefore decreases at larger L than the profile of low-energy particles. This explanation is included Rymer et al. (2007) but there the interchange is considered as a more steady phenomenon.

Losses at moons should not only affect the electrons but also the proton profiles. Since the proton profiles fall in general faster towards the planet, a small modification in the slope due to a moon is harder to recognize compared to the electron profiles. What makes a confident claim about this issue difficult is the fact that it is easy to imagine gradient-changes in the large scattering of the middle magnetosphere. However, a careful inspection of Fig. 4.8 and 4.9 shows that gradient-changes also seems to occur for protons. The cases where this occurs not exactly at the moon orbit might result from the overall scattering. The fact that the gradient also changes smoothly in between the orbits is different to the electrons. This, however, does not exclude the significance of moon losses. For example, PSD profiles under the assumption of pure radial diffusion follow a power law. Such functions are consistent with the observed profiles in between the orbits, as it will be shown in Sec. 6.3.

Alternatively or additionally to the losses at the moon orbits, distributed losses in the gas and grain environment might contribute to the decay of the PSD. This will be discussed more in Sec. 6.3.1.2.

Calculating phase space densities of energetic particles is nothing new and has been done before. An overview on PSDs from previous missions can be found in Van Allen (1984) and references therein. The advantage of the data as it is presented here is the larger data set and a higher awareness of the importance of backgrounds and contamination. Both makes a comparison between the PSDs here and in literature difficult: Even comparing energy spectra between LEMMS and other instruments yields differences both in absolute values as in qualitative details. A difference in spectra naturally translates to a difference in PSD profiles. Additionally, previous procedures to derive PSDs used assumptions that are not necessary and not used for our large data set: Although this is not always clearly stated (Hood 1983, Armstrong et al. 1983), it was apparently common to assume that the spectral index is constant over L (Van Allen et al. 1980a). This works well when only a small L -range is used (Thomsen et al. 1977) but can for some energies cause deviations when studying large L -intervals.

We performed an exemplary comparison for protons measured by LEMMS' PHA chan-

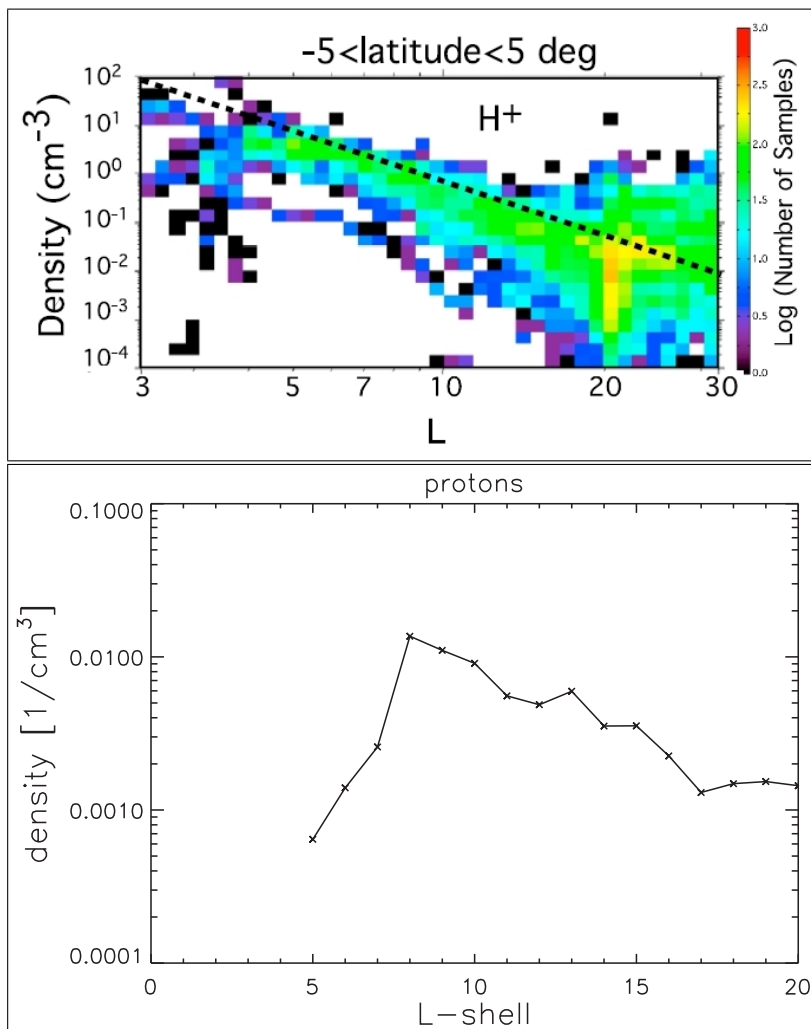


Figure 4.10: Real space density of different proton populations. *Upper panel:* Protons below 50 keV, as measured by CAPS close to the equatorial plane. Color indicates the number of samples. The dashed line represents an estimated upper bound. Figure adapted from [Thomsen et al. \(2010\)](#). *Lower panel:* Protons above 34 keV, as measured by LEMMS.

nels and Voyager's LECP data. Although they roughly agree, there are deviations. Some of these match the edges of the mission-average 1σ or 2σ error bars. These might be coincidental and follow from the fact that a single orbit not necessarily represents the average state of the magnetosphere. Additionally, it is known nowadays that at least LECP's PL01 to PL05 ion channels were severely contaminated by electrons, which were in parts measured by the E β channels (T. P. Armstrong , priv. comm., 2010). Intercalibration and, eventually, comparison and interpretation of the data, is a difficult topic for all energetic particle instruments and should not just apply to the tested channels. It is a persistent problem in the overlapping energy ranges between LEMMS and CAPS and even the E and F detectors within LEMMS itself. We therefore decided not to pursue this topic further but trust the LEMMS calibration as it is currently used. This is the reason why comparisons with published PSDs are mostly qualitative throughout this thesis.

4.4 Real space densities

In Sec. 2.1.2 we claimed that energetic particles do not have a significant (charge) density compared to the plasma. We check this assumption here.

The density n in real space is the number d^3N of particles per volume d^3V_x in real space. It is related to the density f in phase space via

$$n = f d^3V_p = f p^2 dp d^2\Omega \quad (4.8)$$

dV_p is the infinitesimal volume in momentum space. The second equality in (4.8) expresses it in spherical coordinates.

To calculate n , we use a macroscopic interval Δp that is equivalent to the energy range ΔE of the used channels. We assume isotropy and therefore the solid angle to be $d^2\Omega = 4\pi$. The total density of all particles within the energy range of LEMMS is derived by integrating over the contributions from all channels. The resulting density as a function of L is shown in Fig. 4.10, lower panel.

The same energy range is used for all L . Under these conditions it was not possible to calculate densities within the radiation belts, since there are only measurements from the high-energy channels available. Also, it was necessary to include channels that are flat due to instrumental background at large L . This implies that the density calculated here is an upper limit. However, even this upper limit is well below the densities of the thermal plasma, as they are displayed in the upper panel of the figure.

It is interesting to mention that the density is largest in the region where Connerney et al. (1981) proposed the ring current ($8.5 \leq L \leq 15.5$).

Since the energy spectrum of electrons has more gaps than the proton one, we did not derive electron densities so far.

One should mention here that while the density of energetic particles is indeed negligible compared to the plasma, this is not the case for their pressure. While the energetic particle pressure is well below the plasma one at small L , the contributions are roughly the same outside about $12R_S$ (Sergis et al. 2009, Bagenal and Delamere 2011).

5 Processes in the proton radiation belts

5.1 Introduction

Radiation belts commonly form around a planet where its magnetic field is capable and strong enough to provide stable trapping even against electromagnetic fluctuations, and losses are slow or not existing. The origin of the radiation belt particles, at least for protons above 10 MeV, is believed to be CRAND (Sec. 2.4.2).

The spatial distribution and energy spectra of Saturn's belts have been shown in the previous section 4. They are unique in the Solar System due to their strong separation along the orbits of several moons. These moons are Janus and Epimetheus (which share a similar orbit), Mimas, Enceladus, and Tethys. The belts do not extend inward of the Main Rings ($L < 2$) because the rings absorb charged particles bouncing through them fast.

In comparison, the inner part of Earth's radiation belts is also populated by CRAND. The outer part, however, is mainly populated by particles originating from the solar wind.

In addition to these *classic* radiation belts, exists a secondary belt for both Earth and Saturn (Moritz 1972, Krimigis et al. 2005). These are thought to originate from the charged particles that were lost to the atmosphere due to charge exchange. In this process, they were converted to energetic neutral atoms (ENAs) but reionized again.

Due to solar activity, the particle populations within magnetosphere and radiation belts can be enhanced for a limited period. At Saturn, this occasionally increases the intensity in a large range outside the classic belts. This intensity diminishes until only particles within a confined region between Tethys and Dione are present. This then is a transient radiation belt that sometimes is referred to as the *Dione belt*. This belt decays on the time scale of months and finally vanishes (Roussos et al. 2008b).

This section focuses on the classic proton belts. Our goal is to identify the various processes that create the particles and distribute them in the way that is observed. We will use models reproducing measurements of the belts as a tool to determine the relative importance as well as absolute parameters of the processes (Sec. 5.2). The results are partly phenomenological and will be interpreted. In contrast to the high energies, especially the origin of protons with energies below 10 MeV was not conclusively solved so far. As a second step, we therefore focus on the nature of the source process and discuss different possibilities to explain it (Sec. 5.3).

Using modeling (Cooper 1983, Santos-Costa et al. 2003, Gubar 2004) of Saturn's radiation belts in order to quantify the acting processes (Van Allen et al. 1980a, Armstrong et al. 1983) has been done before. Nevertheless, previous works only had data sets from

the flyby missions available. These data sets are not only short but also only include little spectral information of the radiation belts. Here, we use the described mission-averaged data set which has a good spectral resolution. The model treats the entire region of the radiation belts consistently, respecting simultaneously all relevant processes within a large energy range.

5.2 Proton belts model

5.2.1 The model

This model assumes that the protons trapped in the radiation belts conserve their first and second adiabatic invariants and that the radial phase space density profiles can be described with the diffusion equation (2.56). This equation summarizes the processes that form and sustain the belts: first, the protons are supplied (source), then they redistribute (diffusion) and finally get lost (sink). In case that all processes cancel each other out, a steady state is reached. The equation can both describe time-dependent PSDs at a given instant as well as time-averaged PSDs, depending if instantaneous or averaged rates of the processes are used. It should be pointed out here that average PSDs are well-defined and meaningful even in case of a non-steady state.

All rates of the given processes are changes of PSD per time. In this thesis, absolute values for the rates are given in units of $s^2/(kg^3 m^6)$. In order to understand the magnitude of these values, relative rates are provided that have been normalized to the PSD at the given location and invariants and are given in units of %/s. These values may be converted by the reader to (residence, loss, or build-up) times (depending on the process) by inverting them. To get a number in years, a relative rate in %/s has first to be multiplied by $\approx 3 \cdot 10^5$ and then inverted.

We chose to solve the diffusion equation (2.56) numerically in order to be as flexible as possible considering assumptions and boundary conditions. The solutions are provided by the computational software Mathematica ([Wolfram Research 2008](#)) and typically feature a residuum (which is in the steady state equal to $\partial f / \partial t$) that is orders of magnitude smaller than the other terms.

Throughout this work, the radiation belts are calculated partly separately and partly as an extended region. While the various belts can have different boundary conditions, all are subject to the same functions describing diffusion, sources, and losses. These functions depend on L and other quantities but, for the sake of consistency, are not switched in between the belts.

5.2.1.1 Sources

The model accounts for the proton production by using a phenomenological source which is included in the diffusion equation (2.56) with the term $\delta f / \delta t|_S$. At least one contribution of the source is CRAND. Since this is an energy-dependent process, also the total source can be so. In order to decide on a function $\delta f / \delta t|_S(E)$, first the steady state spectrum $f(E)$ is studied.

Fig. 5.1 is similar to Fig. 4.4 but shows spectra obtained of every single radiation belt, very close to its maximum. While these spectra are offset from each other, their shape is

strikingly similar. This can be a signature of a common source process. We therefore use a model source with an energy dependence that approximates the spectrum, as shown by the smooth cyan line in Fig. 5.1. It consists of a power law

$$\left. \frac{\delta f}{\delta t} \right|_{S,\text{low}} = s_0 \epsilon^{-\gamma_f} \quad (5.1)$$

representing the low-energy source process, and a log-log scale parabola

$$\log \left(\left. \frac{\delta f}{\delta t} \right|_{S,\text{high}} \right) = -7(\log(\epsilon) - \log(\epsilon_C))^2 + \log(ss_0) \quad (5.2)$$

representing the high-energy source process. We will refer to this as the low and high-energy source or the power law and CRAND peak part. ϵ is the dimensionless energy $\epsilon = E/E_0$ with the arbitrary energy E_0 . $\gamma_f = 3.9$ is the slope of both the PSD spectrum and the source. $\epsilon_C = 12.4$ MeV is the assumed position of the CRAND peak. s is typically chosen in a way that the CRAND peak at ϵ_C is a factor of 20 above the power law part. Both functions cross at 8 MeV where a smooth transition is enforced. This is implemented by multiplying the functions with a cold Fermi function that smoothly changes from 1 to 0 (or vice-versa) at 8 MeV.

Since the energy of protons with a given (μ, K) -set changes with L , the energy dependence of the source transforms to an L -dependence. Additionally, we allow for the overall amplitude of the source s_0 to change with a power law

$$s_0 = S_0 \left(\frac{L}{L_0} \right)^{-m} \quad (5.3)$$

This is reasonable for the CRAND process where the neutrons are emitted from Saturn and its rings. We assume that the low-energy source operates with the same scaling and have not found evidence for the contrary.

We expect $0 > m > 2$ for CRAND. Even neutrons with 100 keV need only 70 s to travel $5 R_S$, which is 8% of their lifetime. If they are emitted isotropically and the decay is neglected, their intensity will scale as r^{-2} (radial distance r). The proton intensity would therefore scale with $m = 2$ if no magnetic field was present around Saturn. This also holds for equatorially mirroring protons that are produced from neutrons that decayed at the magnetic equator. If the neutrons decay at high latitudes instead, they will produce protons with $\alpha_0 \neq 90^\circ$ at $L > r$. Their intensity therefore decays slower with L , which can be approximated by a value $m < 2$. Since the intensity will always decrease with distance, m can never become negative.

In the literature, the L - and α_0 -dependence of the proton source is usually combined into an injection efficiency χ (Dragt et al. 1966). For neutrons from Saturn's Main Rings and atmosphere that decay within $1.5 \leq L \leq 3.9$, it is $10^{-2} < \chi < 1$, changing up to one order of magnitude between different L -shells or pitch angles (Cooper 1983, Blake et al. 1983).

5.2.1.2 Diffusion

Competing with the source is radial diffusion. While the source always provides particles ($\delta f/\delta t|_S > 0$), the role of diffusion depends on gradient and curvature of the PSD profile

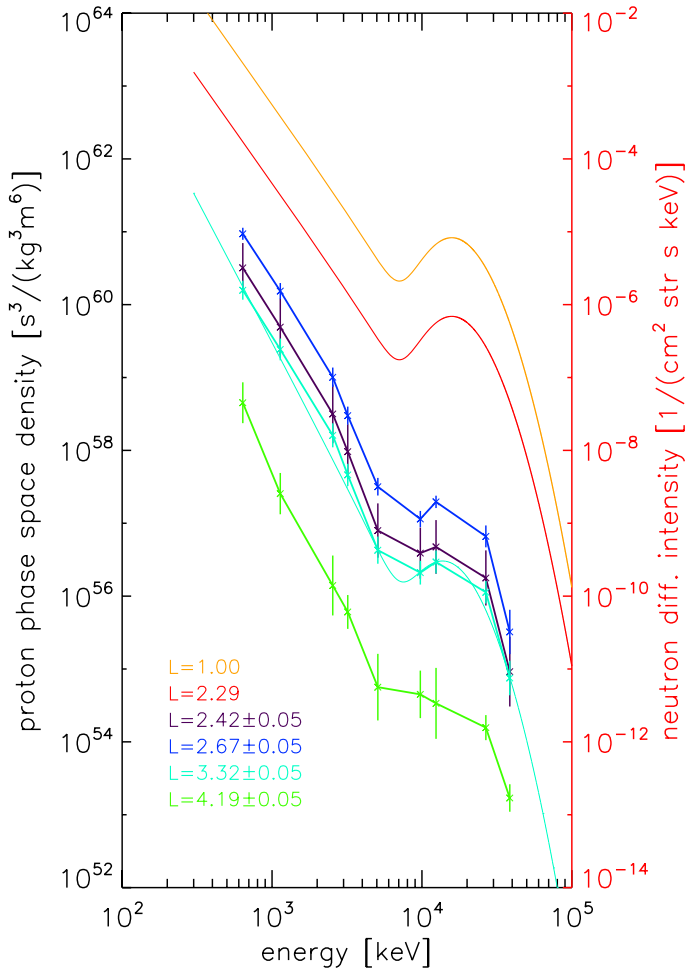


Figure 5.1: Measured proton and modeled neutron spectra. *Lines with points:* Mission-averaged measurements of proton phase space densities at the peak positions of Saturn's radiation belts (precise positions given in the legend). *Cyan smooth line:* Function used in the model to approximate the proton spectra and the source rate. *Orange and red smooth lines:* Neutron differential intensity spectra derived from the model at the positions of atmosphere, and Main Rings, respectively.

as a function of L . Diffusion tends to eliminate local extrema and therefore transports protons away from the peaks of the radiation belts (causing a local loss, $\widehat{D}f < 0$) and into the sweeping corridors of the moons (refilling them, $\widehat{D}f > 0$).

From the theory of diffusion caused by electromagnetic fluctuations (Sec. 2.2.1.3-2.2.1.4) it is expected that the diffusion coefficient scales with a power law in L , unless P (which describes the fluctuations) is strongly L -dependent or its dependence on frequency cannot be described with a power law. We neglect this first since we have the option to change our approach if it does not succeed. Additionally, any possible dependence of the diffusion coefficient on μ or α_0 is neglected.

In summary, the radial diffusion coefficient D_{LL} is parametrized as

$$D_{LL} = D_0 \left(\frac{L}{L_0} \right)^n \quad (5.4)$$

We will refer to n as the diffusion exponent. D_0 is the diffusion coefficient at L_0 , which is an fixed but arbitrary L -shell. As starting values $n = 7$, and $D_0 = 10^{-9} \text{ s}^{-1}$ at $L_0 = 3.5$ are used, based on Sec. 2.2.1.7.

5.2.1.3 Sinks

Compared to source and diffusion, the loss processes are fairly well constrained.

A dominant control of the radiation belt shape is exerted by absorption processes at Saturn's icy moons and Main Rings. The loss processes resulting from this will be treated using two different methods: boundary conditions and sink terms.

Throughout the *boundary method*, every belt has two boundary conditions equal to values measured outside the sweeping corridor. As long as no profiles within the sweeping corridors are calculated, it is not necessary to use a loss term in the diffusion equation (2.56) that accounts for moons or rings. Their presence is in this method hidden in the boundary conditions since their value is determined by all relevant processes, including the moons. The method is robust since it does not require information about the moon losses and is not too sensitive to other processes since the L -range of a single radiation belt is relatively small.

To describe the particle profiles also within the sweeping corridors, it is necessary to properly describe the losses there. The lifetime of charged particles against absorption along a moon orbit is determined by the encounter time τ_{enc} between moon and particle, and the absorption probabilities a (Sec. 2.3.6). The loss term that results from this is

$$\frac{\delta f}{\delta L} \Big|_M = a \frac{f}{\tau_{\text{enc}}} \Theta(L - L_{M,\text{in}}) \Theta(-L + L_{M,\text{out}}) \quad (5.5)$$

τ_{enc}/a is assumed to be constant within the sweeping corridor that is contained by the step functions Θ . This is a reasonable assumption, although in reality there should be a smooth transition towards the corridor and fluctuations of τ_{enc}/a within it (Bell and Armstrong 1986).

We will refer to using Eq. (5.5) for treating a moon as the *sink method*. If particles are exchanged between the belts in a way that there is a persistent PSD within the sweeping corridors, this method can be used. Unlike the boundary method, it can simultaneously treat several belts that are separated by moons. The sink method is inappropriate if the belts exist independent of each other. In that case, trying to solve the diffusion equation (2.56) for one profile to describe multiple belts does not make sense. The numerical solutions that can be found despite that always describe only one belt at a time but do not fulfill (2.56) in other regions.

The question if the radiation belts exist independent or not is not just a technical detail for the modeling but of physical importance. It will be studied in Sec. 5.3.3.

While the moons cause very localized losses close to their orbits, there also exist distributed losses in the magnetosphere. Close to the orbit of Enceladus ($L = 4$) resides the peak of the Neutral Torus (Sec. 1.2). Energetic particles gradually lose energy within its gas, and protons can additionally undergo charge exchange (CE). The rates of these two processes have been given in Eq. (2.76) and (2.64). They are adapted here to account for multiple neutral species

$$\frac{\delta f}{\delta t} \Big|_{\text{Ex}} = - \sum_j \frac{v}{p^2} \frac{\partial}{\partial E} \left(p^2 F \frac{dE_j}{dx} \right) \quad (5.6)$$

$$\frac{\delta f}{\delta t} \Big|_{\text{CE}} = - \sum_j \sigma_{\text{CE},j} v \tilde{n}_j f \quad (5.7)$$

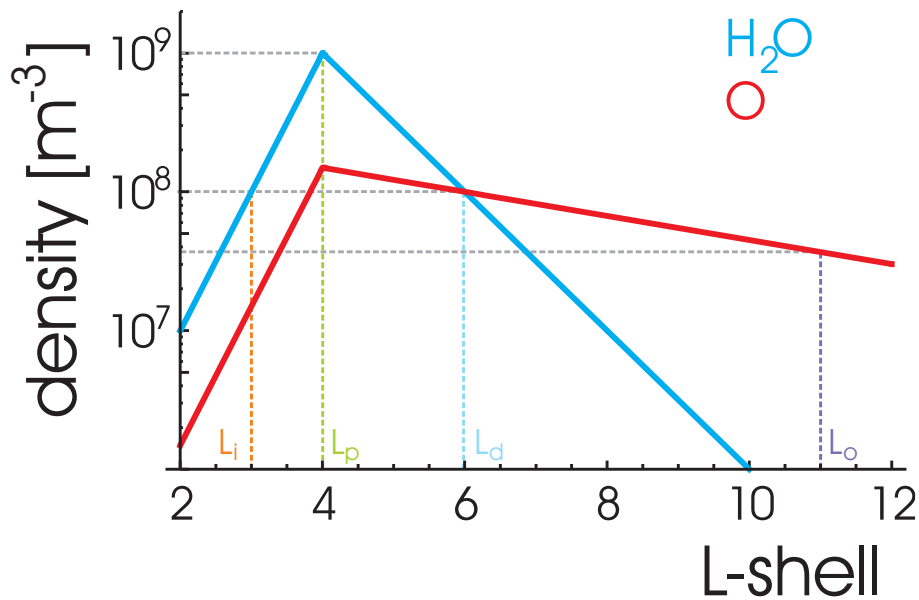


Figure 5.2: Equatorial density of the Neutral Torus as assumed in the model. It is defined by the densities given at the L -shells marked by dashed lines.

where the index j describes the neutral particle species.

The phase space density in (5.7) is $F(L, E) = f(L)S(E)$, where $f(L)$ is the PSD profile of a given (μ, K) -set and $S(E)$ describes the spectrum. In the model, $f(L)$ is taken to be the solution of the diffusion equation (2.56) and it is assumed that $S(E)$ has the same energy dependence as $\delta f/\delta t|_S$.

\tilde{n}_j is the density for species j of the Neutral Torus. The model uses a simple representation of the torus that roughly reproduces its main features that have been described in Sec. 1.2.2. The model torus consists of H_2O and O and is plotted in Fig 5.2. It peaks at $L_p = 4$ with a density of H_2O referred to as n_p , which is one of the parameters it is optimized for in Sec. 5.2.2 for. H_2O decays exponentially in both directions: to n_i at $L_i = 3$, and to n_d at $L_d = 6$. Outward of L_d , the total density is dominated by O -atoms. Also these decay exponentially from L_p on: outward to n_d/e at L_o , inward with the same slope as H_2O .

We assume that the vertical density profile behaves as a Gaussian with maximum n_0 at the equatorial plane. We will refer to the distance of the points where the density drops to n_0/e as thickness H and assume $H = 1R_S$ for all L . Charged particles bouncing at $L = 4$ through a gas of this profile experience a path-averaged density that can be an order of magnitude below the equatorial value: $\tilde{n} = 0.1n_0$ for $\alpha_0 = 10^\circ$ and $\tilde{n} = 0.3n_0$ for $\alpha_0 = 50^\circ$.

$dE_j/dx(E)$ in (5.7) is the energy loss per distance in a gas of species j with density \tilde{n}_j . Values as they are described in Sec. 2.3.3 are used. A crucial feature in Eq. (5.6) is that $\delta f/\delta t|_{Ex}$ can change its sign depending on how F and dE/dx vary with energy. This is illustrated in Fig. 5.3. For the typical case of a falling energy spectrum, energy loss causes a net loss of particles. However, for an increasing spectrum, a specific energy can receive more particles from higher energies than losing to lower energies, so that the energy loss causes a net particle gain. This is the case at the onset of the CRAND peak and towards the losses at low energies. We will continue referring to energy loss as being

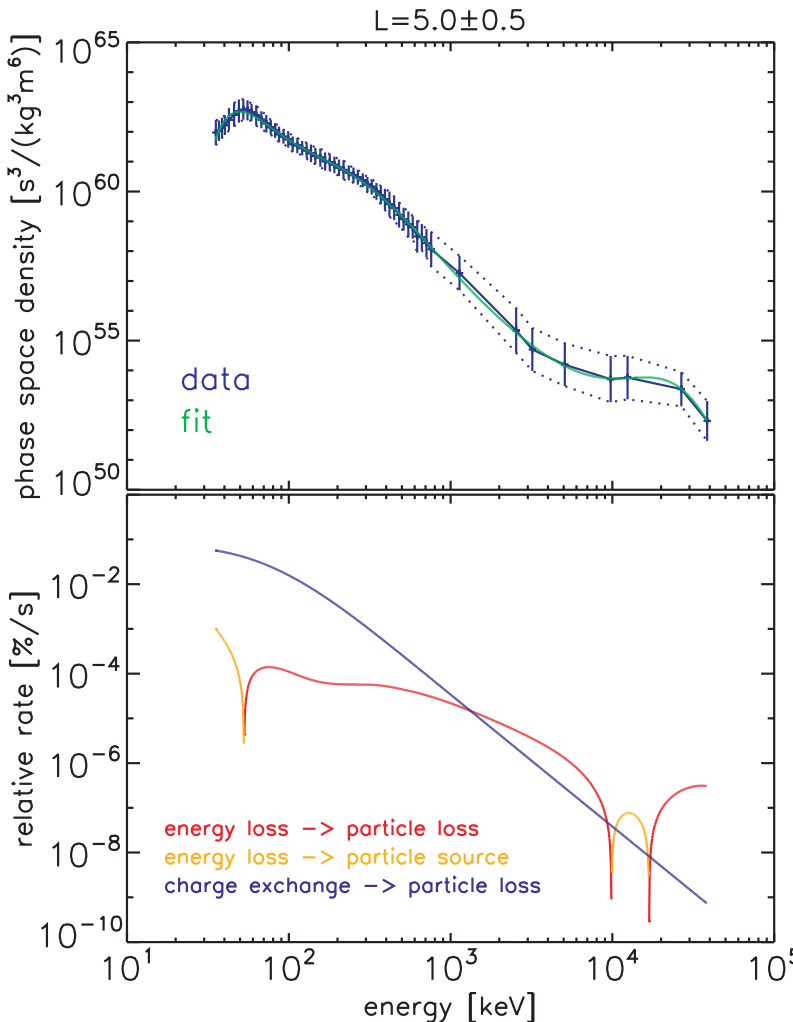


Figure 5.3: *Upper panel:* Measured proton spectrum as a function of energy at $L = 5 \pm 0.5$ (blue), and a polynomial fit (green). *Lower panel:* Relative rates $(\delta f / \delta t)|_{CE,Ex} / f$ due to charge exchange (blue) and energy loss in the Neutral Torus. Depending on the spectral slope, energy loss either acts as a loss (red) or source (orange) for the shown energies.

in the category of loss processes despite this fact.

Using the gas density of the model torus it is also possible to estimate the loss rates of charge exchange. Sample results for $L = 5$ are included in Fig. 5.3. As it can be seen there, charge exchange is the fastest process at energies $E < 1$ MeV. Energy loss is mostly dominant for $E > 1$ MeV. The total loss rate is therefore not sensitive to the uncertainties of the charge exchange cross section at these energies.

Although also other types of losses can occur, they can be neglected, as it is argued in the following.

Energy loss does not only occur in the neutral gas but also within the plasma environment. Since Saturn's magnetosphere is special in the respect that the neutral density exceeds the plasma density (Sec. 1.2.3), this can be neglected.

Overlapping with the Neutral Torus is the E ring (Sec. 1.2). As we will show in Sec. 6.2, the energy loss within its grains is negligible with respect to charge exchange and smaller than energy loss in the Neutral Torus, at least at $L \approx 7$ and $E < 1$ MeV. Towards $L = 4$, the grain density rises about an order of magnitude but this is also true for the gas. Therefore, the E ring is for energetic protons probably unimportant throughout the whole magnetosphere. An extrapolation of the loss rates in gas and grains to higher energies shows that this probably also applies to the energies considered in this work. We

therefore do not consider the E ring in this part of the thesis.

Energetic particles do not only lose energy within matter, they can also be scattered. For protons (which are relatively heavy compared to electrons) this effect is negligible (Jackson 1998, Fok et al. 1991).

Wave-particle interactions can cause pitch angle diffusion, which can scatter particles to the loss cone, and energy diffusion. Indeed, there is a large variety of waves observed at Saturn (Mauk et al. 2009). Common types of waves causing wave-particle interactions are whistler and ion-cyclotron waves (Thorne 2010). At Saturn, these waves are considered to be weak and are not expected to contribute to diffusion (Kurth 1992). Therefore, they are commonly ignored at Saturn, although sometimes only implicitly by using the radial diffusion approach (Van Allen et al. 1980a, Santos-Costa et al. 2003). Even at Earth, energy diffusion and, in case of ions, also pitch angle diffusion are often neglected (Beutier and Boscher 1995, Beutier et al. 1995).

5.2.2 Model results

5.2.2.1 Optimization

Figure 5.4 shows measured phase space density profiles of the radiation belts for nine different sets of μ and K . The range of (μ, K) -values that LEMMS can measure is determined by its energy coverage and the L -range of interest. The left and right columns of Fig. 5.4 represent the edges of this range. The middle column was chosen in a way that their profiles lie approximately between the profiles shown in left the right columns.

Typically numerical solutions of the model are calculated for all nine (μ, K) -sets and compared to the measurements. The boundary method is used by default in order not to assume anything yet about particle exchange between the belts. If the trial solutions do not match the observations, the assumptions on D_{LL} and $\delta f/\delta t$ in Eq. (2.56) are changed and the calculation is repeated until the resulting profiles converge towards a minimum in the deviation Δ . This is defined here as

$$\begin{aligned} \Delta &= \sum_{i,j} \sqrt{\log(f_e)^2 - \log(f_t)^2} \\ f_{e,t} &= f_{e,t}(L_i, \mu_j, K_j) \end{aligned} \quad (5.8)$$

$f_{e,t}$ is referring to (e)xperimental measurements and (t)heory/model results. i counts L -bins and j counts (μ, K) -sets. Δ_1 shall sum over all nine (μ, K) -sets shown in Fig. 5.4, and Δ_2 only over the first set (Panel 1 in Fig. 5.4).

Δ considers every point with the same weight. This seems fair and is easy to calculate but causes that the reproduction of small features in the distribution (like the narrow radiation belt contained between Janus and Mimas), which still can be important, only causes a small change in Δ . Therefore, the final selection of the optimal parameters is done by eye.

Since the resulting model profiles always go through the points defined by the boundary conditions, they can never be completely off from the observation. However, the precise shape in between the boundaries will only match the measurements if the assumptions are sufficient.

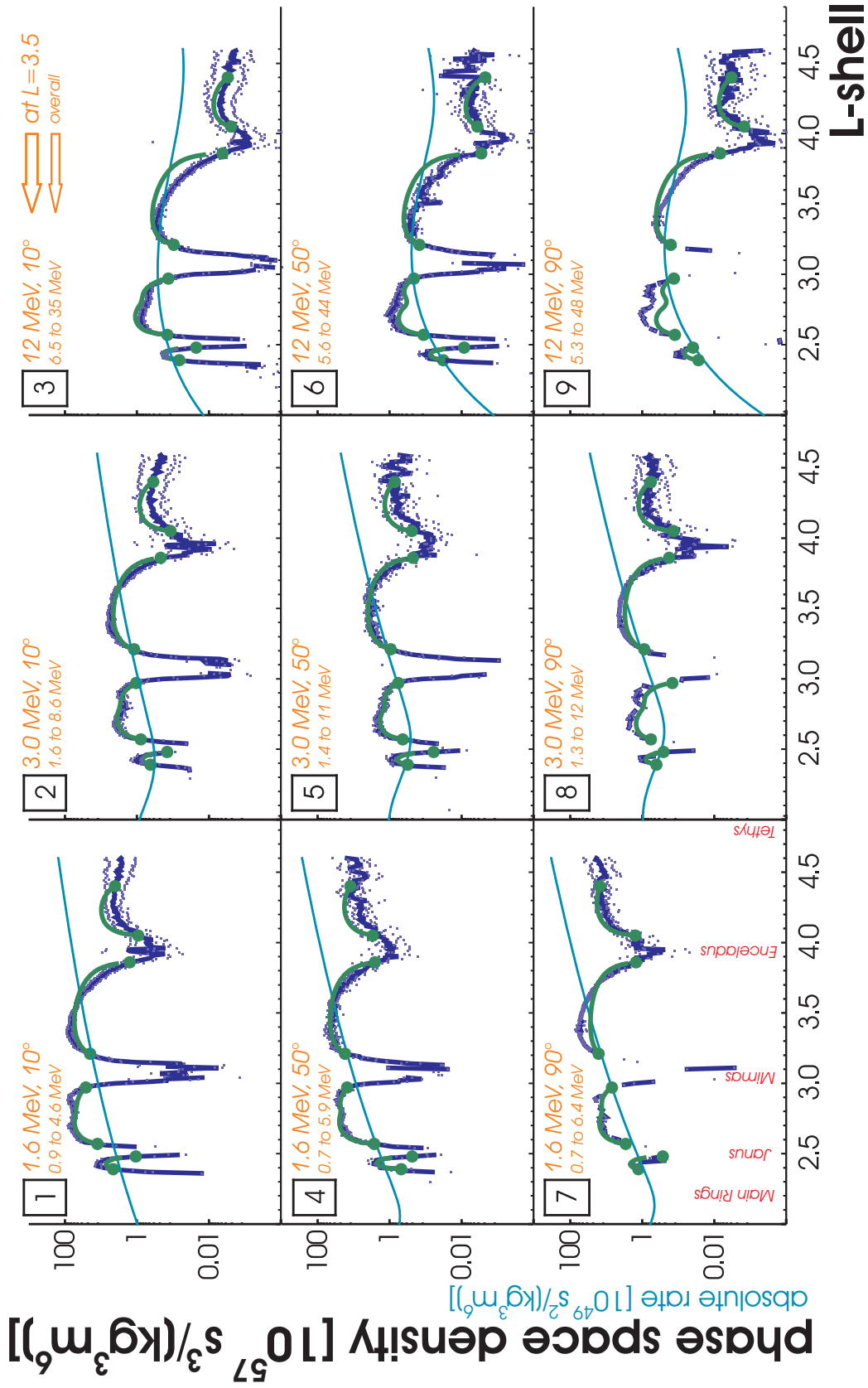


Figure 5.4: Phase space density profiles of the radiation belts at different sets of (μ, K) , and absolute source rates. The two quantities are scaled to be displayed on the same scale. Their units and scaling factors are given in the two labels of the left axis. The values of energy and equatorial pitch angle given in the upper line of each panel are fulfilled at $L_0 = 3.5$, the energy range given in the second line is for the covered L -range. *Dark blue lines:* Measurements. *Dark blue points:* 1σ standard deviation of mission average. *Green lines:* Model results. *Green points:* Boundary conditions. *Light blue lines:* Source rate $\delta f / \delta t_S$. The model assumptions are given in Table 5.1.

parameter	variable	value	comment
source	S_0	$10^{63} \text{ s}^2/(\text{kg}^3 \text{m}^6)$	lower limit, sensitive to ratio with D_0 and n_p
	m	3	larger yields better fit, insensitive to sum with n
	γ_f	3.9	sensitive
	L_0	3.5	definition
	E_0	1 keV	definition
diffusion	D_0	$0.3 \cdot 10^{-9} \text{ s}^{-1}$	lower limit, sensitive to ratio with S_0 and n_p
	n	10	larger yields better fit, insensitive to sum with m
	L_0	3.5	definition
loss	$n_i(L_i = 3)$	10^8 m^{-3}	fixed
	$n_p(L_p = 4)$	10^9 m^{-3}	smaller yields better fit, sensitive
	$n_d(L_d = 6)$	10^8 m^{-3}	insensitive
	H	$1 R_S$	fixed

Table 5.1: Summary of the model parameters that yield the best possible match with the observations. The used variables are explained in Appendix B.

5.2.2.2 Overall strength of processes involved

We divide the processes involved in forming the radiation belts into four groups: radial diffusion $\widehat{D}f$, source process $\delta f/\delta t|_S$ (high- and low-energy part), losses in the Neutral Torus $\delta f/\delta t|_{CE,Ex}$ (charge exchange, energy loss), and losses to the moons $\delta f/\delta t|_M$. We parameterize each of them with an overall strength (D_0 , S_0 , n_p , m_0) and a quantity describing their scaling with L -shell (n , m , n_i , $-$). All parameters have to be chosen properly in order to get a solution of the diffusion equation (2.56) that matches the observations.

A set (D_0 , S_0 , n_p , m_0) that achieves a good match is mathematically not unique. Multiplying it with an arbitrary factor yields the same result since this factor can be canceled again from Eq. (2.56). If all parameters would be fully unknown, it would therefore only be possible to derive their ratios. Since the physics of the loss to moons is well understood ($m_0 = 1$) it becomes possible to derive absolute values of the parameters.

To find the parameters, only the regions outside the sweeping corridors are considered, so that m_0 can be ignored. The initial parameters are chosen in a way that the radiation belts are mainly shaped by diffusion plus source: $(|\delta f/\delta t|_S|, |\widehat{D}f|) \gg (|\delta f/\delta t|_{CE}|, |\delta f/\delta t|_{EX}|)$. To approach to the optimal parameters, the value of S_0 is searched that reproduces the measurements, i.e. where Δ_1 is as small as possible. The development of Δ_1 with changing parameters is displayed in Fig. 5.5. Profiles resulting from this very simple model already yield very good results.

It should be pointed out here that the source process needs to supply all energies. If we would consider only the high-energy peak, initially existing < 1 MeV particles would be lost due to diffusion and not populate the belts in the steady state. Fig. 5.4 illustrates how m affects the peak values of the radiation belts *inside* of Enceladus' orbit. Besides the PSD profiles, the figure also shows the L -dependence of $\delta f/\delta t|_S$ as a cyan line. Moving from large L inward is equivalent to moving towards large E in the source spectrum. Within the power law energy range (low μ) this yields an decreasing source rate and explains why in the left column the outer radiation belts are generally higher in PSD than the inner ones. For high μ values, as within the right column, the covered L -range is equivalent to the E -range of the CRAND peak. Therefore, the middle belts have a larger PSD than the

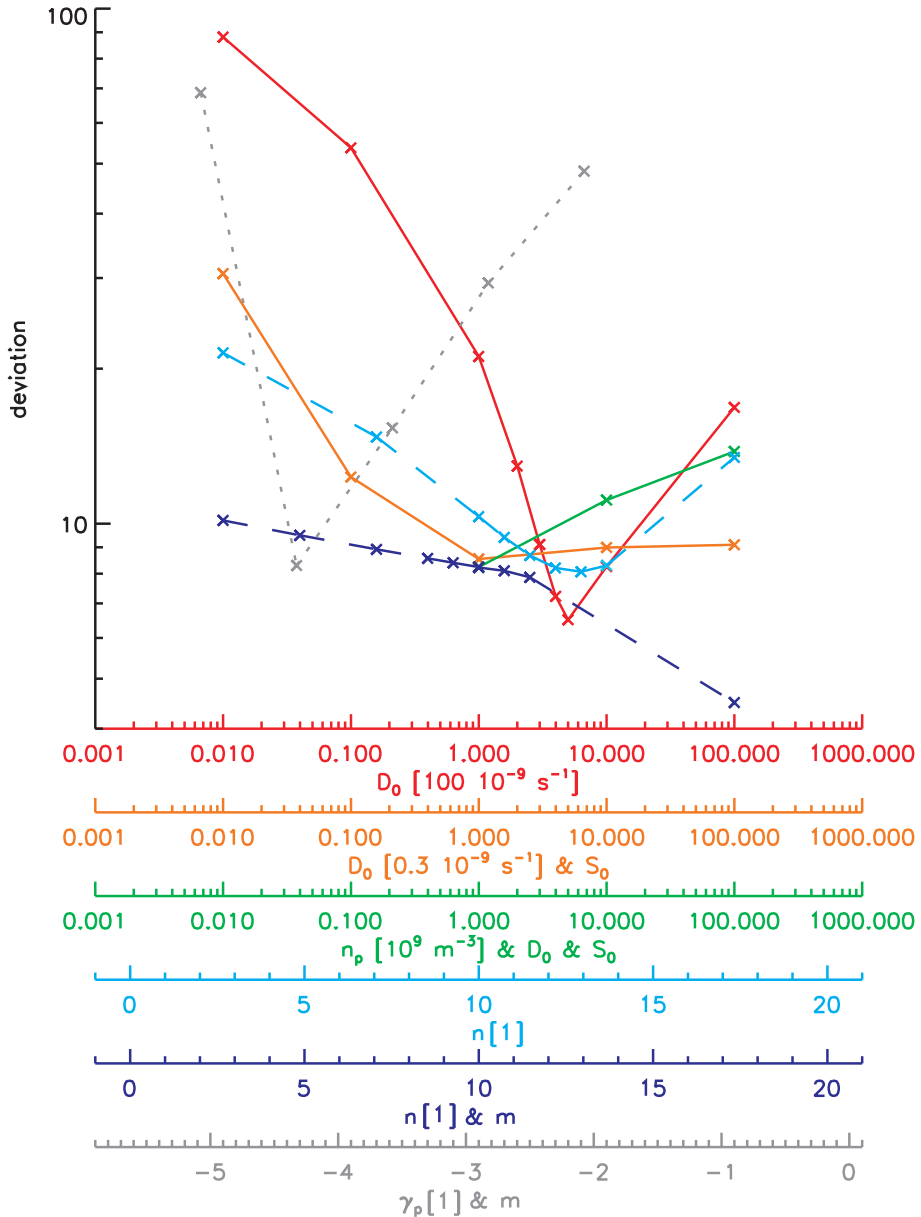


Figure 5.5: Parameter study of the radiation belt model showing the deviation Δ , which is the difference between measurement and model. *Red line:* Δ_1 for changing diffusion coefficient D_0 , while the source is $S_0 = 10^{66} \text{ s}^2/(\text{kg}^3 \text{m}^6)$. *Orange line:* Δ_1 for changing D_0 , while the ratio $D_0/S_0 = 0.3 \cdot 10^{-73} \text{ kg}^3 \text{m}^6/\text{s}^3$ is kept constant. *Green line:* Δ_2 for changing n_p , while the ratios D_0/S_0 and $D_0/n_p = 0.3 \text{ m}^3/\text{s}$ are kept constant. For $n_p \leq 10^{-8} \text{ m}^{-3}$ the belts are fully independent and Δ_2 becomes meaningless. *Cyan dashes:* Δ_1 for changing diffusion exponent n , while the source exponent is $m = 0$. *Blue dashes:* Δ_2 for changing n , while $n + m = 13$ is kept constant. *Grey dots:* Δ_1 for changing spectral slope γ_f of the source, and using $m = n - 3(\gamma_f + 3.9)$. If not stated otherwise, the other parameters are as in Tab. 5.1.

inner and outer ones.

Due to the initial assumptions, D_0 is still orders of magnitude above the value that is expected in this region. Therefore, both D_0 is now lowered, keeping the ratio to S_0 constant. For now, the neutral density n_p stays fixed to the expectation from literature. (Lowering D_0 therefore also lowers the ratio D_0/n_p .) We find that when the loss rate becomes comparable to the other rates, the model profiles become depleted (lower panel of Fig. 5.7) and do not fit the observations anymore. It is concluded from this that the radiation belts within the observed energies are not strongly affected by losses in the Neutral Torus.

With this, already a fundamental feature of the radiation belts has been found: The main processes in the radiation belts are source and diffusion. This is different to the middle magnetosphere, as it will be demonstrated in Sec. 6.2.

We consider the ratio D_0/n_p as the best one, where D_0 is close to the electron value (and therefore as low as possible), but the model still yields reasonable results. Since losses act strongest at low energies, the limit we found for D_0/n_p would have been at even lower values if we only had considered profiles with large energies (for example only the right column in Fig. 5.4). Using a large energy range is therefore of utter importance.

Charge exchange cross sections are strongly energy dependent. Profiles of protons with lower energies as they can be considered here (< 600 keV) will therefore be very sensitive to the density of the Neutral Torus. Due to penetrating radiation that contaminates the measurements of all instruments flown so far, there are no reliable data of the low-energy radiation belts available to date. Since it is therefore unknown if and in how far their profiles are modified by losses, we cannot tell if D_0/n_p should be larger than it is derived here. The found D_0/n_p can only be considered as a lower limit.

In order to constrain the absolute values of the set (D_0, S_0, n_p) further, a quantity is needed that is already better constrained than all of them. This is the case for loss along moon orbits. Therefore, we extend our consideration to the sweeping corridors by using the sink method. Examples of results are displayed in Fig. 5.6.

It is found from this that the expected densities of the Neutral Torus require such a strong source and diffusion to dominate over it that this would populate the sweeping corridors. However, if all values of (D_0, S_0, n_p) are slightly lowered (i.e. keeping their ratio constant) the PSD in corridors is reduced again, yielding more realistic profiles.

Fig. 5.4 and Fig. 5.6 show profiles where all parameters have been optimized as described. The optimal value of the diffusion coefficient at $L_0 = 3.5$ is found to be $D_0 = 0.3 \cdot 10^{-9} \text{ s}^{-1}$, which is close to the one that [Roussos et al. \(2007\)](#) found for electrons. The source rate is $S_0 = 10^{63} \text{ s}^2/(\text{kg}^3 \text{ m}^6)$ at $E_0 = 1 \text{ keV}$ and $L_0 = 3.5$. In order to compare it with the literature, its radial scaling is required that is derived in the next section. The peak value of the modeled Neutral Torus is $n_p = 10^9 \text{ m}^{-3}$, which agrees with the lower end of the published values, as for example given by [Dialynas et al. \(2012\)](#) (Sec. 1.2.2). A compilation of all optimum values can be also found in Tab. 5.1.

5.2.2.3 Radial scaling

After discussing the overall strength of the effects, it is studied here how they scale with distance to Saturn. Diffusion and source are both treated as power laws with exponents n and m , respectively. To constrain them, we use again the boundary method and assume

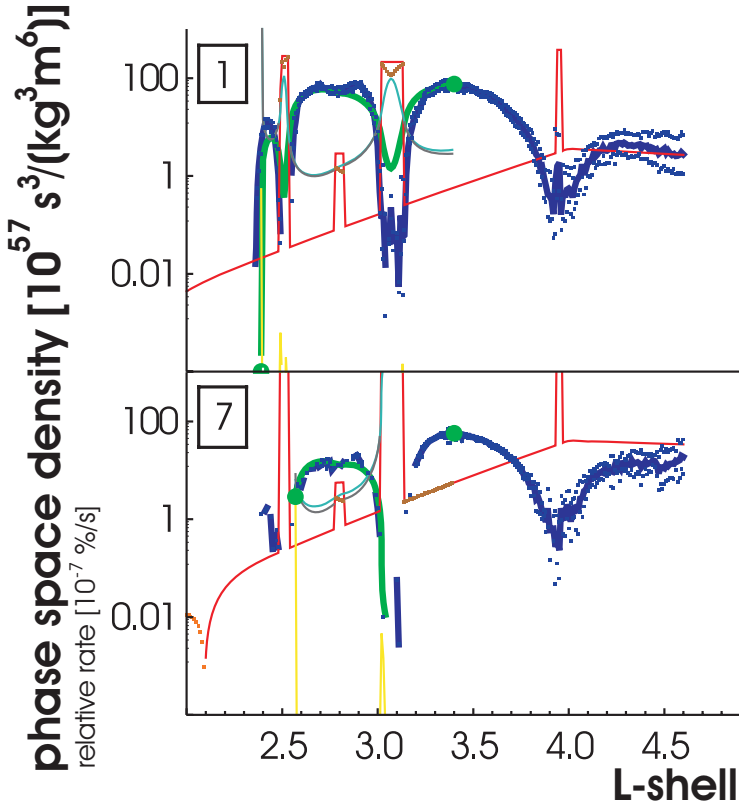


Figure 5.6: Phase space density profiles of the radiation belts and relative rates of all involved processes: PSD measurements (blue line), PSD model results (green line), source rate $(\delta f / \delta t|_S) / f$ (cyan line), diffusion rate $(\bar{D}f) / f$ (< 0 black line, > 0 brown points), loss rate $(\delta f / \delta t|_L) / f$ (> 0 red solid line, < 0 orange dotted line), residuum $(\partial f / \partial t) / f$ (yellow lines). Latter is negligible outside the edges of the belts. The (μ, K) are the same as in Panels 1 and 7 of Fig. 5.4. Different to this figure, we include the moons via sink terms and chose different boundary conditions.

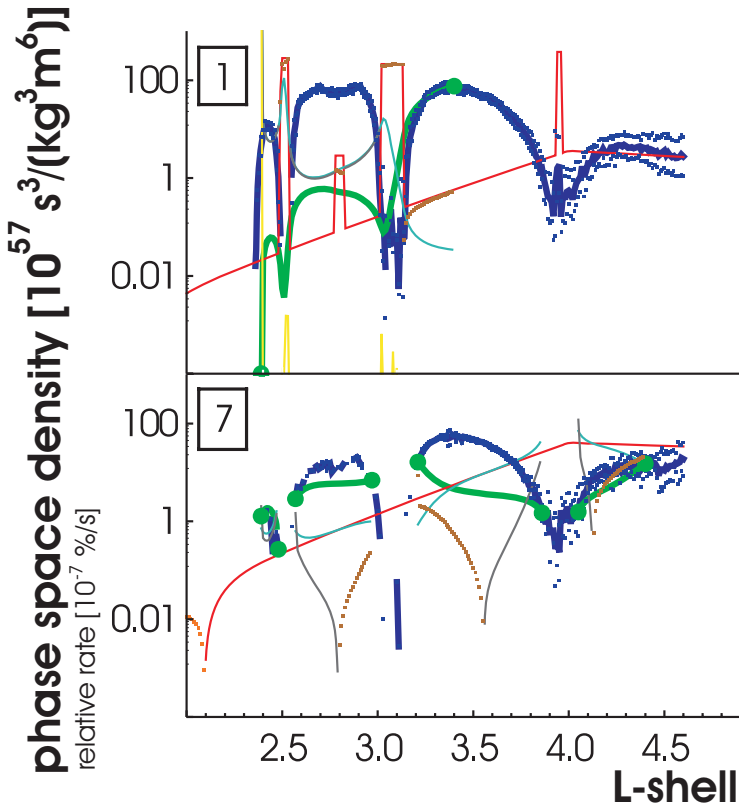


Figure 5.7: Test fits to illustrate mismatch of model and data under different conditions. *Upper panel:* Radiation belts in case that the source rate would be two orders of magnitude below the optimum. Panel is otherwise equivalent to Panel 1 of Fig. 5.6. *Lower panel:* Radiation belts if the Neutral Torus would be denser. This was implemented by decreasing D_0 and S_0 by one magnitude below optimum. Panel shows the same (μ, K) as Panel 7 of Fig. 5.4.

diffusion and sources are the dominant processes. We find a minimum of Δ_1 for $n = 13$ in case that $m = 0$ i.e. that the source is not space dependent. This minimum is shallow, as shown in Fig. 5.5, cyan line. If we vary m instead, we find that this variation can be countered by changing n . The best solution always fulfills $n + m = 13$.

In order to derive separate values for n and m , we change n and m while keeping their sum constant. It is found by this that Δ_1 continuously decreases for increasing n , but this is biased by the choice of the (μ, K) -sets that are used to derive Δ_1 . Fig. 5.8 explains this and points out a special feature of the one belt centered between Mimas ($L = 3.1$) and Enceladus ($L = 3.9$). The maximum of this belt changes its position with μ . Within the covered μ -range, it moves two times from the center between the moons towards Mimas and back. The figure only displays this for $\alpha_0 = 90^\circ \pm 10^\circ$ but it is also true for other pitch angles. For $n > 0$ all model profiles become increasingly asymmetric and shifted towards Mimas. Δ_1 prefers this case because it is biased by the selection of (μ, K) -values: They include more asymmetric cases (left and right column in Fig. 5.4) than symmetric ones (middle column). Therefore Δ_1 cannot be used to objectively judge on n .

We repeat the procedure using the sink method. Since D_0 is fixed at $L_0 = 3.5$, $n \gg 0$ yields a small diffusion coefficient for $L < L_0$, which is most of the model's range. As we have seen before, this increasingly depopulates the sweeping corridors in this region and is therefore preferred. Since we do *not* expect the diffusion coefficient to be $n \gg 10$ (Sec. 2.2.1) and not expect the source to scale with $m \gg 2$ (Sec. 5.2.1.1), we consider $n = 10$, $m = 3$ as the best exponents.

Finally, we discuss the radial dependence of the Neutral Torus. Our model is not sensitive to its outward decay since this occurs on much larger scales than the modeled range. We assume $n_d = 0.1n_p$ at $L_d = 6$ in agreement with Cassidy and Johnson (2010). A fast decay inward of Enceladus is favored by the model favors since in this case losses become increasingly negligible. The previous discussion was based on $n_i = 0.1n_p$ at $L_i = 3$. We consider this as the best value since it yields a good match. This value is lower but still realistic (Sec. 1.2.2). The O density given by Melin et al. (2009) is for example $n_i = 0.3n_p$. Reducing n_i further is unrealistic but yields a better fit. For the price of returning to the current deviation it would then become possible to also reduce D_0 and S_0 further.

With the values derived so far it is now possible to calculate diffusion coefficients and process rates throughout the entire the radiation belts. We show the evolution of the diffusion coefficient over L in Fig. 5.9 in comparison with previous works. As it can be seen there, the results found here are reasonably consistent.

Rates derived from our model are shown in Fig. 5.10. We find that source and diffusion rate are approximately the same (cyan an gray lines are close to each other) as long as only weak losses (red line) occur. If one compares the values at the peaks of the belts, they range for the (μ, K) as they are considered here from 10^{-7} %/s (between Janus and Mimas) to 10^{-5} %/s (between Enceladus and Tethys). Conversion to time scales yields hundreds of years and years, respectively. These values are used now for a comparison with previous works, and in order to check if the initial assumption of a steady state was fulfilled.

Schardt and McDonald (1983) analyzed the flux of 63 to 160 MeV protons within the sweeping corridor of Mimas and found a source rate of $6 \cdot 10^{-4} \text{ %/s}$. The difference to our values can be because they neglect diffusion for the refilling of the corridor and due to contamination or instrumental noise within the corridor. Van Allen et al. (1980a) utilized

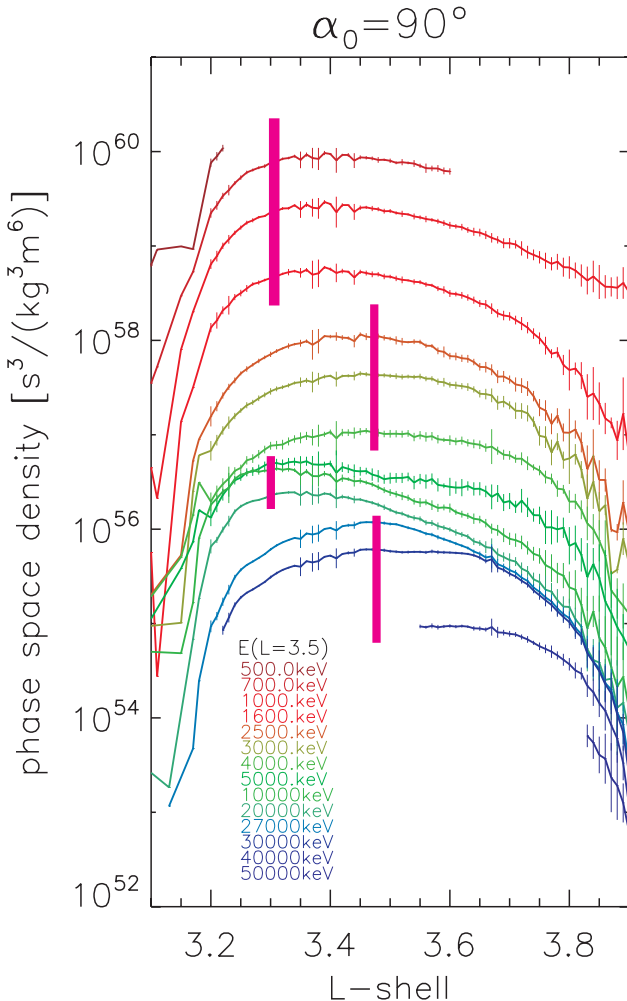


Figure 5.8: Measured phase space density profiles between the orbits of Mimas and Enceladus for a large range of μ (colors) and $K = 0$, equivalent to $\alpha_0 = 90^\circ$. The pink line illustrates how the symmetry of the belt changes.

a more reliable approach by considering the belt itself. At > 80 MeV and for the belt that lies within Mimas' orbit, they derive under the assumption of constant values for diffusion ($D_{LL} = 10^{-9}$ s $^{-1}$) a source rate of $3 \cdot 10^{-7}$ %/s, which is very close to our value.

Compared to the middle and outer magnetosphere, the radiation belts are very stable. Nevertheless, they are not fully static but change their intensity within the time scale of years (Roussos et al. 2011). This is illustrated in Fig. 5.11. Within our data set, the relative rate $(\partial j/\partial t)/j$ of the change is in case of the outermost belt between Enceladus and Tethys several 10^{-7} %/s, equivalent to a timescale of roughly 10 years for all energies. This is small enough that the steady state is approximately fulfilled, since the optimal source rate is 10^{-5} %/s in this belt. The rates of the other belts are smaller but known with less certainty since they were observed less frequently. In any case, they appear to be at least comparable if not a magnitude smaller than the rates within our model, so that also there a steady state can be assumed.

It is interesting to point out that the very recent change in the radiation belt intensity that can be seen in Fig. 5.11, is significantly faster than during most of the mission. Because of this it is possible that the outermost proton radiation belt might diminish during a solar cycle.

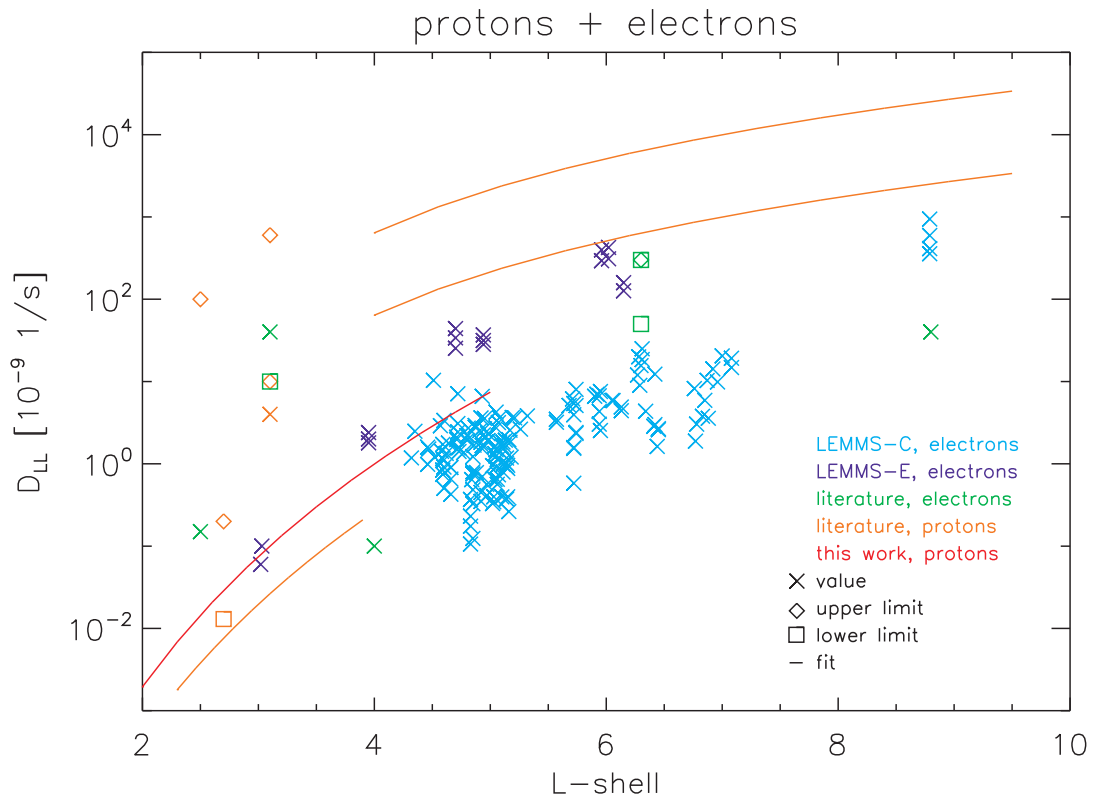


Figure 5.9: Radial diffusion coefficients for energetic particles of various energies. *Blue and violet:* Derived from LEMMS electron microsignatures, see Fig. 2.3. *Green and orange:* Values obtained from literature, as summarized by Van Allen (1984). *Red:* Best parameters of our radiation belt model.

5.2.2.4 Higher-order effects

The processes discussed up to now describe the radiation belts well to first order. There exist several loss processes that modify the large-scale structure in narrow regions by a small amount. One example are the moons Anthe ($L = 3.3$) and Pallene ($L = 3.5$). They, or potential rings or arcs associated with them, cause drops in the measured intensity. Since these drops are too small to be even seen on the displayed scales, we ignore this.

More important are the *G ring* and its arc, which are responsible for the dip visible in Figures 4.3 and 5.4 at $L = 2.8$. They consist of ice grains that cause the bouncing particles to lose energy. We gave a method to derive the resulting loss or source rate in Sec. 2.3.3. It relies on numerical calculations of the energy losses within the single grains, which depends on their size. The rates additionally depend on the grain density, and the shape of the spectrum, which is not a simple power law in the region of interest, but features the CRAND peak. Although it should be possible to derive a fit function for the rates in dependence of some input parameters, we do not have this available to date. Since the G ring is just a small-scale feature anyway, we did not invest time in it and simply used a crude loss term of the form

$$\left. \frac{\delta f}{\delta t} \right|_G = \xi \frac{f}{T_B} \Theta(L - L_{G,\text{in}}) \Theta(-L + L_{G,\text{out}}) \quad (5.9)$$

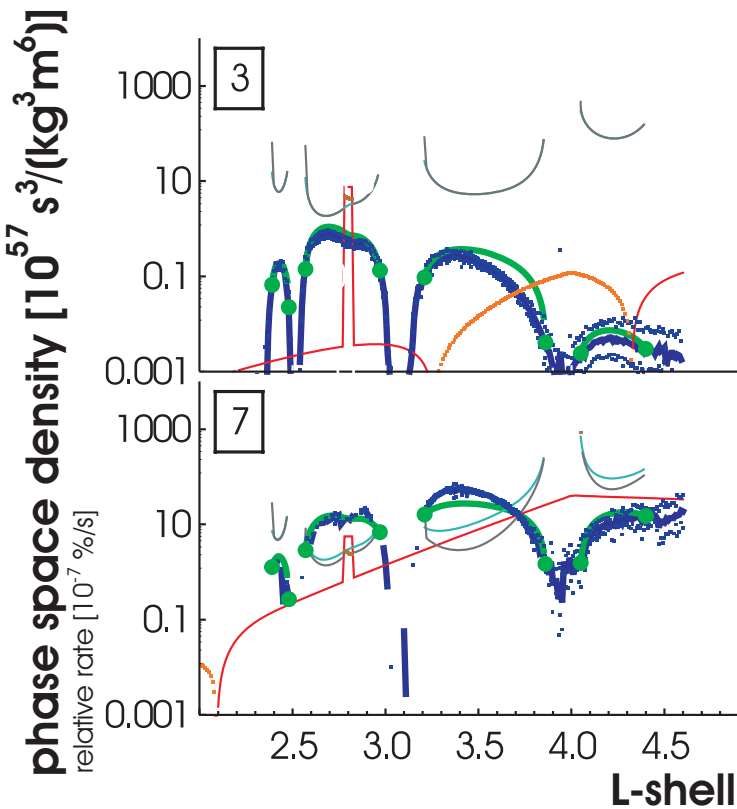


Figure 5.10: Relative rates of all processes acting in the radiation belts, for orientation plotted together with the associated phase space density profiles. PSD measurements (blue line), PSD model (green line), source $(\delta f / \delta t|_S) / f$ (cyan line), diffusion $(Df) / f$ (< 0 gray line, > 0 brown points), and loss $(\delta f / \delta t|_L) / f$ (> 0 red solid line, < 0 orange dotted line). Otherwise, the figure is identical to Panels 3 and 7 of Fig. 5.4.

However, the method described in Sec. 2.3.3 will be used to describe the E ring in Sec. 6.2.2.

Both ring and arc have a sharp inner edge at $L = 2.78$. From this point on, the normalized reflectance I/F of the arc has a radial FWHM of 250 km. The ring is much broader and has a diffuse outer boundary with FWHM of about 2.5 Mm (Hedman et al. 2007). As for moon sweeping corridors (see Eq. (2.84)), the effective radial extent is increased due to the particles' gyro radius.

If in the model $L_{G,\text{out}} - L_{G,\text{in}}$ is decreased from an initial value that fits the observations, the match can be roughly conserved if ξ is increased simultaneously. Our model yields a better match by visual inspection for values of $L_{G,\text{out}} - L_{G,\text{in}}$ matching the extent of the ring (and using $\xi \approx 10^{-7}$) than for the extent of the arc (and $\xi \approx 10^{-6}$). However, the model is not sensitive to this.

Electrons are depleted within the arc (Hedman et al. 2007). Due to the described difficulties, we are not able to determine yet if this also applies to protons.

5.3 Origin of the belts

The radiation belts require a source extending over all energies in order to be stable, as we have shown in the previous Section 5.2. While it is widely accepted that the origin of the source at high > 10 MeV energies is CRAND, there has been no confidence so far about the mechanisms producing the lower energies.

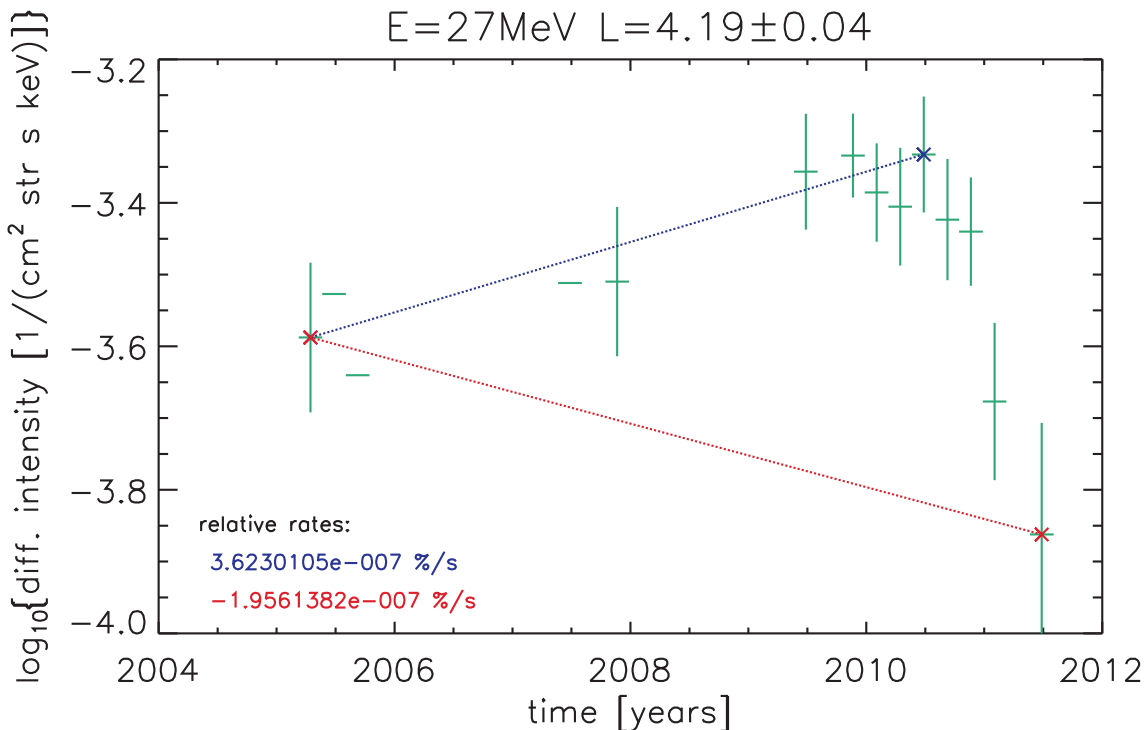


Figure 5.11: Evolution of the differential intensity of protons within an energy interval around $E = 27 \text{ MeV}$ and $\alpha_0 = 10^\circ \pm 10^\circ$ at the peak of the radiation belt between Enceladus and Tethys. The maximal intensity was reached around solar minimum and is decreasing since then.

5.3.1 CRAND

5.3.1.1 CRAND from the rings

The CRAND process was introduced in Sec. 2.4.2. Previous works on CRAND at Saturn (Cooper 1983, Blake et al. 1983) focused on neutrons $\geq 10 \text{ MeV}$ created by the impact of cosmic rays on Saturn's Main Rings. Unfortunately, their energy spectra have their maxima close to the lower edge of the energy range they considered. The peak in the observed proton spectrum is centered close to 10 MeV. It has not been shown so far if the neutron spectrum resembles the proton spectrum below 10 MeV.

At the onset, it should be pointed out that the spectra of neutrons and steady-state CRAND protons are similar but not identical. The difference is not attributed to the minor fraction of energy that is transferred to the electron and the neutrino created in the neutron's decay. It is caused by diffusion and losses, which fully counter the CRAND source in the steady state. Radial diffusion smears out the initial radial profile of CRAND protons and the associated adiabatic heating and cooling modifies their spectrum. The separation of Saturn's radiation belts constrains the possible change of L and E so that the resulting proton spectrum should be still similar to the initial one. This means that if only neutrons within a narrow energy range would be produced, only CRAND protons close to this range would be found.

In order to answer the question how the neutron spectrum evolves at $< 10 \text{ MeV}$ energies, we simulated the interaction of cosmic rays with Saturn's Main Rings. As a simulation

tool, we used the geometry and tracking (GEANT4) toolkit that was developed to simulate the passage of particles through matter using Monte Carlo methods (Geant4 Collaboration 2011, Agostinelli and et al. 2003). Saturn’s rings were represented by a slab of water and the cosmic rays were taken to be protons since these are more abundant than other species at the same energy.

Cosmic ray protons and electrons can only reach into a dipole field if they have a sufficiently high rigidity (Sec. 2.1.2.5). The cutoff energy at $L = 1.7$ (this is about the position of the B ring) is $E_c \approx 30$ GeV. Since the cosmic ray spectrum can be approximated by a power law that falls with energy, most cosmic rays at the rings have energies close to E_c .

We show the result of two simulation runs in Fig. 5.12. A slab of 10 cm of water yields a CRAND peak at ≈ 100 MeV, which is too high in energy compared to the proton spectrum. Much thicker slabs (for example 10 m) are required to slow the particles sufficiently down that the peak of the neutron spectrum shifts towards the observed 10 MeV.

The grains within Saturn’s Main Rings have size distributions that are described well with a power law $n_r \propto r_r^{-3}$ over a large range extending over the magnitudes from 1 mm to 10 m (Colwell et al. 2009). Therefore, most of the cosmic rays will pass through the abundant small grains. All the encounters during one passage of the ring add up to a distance h_r . This is on the order of 1 m, in between the two slab thicknesses. Some cosmic rays might pass through more material than h_r if they encounter larger but less abundant grains (or even moonlets), or pass the rings parallel to the ring plane.

The given estimate of h_r can be derived by using a density $n_r = 10^4 \text{ m}^{-3}$ of grains with radius $r_r = 1 \text{ cm}$ (Colwell et al. 2009), the ring thickness $H_r = 10 \text{ m}$, and the relation $h_r = n_r H_r \pi r_r^2 \cdot 2r_r$. A similar result can be derived assuming the total mass $M = 10^{20} \text{ kg}$ of the rings (which lies within limits $3 \cdot 10^{19} \text{ kg} < M < 6 \cdot 10^{20} \text{ kg}$ as given by Charnoz et al. (2009)), its area A , the water density ρ , and $h_r = M/(A\rho)$.

A more thorough study of CRAND from the rings should check if there is a significant contribution from secondary protons. These become trapped in the magnetic field and repeatedly encounter the rings until stopped completely but produce in the meantime a cascade of tertiary particles.

5.3.1.2 CRAND from the atmosphere

As it can be seen in Fig. 5.12, the neutrons produced within the rings can *not* account for the protons in the power law part of the spectrum. For this, the neutrons have to be significantly decelerated, which requires more material than found in the rings. This can be satisfied by the surfaces of Saturn’s moons and its atmosphere. A neutron spectrum of power law shape is for example known to be produced at the Earth’s moon (Ota et al. 2011). The neutron spectrum in the vicinity and the atmosphere of Earth is even more similar to the proton spectrum at Saturn since it features both a power law and a peak. (For neutron spectrum in Earth’s atmosphere see Fig. 2.14, Hess et al. (1959), or Goldhagen et al. (2002). Hess et al. (1961) derived from the atmospheric spectrum the one in space.) Due to this similarity we propose here that at least the power law part of the protons derives from Saturn’s atmosphere.

Although Saturn’s moons differ from Earth’s moon the neutron deceleration also works there. Therefore, there might be an additional contribution from the icy moons.

No major contributions should come from the Neutral Torus and the E ring since both

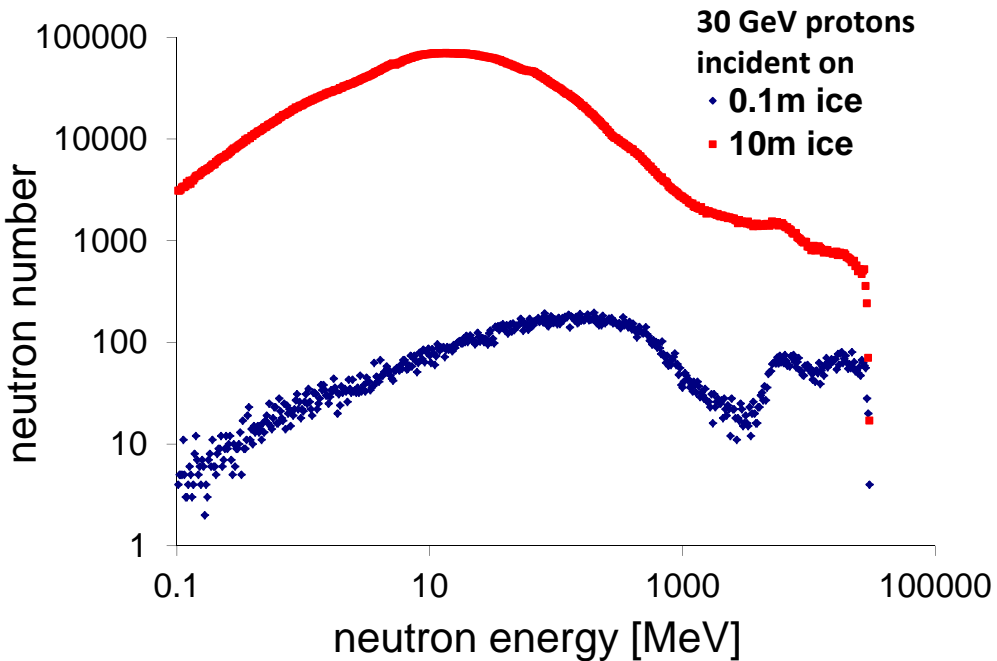


Figure 5.12: Secondary neutron spectra from Monte Carlo simulation of 30 GeV protons passing slabs of water with 10 cm (blue) and 10 m (red) thickness. This represents the CRAND neutrons created from cosmic rays incident on Saturn’s Main Rings. The data was provided by D. K. Haggerty (2011).

their column density and their total mass are negligible compared to the Main Rings. The column mass density can be calculated as

$$\bar{\rho} = nmH_r \quad (5.10)$$

with n and m number density and mass of either a molecule or a grain. Using the values given for the main rings this yields $\bar{\rho} = 10 \text{ g/cm}^2$. For the peak of the model Neutral Torus it is $\bar{\rho} = 10^{-10} \text{ g/cm}^2$. In Sec. 6.2 we will estimate parameters for the E ring at $L = 7$. Assuming that the peak density is an order of magnitude higher than this yields $\bar{\rho} = 10^{-11} \text{ g/cm}^2$. Taking into account that Neutral Torus and E ring cover a larger area than the Main Rings cannot reduce the difference of their importance by more than two orders of magnitude.

5.3.1.3 Comparison with data

The energetic proton pitch angle distribution is consistent with the CRAND process. If neutrons are knocked from a nucleus they are emitted close to the direction of the incident cosmic ray. If there is an anisotropy in the cosmic rays, it will also be found in the neutrons and resulting protons. High-energy neutrons at Earth are indeed anisotropic (Hess et al. 1961). As we have discussed in Sec. 4.2.4, also protons at Saturn with energies $E \geq 10 \text{ MeV}$ are highly anisotropic (mainly equatorially mirroring). At lower energies, the neutrons originate either from evaporation, which is isotropic, or from deceleration,

which makes their distribution isotropic. This behavior is found at Earth's neutrons. At Saturn, the PAD of the power law protons differs to the high-energy ones and is indeed more isotropic: While the equatorial PAD at high energies was persistent even in the mission average, the field-alignment at lower energies is weak and vanishes in the average.

While the general shape of the neutron spectrum from Earth's atmosphere is the same as the proton spectrum at Saturn, they differ in their details. For example, the CRAND peak at Saturn is centered at ≈ 10 MeV instead of ≈ 1 MeV.

Cosmic rays can hit the atmosphere in the polar region ($\lambda = 90^\circ$, $L = 1$) at any energy ($E_c = 0$) but the equator only at the cutoff energy E_c . This is 95 GeV at Saturn and therefore approximately 6 times larger than at Earth (Sauer 1980). The different energy affects at least the neutrons from the cascade process.

The energy of knock-off neutrons depends to first order on the size of the target nucleus. Peak position and fine structure of the evaporated neutron spectrum depend on the excitations possible for the target species (Serber 1947). The difference in the peak positions can therefore be a signature of the fundamentally different atmospheric compositions.

Saturn's atmosphere is mainly composed of H_2 with a minor contribution of He (He number density < 6% of H_2 , Fouchet et al. (2009)). Heavier elements as C (in CH_4) and O (in H_2O) exist only as traces. Although H_2 does not contain neutrons that could be knocked off, the involved protons can be excited and contribute to CRAND for example via the net reaction $p + p \rightarrow p + n + \pi^+$, where p stands for proton, n for neutron, and π^+ for positive pion (Glass et al. 1977). Hydrogen also acts efficiently as a moderator and absorber of neutrons, since H has a similar mass as a neutron and forms stable deuterium when capturing one. Helium typically contains 2 neutrons. To remove one neutron from 4He and produce 3He during CRAND, 20 MeV are required, which can be easily satisfied by cosmic rays.

The H_2 of the atmosphere will also contribute to CRAND when hit by heavy cosmic rays. In the reference frame of the cosmic rays, they become the target and will produce neutrons in the same manner as discussed before. The He^+/H^+ ratio is $\approx 6\%$ for 100 GeV cosmic rays (Webber and Lockwood 2001) and $\approx 12\%$ overall (Schlickeiser 2002). This is on the same magnitude as the He/H_2 ratio in the atmosphere. In Saturn's frame, the produced neutrons have energies close to the cosmic ray energy. Therefore, despite the fact that this process will contribute to the overall neutron population, it can not account for the observed CRAND peak at 10 MeV.

We now use the proton source rate derived previously in Sec. 5.2 in order to predict the neutron intensity under the assumption that the source is provided by CRAND alone. The relation between neutron differential intensity j_n and the source rate $\delta f/\delta t|_S$ is (Dragt et al. 1966)

$$\frac{\delta f}{\delta t} \Big|_S = \frac{\chi j_n}{\gamma \tau_n p^2} \quad (5.11)$$

χ is the injection efficiency that we assume here as 1. τ_n is the neutron lifetime. If the optimum values of S_0 and m (see Table 5.1) are used to describe the source process, the neutron spectrum displayed in Fig. 5.1 is found. The neutron differential intensity at the model's CRAND peak (16 MeV) is $10^{-6} j_u$ at the Main Rings ($L = 2.3$) and $10^{-5} j_u$ at the atmosphere ($L = 1$). We used the definition $j_u = 1 \text{ cm}^{-2} \text{s}^{-1} \text{str}^{-1} \text{keV}^{-1}$. These values are consistent with neutrons created by Saturn's Main Rings and similar to what is observed at Earth's atmosphere.

Cooper (1983) derived a value of $0.7 \cdot 10^{-6} j_u$ for 20 MeV at the position $L = 2.3$ for rings with a column density of 100 g/cm^2 (equivalent to a thickness of 1 m). Column densities in the range between 10 and $\gg 500 \text{ g/cm}^2$ yield intensities that are only a factor of < 3 smaller. A precise comparison cannot be used to constrain the ring thickness since decreasing the source's radial exponent m of our model by 1 yields a comparable change in j_n without a significant degradation of the model.

Hess et al. (1961) derived values on the order of $10^{-5} j_u$ for Earth's CRAND peak (0.5 MeV) at $L = 1$. This is comparable to the results of our model implying that the differences of Saturn and Earth are roughly canceling out. Detailed studies are required in order to check if this is consistent with theory.

The power law spectrum of decelerated neutrons should scale as $j_n \propto E^{-\gamma_j}$ with $\gamma_j \approx 1$ (Sec. 2.4.2.) This exponent is related to the one of the proton source via $\gamma_f = \gamma_j + 1$ (due to (5.11) and $p^2 \propto E^1$ for the non-relativistic case). Our model uses $\gamma_f = 3.9$, which was not varied up to now. This value is larger than the expectation from CRAND. If we assume that the high-energy part of the model source is identical with the actual CRAND peak, this means that Saturn's radiation belts require a larger source of low-energy protons than CRAND alone can supply. This discrepancy is increasing towards smaller energies.

Running the model with smaller γ_f yields profiles that poorly match the observations. This can be improved when m is changed simultaneously with γ_f and we fix the source rate at one point within the power law ($E_0 = 1 \text{ MeV}$) and one within the CRAND peak (constant s). Changing both m and γ_f helps because the source rate mostly follows a power law in both L and E ($\delta f / \delta t|_S \propto E^{-\gamma_f} L^{-m}$). For equatorial particles (where $E \propto \mu L^{-3}$) this can be expressed as $\delta f / \delta t|_S \propto L^{3\gamma_f - m}$. Therefore, if $3\gamma_f - m$ is kept constant, the model profiles should approximately look the same. However, they do not, and the results are not satisfactory (Fig. 5.5, gray line).

This can mean that although CRAND does provide protons, it is not the only effect. However, there are other possibilities to explain the mismatch in γ_f .

One possibility to explain it is that the measurements at lower energies become increasingly contaminated by radiation belt background. As shown throughly by Roussos et al. (2011), this contamination cannot be dominating. Still, there might be a contribution and this could affect γ_j .

It is also possible that the discrepancy is an artifact of our assumption of an energy-independent diffusion coefficient. Alternatively or additionally it could be due to the approximation $\partial f / \partial t \approx 0$ in the diffusion equation (2.56). This approximation can be avoided by defining an effective source rate

$$\frac{\delta f}{\delta t} \Big|_{\bar{S}} = \frac{\delta f}{\delta t} \Big|_S - \frac{\partial f}{\partial t} \quad (5.12)$$

and use the same function and values for it as we did up to now for the (physical) source rate $\delta f / \delta t|_S$. With this, our model profiles exactly solve (2.56). The difference of $\delta f / \delta t|_{\bar{S}}$ to our expectation of a CRAND source $\delta f / \delta t|_S$ might therefore be the contribution of $\partial f / \partial t$.

Another possibility is that $\delta f / \delta t|_S$ as used in the model is not necessarily identical with the the *original* source rate. CRAND might produce protons with the expected, flat spectrum. Then another process redistributes the protons in energy and brings the source spectrum to the form of $\delta f / \delta t|_S$ that is used in the model. Since the resulting spectrum is

steeper than the original one, this cannot be achieved by energy diffusion, which tends to even out differences.

This theory is compelling since all spectra at Saturn can over large intervals in energy and L be approximated by power laws. This is even true for ions that cannot be produced by CRAND (Fig. 4.5). The process responsible for this could also shape the proton spectra at small L .

What supports the CRAND origin of the particles despite all doubt is a finding recently presented in [Roussos et al. \(2011\)](#). Since the CRAND process is initiated by cosmic rays, it is expected to rise and fall with the solar cycle that modulates the overall intensity of charged particles that are able to enter the heliosphere. [Roussos et al. \(2011\)](#) indeed observed that the peak intensity of the radiation belts was rising until the date of publication. Fig. 5.11 now covers a larger time interval and shows that the intensity after passing the solar minimum is decreasing again. This is true at all energies, including the power law regime. The source of the power law portion of the proton spectrum is therefore at least correlated with the cosmic ray intensity.

5.3.2 Stripped ENAs

5.3.2.1 >500 keV ENAs and the Neutral Torus

How ENA stripping can provide a source was explained in Sec. 2.4.3. To calculate values for this process, we first derive the ENA production rate \mathcal{P} of L -intervals throughout the magnetosphere

$$\mathcal{P} = \frac{\delta f}{\delta t} \Big|_{CE} R_S^3 L^2 \Delta L 4\pi \sin(\lambda_m) \quad (5.13)$$

ΔL is the bin size and λ_m the mirror latitude of the original ions. The ion loss rate $\delta f / \delta t|_{CE}$ was given before in Eq. (2.64). The path-averaged gas density that appears in this equation can assumed to be the equatorial density of the Neutral Torus since we will consider only ions that mirror close to the equator. For the density profile we use the same model as described in Sec. 5.2.1.3.

We show the result of \mathcal{P} for the radiation belts and the middle magnetosphere in Fig. 5.13 exemplarily for one energy. At all energies included here (> 500 keV), the ENA production is consistently highest in the radiation belts.

The behavior is opposite to lower energies, as it is well known from other instruments. INCA detected only a weak ENA emission from the radiation belts, while most ENAs with < 50 keV are emitted from the middle magnetosphere ([Krimigis et al. 2005](#)). Centered at $9 R_S$ with an intensity-FWHM of $3 R_S$ ([Carbary et al. 2008](#)), strong ENA emissions periodically add to a slowly varying component ([Paranicas et al. 2005](#)). CHEMS shows that there are no significant proton intensities for < 200 keV at $L < 5.5$ ([Paranicas et al. 2008](#)), so that there is barely a source population for ENAs in the radiation belts at that energy. At $L < 4$ and the same energies, both CHEMS and LEMMS have strong contributions of background, so that no reliable measurements exist there. Nevertheless, we do not expect the situation to be different to the measurements at $L \approx 5.5$.

Above at least 500 keV, the belt between Enceladus ($L = 3.9$) and Tethys ($L = 4.9$) is the one that emits the fewest ENAs, as visible in Fig. 5.13. It therefore loses relatively few protons due to charge exchange while gaining a relatively large amount of stripped

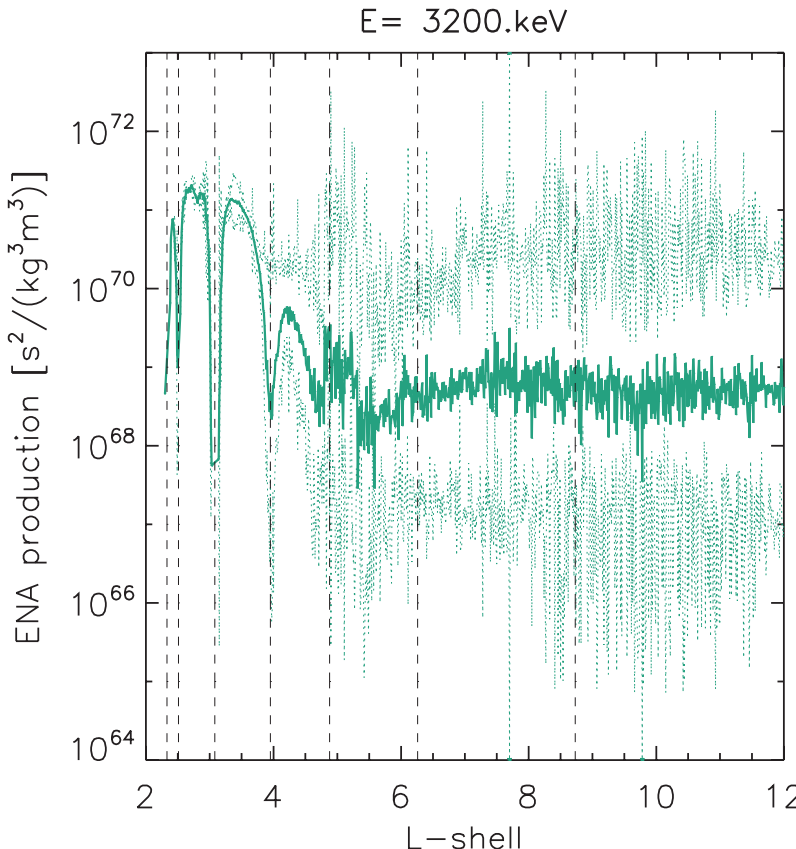


Figure 5.13: ENA production \mathcal{P} for L -bins of size $\Delta L = 0.01$ throughout the magnetosphere. This is calculated from proton measurements at $E \approx 3.2$ MeV and the Neutral Torus model. The ENAs move close to the equatorial plane since the pitch angle of the original protons was $\alpha_0 = 80^\circ \pm 10^\circ$. Error bars show the 3σ standard deviation of the mission-averaged data.

ENAs. Using (2.87) we calculate now the rate $\langle \delta f / \delta t \rangle_{\text{str}}$ at which stripping supplies this belt. Comparing this with the rate $\langle \delta f / \delta t \rangle_{\text{CE}}$ at which charge exchange depletes it will answer the question if stripped ENAs play a significant role for the proton population.

$$\left\langle \frac{\delta f}{\delta t} \right\rangle_{\text{CE}} = - \int_{\text{rb}} \frac{\delta f}{\delta t} \Big|_{\text{CE}} dV \Bigg/ \int_{\text{rb}} dV \quad (5.14)$$

We show the results in Fig. 5.14. The used stripping cross sections have been given in Sec. 2.4.3. We find for the average state of the magnetosphere that stripping only provides a number of particles that is $< 0.01\%$ of the number lost to charge exchange. Considering that charge exchange is a minor process compared to diffusion (Sec. 5.2.2.2), this becomes even more negligible. Even in a theoretical extreme case where the proton intensity would be 3σ above average in the magnetosphere and 3σ below in the considered radiation belt, the ratio is $< 1\%$.

Values as small as that can be understood without calculations when one assumes homogenous values of n_j and f . In this case, a loss requires a proton encountering a gas particle once, but a gain requires a second encounter, which is improbable. $\sigma_{\text{str}} > \sigma_{\text{CE}}$ does not change that, unless their difference is extreme. It can therefore be concluded that at least at energies > 500 keV the stripping within the Neutral Torus of equatorial ENAs that originate from $L > 2$ does not provide a significant contribution to the classical radiation belts.

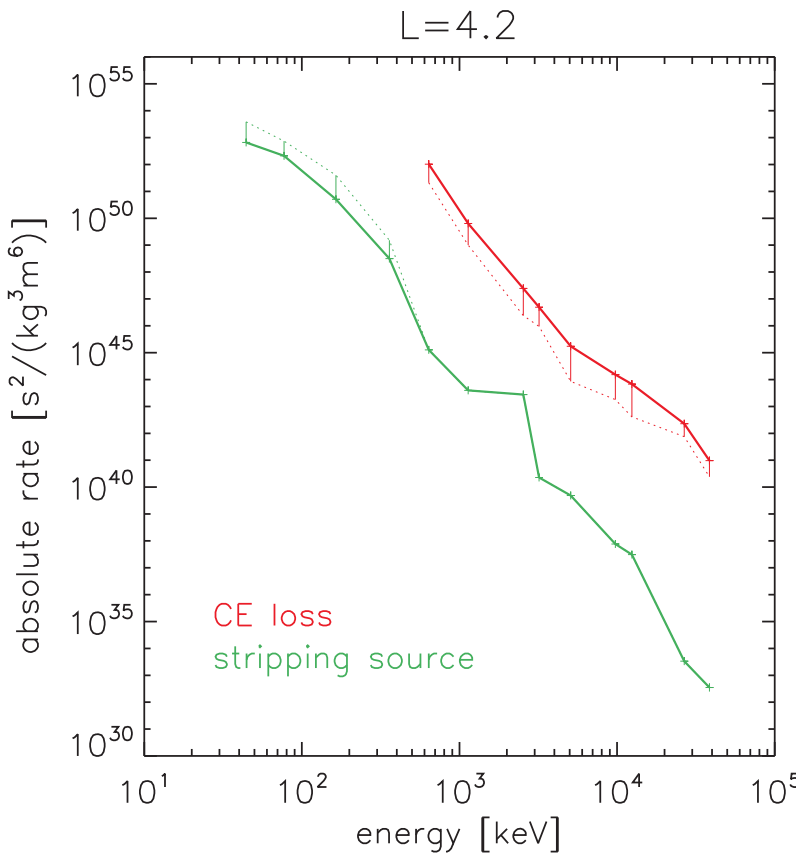


Figure 5.14: Absolute rates $\langle \delta f / \delta t \rangle_{\text{CE,str}}$ of loss from charge exchange (red) and gain from ENA stripping (green), averaged over the radiation belt between Enceladus and Tethys. Error bars show the extreme case where the intensity in this belt is 3σ lower than the average and in all other regions 3σ larger.

5.3.2.2 Other pathways

At lower energies than discussed above, the importance of stripping could be different. If the radiation belts are populated at these energies with an intensity that is finite but much lower than in the rest of the magnetosphere, they might gain significantly from stripping. This, however, can not explain the source at the energies considered here.

ENAs might also be stripped within the upper atmospheric layers instead of the Neutral Torus. If this happens close to the equator, the ions will stay in the atmosphere. If this happens at high latitudes, the particles will bounce, but frequently reencounter the atmosphere. If the local pitch angle at the time of production is not 90°, they will even penetrate deeper. Scattering might change their pitch angle and lower their mirror point, allowing them to permanently leave the atmosphere and supply the equatorial proton population. While electrons can generally be easily deflected in matter, ions barely change their direction. Decelerating ≥ 100 keV protons in hydrogen gas to full stop changes on average their angle only by $< 1^\circ$ (Ziegler 2008). We therefore do not expect the change in pitch angle being efficient enough that a significant part of the produced ions can escape charge exchanging again and being lost.

What also was not discussed yet is the origin of the innermost radiation belt located within the orbit of the Main Rings and its contribution to the ENA production. At Earth, stripping in the high atmosphere gives rise to the formation of a secondary radiation belt. It is possible that this is similar at Saturn and that this belt actually has a significant contribution from stripping. Since the ENA emission from this belt is weak we do not expect that it contributes much to the ENA production of the magnetosphere or the stripping

source within the classical belts.

Based on this it can be concluded that ENA stripping is no important source mechanism.

5.3.3 Radial diffusion

Another theory to supply the radiation belts is that they originate from particles that radially diffused from the middle magnetosphere inward. [Roussos et al. \(2008b\)](#) reported unusually high intensities at $L > 5$ and the formation of a transient radiation belt following enhanced solar activity. These events do not increase the intensity of the classic belts. It is commonly concluded from this that the icy moons efficiently shield the radiation belts from each other and the rest of the magnetosphere. Nevertheless, it could be possible that this shielding is not perfect and that particles from the middle magnetosphere can penetrate on long time scales into the outermost belt and from there on inward to the others. If this time scale would still be comparable to the lifetime against losses or diffusion, this process would still be significant.

The model that was described in Sec. 5.2 is now used to determine this by answering two questions: Are particles exchanged between the belts via diffusion at all? Can allowing this exchange within the model replace the need for a source in it?

To answer the first question, we discuss Fig. 5.6 again, which shows model results using the sink method and the optimum model parameters. The protons represented in the upper panel have pitch angles of $\alpha_0 \approx 10^\circ \pm 10^\circ$. They escape absorption efficiently enough so that their PSD stays finite throughout the corridor. As it can be seen in the rates plotted in this figure, most of the particles within the corridor were diffusing into it (brown points) and not created there by the source (cyan line).

The lower panel of the Fig. 5.6 shows protons with $\alpha_0 = 90^\circ \pm 10^\circ$. Our numerical solution is not able to describe the full range in between the selected boundary conditions properly and the model result satisfies the diffusion equation (2.56) only within one belt. This implies that at least protons with these pitch angles are so efficiently absorbed by the moons that they are not exchanged between the belts. The fact that the measured PSD is still finite within the corridor does not necessarily contradict this statement because we cannot rigorously exclude the possibility that the very small values measured there are only background contamination of the instrument.

Despite the fact that the belts of field-aligned protons are connected in the model, this does not render the source obsolete. A reduction of the source yields model results as shown in the upper panel of Fig. 5.7 where the peak PSD of the belts becomes increasingly smaller after every passage of a moon orbit. Diffusion from other belts or the middle magnetosphere does therefore not significantly contribute to the particle population, which answers the second question.

5.3.4 Injection events

Injections were introduced in Sections 2.2.2 and 2.2.3. They provide a means of radial transport that might occur on time scales faster than the encounter time with moons and could therefore transport particles across the moon orbits.

Most injections occur at $L \approx 7.5$ ([Chen et al. 2010](#)) and appear in our data only as far in as $L \geq 4$. However, this fact alone cannot hold to exclude them. The number of particles

transported by them might be much smaller than the number of particles already present in the radiation belts. These particles would therefore not cause an intensity well above the normal or surrounding one. Despite the fact that injections therefore might occur and could accumulate particles within the belts, it would not be possible to detect them. We therefore argue instead that injections are not expected to reach the belts in the first place.

Dipolarization as one mechanism of injections does not change the strong magnetic field close to the planet and therefore does not operate within the radiation belts.

Another mechanism for injections is the centrifugally-driven interchange of flux tubes. Since particles with increasing energy leave the flux tube increasingly fast, which ends the radial motion of the particle, interchange becomes inefficient towards MeV energies. Additionally, interchange requires the presence of a force acting on the particles. In the absence of strong plasma pressure, this force is the sum of gravity and centrifugal force. It is zero around $L = 2$ and therefore much weaker in the radiation belts than in the middle magnetosphere, where injections are observed.

5.3.5 Discussion

Our calculations suggest that the stripping of ENAs that were created in the magnetosphere and stripped in the Neutral Torus do not contribute to the proton population of the radiation belts. Using our model, we could also exclude that diffusion across the orbits of the icy moons is a relevant source, independent on the time scale considered.

CRAND from the Main Rings can contribute to the population, but only at energies $\geq 10 \text{ MeV}$.

Several pieces of evidence suggest that atmospheric CRAND is at least contributing to the proton population of all energies, if not the dominating effect. Below 10 MeV, it appears to provide too few protons and a too flat spectrum. Still, it is the most promising candidate process, since many others could be excluded.

6 Processes in the middle magnetosphere

6.1 Introduction

In Sec. 4.2 the terms *middle* and *outer magnetosphere* were defined. We show a sketch where they are approximately located in Fig. 6.1. The middle and outer magnetosphere differ from the radiation belts and are *not* significantly populated by products of the CRAND process. At Earth, most of the particles outside the radiation belts originate instead from the solar wind plasma that entered the magnetosphere during reconnection and became accelerated afterwards. At Saturn, the solar wind is no major plasma source. Otherwise, the density of helium ions, which are brought mainly by the solar wind, would be higher. The dominating source is Enceladus that continuously ejects water gas and ice. Parts of this water is dissociated, ionized and accelerated, which explains the large abundance of water group ions (DiFabio et al. 2011).

Additionally, the relevant processes acting on the particles in the middle and outer magnetosphere are different to the radiation belts. While in case of the belts it is obvious that the colocated moons dominantly shape the particle profiles, this is not clear in the middle magnetosphere. Since we will consider mainly particles with lower energies in this region (due to the limitations of LEMMS), distributed loss processes in the gas and grain environment might be more important instead. It was an open question which of the possible loss mechanisms is the dominant one (charge exchange, energy loss in gas or in grains), i.e. if the interaction with the Neutral Torus or the E ring is more important. We will answer this question throughout Sec. 6.2.

6.2 Studies at $7R_S$

In this section, we will calculate and compare rates for most processes that were introduced in Sec. 2 for protons and electrons at $L = 7 \pm 0.5$. Our considerations will be based on estimates of gas and grain densities, as they were partly already given in Sec. 1.2.2. The poorly known vertical extents of Neutral Torus and E ring does not play a role for particles that stay close to the equatorial plane. We therefore limit ourselves to equatorially mirroring particles to reduce the number of uncertain parameters.

We chose $L = 7$ since it was not possible for us to study $L = 4$ with confidence. The gas and grain densities might be known best near Enceladus, but there the LEMMS data is partly contaminated by radiation belt background. This problem does not exist at $L = 7$.

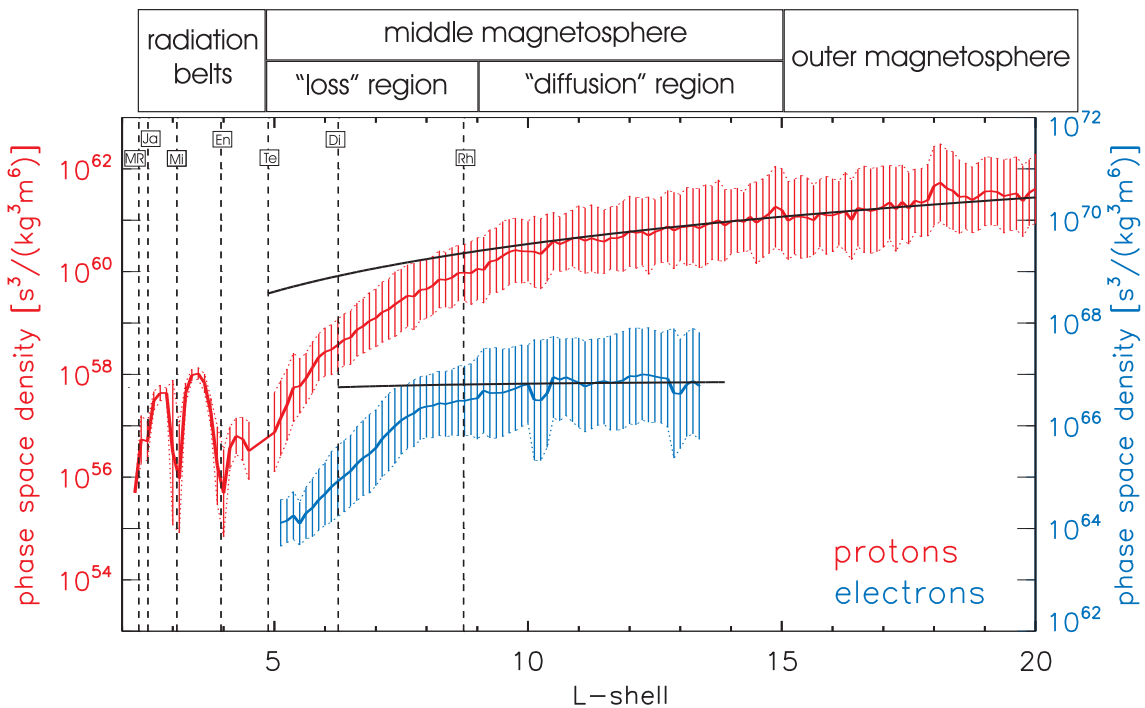


Figure 6.1: Illustration of the various regions throughout Saturn's magnetosphere. The radial boundaries are estimates and not clearly determined. The radiation belts were treated in Sec. 5. The middle magnetosphere is the focus of the present section 6, although the outer magnetosphere is partly included there. We propose that the middle magnetosphere is differentiated in two regions that we refer to as "loss" and "diffusion" region. Despite the names, loss and diffusion are not the only processes acting there, as it will be discussed in Sec. 6.3. *Red line* and left axis: Protons with $E = 300 \text{ keV}$ and $\alpha_0 = 10^\circ$ at $L = 9$. *Blue line* and right axis: Same, but for electrons with $E = 60 \text{ keV}$. *Black lines*: Theoretical functions assuming solely radial diffusion (see Sec. 6.3.1.1 for details). *Dashed lines*: outer edge of the Main Rings (MR), Janus (Ja), Mimas (Mi), Enceladus (En), Tethys (Te), Dione (Di), Rhea (Rh).

This region also has the advantage that it is still relatively close to Enceladus and within a relatively wide gap in between two moons that could otherwise influence the particle profiles. These moons are Dione and Rhea and their orbits are $2.5R_S$ apart.

6.2.1 Charge exchange

First charge exchange with neutral gas is studied. As shown in Fig. 4.5, the dominant ion species in the region considered here is protons, so we will use their CE cross sections, as their were shown in Fig. 2.10.

The lifetime τ_{CE} for CE losses was given in Eq. (2.64) and does not depend on PSD (different to the rate). The path-averaged gas density \bar{n} is taken equal to the equatorial density n_0 since we want to calculate the lifetime of exactly equatorially mirroring particles.

To estimate the charge exchange loss rate, only the dominant neutral species is taken into account, which at $L = 7$ should be O -atoms. Since all major species have similar charge exchange cross sections, this assumption is not critical. Nevertheless, it implies

that our assumed density of "effective" O should be taken slightly larger than the real O -density. If H_2O , OH and H were equally abundant and have exactly the same cross sections, the effective density would need to be 4 times larger than the real O density.

We use $n_0(7R_S) = 10^8 \text{ m}^{-3}$ as the equatorial peak value of effective O . This is roughly consistent with O densities given in Melin et al. (2009), Smith et al. (2010), Cassidy and Johnson (2010), Dialynas et al. (2012), and approximately one order of magnitude less than the peak value at $L = 4$, which was discussed in Sec. 1.2.2.

The results are shown in the left panel of Figure 6.2 as green crosses. It can be seen that they strongly depend on energy and vary between days ($\approx 10^5 \text{ s}$) and several years ($\approx 10^8 \text{ s}$). Only lifetimes below 1 MeV were calculated since for higher energies the used charge exchange cross sections are not reliable.

The results shown are *energy lifetimes*, to be precise. Since the charge exchange loss rate only depends on the PSD at a given energy (and does not have source contributions that depend on the PSD at higher energies), they can be easily converted to *channel lifetimes* using (2.71). The result is indistinguishable on the scale of the figure because the used PHA channels are narrowly spaced in energy.

6.2.2 Energy loss in grains

The channel lifetimes for particle loss or gain following energy loss in macroscopic grains was given by Equations (2.72) and (2.68). The integral in (2.68) is here calculated numerically. We use values of the differential energy loss as they were shown in Fig. 2.11.

The number of encounters between energetic particles and ice grains is called M . It depends on the energy of the energetic particle, energy interval and position of the used channel, the target material, and the grain size.

For simplicity, we only consider *typical* grains here, i.e. grains where the product of cross section and number density is maximum. We estimate the typical grain size to be $0.1 \mu\text{m}$ (Sec. 1.2.2).

If we apply this to LEMMS' PHA channels and $0.1 \mu\text{m}$ -grains, we find that protons below 90 keV lose enough energy within a single grain to leave the channels already after one single encounter, even if they start at the upper limit of a channel's energy range. For energies below 45 keV, they lose so much energy that they miss the energy range of the channel directly below them.

Electrons at the upper limit of a PHA channel need several encounters to leave even the lowest channels (which are especially narrow in energy and measure energies where the differential energy loss is high). For example, to enter the lowest electron channel at 25 keV from the upper limit of the closest channel above, it requires 25 encounters. Because of the smaller energy loss, electrons typically do not overshoot and miss channels at lower energies.

Protons and electrons at the lower limit of a channel always only need one encounter with a grain to leave the range of the channel. We illustrate the described behavior in Fig. 6.3.

Larger grains allow for smaller M to achieve the same ΔE . As long as the differential energy loss does not significantly change in the energy interval covered by ΔE , the relation of grain size and M is roughly linear.

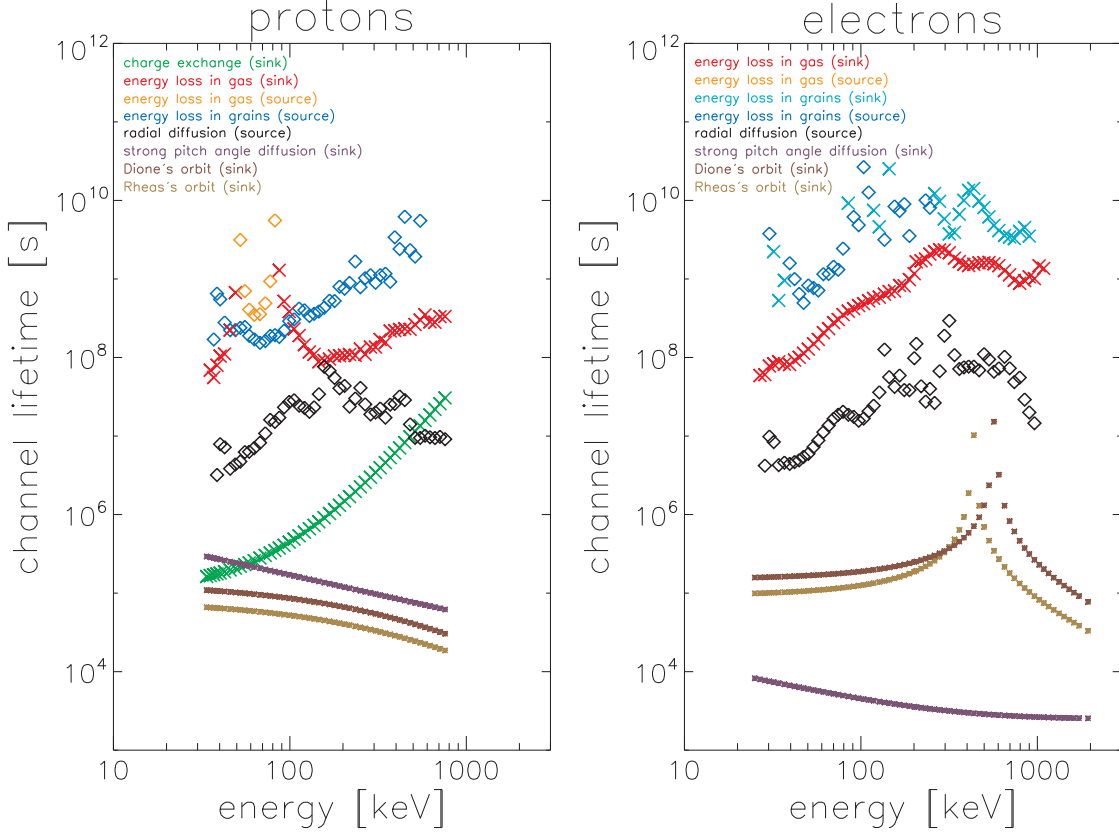


Figure 6.2: Energy and channel lifetimes of equatorially mirroring protons (left) and electrons (right) against various processes at $L = 7 \pm 0.5$. Different colors describe different processes as explained in the legend and discussed throughout Sec. 6.2. x-symbols represent loss processes, \square -symbols sources. The small *-symbols are either lower limits or apply to neighboring L -shells and will be explained in later sections. Remember that 10^5 s are approximately a day and 10^{10} s are hundreds of years.

The channel lifetime, however, does not only depend on M but furthermore on the full PSD spectrum at all energies above the channel. Since \tilde{f} in (2.72) is the PSD measured within the mirror points of the considered pitch angle, we can use values as they have been presented for example in Fig. 4.8 to calculate the channel lifetime. The fact that the shape of the spectrum changes the channel lifetimes can be seen when comparing Fig. 6.3, upper panel with Fig. 6.4, left panel.

Assuming larger grains causes every M -value to occur at larger energies. This increases the contribution of energies above the channel and therefore the importance of the spectral shape. An illustration is given by Fig. 6.3, lower panel and Fig. 6.4, right panel: For $0.1 \mu\text{m}$ -grains electrons with 106 keV already need $M = 100$ encounters to enter the channel. In case of larger $1 \mu\text{m}$ -grains, electrons with the same energy require only $M \approx 10$ encounters. Therefore, the contribution from 106 keV is 10 times higher in the latter case.

The required continuous spectrum is derived here by interpolation of the existing measured spectrum with cubic splines on a log-log scale. Since we aim for lifetimes to describe equatorially mirroring particles, we use measurements at $\alpha_0 = 90^\circ \pm 10^\circ$. Con-

sidering exactly 90° particles is not feasible since these are rarely sampled, only during occasions where both Cassini is at the magnetic equator *and* LEMMS points into an appropriate direction.

To estimate if including other pitch angles causes a strong discrepancy between n_0 and \tilde{n} , the vertical density profile is assumed to be Gaussian and following $n_r(\lambda) = n_0 \exp(-\lambda^2/\lambda_r^2)$, with λ_r being the latitude at which the density drops to $1/e$ of the equatorial value. The approximation $\lambda_r \approx \text{ArcTan}(H/(2LR_S))$ can be used if the thickness H of the torus varies slow enough with L . If one uses this and further assumes $H = 1R_S$, as in the radiation belt model, then the path-averaged density for 80° -particles is with $\tilde{n} = 0.65n_0$ in the same order of magnitude as n_0 . Averaging over the interval from 80° until 90° yields values even closer to n_0 , depending on the precise shape of the PAD. Including other than equatorial pitch angles is therefore not critical. This would change though for a thinner torus of $H = 0.1R_S$ that yields $\tilde{n} = 0.064n_0$.

The value of the number density n_0 for typical grains is not precisely known (Sec. 1.2.2). We therefore estimate it here using the optical depth, which is approximately $\eta(7R_S) = 10^{-7}$, about one order of magnitude below the peak value at $L = 4$ (Hood 1983). The vertical extent of the $0.1\ \mu\text{m}$ -sized grains can be derived from simulations (Horányi et al. 2008, Beckmann 2008). We assume $H = 1R_S$. With the relation $\eta = nH\sigma$, we get a peak density of $n_0(7R_S) = 10^{-1}\ \text{m}^{-3}$.

This density is used to calculate channel lifetimes for the LEMMS PHA channels. The absolute values of the results are shown in Fig. 6.2. It is apparent from the figure that the interaction with grains is the slowest of all processes and occurs on time scales of years ($\approx 10^8\ \text{s}$) or even hundreds of years ($\approx 10^{10}\ \text{s}$).

Keep in mind that channel lifetime is not a quantity of an isolated energetic particle but also depends on the intensity of other energetic particles at other energies, and the instrument used to measure them. Therefore the lifetimes are not plotted over arbitrary energies, but over the mean energy of the used channels. Because every channel is unique in energy range and center energy, the channel lifetimes are scattering.

For protons at least below 500 keV and electrons between approximately 40 keV and 300 keV, the channels experience a net gain of particles. This means that despite the fact that the ice grains ultimately stop the energetic particles, they act as a source and *increase* the PSD measured by the channels.

Blue crosses in Fig. 6.2 indicate that losses from the channel dominate, cyan diamonds that the channels experience a net gain in particles. In case of electrons, the gain occurs for energies, where their spectrum is relatively flat (see spectrum in Fig. 4.4). This is because flat spectra have more particles at high energies that can supply the lower channels, than steep spectra. It can be expected that regions with $L \geq 8$, where the spectra become steeper, have a weaker source or even a loss in this energy range.

To derive the lifetimes shown in Fig. 6.2 we integrated (2.72) up to the upper energy limit of the used PHA channels (760 keV for protons, 1.6 MeV for electrons). There is the danger that energies close to this upper limit might in the calculation not be sufficiently supplied from higher energies because there is no spectral information available. The fact that high-energy electrons are lost while electrons at lower energies are added to the channels might therefore just be an artifact of the calculation. To check and exclude this, the influx from energies directly above every channel is compared with the (smaller) influx coming from the highest considered energy. Convergence is only assumed if the

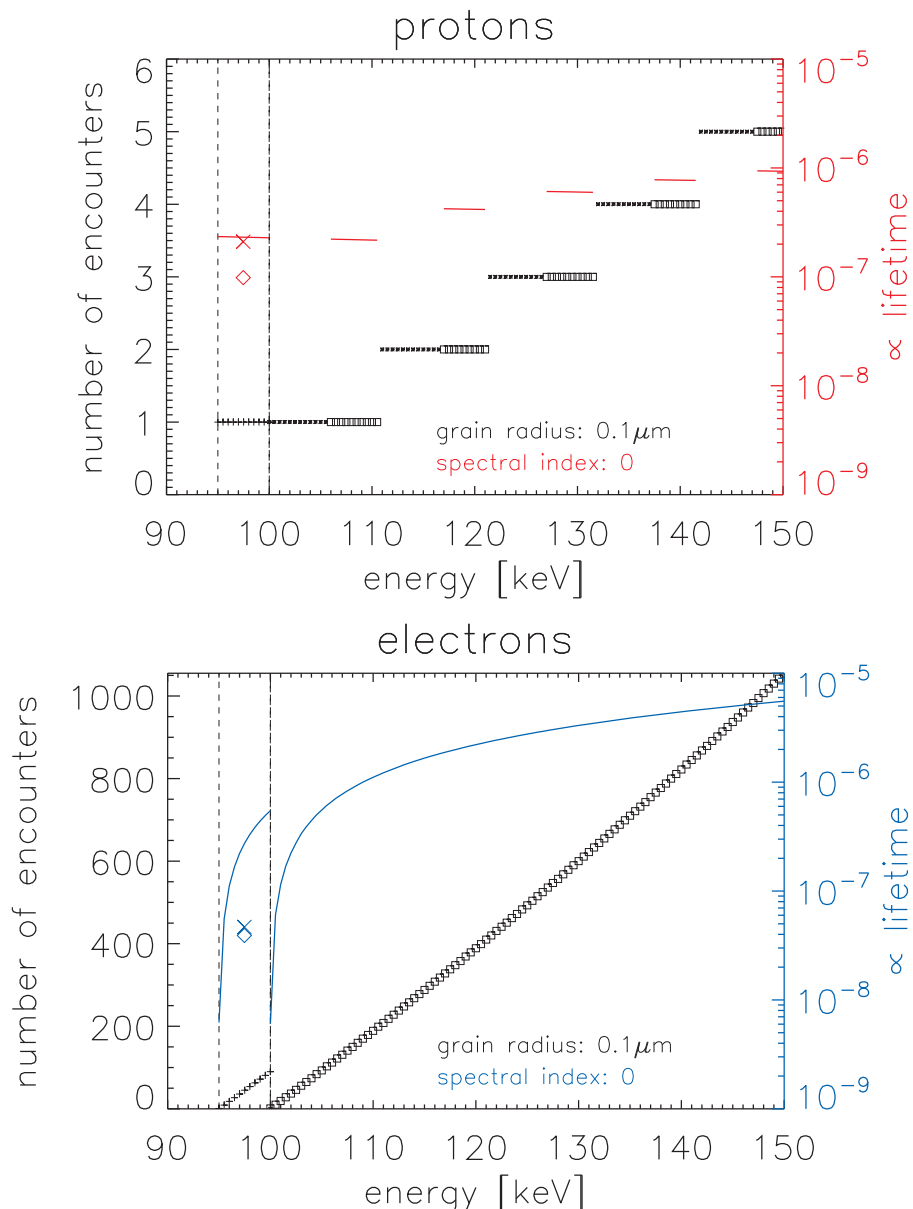


Figure 6.3: Number of encounters between energetic particles and ice grains necessary to enter (\square) or leave ($+$) an instrument channel (left axis). If the energy loss in the grain is so large that the particle overshoots and misses the channel, $*$ -symbols are used¹. The channel is fictive and extends over the energy range marked by the *dashed lines*. *Colored lines* are proportional to energy lifetimes and assume that the PSD spectrum is flat. The X-symbol displays the channel loss time, the \diamond -symbol the channel source time (right axis)². The net channel lifetime would be the sum of both. Protons are displayed in the upper, electrons in the lower panel. The grains have a radius of $0.1\mu\text{m}$.

¹ An example: Protons within the channel need one encounter to leave it (+). Protons with energies directly above the channel lose so much energy during one encounter that their final energy is below the channel (*). Protons above 106 keV need one encounter to enter the channel, protons above 117 keV need two encounters (\square), etc.

² Channel loss and source times are related to the number of encounters as given by (2.72).

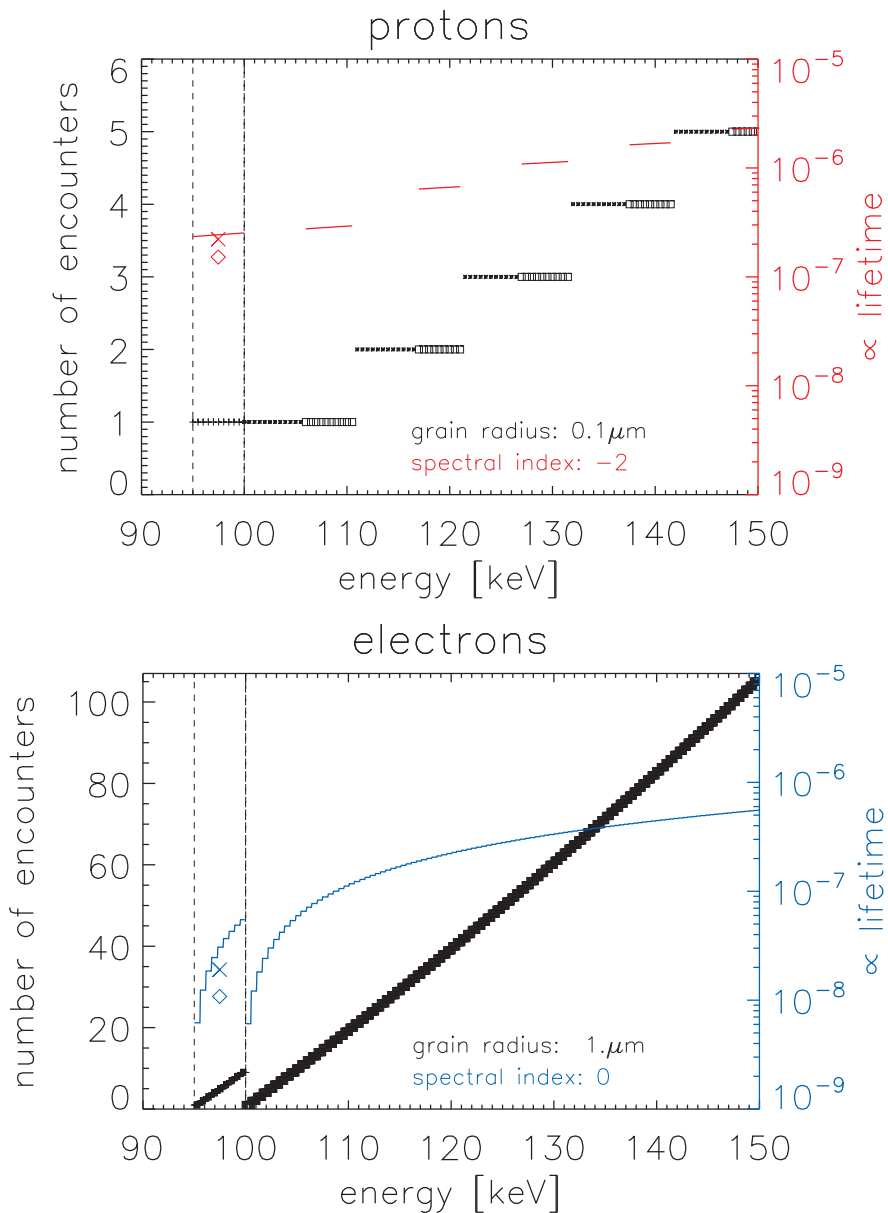


Figure 6.4: Same as Fig. 6.3 besides the following. *Left panel:* The PSD-spectrum is not flat but follows a power law with $\gamma_f = 2$. *Right panel:* The grains are larger and have a radius of $1\mu\text{m}$. The energy resolution was increased here compared to the other plots.

ratio between the two fluxes is smaller than 1 %. Channels that do not fulfill this criterium have been skipped and are not shown within Fig. 6.2. Because of this check we are confident that the loss of high-energy electrons is no artifact, but a real effect. The loss of protons at the single channel at ≈ 500 keV, however, is probably an artifact since all other lossy channels did not fulfill the 1 % criterium.

6.2.3 Energy loss in gas

We calculate the energy loss within the Neutral Torus as it was described in Sec. 2.3.4. For the torus, we again assume that it mainly consists of O with a density of 10^8 m^{-3} .

The resulting lifetimes are shown in Fig. 6.2. In most cases the particles are lost from the channels (red crosses). Only within approximately $50 \text{ keV} \leq E \leq 80 \text{ keV}$, where the proton spectrum is flat (Fig. 4.4), the energy loss increases the PSD.

The interaction with plasma can be treated in a similar as for the gas. We neglect the plasma here since its density is an order of magnitude below the neutral density (Sec. 1.2.3).

6.2.4 Radial diffusion

Radial diffusion was discussed in Sec. 2.2.1. Expansion of (2.37) yields the rate at which diffusion changes the PSD:

$$\frac{\delta f}{\delta t} \Big|_D = L^2 \frac{\partial(D_{LL}/L^2)}{\partial L} \frac{\partial f}{\partial L} + D_{LL} \frac{\partial^2 f}{\partial L^2} = \frac{f}{\tau^*} \quad (6.1)$$

In a steady state, this rate has to be equal to the combined rate of all other source and loss processes. Therefore it can be interpreted as an effective loss (or source) rate that can be derived from the radial particle profiles without assuming anything about the loss processes (neutral density, species, etc.)

What has to be assumed instead is the function $D_{LL}(L)$. For this, we use a fit to the data shown in Fig. 2.3 which yields $D_{LL} = 0.12 \cdot 10^{-9} \text{ s}^{-1} \cdot (L/3.5)^{7.0}$ with s being the unit second.

We calculate τ^* for several μ values of equatorially mirroring particles. μ is chosen so that the energy at $L = 7$ matches the average energies of the LEMMS channels.

From (6.1) it can be seen that τ^* depends not only on D_{LL} but also the first two derivatives of f . Since not even f is known with certainty due to the large scattering of the mission-average (Fig. 4.8), and derivatives are sensitive to any fluctuations, τ^* is difficult to calculate. We therefore smooth the f -profiles first, see Fig. 6.5. Since the derivatives even of the smoothed curve scatter, we apply linear fits to them. These fits are then substituted in (6.1) in order to derive the channel lifetime τ^* of diffusion. The results are also included in Fig. 6.2. Details of the smoothing and fitting change the values of τ^* , but not its order of magnitude or general dependence on energy.

Interestingly, diffusion usually acts as a source process. This is different to the radiation belts, as it was illustrated in Fig. 5.10. There, diffusion drives the particles away from the radiation belts, causing a loss.

In the range of approximately 400 keV to 700 keV, τ^* of electrons is strongly scattering. In case that we do not use the fit to the derivatives, it can occur that τ^* changes its sign,

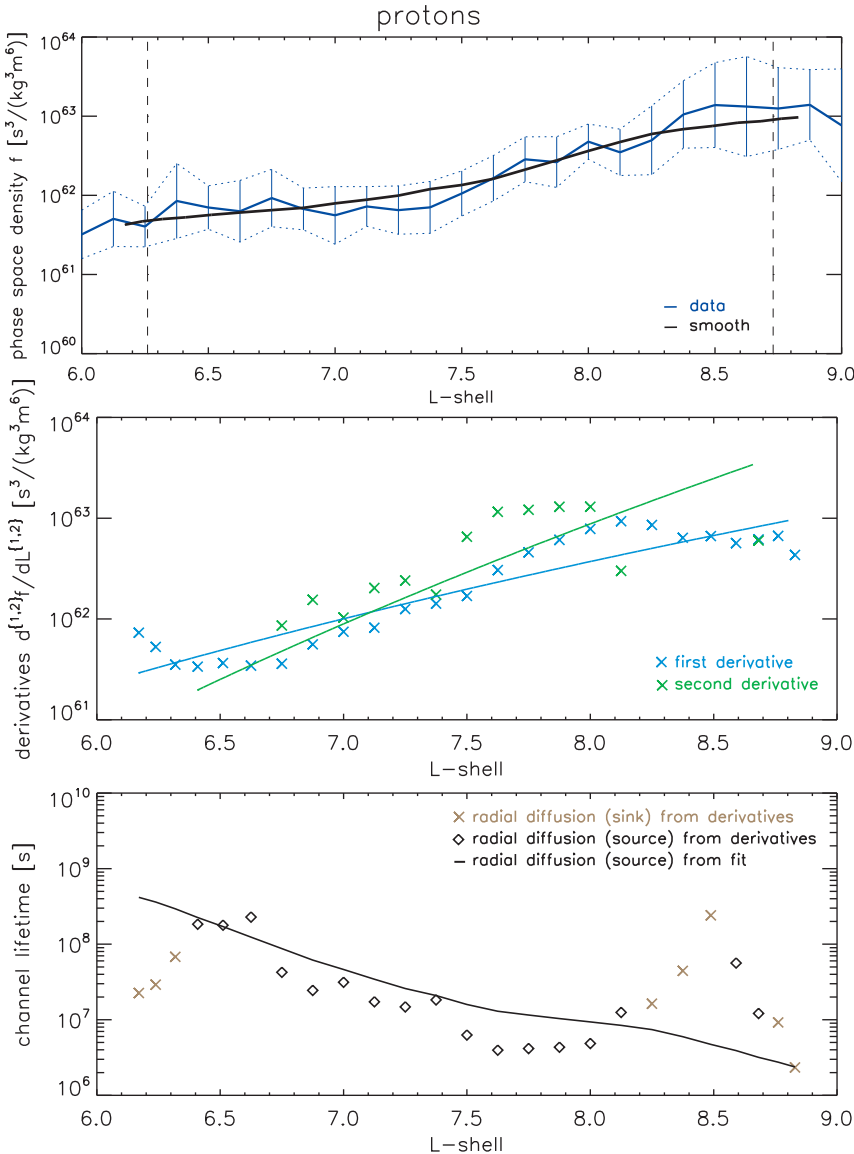


Figure 6.5: Illustration how the channel lifetime for radial diffusion is derived here. *Upper panel:* PSD of protons with $E = 93 \text{ keV}$ and $\alpha_0 = 90^\circ \pm 10^\circ$ at $L = 7$. Blue line: L -binned data. Black solid line: Smoothed bins. Black dashed lines: Orbits of Dione and Rhea. *Middle panel:* x-symbols show derivatives of the smoothed PSD, lines are linear fits to the derivatives. *Lower panel:* Radial diffusion lifetime calculated from the derivatives (symbols) and from the fit to the derivatives (line).

turning diffusion at these energies into a loss process. Both is related to the fact that the PSD profiles at these energies are very flat (see Fig. 4.8). Therefore, the derivatives are very small. This makes τ^* not only large but also very sensitive to changes in the derivatives, which cannot be determined with certainty.

6.2.5 Pitch angle and energy diffusion

So far we only considered radial diffusion, which is a common approach (Van Allen 1984, Mauk et al. 2009) and is supported by the data (Sec. 5.2). Here, we discuss the importance of other types of diffusion and calculate the lifetime due to pitch angle diffusion for an extreme case.

Pitch angle diffusion can arise from scattering in matter (Sec. 2.2.1.6) and wave-particle interactions (Sec. 2.2.1.5). Energy diffusion is mainly caused by wave-particle interaction with waves that have strong electric field components. Also mixed types of diffusion occur. As already argued in Sec. 5.2.1.3 are waves at Saturn weak and commonly neglected.

Scattering of protons in matter is negligible due to their relatively large mass (Fok et al. 1991, Jackson 1998). For electrons, however, there is the possibility that the small deflections of single encounters accumulate to significant ones on time scales fast enough to become relevant (Spitzer 1962). Of all processes that we did not treat quantitatively, it is probably the most important one.

Pitch angle diffusion has two effects. First, it is redistributing between different pitch angles, so that a given pitch angle can gain or lose particles from or to neighboring pitch angles. The pitch angle distribution in the mission average can be considered as isotropic (Sec. 4.2.4). Pitch angle diffusion will only sustain such a distribution. Therefore, the numbers of particles entering or leaving a pitch angle cancel out.

Second, pitch angle diffusion can drive particles towards the loss cone. It extends from 0° to $\alpha_L = 3^\circ$ at $L = 7$. If pitch angle diffusion due to any process would occur, also particles initially outside this cone can be lost. A limit on this is the assumption of strong pitch angle diffusion. The lifetime of this process can be calculated by (2.78) and is included in Fig. 6.2.

Keep in mind that strong diffusion would yield an isotropic PAD, which is usually not observed at Saturn. Realistic losses due to scattering to the loss cone will therefore be slower than τ_{PA} or even negligible. This means that τ_{PA} can only be used to exclude pitch angle diffusion.

A full treatment including pitch angle diffusion from scattering and other effects should be subject of future studies.

6.2.6 Discussion

We now compare the lifetimes of all processes discussed so far. Inspection of Fig. 6.2 yields that charge exchange is the fastest process acting on protons. Even if pitch angle diffusion would cause scattering to the loss cone as fast as possible, CE would be faster at least below 100 keV. Charge exchange is two to three orders of magnitude (depending on energy) faster than energy loss in ice grains. Even considering that these lifetimes are based on rough order-of-magnitude estimates, this distance is large enough to claim that the E ring does not have an impact on the proton PSD. Below 1 MeV CE is one to three magnitudes faster than energy loss in gas. As we have seen in Fig. 5.3, this behavior changes at higher energies and energy loss in gas becomes dominant.

Energy loss in gas appears to be about an order of magnitude faster than the one in grains. However, considering the rough estimates applied here, this difference is not large enough for a confident conclusion.

For electrons, the lifetime due to energy loss in neutral gas is faster than in ice, but by less than one order of magnitude. This difference is again not large enough to claim a dominance. We therefore carefully conclude that both effects have similar importance within the considered energy range.

The lifetimes against moon absorption are only shown for comparison within Fig. 6.2. They do not apply to $L = 7 \pm 0.5$ since no moon is orbiting there. Although the losses along the moon orbits are fast compared to the other shown processes, one should be aware of the fact that they only act within the narrow sweeping corridors as given by (2.84). The distributed losses calculated here act in comparison over a large range and change their rates only on the scale of several R_S .

mechanism	protons	electrons
charge exchange loss	dominating for $< 1 \text{ MeV}$	does not apply
energy loss in gas	weak for $< 1 \text{ MeV}$ causes mainly particle loss	weak causes particle loss
energy loss in plasma	weak	weak
energy loss in ice grains	weak causes particle gain	weak causes both particle loss and gain
scattering into loss cone	probably weak	probably dominating
radial diffusion	weak causes particle gain	strong causes particle gain
CRAND source	dominating for $> 10 \text{ MeV}$	occurs for $< 800 \text{ keV}$
injection source	probably dominating strongest for lowest energies	probably strong strongest for lowest energies
other effects	probably weak	probably weak

Table 6.1: Summary of the different source and loss mechanisms at $L = 7$.*Summary:*

- (1) For protons, charge exchange dominates over energy loss in gas for energies below 1 MeV. Energy loss in grains does not play a major role.
- (2) For electrons, energy loss in gas appears to be faster than energy loss in grains, but not significantly.

6.2.7 Further sources and losses

The average middle magnetosphere should be close to a steady state. This is equivalent to the statement that all source and loss processes cancel out on long time scales. If this were not the case, the overall PSD would show a trend in time that is larger than the scattering, as it is the case for the proton radiation belts (Fig. 5.11). However, Fig. 6.2 shows that the processes considered so far do *not* cancel out. The losses in material are either too fast or too slow to counter the source from radial diffusion. There is roughly one order of magnitude difference between them.

If we had calculated the lifetimes only of protons or of electrons, this mismatch could be easily interpreted as a result of a wrong neutral density or diffusion coefficient. Our results could then be used to tweak the parameters until a steady state is reached. However, as we have lifetimes from protons *and* electrons available, it is obvious that this would be wrong. A better match of one species would make the the match of the other species worse. Changing the parameters of diffusion and loss therefore does not help.

What can allow a steady state nevertheless is the fact that we still did not calculate rates of all processes so far. What is missing for example are source rates from injections and CRAND.

Injections should provide particles to the middle magnetosphere and by this act as a distributed source.

Even if it would in theory be possible to include injections into the diffusion coefficient, we did not apply this here. This is because the assumed diffusion coefficient was derived from microsignatures that are not (steadily) refilled by injections. Injections therefore need to be treated as a separate process within this thesis.

If we use the conservative assumption that CRAND only supplies protons around the CRAND-peak at 10 MeV, it would be not important in this section, since we only analyze lower energies here. However, we have shown in Sec. 5.3 that CRAND at least contributes to lower energies. This contribution is decreasing towards the middle magnetosphere. Nevertheless, it might still be relevant.

Assuming that all previously calculated rates have been right, the source rate $\delta f / \delta t|_S$ at $L = 7$ can be calculated.

$$\left. \frac{\delta f}{\delta t} \right|_{CE,Ex} + \left. \frac{\delta f}{\delta t} \right|_{\alpha,E} + \left. \frac{\delta f}{\delta t} \right|_D + \left. \frac{\delta f}{\delta t} \right|_S = 0 \quad (6.2)$$

For protons, the term $\delta f / \delta t|_{CE,Ex}$ is dominated by the loss rate of charge exchange. The term $\delta f / \delta t|_{\alpha,E}$ represents losses from pitch angle and energy diffusion, which we expect to be negligible for protons. Since both statements are questionable for electrons, we do not apply (6.2) to them.

The resulting proton source rate is shown in Fig. 6.6. It can be seen there that in order to create a steady state, a source that is strongest at low energies is necessary. A power law fit between 0.1 and 1 MeV yields an exponent of $\gamma_j \approx 2$, which is smaller than our expectation of a CRAND source ($\gamma_j \approx 3$, Sec. 5.2.1.1). However, the source rate qualitatively agrees with our expectation for injections: Since most injection events are observed at lower energies, their source should be strongest there. It therefore is probable that the source rate in the middle magnetosphere is dominated by injections. Since injections occur sporadically but often during the mission, this rate is a time-averaged value and does not yield information about single events.

Considering the large number of assumptions, there can be no confidence about the value of the source rate. Nevertheless, Fig. 6.6 shows that sources are important processes that should not be neglected.

Remembering our definition of injection events as dispersed intensity enhancements (Sec. 2.2.2.1), it would be plausible if injections are only second-order effects that only slightly perturb a distribution that is shaped by diffusion and losses. However, if the source that we found really is injections, this would imply that this interpretation is not valid. On the contrary: injections might significantly contribute in shaping the energetic particle distribution.

Further inspection of Fig. 6.6 shows that $\delta f / \delta t|_S$ turns negative for energies above 600 keV. The most probable explanation is not that this is a signature of yet another loss process. Instead it should follow from the fact that the chosen neutral density and diffusion coefficient are indeed not fully correct.

If the source follows from injections, then the source rate of electrons should be the same as for protons. If the source also includes CRAND, also this will provide electrons, although with a different spectrum than for protons.

The loss that is needed to counter all electron sources (radial diffusion, injections, CRAND) needs to be distributed in L and dominating over the losses that were calculated

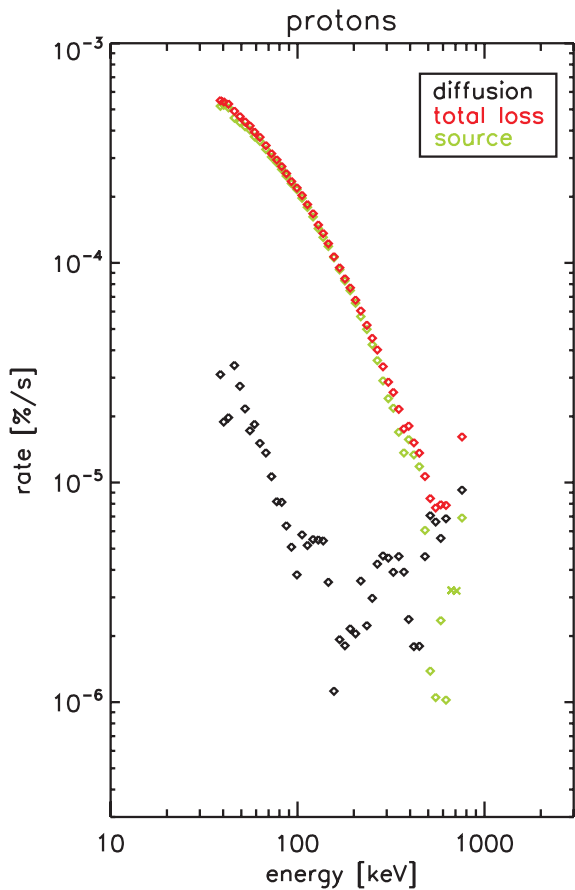


Figure 6.6: Relative rates for different processes acting on equatorially mirroring protons at $L = 7$. *Red:* Loss, mainly due to charge exchange. *Black:* Source, from radial diffusion. *Green:* Difference of the previous processes. Diamonds: Additional source, due to injection events and/or CRAND. x-symbols: Additional loss, probably an artifact.

(energy loss in matter). We do not calculate values of this loss rate since the uncertainties accumulated for it would be too large.

A possible mechanism for an additional electron loss mechanism is scattering into the loss cone, which arises from pitch angle diffusion. It is clearly visible from Fig. 6.2 that this process can indeed be faster than any other process acting on electrons. The pitch angle diffusion can be caused by scattering in matter, which is unimportant for protons.

Summary:

- (1) Protons around $L = 7$ are mainly lost from charge exchange and supplied by injections and/or CRAND.
- (2) Electrons in that region are supplied by radial diffusion, injections and/or CRAND. Their main loss mechanism might be scattering to the loss cone.

6.3 Global studies

6.3.1 Radial profiles

In the previous Sec. 6.2 we studied in detail the processes acting around $7R_S$. Here, we discuss how these processes shape the radial profiles throughout the entire middle magnetosphere.

We concluded that the region around $L = 7$ is dominated by distributed sources and losses. This is likely true for a large region beyond $L = 7$, which we assign with the name

loss region. We expect it to extend from the radiation belts to at least $L = 7$.

In Sec. 5 we found that the main processes in Saturn’s radiation belts are radial diffusion and the CRAND source. Since the neutrons responsible for CRAND originate from Saturn and its rings, this source should become unimportant for $L \gg 7$.

Also distributed losses and injections should become a second order effect at large L . This is because the density of neutral material is decaying with increasing L and most injections are observed around $L = 7.5$. It is therefore reasonable to assume that in the outer part of the middle magnetosphere radial diffusion alone is acting. We will use this assumption in Sec. 6.3.1.1 and assign the name *diffusion region*.

Using these names facilitates the distinction of the two regions. It will turn out during the following discussion how well the names represent the actual physical effects in these regions.

6.3.1.1 Profiles assuming pure radial diffusion

Here, we aim to fit the PSD profiles within the *diffusion region* assuming pure radial diffusion. In case that the diffusion coefficient follows a power law with exponent n , also the PSD profiles follow a power law, yet with exponent $3 - n$. Such a profile was given by Eq. (2.38) and has three free parameters. They can be uniquely defined for example by the diffusion exponent and two points (boundary conditions) of the profiles. The diffusion exponent determines the shape of the profile between and outside of the boundary conditions.

From the mathematical point of view the two boundary conditions are completely arbitrary. In Fig. 6.7 for example, we choose the points A and B and calculate the green PSD profile from them. Any other point that lies exactly on the green profile yields exactly the same profile. However, if a point is chosen that slightly deviates from the green curve (as the points a and b in the figure), the resulting profile can deviate significantly outside the boundaries. To reproduce the measured PSD profiles by a power law we therefore will need to choose the boundary conditions with care.

Boundary conditions in general can be used to enforce a gradient of the PSD profile without any source or loss process acting throughout the whole region where the profile is valid. By this, they can account for the fact that *outside* the region where only diffusion is acting, still sources and losses might be acting.

A falling PSD towards small L , as it is observed at Saturn, is a signature that there is a particle sink at small L . Due to diffusion, the loss at this sink influences the entire radial profile and ultimately can deplete particles at any L . It is possible that the sink causes localized losses that are so efficient that (independent on the neighboring particle population) the PSD at this point is always zero. Such sinks are then points that are extraordinary in a physical sense. It is both useful and physically meaningful to use such a point as a boundary condition instead of an arbitrarily picked one.

In the case of Saturn, there are several L at which very strong losses can occur. This might already be the case at the orbits of some icy moons, and the peaks of the Neutral Torus or E ring, but is latest fulfilled at the edge of the dense Main Rings. In order to reproduce the profiles we therefore chose the inner boundary condition being zero at $L = 2$, which is approximately the outer edge of the Main Rings. The resulting PSD profile is not sensitive at large L to the precise L -value of the inner boundary condition.

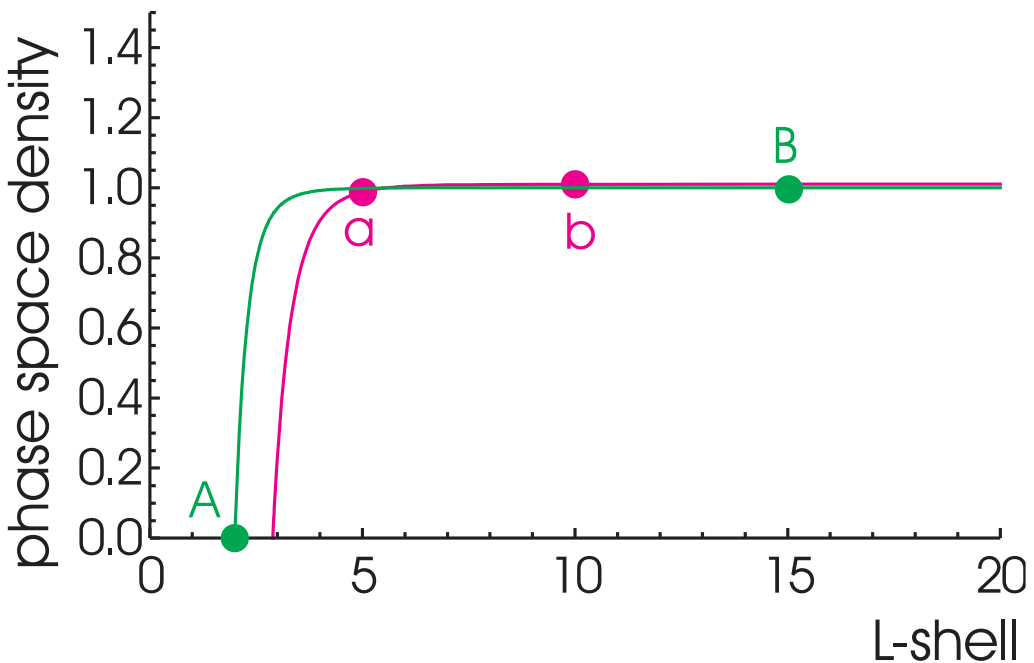


Figure 6.7: Sketch to illustrate how a PSD profile depends on the boundary conditions. *Green points* are boundary conditions, assumed to be $f(2) = 0$ and $f(15) = 1$. Assuming a diffusion exponent $n = 10$ results in a PSD profile shown as the *green line*. The *red points* do not lie exactly on the green curve but deviate by 0.01. They result in the *red profile* that shows an extreme deviation outside the interval contained by the boundary conditions.

This is a crucial advantage towards using a finite PSD value measured at larger L as inner boundary.

To enforce a steady state, the losses occurring at the inner boundary have to be compensated somewhere. In the real magnetosphere this might occur in a distributed region throughout the middle magnetosphere, for example via injections. If we assume pure diffusion, the source has to be located outside the region where only diffusion acts. We consider this to be outside the region described by the power law profile, somewhere in the outer magnetosphere. From this follows that there is no further extraordinary point (as a powerful, localized source) that could be used as outer boundary condition. We leave the outer boundary for now as a free parameter.

With the inner boundary at the rings and the assumption of a diffusion exponent, we already have two of the three parameters describing the power law profile (2.38). The PSD is therefore a function with one free parameter. It could be easily determined by choosing an arbitrary PSD measurement as the outer boundary. Since the result would be too sensitive on this choice, we do not use this approach. Instead, we determine the free parameter by fitting the function to all measurements taken within a large L -range.

The result of this procedure is shown in Fig. 6.8. We find that a power law profile can only match the measurements if the diffusion exponent ranges approximately within $-4 \leq n \leq 4$ and depends on pitch angle.

This is highly unusual for radial diffusion. As explained in Sec. 2.2.1, the diffusion exponent should only depend on the process causing diffusion. The value of the diffusion

coefficient might depend on pitch angle and energy, but the exponent should not. In case that several diffusion processes act simultaneously, this would not change the exponent but hinder that the diffusion coefficient could be properly described with a single power law in the first place.

Negative exponents are also unusual. Electromagnetic fluctuations are strongest relative to the unperturbed field at large L . Any diffusion caused by such fluctuations should therefore be increasingly efficient with increasing L , equivalent to a positive exponent. The only diffusion process that we are aware of and that could be stronger at low L is scattering in material, which is increasingly dense towards $L = 4$. However, if this would be the case then electrons should have a more negative exponent as the protons since they are more easy to scatter (Sec. 2.2.1.6).

The fact that we do not understand the exponent, implies that we do not understand the mechanism causing it, but does not necessarily exclude radial diffusion in general.

A diffusion coefficient falling with increasing L was already reported by Armstrong et al. (1983). They solved the diffusion equation (2.37) for the diffusion coefficient and then used measurements within about $4 \leq L \leq 8$ to calculate its value. They understand this result as a signature of a wrong assumption: In this region exist significant densities of the Neutral Torus and E ring. Assuming pure diffusion without losses must therefore yield a result that is not meaningful.

The profiles considered in Fig. 6.8 are fits to the PSD within $9.5 \leq L \leq 20$. Contrary to the region studied by Armstrong et al. (1983) there is only few gas and grains and we expect only weak losses. However, as we have shown in Sec. 6.2.7, at least at $L = 7$ diffusion is not the only relevant process. Distributed sources as injections play a major role. We therefore suspect that sources are the reason why fitting the profiles under the assumption of pure diffusion is problematic.

This would imply that the diffusion exponents and values that are extracted from Fig. 6.8 quantify not radial diffusion alone but phenomenologically fit the combined processes of diffusion, source, and anything else.

Summary:

The PSD profiles of the diffusion region of the middle magnetosphere can be interpreted in two ways:

- (1) As a signature of an unusual type of radial diffusion.
- (2) As a signature of some other process that acts additional to radial diffusion. This process might be injections.

6.3.1.2 Origin of the profiles' gradient

The PSD of both protons and electrons generally decreases towards Saturn. Keeping in mind the previous discussion about a powerful sink from the Main Rings and distributed losses in the Neutral Torus and E ring, it is tempting to explain this trend with these losses. The profiles of equatorial particles show the steepest profiles. This seems to be consistent with the loss theory, since the matter that causes the losses is close to the equator and therefore affects the equatorial particles most.

If this theory was valid, then a difference between the pitch angles should already be apparent from the (intensity) measurements at constant energy. However, the mission-averaged data are isotropic. Both the PSD gradient itself as its difference in pitch angles

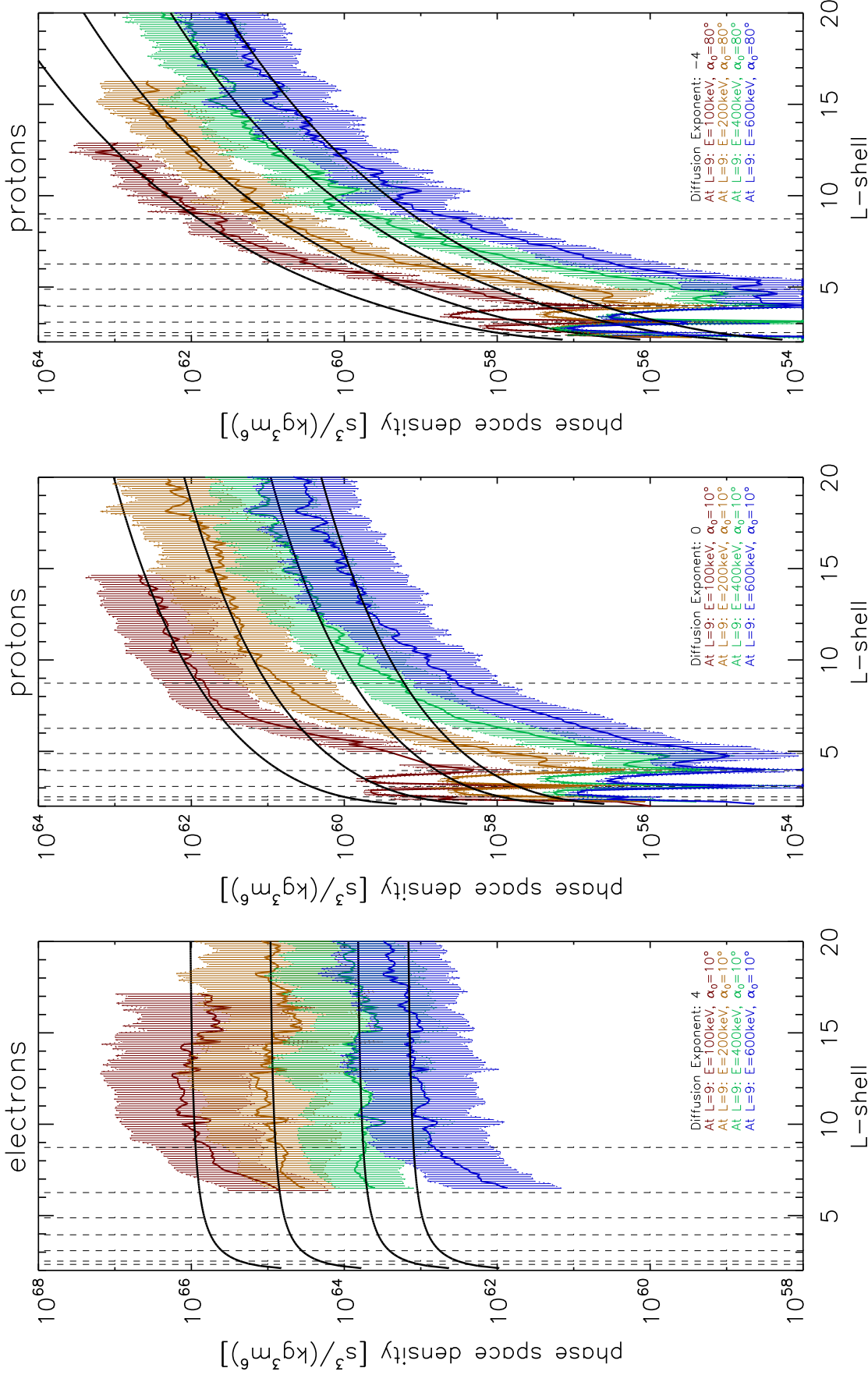


Figure 6.8: PSD profiles of protons and electrons at pitch angles (*colors*) as indicated in the legends. The overplotted *black lines* are fits to the data within $9.5 \leq L \leq 20$ assuming a diffusion coefficient n as given in the legend and $f(L = 2) = 0$. For $\alpha_0 \rightarrow 0^\circ$ the PSD profiles become increasingly flat. Field-aligned electrons (left panel) have the flattest profiles. The flatter the profile, the larger n needs to be in order to achieve a good fit. Steep profiles (as in the right panel) require $n < 0$.

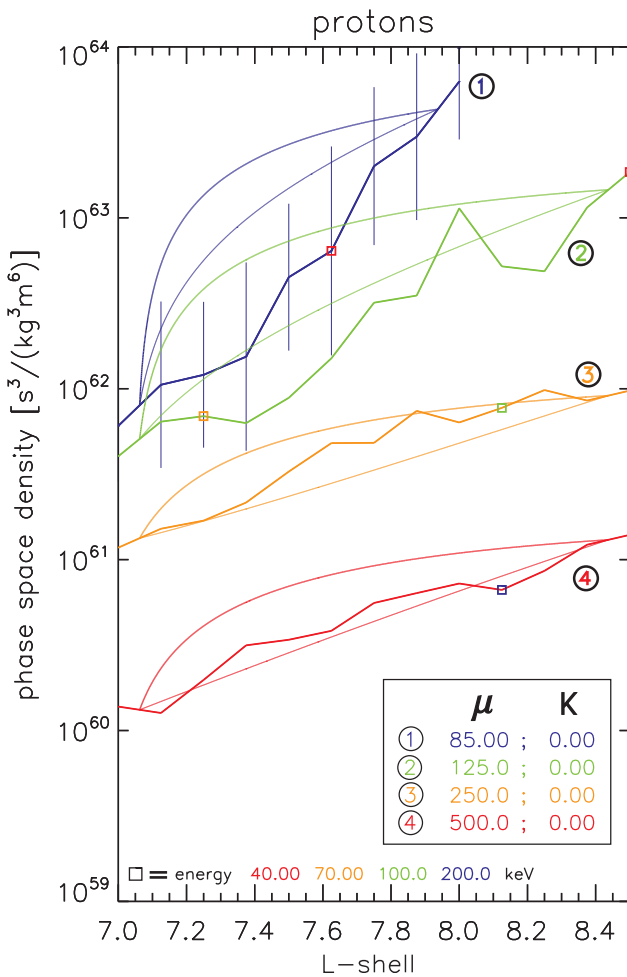


Figure 6.9: Phase space densities of protons within the loss region. *Colors* mark different values of μ and are explained in the legend. The pitch angle is $\alpha_0 = 90^\circ$ for all L . The overplotted *smooth lines* are solutions of (2.38), assuming pure radial diffusion and using averaged measurements at the edges of the figure as boundary conditions. The upper lines use a diffusion exponent of $n = 10$, the lower lines of $n = -10$. Even the latter assumption can not fit the low- μ profiles. The \square -symbols are color coded for the approximate energy at the given position.

can be explained instead with adiabatic heating alone.

In the isotropic case, the phase space density at constant first and second adiabatic invariant only depends on L and $E(L)$. Spectra at Saturn approximately have the same shape for all L , as we have seen in Figures 4.4 and 5.1. Because of this it is feasible factorizing the expression of the PSD.

$$f(L, E(L)) = f_L(L) f_E(E(L)) g(E, L) \quad (6.3)$$

f_E is the dimensionless spectral shape and f_L scales it to the observed value as a function of L . $g(E, L)$ shall correct for all the errors that occur due to the factorization. Since we first consider only first-order effects, we assume $g = 1$.

If the particles diffuse across the middle magnetosphere, their energy can change significantly and cover the whole energy range of LEMMS: For example a 100 keV equatorial proton diffusing from $L = 20$ to $L = 2$ is heated to 100 MeV (Fig. 2.2). The energy spectrum taken by LEMMS ranges over 5 orders of magnitude. The spectra of different L , on the other hand, only differ by about a single order of magnitude. The L -gradient of f is therefore primarily determined by the spectral shape f_E and the adiabatic heating $E(L)$, but not by f_L . Since $E(L)$ changes fastest for equatorially mirroring particles (Fig. 2.2), these are the ones with the largest gradient.

This is different to the radiation belts which only cover a small extent in L : A 1 MeV

equatorial proton for example is from $L = 4$ to $L = 3$ only heated up to 2.4 MeV. The spectrum does not vary much on these scales. The radial profile f_L of the belt as it is measured by LEMMS however covers about two magnitudes and falls significantly between the peak of the belt and the sweeping corridors. The PSD profiles of the belts are therefore determined by f_L .

After finding the explanation of the spatial distribution in the energy distribution, the next logical step would be understanding the origin of the energy distribution function. We identify in this thesis several spectral features that are or might be caused by sources, or losses. We also show how the spectral shape influences loss rates and therefore the spectrum itself. How the overall shape of the spectrum is created was briefly sketched in Sec. 1.2.3 but a detailed discussion is beyond the scope of the present work. It will not be analyzed here but offers itself for future studies.

We return to the middle magnetosphere. Contrary to the previous discussion, we focus now on the *loss region*. Also there, the role of f_E is dominating, which implies that even small features in the spectra translate to features in the radial PSD profiles. The proton and watergroup spectra within $L < 8$ and $E < 100$ keV (Fig. 4.5) are decreasing with decreasing energy, opposite to the usual behavior. Fig. 6.9 shows measured PSD profiles that result from these spectra. We compare them in the figure to theoretical profiles as they would occur if only radial diffusion would act. The profiles where the spectrum is unusual are so extremely steep that even a diffusion exponent of $n = -10$ could not fit the measurements. This is a clear difference to the profiles within the diffusion region (large L displayed in Fig. 6.8). We attribute this to distributed losses from charge exchange.

At energies above 100 keV, the theory profiles in the loss region (Fig. 6.9) match as good or bad as the profiles in the diffusion region (Fig. 6.8). This does not necessarily mean that the same processes are dominating. Since the loss region is narrower than the diffusion region, it is easier there for an unphysical profile to match the observations. Inspection of Fig. 6.8 shows that theory curves that match the observations well in the diffusion region, deviate significantly in the loss region, including energies *above* 100 keV. There are two mechanisms that can cause this.

The first mechanism is that the protons are diffusing inward and are stepwise depleted at every moon orbit. Many orbits indeed coincide with the loss region. How this affects the PSD profiles is explained in detail in the next Section 6.3.1.3. Hood (1983) used moon losses, radial diffusion, and losses in the E ring in order to reproduce proton PSD profiles. Since his PSD profiles are relatively flat, he was able to succeed using a small but positive value of the diffusion coefficient, which is consistent with corotating particles in a fluctuating electrical field as given in Eq. (2.46). Despite some imperfections of the model, it is able to qualitatively reproduce the measurements using mainly moon losses.

The second mechanism could be that the protons only experience a single but powerful loss. This can occur at the orbit of Enceladus, which is embedded in the peak region of both Neutral Torus and E ring. Due to diffusion, maybe in combination with a distributed source, this loss causes not a sharp dropout but reduces the PSD within a large L -range. The localized losses at $L \approx 4$ could therefore shape the PSD profiles throughout the entire loss region.

Summary:

- (1) The proton PSD profiles in the loss region are steeper than in the diffusion region. This can be caused by

- (1a) consecutive, weak losses at several moon orbits and/or
- (1b) a strong loss at the peak of Neutral Torus and E ring.
- (2) The profiles at energies $< 100 \text{ keV}$ are even steeper and are affected by distributed losses due to charge exchange.

6.3.1.3 Electron model around Rhea

Not only the proton, but also the electron energy spectrum shows a peculiar feature (Fig. 4.4). For $L \leq 7$ it is flattened from several 10 keV to several 100 keV. In Sec. 4.2.3 we discussed several theories to explain this. Considering the arguments in the previous section 6.3.1.2, we favor the theory that the feature in the spectra is equivalent to a feature in the electron PSD profiles. This feature is the abrupt change in gradient near the orbit of Rhea (Fig. 4.8), caused by losses at this moon's orbit.

We already illustrated in Fig. 2.9 how localized losses, as of a moon, are expected to affect PSD profiles in case that only diffusion is acting: It will not only cause losses but also change the gradient of the profile outside the region where the loss occurs. This can be explained as follows. For pure diffusion and a diffusion coefficient following a power law, the phase space density f also evolves like a power law in L , see (2.38). If f is constant at some L that is taken as a boundary condition, this yields $A = 0$ in (2.38). Because of this, f will stay constant throughout the region of pure diffusion. The phase space density of field-aligned electrons approximately fulfills this outside of Rhea's orbit. Within a moon's sweeping corridor, losses occur and f decreases with (2.57), a modified Bessel function. At the inner edge of the sweeping corridor, f will have a finite gradient. This gradient and the value of f can be used as a boundary condition for the region far inside of Rhea's orbit, which is again considered as purely determined by diffusion. In contrast to the boundary condition used before, it yields this time $A \neq 0$, which means that f is continuing to decrease even outside the sweeping corridor of the moon.

The gradient change of field-aligned electrons was shown in Fig. 4.8 and 4.9 in the right panels. It can be seen there that the change only occurs for $\mu \leq 5 \text{ MeV/G}$ and for $\mu \geq 30 \text{ MeV/G}$, not inbetween. To understand this, we estimate the energy E_{mr} where these electrons are stationary with respect to Rhea (see Sec. 2.3.6). Assuming the corotation to be 70 % of the rigid value (in agreement with Mauk et al. (2005) and the lower limit given by Müller et al. (2010) and Wilson et al. (2008)) yields $E_{\text{mr}} = 360 \text{ keV}$. The legend of Fig. 4.8 and 4.9 show that the electron energies at the indicated μ and L are far off from E_{mr} . These electrons can therefore be absorbed by Rhea. As discussed above, this absorption causes a change in the gradient of the phase space density. Electrons with μ values in between the ranges given above display no change in gradient. Their energy at $L = 9$ is close to E_{mr} , so that they barely encounter Rhea and do not get absorbed.

Considering this argumentation it should be possible reproducing the electron PSD profiles around Rhea with a model that uses diffusion, and losses at the orbit. The assumption of pure radial diffusion yields profiles that are difficult to interpret, as it could be demonstrated in Sec. 6.3.1.1. However, the profiles match the observations phenomenologically.

For our model, we assume that radial diffusion (or an effective process that can be mimicked by diffusion) is dominating everywhere beside Rhea's orbit. The (effective) diffusion coefficient D_0 and its exponent n are considered as free parameters. The extent of the sweeping corridor and the loss rate throughout it are calculated as described in Sec.

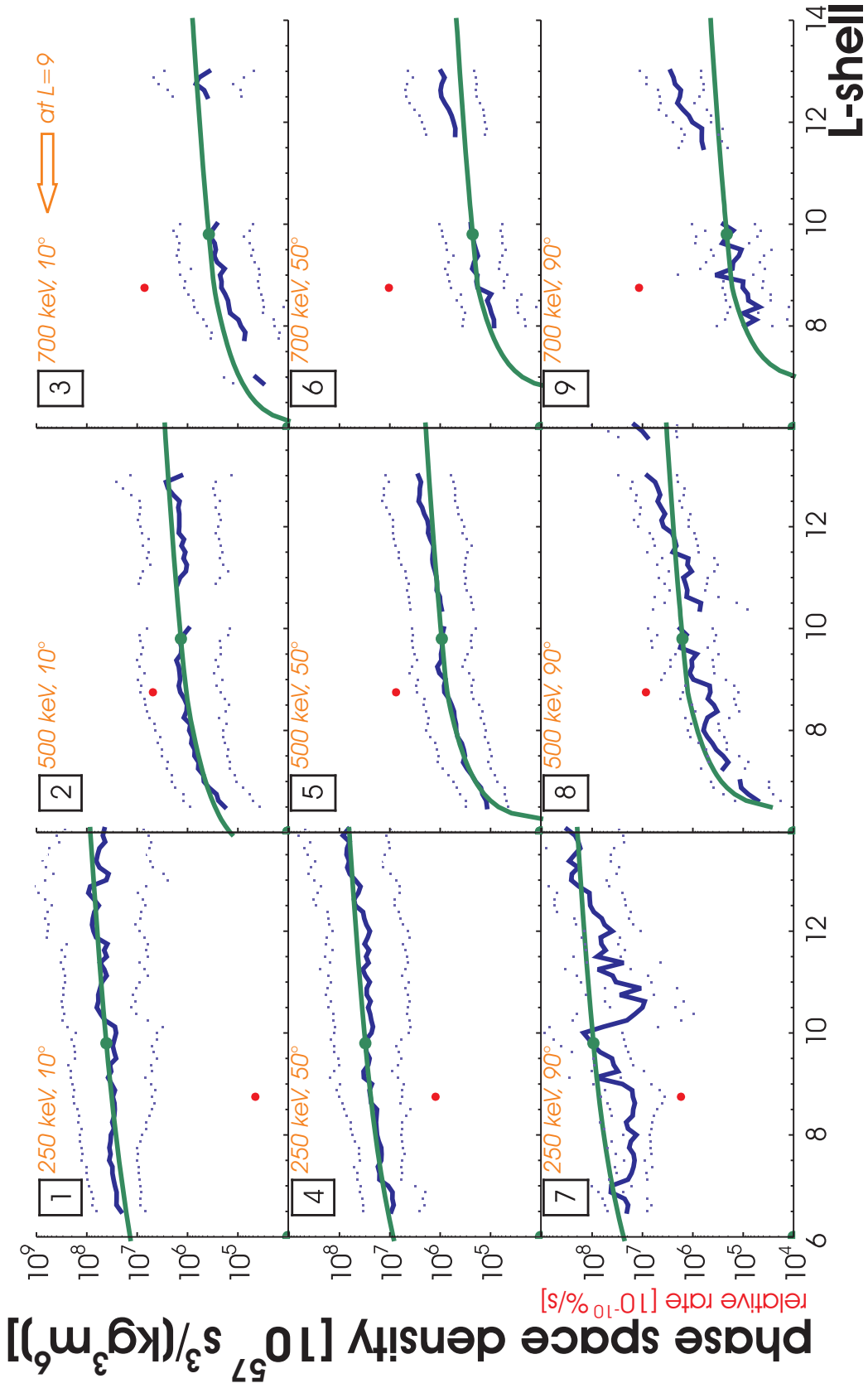


Figure 6.10: Phase space density profiles of the middle magnetosphere at different sets of (μ, K) , and relative loss rates. The two quantities are scaled to be displayed on the same scale. Their units and scaling factors are given in the two labels of the left axis. The values of energy and equatorial pitch angle given in the upper line of each panel are fulfilled at $L_0 = 9$. *Blue lines:* Measurements. *Blue points:* 1σ standard deviation of the mission average. *Green lines:* Model results. *Green points:* Boundary conditions. The green point in the lower corner of each panel represents $f(L = 2.2) = 0$. *Red points:* Value of the relative loss rate at Rhea's orbit. It is zero at all other locations. The model assumptions are given in the text.

2.3.6. We consider the corotation rate also as a free parameter.

Equivalent to our radiation belt model, we again pick nine sets of adiabatic invariants, covering three energies and three pitch angles at Rhea. Since at energies below E_{mr} distributed losses in the Neutral Torus and the E ring might contribute to the decrease in f , only energies above E_{mr} are taken into account.

The model profiles here are not calculated numerically as practiced in the radiation belts in Sec. 5.2 but from the analytical expressions given by Equations (2.38) and (2.57). The inner boundary condition is in all cases $f(L = 2.2) = 0$, meaning that we assume that the outer edge of the Main Rings is a powerful sink. As outer boundary we pick the measured PSD at $L = 9.8$ (at $L = 10$ is a gap due to suspected instrumental background).

Preliminary results are shown in Fig. 6.10. The model reproduces successfully the change in gradient. The change is larger for larger energies and occurs at all pitch angles, as it is observed.

The best parameters found so far are $D_0 = 1.7 \cdot 10^{-6} \text{ s}^{-1}$ at $L_0 = 9$ for the value of the diffusion coefficient, and $n = 1$ for its exponent. The value is equivalent to $D_0 = 660 \cdot 10^{-9} \text{ s}^{-1}$ at $L_0 = 3.5$. A comparison with published diffusion coefficients shown in Fig. 5.9 reveals that this value is consistent with large published values. A loss process that is stronger than used in the model, as caused by scattering to the loss cone (see both Sections 2.3.5 and 2.3.6), would change the value of D_0 but not the shape of the profile. This is because (2.57) only depends on the product of moon lifetime and diffusion coefficient.

The resonance energy between moon and electrons is in the model determined by the corotation fraction. The best value for it is 44 % of rigid corotation, which is very low (Sec. 2.1.2.4). The reason for this might be the fact that the azimuthal drifts at radial distances as large as Rhea's cannot be properly derived from the dipole model (Carbary et al. 2009). Using drifts in the observed magnetic field might allow to reach the same resonance energy (and therefore the same model profile), but for a larger corotation fraction.

Since these are preliminary results we did not check so far if the found parameters are unique and what effect the choice of the outer boundary condition has.

The described model cannot account for the pitch angle dependent overall slope, which is superposed on the gradient-change at Rhea. This is because the diffusion coefficient is assumed as pitch angle independent and because the boundary conditions do not include information about the energy spectrum.

The model profiles can be forced to follow the measured gradients if both boundary conditions are taken from PSD measurements. We managed reproducing the measured profiles also by using two boundary values outside Rhea's orbit. The necessary parameters are completely different and require for example $n = -10$. This does not necessarily contradict the parameters given above because such a model differs from the one above not just by a mathematical detail but by the physical situation. The different boundary conditions do not account for the Main Rings. This can be critical since the rings might affect the PSD profiles even far away from them.

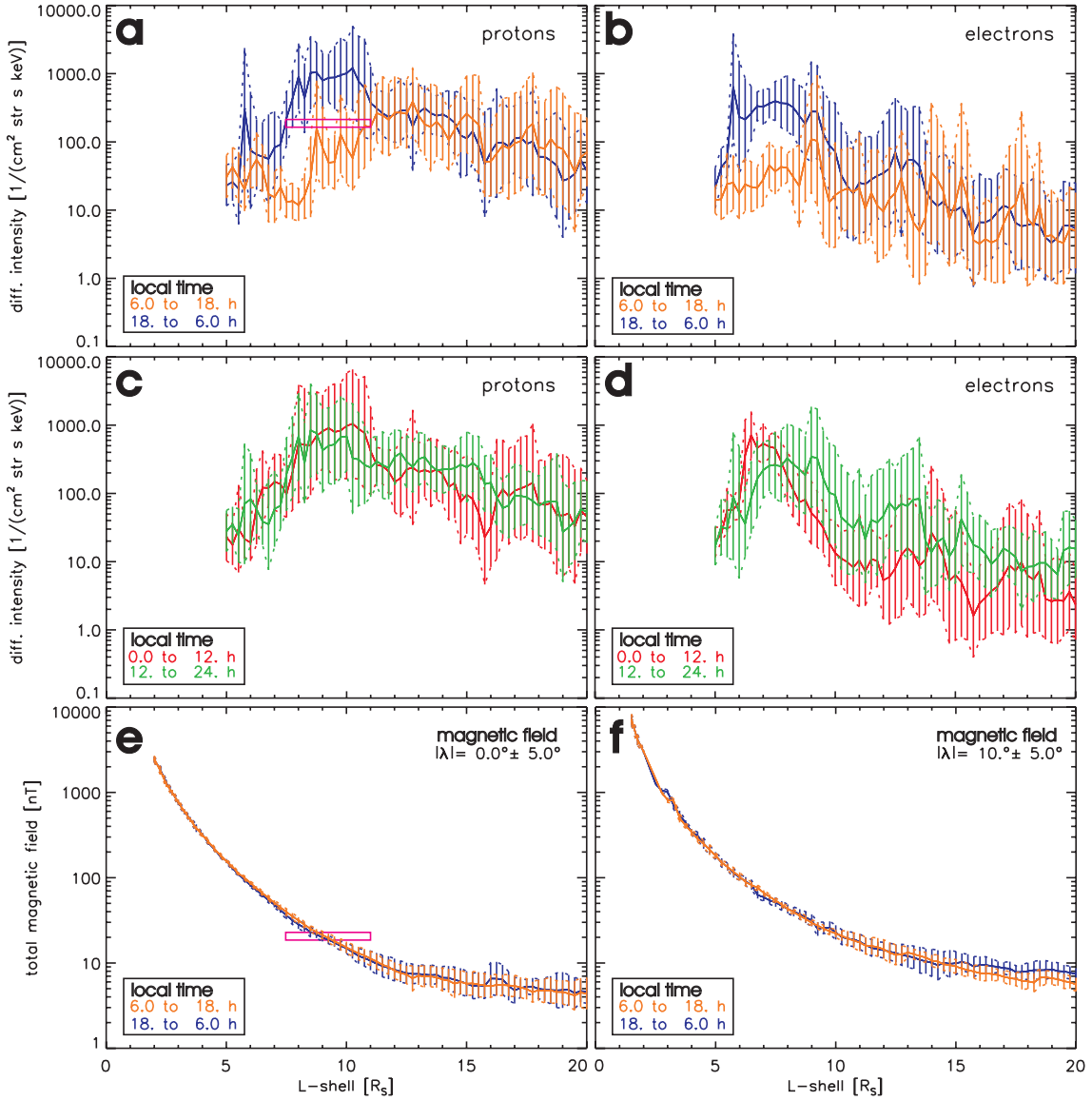


Figure 6.11: Differential intensities and total magnetic field for different local time bins. *Panels a and b:* Differential intensities of protons (left) and electrons (right) split for dayside and nightside of the planet ($9 \text{ h} \gtrless \varphi \gtrless 21 \text{ h}$). *Panels c and d:* Same, but split for dawn and dusk ($0 \text{ h} \gtrless \varphi \gtrless 12 \text{ h}$). Protons have energies of $E = 40 \text{ keV}$, electrons of $E = 118 \text{ keV}$, both are at $\alpha_0 = 80^\circ \pm 10^\circ$ equatorial pitch angle. *Panel e:* Total magnetic field split for dayside and nightside at the magnetic equator. *Panel f:* Same but for latitudes of $\lambda = 10^\circ \pm 5^\circ$. Since the L -shell is calculated purely geometrical, it is possible to convert the x -axis of panel f to radial distance $r = L \cos^2(\lambda) \approx 0.97L$. All values in the figure are logarithmic long-term averages. The right and left end of the pink bar in panel a exemplarily marks L -shells of the dayside and nightside where particle intensities are equal. If the magnetic field would cause the particle asymmetry, the equatorial magnetic field profiles of dayside and nightside should be separated by approximately the same distance. The pink bar in panel e shows that this is not the case.

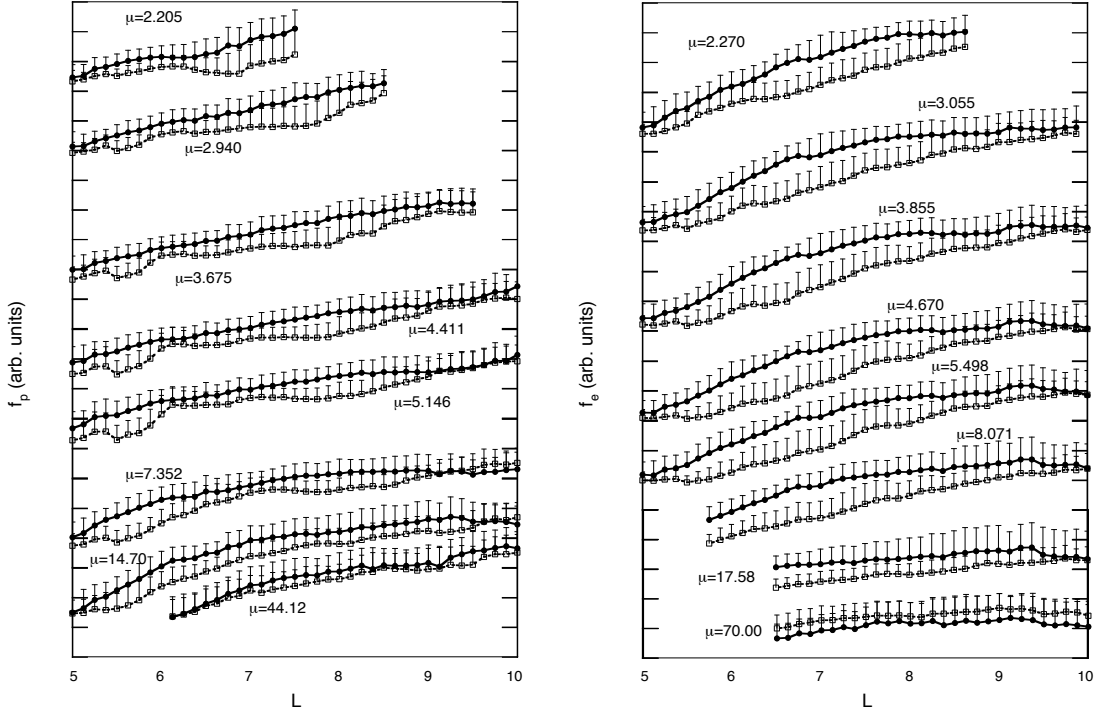


Figure 6.12: Long-term averaged phase space densities of protons (left) and electrons (right). *Full circles*: Bins to the nightside ($18 \text{ h} \leq \varphi \leq 6 \text{ h}$). *Open squares*: Bins to the dayside ($6 \text{ h} \leq \varphi \leq 18 \text{ h}$). Only half of the 1σ error bars is shown. The shown PSD is for values of the first adiabatic invariant μ as labeled in the figure in units of MeV/G. The second invariant is $K = 1.67 \sqrt{GR_S}$, corresponding to $\alpha_0 = 10^\circ$ at $L = 8$. Figure from Thomsen et al. (2011), based on data from this work.

6.3.2 Local time asymmetries

The data set that we introduced in Sec. 4 averages the measurements in local time. This provides a large data set, as it is important to have in case that the fluctuations are as large as here. For the calculation of rates of the various processes, as we did it throughout this thesis, this was sufficient since we were only interested in local time averaged rates.

Indeed, it is known that the proton radiation belts are highly symmetric in local time (Paranicas et al. 2010). However, this is different for energetic electrons at $5 < L < 10$. These particles show higher intensities on the nightside of the planet (Carbary et al. 2009, Paranicas et al. 2010). For this reason, our approach of averaging over all local times yields a simplified configuration of the magnetosphere.

For a more detailed view, we now divide the magnetosphere in two: The upper panels of Fig. 6.11 distinguish between dayside (local time $9 \text{ h} \leq \varphi \leq 21 \text{ h}$) and nightside ($21 \text{ h} \leq \varphi \leq 9 \text{ h}$) of the planet. These profiles are consistent with previous work on electrons. Beyond that they show that protons are distributed in a similar way. Fig. 6.11 only shows this behavior for one energy and pitch angle. However, it extends up to energies of several 100 keV in all pitch angles.

The asymmetry should not arise from poor sampling, since we used large 12 h-wide

local time bins. Dividing the data set into dawnside ($0 \text{ h} \leq \varphi \leq 12 \text{ h}$) and duskside ($12 \text{ h} \leq \varphi \leq 0 \text{ h}$), as it is shown in the middle panels of Figure 6.11, reveals no significant difference of the averaged intensities.

In Fig. 6.12 we convert the data to phase space densities at constant first and second invariant and use smaller local time bins than before. The asymmetry is persistent there. Recently, Thomsen et al. (2011) collected data from several other studies and showed that for example also the plasma temperatures show the same asymmetry, as well as energetic electrons at the outer edge of the Main Rings (Paranicas et al. 2010).

Grodent et al. (2010) demonstrates the existence of a faint outer auroral emission at Saturn's southern polar region, which is stationary on the nightside. This emission maps to a region in the equatorial plane between 4 and $11R_S$. Energetic electrons in this region can provide enough power to explain the brightness of the aurora. We therefore theorize that the asymmetry of the outer aurora is a signature of the energetic electron asymmetry.

One possible cause of the day/night intensity-difference is a non-axisymmetric magnetic field. In case of a steady-state magnetosphere and a purely radial (or absent) electric field, equatorially mirroring energetic particles drift along trajectories of equal magnetic field. If the particles are evenly distributed in drift phase, and no sources or losses occur during a drift period, regions with the same magnetic field show the same intensity of particles (Liouville's theorem, Sec. 2.2.1.1). This means that if the magnetic field is axisymmetric, the regions of equal fields are circles and therefore the particle distribution is symmetric, showing the same intensity at all local times.

If the field is asymmetric, a circle around the planet (like a dipolar L -shell) would have different magnetic field strengths at different local times and therefore different particle intensities. The high intensity at L_1 (arbitrary chosen within $5 < L < 10$) on the nightside would then be the same intensity that is found at $L_2 > L_1$ on the dayside.

We test for an asymmetry in the magnetic field. Fig. 6.11, panel e shows the total magnetic field strength in the equatorial plane as a function of radial distance, split for dayside and nightside. While the particle intensities within $L < 10$ differ significantly between the two halves, this is not the case for the magnetic field. There, the differences for $L < 10$ are small and without trend. Regions (in L and local time) with the same intensity do not have the same magnetic field, which means that at least the long-term averaged magnetic field has no local time asymmetries that are strong enough to cause the observed asymmetry in intensity.

We show in Fig. 6.11 particles with equatorial pitch angles of $\alpha_0 = 80^\circ \pm 10^\circ$ instead of $\alpha_0 \approx 90^\circ$ because we have better statistics for them and achieve therefore a higher certainty that the asymmetry is not just resulting from poor sampling. The disadvantage of this approach is that these particles bounce and do not exactly move on trajectories of equal equatorial magnetic field. This leads to L -shell splitting (Roederer 1970). This term describes the fact that the more field-aligned the particles are and the more asymmetric the magnetic field is, the more the trajectories deviate from the explained case. We neglect this effect here.

Particles with $\alpha_0 = 80^\circ \pm 10^\circ$ bounce up to latitudes of $|\lambda| \approx 10^\circ$. Fig. 6.11, panel f, shows the magnetic field at this latitude split for dayside and nightside. It can be seen that it has a similar high symmetry as the equatorial field. Higher latitudes suffer decreasing statistics, but differences between dayside and nightside show no $|\lambda|$ -trend for $L < 10$ and are supposed to be random.

It could therefore be shown that the magnetic field cannot be responsible for the observed particle asymmetry.

Another possible explanation for it could be a loss mechanism. There is evidence that neutral gas around Saturn is indeed unevenly distributed in local time (Shemansky and Hall 1992, Melin et al. 2009) and this is also expected for the E ring (Juhász and Horányi 2004). If the asymmetry in the density is stationary in local time and the loss occurs on time scales much faster than the drift period, this would cause an asymmetry in energetic particle intensities. However, the Neutral Torus density is not stationary but densest close to Enceladus (Cassidy and Johnson 2010, Perry et al. 2010). Also, the orbit period of energetic particles (beside quasi-resonant electrons) at $L = 10$ is $< 10^5$ s and therefore faster than any loss process in the neutral material (see Fig. 6.2). Additionally, one has to take into account that the interaction of protons and electrons with matter is different in mechanism and strength. It would be a large coincidence if these different processes are causing asymmetries for both species of likewise extend at similar energies. Therefore, asymmetries in losses due to E ring or Neutral Torus should not account for the asymmetry.

The day/night asymmetry can also be caused by a source at the nightside (Paranicas et al. 2010). Injection events frequently occur in the L -range of the asymmetry and can act as a source. They mainly originate at the night and morning quadrant of the planet (Sec. 2.2.3). After occurrence, their intensity is deceasing due to losses and dispersion. If this decrease is significant over half a drift period around Saturn, then injections could account for the asymmetry. This is not explored so far.

Finally, the asymmetry can follow from an electric field that is not purely radial but has a component along the noon-to-midnight direction. This then modifies systematically the drift paths of energetic particles in the same way as it was discussed above for an asymmetric magnetic field.

The electric-field theory is supported by the fact that electron microsignatures are often not observed along the orbit of the moon that caused them but are displaced, typically by less than $1R_S$ (Roussos et al. 2005, Andriopoulou et al. 2012). This kind of asymmetry cannot be explained by the theories described above.

These and all other observed asymmetries complied by Thomsen et al. (2011), including the PSDs shown here, can be explained by the same electric field. The necessary field strengths to reproduce the various observations are found to be roughly consistent: The strength decreases with increasing distance from Saturn from ≈ 1.5 mV/m at $L = 2$ to ≈ 0.1 mV/m at $L = 10$ (Thomsen et al. 2011).

Summary

In this thesis, energetic proton and electron measurements in Saturn's magnetosphere within an energy range from several 10 keV to several 10 MeV are used (Sec. 4), which are obtained by the MIMI/LEMMS instrument onboard the Cassini spacecraft. As tools to analyze the data, mathematical expressions are utilized that describe a large range of physical processes relevant for energetic particles in Saturn's magnetosphere (Sec. 2). These expressions are either used to model radial particle profiles (Sec. 5.2) or to compare the importance of various processes (Sec. 6.2). This combination of measurements and theory allows to answer several fundamental questions regarding Saturn's magnetosphere.

How do energetic particles distribute around Saturn?

The data included in this thesis covers seven years of the Cassini mission, equivalent to 145 orbits, which provides an unprecedented good statistics. These data are averaged to bins in L -shell and equatorial pitch angle and are organized in several useful ways: as radial profiles at constant energy or at constant first and second adiabatic invariant, as energy spectra, and pitch angle distributions (Sec. 4).

The magnetosphere can be organized in radiation belts (within $5R_S$ distance to Saturn), and the middle and outer magnetosphere (Fig. 6.1). The phase space density at constant first and second adiabatic invariant is generally decreasing towards Saturn, except in the radiation belts (Fig. 4.8). These are separated by the orbits of the inner moons. The phase space density at dipole L -shells roughly between 5 and 10 is enhanced on Saturn's nightside (Fig. 6.12). The particle intensity is generally decreasing towards higher energies (Fig. 4.4). The most important exception is a peak around proton energies of 10 MeV.

The magnetosphere is highly dynamic and fluctuates around its average state. Outside of the radiation belts, the standard deviation of the averaged data can extend over up to two orders of magnitude (Fig. 4.1). The proton belts are relatively stable, but vary slowly over the solar cycle (Fig. 5.11).

Why do the particles distribute in the observed way?

Since both the energetic particles and the icy moons encircle Saturn, they regularly encounter each other, causing the moons to absorb the particles. This process is so efficient within the radiation belts that the single belts become strictly separated by the moon orbits (Fig. 5.4). A minor particle depletion is additionally caused by the G ring and/or its arc.

The moons outside the radiation belts do not yield such strict separations. Although moons barely change the phase space density of the particle population along their orbits, they can change the PSD gradient and contribute to the general decrease of the phase space density towards Saturn. This follows from the fact that different regions of the magnetosphere are coupled via radial diffusion or by other means of transport. A distinct

gradient change is clearly visible for electrons around the orbit of Rhea (Fig. 4.8). There are indications that protons are affected in a similar way.

Protons below 100 keV are additionally depleted by charge exchange losses in the gas of the Neutral Torus. Since its density increases towards $L = 4$, this contributes to the general decrease in PSD towards Saturn. In the absence of moons and gas, the PSD decrease is caused by the combination of radial diffusion and the shape of the energy spectrum (Sec. 6.3).

The most probable theory to explain the enhanced phase space density on the nightside is the presence of a noon-to-midnight electric field. This field causes that the particles do not drift along dipole L -shells anymore. In case that more meaningful L -shells were used, which account for this electric field, the apparent asymmetry would vanish (Sec. 6.3.2).

Where do the energetic particles come from in the first place?

Protons at and above 10 MeV in the radiation belts derive from the cosmic ray albedo of Saturn's Main Rings (Fig. 5.12) and/or its atmosphere, followed by the decay of secondary neutrons. Protons below these energies derive at least in part from the cosmic ray albedo of Saturn's atmosphere (Sec. 5.3.1). Both processes are abbreviated as CRAND. We were able to exclude other possibilities as ENA stripping and radial diffusion (Sec. 5.3).

Energetic particles at least in the loss region of the middle magnetosphere, maybe throughout the entire middle and outer magnetosphere, are provided by a source process that might be injection events (Fig. 6.6). Such events transport particles at low energies and large L radially inward, heating them in the process to the observed high energies.

Which processes govern the evolution and distribution of energetic particles?

The main processes in the proton radiation belts are the source process, which includes CRAND, and radial diffusion. Diffusion drives the protons towards the orbits of the moons, where they are absorbed. Distributed losses from the Neutral Torus and the E ring do not play a significant role (Fig. 5.10).

Using a model we were able to determine parameters of the processes acting throughout the proton belts. We found that the radial diffusion coefficient is well described with a function $\propto L^{10}$ and a value that is close to the one of electrons: $0.3 \cdot 10^{-9} \text{ s}^{-1}$ at $L_0 = 3.5$. Both diffusion and source deplete, respectively provide, PSD with rates ranging from 10^{-7} %/s to 10^{-5} %/s , depending on L -shell (Fig. 5.10). The model prefers if the peak density of the Neutral Torus is 10^9 m^{-3} of H_2O , which is at the lower edge of expectations from literature. It also prefers a fast radial decay inward: one order of magnitude within $1R_S$ (Tab. 5.1).

Around $L = 7$, which is within the loss region of the middle magnetosphere, protons below 1 MeV are mainly lost due to charge exchange with the Neutral Torus. The lifetime for 10 keV protons is on the order of days and rises to several years at 1 MeV (Fig. 6.2). The E ring does not play a major role: The lifetimes in this ring range from years to hundreds of years. At energies above 1 MeV, energy loss in gas is dominating (Fig. 5.3). Interestingly, energy loss does not necessarily reduce the intensity within an energy interval, as sampled by a particle instrument. Depending for example on the spectral shape, it can, on the contrary, enhance the intensity. For energy loss in gas this is the case around 100 keV (Fig. 5.3).

While radial diffusion was depleting the radiation belts, it causes a net gain at $L = 7$. This gain, however, is not fast enough to counter the loss from charge exchange. We hypothesize that injection events provide the missing particles. The dominant processes then would be charge exchange and injections. The rates of these processes range from 10^{-3} %/s to 10^{-6} %/s , depending on energy (Fig. 6.6).

Electrons at $L = 7$ are affected both by energy loss in the gas of the Neutral Torus and in the water ice grains of the E ring, although the effect of the gas tends to be stronger. Energy loss in grains is enhancing the electron intensity throughout the covered energy range (Fig. 6.2).

In order to counter the source of diffusion and injections, it can be hypothesized that electrons are additionally lost because they are scattered in gas and grains until their pitch angle is so field-aligned that they become lost to Saturn's atmosphere (Sec. 6.2.7). The dominant processes in this case are loss from scattering, and sources from injections and/or radial diffusion (Tab. 6.1).

At larger distances, different processes might be important. Distributed losses from charge exchange or scattering lose their importance since the gas and grain densities are decaying with distance. The PSD profiles might be consistent with radial diffusion, but we are not aware of a diffusion mechanism that would have the necessary properties. We therefore hypothesize that radial diffusion is not the only process that is important in this region (Sec. 6.3).

Outlook

Although there was a tremendous amount of work going into this thesis, there are still many possibilities to refine the results and expand the physics.

The mission-averaged data set can be improved by using an advanced magnetic field model that even adapts to local season and solar wind pressure and that represents the magnetic field better. Also, there are efforts ongoing to modify the LEMMS calibration, which can yield more precise intensities, energies, and pitch angles. By subtracting the measurements of different channels from each other it might even be possible to compensate for the radiation belt background. This would allow for an easier and more confident analysis especially of the electron radiation belts, which were barely considered throughout this work.

Energy and pitch angle diffusion should be included in a quantitative way in our studies. Appropriate diffusion coefficients became recently available to us (L. Lorenzato, priv. comm., 2011). As a first step, the resulting rates can be estimated. In case that they are significant relative to the other processes, it would be fruitful to include more diffusive processes for example in the radiation belt model and to constrain the diffusion coefficients by optimization of the model parameters.

Our conclusion that the radiation belts are at least in part supplied by atmospheric CRAND was mostly based on argumentation. GEANT4 simulations of cosmic rays impacting a model atmosphere would allow to quantify the production rates of neutrons at different energies. CRAND from the rings could be studied by analyzing orbits where Cassini was flying over the Main Rings. (This occurred only during SOI so far but will be repeated several times towards the end of the mission.) Since particles bouncing through

Summary

the rings would be efficiently lost, most detected particles should just have been created from CRAND. This then could be used to probe the Main Rings. However, it would be difficult to distinguish these weak signals from instrumental background.

There is an increased interest in Jupiter because the Juno spacecraft (also referred to as Jupiter Polar Orbiter) will arrive there 2016. Also ESA studies a mission to this planet, which is called JUICE (Jupiter Icy Moon Explorer), formerly known as EJSM/ Laplace. This provides an opportunity to study old data from the energetic particle detector (EPD) onboard the Galileo spacecraft by adapting the methods that were described here. EPD is very similar to LEMMS and the data are available to us. The analysis can prepare for scientific analysis of upcoming data and even support the new spacecraft design: Since the particles measured by EPD contribute to the radiation dose of the spacecraft, their knowledge is crucial.

A Used LEMMS channels

Channel	Low	High	Mid	Channel	Low	High	Mid
A5	506	805	638	E3	600	4950	1723
A6	805	1600	1135	E4	790	4750	1937
A7	1615	4000	2542	E6	1600	21000	5797
P2	2280	4492	3200	E7	7000	20000	11832
P3	4491	5744	5079	E1_19	24.20	26.00	25.07
P5	8311	11449	9755	E1_20	26.00	27.70	26.82
P6	11474	13433	12415	E1_21	27.70	29.50	28.57
P7	12101	58902	26698	E1_22	29.50	31.20	30.32
P8	25185	59000	38548	E1_23	31.20	33.00	32.06
A_13	33.00	34.60	33.81	E1_24	33.00	35.60	34.24
A_14	34.60	36.20	35.42	E1_25	35.60	38.20	36.86
A_15	36.20	37.90	37.04	E1_26	38.20	40.80	39.48
A_16	37.90	39.50	38.66	E1_27	40.80	43.40	42.11
A_17	39.50	41.10	40.27	E1_28	43.40	46.10	44.73
A_18	41.10	44.30	42.67	E1_29	46.10	48.70	47.35
A_19	44.30	47.60	45.91	E1_30	48.70	52.20	50.40
A_20	47.60	50.80	49.14	E1_31	52.20	55.70	53.90
A_21	50.80	54.00	52.38	E1_32	55.70	59.20	57.40
A_22	54.00	57.20	55.61	E1_33	59.20	63.50	61.32
A_23	57.20	60.50	58.84	E1_34	63.50	67.90	65.69
A_24	60.50	65.30	62.86	E1_35	67.90	72.30	70.06
A_25	65.30	70.20	67.71	E1_36	72.30	76.70	74.43
A_26	70.20	75.00	72.56	E1_37	76.70	81.90	79.23
A_27	75.00	79.90	77.41	E1_38	81.90	88.00	84.90
A_28	79.90	84.70	82.26	E1_39	88.00	94.10	91.02
A_29	84.70	89.60	87.11	E1_40	94.10	100.00	97.14
A_30	89.60	96.00	92.74	E1_41	100.00	107.00	103.69
A_31	96.00	102.00	99.21	E1_42	107.00	114.00	110.68
A_32	102.00	109.00	105.68	E1_43	114.00	122.00	118.10
A_33	109.00	117.00	112.93	E1_44	122.00	133.00	127.23
A_34	117.00	125.00	121.01	E1_45	133.00	140.00	136.04
A_35	125.00	133.00	129.10	E1_46	140.00	150.00	144.73
A_36	133.00	141.00	137.18	E1_47	150.00	161.00	155.22
A_37	141.00	151.00	146.05	E1_48	161.00	171.00	165.72
A_38	151.00	162.00	156.53	E1_49	171.00	182.00	176.21

A Used LEMMS channels

A_39	162.00	174.00	167.85	E1_50	182.00	196.00	188.39
A_40	174.00	185.00	179.17	E1_51	196.00	206.00	200.69
A_41	185.00	198.00	191.27	F1_26	200.00	213.00	206.19
A_42	198.00	211.00	204.20	F1_27	213.00	226.00	219.52
A_43	211.00	225.00	217.92	F1_28	226.00	240.00	232.84
A_44	225.00	245.00	234.81	F1_29	240.00	253.00	246.17
A_45	245.00	258.00	251.08	F1_30	253.00	271.00	261.65
A_46	258.00	277.00	267.15	F1_31	271.00	288.00	279.42
A_47	277.00	296.00	286.56	F1_32	288.00	306.00	297.19
A_48	296.00	316.00	305.96	F1_33	306.00	328.00	317.11
A_49	316.00	335.00	325.36	F1_34	328.00	351.00	339.32
A_50	335.00	361.00	347.89	F1_35	351.00	373.00	361.53
A_51	361.00	380.00	370.63	F1_36	373.00	395.00	383.74
A_52	380.00	406.00	393.16	F1_37	395.00	422.00	408.10
A_53	406.00	432.00	419.03	F1_38	422.00	453.00	436.90
A_54	432.00	464.00	448.03	F1_39	453.00	484.00	468.00
A_55	464.00	497.00	480.37	F1_40	484.00	515.00	499.10
A_56	497.00	529.00	512.71	F1_41	515.00	550.00	532.34
A_57	529.00	568.00	548.17	F1_42	550.00	586.00	567.88
A_58	568.00	600.00	583.84	F1_43	586.00	626.00	605.57
A_59	600.00	645.00	622.44	F1_44	626.00	679.00	651.98
A_60	645.00	684.00	664.58	F1_45	679.00	715.00	696.69
A_61	684.00	736.00	709.64	F1_46	715.00	768.00	740.84
A_62	736.00	781.00	758.25	F1_47	768.00	821.00	794.15
				F1_48	821.00	875.00	847.46
				F1_49	875.00	928.00	900.77
				F1_50	928.00	999.00	962.66
				F1_51	999.00	1050.00	1025.13
				F1_52	1050.00	1120.00	1087.06
				F1_53	1120.00	1190.00	1158.14
				F1_54	1190.00	1280.00	1237.80
				F1_55	1280.00	1370.00	1326.66
				F1_56	1370.00	1460.00	1415.50
				F1_57	1460.00	1570.00	1512.94
				F1_58	1570.00	1660.00	1610.95

Table A.1: LEMMS channels that are used in this thesis. The left channels measure ions, the right ones measure electrons. In case of the ion channels, the values are valid for protons. Channels with an underscore in the name are PHA channels. *Low* and *high* are the energy range in keV where the channel sensibility is largest (Haggerty and Livi 2004). The *mid* energy is the logarithmic average of the range boundaries.

B Nomenclature

Variable	Explanation
A	area
$\vec{\mathcal{A}}$	magnetic vector potential
α	local pitch angle
α_0	equatorial pitch angle
B	magnetic field
β	velocity normalized to light speed, $\beta = v/c$
c	speed of light
dE/dx	differential energy change per distance traveled in a given material
$\delta f/\delta t$	rate of PSD change per time due to non-diffusive processes
$\partial f/\partial t$	total rate of PSD change, or residuum of a steady-state solution of (2.56)
D_0	radial diffusion coefficient at L_0
\tilde{D}_0	radial diffusion coefficient at L_0 divided by L_0^n
$\tilde{D}f$	diffusion rate, see (2.56)
D_{LL}	radial diffusion coefficient
Δ_1	deviation of all model profiles of Fig. 5.4 to the measurements
Δ_2	deviation of the model profile in Panel 1 of Fig. 5.4 to measurements
e	elementary charge
E	kinetic energy, $E = E_{\text{tot}} - mc^2 \approx mv^2/2$
E_{tot}	total energy from mass and velocity, $E_{\text{tot}} = myc^2 \approx mc^2$, $E_{\text{tot}}^2 = p^2c^2 - m^2c^4$
E_0	kinetic energy where S_0 is given
E_c	vertical cutoff energy, see (2.28) and (2.29)
E_{mr}	energy where electrons have no relative azimuthal velocity to a moon
f	phase space density of energetic particles, see (4.3)
\tilde{f}	phase space density of energetic particles measured within their mirror points
$\langle f \rangle$	channel-averaged phase space density, see (2.70)
γ	Lorentz factor, $\gamma = 1/\sqrt{1-v^2/c^2}$
γ_j	the differential intensity can scale as $j \propto E^{-\gamma_j}$
γ_f	the PSD and the proton source rate scale as $\propto E^{-\gamma_f}$, $\gamma_f \approx \gamma_j + 1$
H	height of the E ring or of the Neutral Torus
h_r	average sum of the sizes of all encountered ice grains during a ring passage
μ	first adiabatic invariant, see (2.16)
j	differential intensity, see (4.1)
j_n	differential intensity of neutrons

j_u	$1 \text{ cm}^{-2} \text{s}^{-1} \text{str}^{-1} \text{keV}^{-1}$
\vec{j}	current density
K	second adiabatic invariant, see (2.20)
λ	magnetic latitude, measured from magnetic equator
λ_m	magnetic mirror latitude
L	magnetic dipole L -shell
L_0	L -shell where D_0 and S_0 are given
L_i	a L -shell inside of Enceladus' orbit
L_p	L -shell where the Neutral Torus has its peak
L_d	L -shell where H_2O and O have the same number density
L_M	semimajor axis of a moon in units of R_S
m	rest mass
m	the source rate scales with $\propto L^{-m}$
M	number of encounters to enter or leave an energy range, see (2.69) and (2.68)
n	energetic particle or plasma number density
n	diffusion exponent, $D_{LL} \propto L^n$
n_g	gas number density in the Neutral Torus
n_j	gas number density of species j in the Neutral Torus
n_r	number density of ice grains in a ring
n_q	charge density, see Sec. 2.1.1.3
n_i	H_2O number density at L_i
n_p	H_2O number density at L_p
n_d	H_2O and O number density at L_d
\tilde{n}	path-averaged number density, see (2.63)
N	particle number
ω	angular frequency/velocity, $\omega = 2\pi/T = v/r$
p	momentum, $p = m\gamma v \approx mv$
\tilde{p}	pressure
P	describes electromagnetic fluctuations in a magnetosphere, see (2.43)
\mathcal{P}	ENA production of the magnetosphere, see (5.13)
φ	local time or azimuth angle
ϕ	gyro phase
Φ	magnetic flux
σ	interaction or geometric cross section
$\tilde{\mathcal{P}}$	produced ENAs that reach a radiation belt
q	electric charge
r	radial distance, usually from Saturn's center
\vec{r}_c	radius of magnetic curvature
r_g	gyro radius
r_r	radius of ice grains
r_M	moon radius
R_S	Saturn radius (60268 km)
$\bar{\rho}$	column mass density, see (5.10)

S_0	source rate at E_0 and L_0
T_B	bounce time
T_g	gyro period
ϑ	co-latitude, measured from north pole, $\vartheta = \pi/2 - \lambda$
θ	scattering angle
Θ	step function
v	velocity of energetic particles, never a frequency "nu"
\tilde{v}	effective velocity, defined in (2.67)
v_{mass}	velocity of a mass/plasma flow, see Sec. 2.1.1.2
e_M	eccentricity of a moon orbit
E_c	cutoff energy
\emptyset	diameter

Table B.1: Explanation of used variables.

Abbreviation	Explanation
CE	Charge Exchange
CHEMS	CHARGE-Energy-Mass Spectrometer
CRAND	Cosmic Ray Albedo Neutron Decay
ENA	Energetic Neutral Atom
eV	electron volts
FWHM	Full Width at Half Maximum
GCR	Galactic Cosmic Rays
GEANT-4	GEometry ANd Tracking toolkit version 4
IMF	Interplanetary Magnetic Field
INCA	Ion and Neutral CAmera
LECP	Low Energy Charged Particle instrument, on board of the Voyagers
LEMMS	Low Energy Magnetospheric Measurement System, main instrument here
LT	Local Time, describes an azimuthal position
MAG	cassini MAGnetometer
MIMI	Magnetosphere Imaging System
PA	Pitch Angle
PAD	Pitch Angle Distribution
PHA	Pulse Height Analyzer, type of LEMMS channel
PSD	Phase Space Density
SOI	Saturn Orbit Insertion
SSD	Solid State Detector
TOF	Time Of Flight

Table B.2: Explanation of used abbreviations.

Term	Explanation
channel lifetime	time to enter or leave the energy interval of an instrument channel
differential intensity	particles per time, area, solid angle, energy interval depends here usually on E , α_0 , and L
diffusion region	outer part of the middle magnetosphere, $L \gg 7$ region where distributed losses are unimportant
energy lifetime	time to enter or leave an infinitesimal energy interval
global lifetime	time until a particle is stopped or converted to another species
number density	number of particles per volume in real space
L -shell	in the equatorial plane equal to the radial distance in multiples of R_S follows at higher latitudes the magnetic field line
local time	describes an azimuthal position 0 h is aligned midnight meridian, 12 h with the noon meridian
loss region	inner part of the middle magnetosphere, $L \leq 7$ region with the same dominant processes as around $L = 7$
Main Rings	Saturn's dense rings A, B, C, and F outer edge at $2.33R_S$
middle magnetosphere	outside the radiation belts but still relatively dipolar
Neutral Torus	neutral gas distribution that peaks near Enceladus' orbit
outer magnetosphere	non-dipolar region
phase space density	number of particles per volume in phase space depends here usually on μ , K , and L
radial profile	profile as a function of L
relative rate	rate normalized to the observed value, inverse to a lifetime
stopping power	differential energy loss per distance
spectrum	short for energy spectrum
water group	water ions and derivative products O^+ , OH^+ , H_2O^+ , H_3O^+
(1.2)	equation with number 1.2
1.2	Section 1.2 or a figure with this number
$\vec{x}\vec{y}$	scalar product between two vectors

Table B.3: Explanation of special terms.

Bibliography

- Abel, B., Thorne, R. M., 1998, Electron scattering loss in Earth's inner magnetosphere 1. Dominant physical processes, *J. Geophys. Res.*, 103, 2385–2396
- Agostinelli, S., et al., 2003, Geant4 - a simulation toolkit, *Nuc. Instr. Meth.*, 506, 250–303
- Alfvén, H., Fälthammar, C.-G., 1963, *Cosmical Electrodynamics: Fundamental Principles*, Oxford University Press, Oxford, U.K., 2nd edn.
- Andriopoulou, M., Roussos, E., Krupp, N., Paranicas, C., Thomsen, M., Krimigis, S., Dougherty, M. K., Glassmeier, K.-H., 2012, A noon-to-midnight electric field and nightside dynamics in Saturn's inner magnetosphere, using microsignature displacements, *Icarus*, in press
- Armstrong, T. P., Paonessa, M. T., Bell, II, E. V., Krimigis, S. M., 1983, Voyager observations of Saturnian ion and electron phase space densities, *J. Geophys. Res.*, 88, 8893–8904
- Armstrong, T. P., Taherion, S., Manweiler, J., Krimigis, S., Paranicas, C., Mitchell, D., Krupp, N., 2009, Energetic ions trapped in Saturn's inner magnetosphere, *Planet. Space Sci.*, 57, 1723–1731
- Arridge, C. S., Khurana, K. K., Russell, C. T., Southwood, D. J., Achilleos, N., Dougherty, M. K., Coates, A. J., Leinweber, H. K., 2008a, Warping of Saturn's magnetospheric and magnetotail current sheets, *J. Geophys. Res.*, 113, A08217
- Arridge, C. S., Russell, C. T., Khurana, K. K., Achilleos, N., Cowley, S. W. H., Dougherty, M. K., Southwood, D. J., Bunce, E. J., 2008b, Saturn's magnetodisc current sheet, *J. Geophys. Res.*, 113, A04214
- Badman, S. V., Cowley, S. W. H., 2007, Significance of Dungey-cycle flows in Jupiter's and Saturn's magnetospheres, and their identification on closed equatorial field lines, *Ann. Geophys.*, 25, 941–951
- Bagal, F., Delamere, P. A., 2011, Flow of mass and energy in the magnetospheres of Jupiter and Saturn, *J. Geophys. Res.*, 116, A05209
- Balogh, A., Beek, T. J., Forsyth, R. J., Hedgecock, P. C., Marquedant, R. J., Smith, E. J., Southwood, D. J., Tsurutani, B. T., 1992, The magnetic field investigation on the ULYSSES mission - Instrumentation and preliminary scientific results, *A&AS*, 92, 221–236

Bibliography

- Barnett, C. F., Hunter, H. T., Fitzpatrick, M. I., Alvarez, I., Cisneros, C., Phaneuf, R. A., 1990, Atomic data for fusion. Volume 1: Collisions of H, H₂, He and Li atoms and ions with atoms and molecules, NASA STI/Recon Technical Report N, 911, 13 238
- Bartlett, S. C., 2011, Magnetospheres of Outer Planets, Illustrations, <http://lasp.colorado.edu/>
- Baumjohann, W., Treumann, R. A., 1996, Basic space plasma physics, Imperial College Press, London, UK
- Beckmann, U., 2008, Dynamik von Staubteilchen in Saturns E-Ring, Ph.D. thesis, Ruprecht-Karls Universität Heidelberg, Heidelberg, Germany
- Bell, E. V., Armstrong, T. P., 1986, Monte Carlo simulation of charged particle impact on the satellites of Jupiter and Saturn, *J. Geophys. Res.*, 91, 1397–1403
- Berger, M. J., Coursey, J. S., Zucker, M. A., Chang, J., 2005, Stopping-Power and Range Tables for Electrons, Protons, and Helium Ions, The National Institute of Standards and Technology (NIST), <http://www.nist.gov/physlab/data/star>
- Bethe, H., 1930, Zur Theorie des Durchgangs schneller Korpuskularstrahlen durch Materie, *Ann. Phys.*, 397, 325–400
- Bethge, K., Walter, G., Wiedemann, B., 2001, Kernphysik - Eine Einführung, Springer Verlag, Heidelberg, Germany, 2nd edn.
- Beutier, T., Boscher, D., 1995, A three-dimensional analysis of the electron radiation belt by the Salammbô code, *J. Geophys. Res.*, 100, 14 853–14 862
- Beutier, T., Boscher, D., France, M., 1995, SALAMMBO: A three-dimensional simulation of the proton radiation belt, *J. Geophys. Res.*, 100, 17 181–17 188
- Bhardwaj, A., Randall Gladstone, G., Elsner, R. F., Østgaard, N., Hunter Waite, J., Cravens, T. E., Chang, S.-W., Majeed, T., Metzger, A. E., 2007, First terrestrial soft X-ray auroral observation by the Chandra X-ray Observatory, *J. of Atm. Sol.-Terrest. Phys.*, 69, 179–187
- Birn, J., Priest, E. R., 2007, Reconnection of magnetic fields : magnetohydrodynamics and collisionless theory and observations, Cambridge University Press, Cambridge, UK
- Bishop, J., 1996, Multiple charge exchange and ionization collisions within the ring current-geocorona-plasmasphere system: Generation of a secondary ring current on inner L shells, *J. Geophys. Res.*, 1011, 17 325–17 336
- Blake, J. B., Hilton, H. H., Margolis, S. H., 1983, On the injection of cosmic ray secondaries into the inner Saturnian magnetosphere. I - Protons from the CRAND process, *J. Geophys. Res.*, 88, 803–807
- Borovsky, J. E., Nemzek, R. J., Belian, R. D., 1993, The occurrence rate of magnetospheric-substorm onsets - Random and periodic substorms, *J. Geophys. Res.*, 98, 3807–3813

- Brice, N. M., McDonough, T. R., 1973, Jupiter's radiation belts, *Icarus*, 18, 206–219
- Burger, M. H., Sittler, E. C., Johnson, R. E., Smith, H. T., Tucker, O. J., Shematovich, V. I., 2007, Understanding the escape of water from Enceladus, *J. Geophys. Res.*, 112, 6219
- Carbary, J. F., Mitchell, D. G., Brandt, P., Roelof, E. C., Krimigis, S. M., 2008, Track analysis of energetic neutral atom blobs at Saturn, *J. Geophys. Res.*, 113, A01 209
- Carbary, J. F., Mitchell, D. G., Krupp, N., Krimigis, S. M., 2009, L shell distribution of energetic electrons at Saturn, *J. Geophys. Res.*, 114, 9210
- Carbary, J. F., Achilleos, N., Arridge, C. S., Khurana, K. K., Dougherty, M. K., 2010, Global configuration of Saturn's magnetic field derived from observations, *Geophys. Res. Lett.*, 37, 21 806
- Carbary, J. F., Mitchell, D. G., Paranicas, C., Roelof, E. C., Krimigis, S. M., Krupp, N., Khurana, K., Dougherty, M., 2011, Pitch angle distributions of energetic electrons at Saturn, *J. Geophys. Res.*, 116, A01 216
- Cassidy, T. A., Johnson, R. E., 2010, Collisional spreading of Enceladus' neutral cloud, *Icarus*, 209, 696–703
- Charnoz, S., Dones, L., Esposito, L. W., Estrada, P. R., Hedman, M. M., 2009, Origin and Evolution of Saturn's Ring System, in *Saturn from Cassini-Huygens*, (Ed.) Dougherty, M. K., Esposito, L. W., & Krimigis, S. M., p. 537, Springer Science+Business Media B.V., Heidelberg, Germany
- Chen, F. F., 1984, *Introduction to Plasma Physics and Controlled Fusion Volume 1: Plasma Physics*, Second Edition, Plenum Press, New York, USA
- Chen, Y., Hill, T. W., 2008, Statistical analysis of injection/dispersion events in Saturn's inner magnetosphere, *J. Geophys. Res.*, 113, 7215
- Chen, Y., Hill, T. W., Rymer, A. M., Wilson, R. J., 2010, Rate of radial transport of plasma in Saturn's inner magnetosphere, *J. Geophys. Res.*, 115, A10 211
- Clarke, J. T., Grodent, D., Cowley, S. W. H., Bunce, E. J., Zarka, P., Connerney, J. E. P., Satoh, T., 2004, Jupiter's aurora, in *Jupiter. The Planet, Satellites and Magnetosphere*, (Ed.) Bagenal, F., Dowling, T. E., & McKinnon, W. B., pp. 639–670, Cambridge University Press, Cambridge, U.K.
- Colwell, J. E., Nicholson, P. D., Tiscareno, M. S., Murray, C. D., French, R. G., Marouf, E. A., 2009, The Structure of Saturn's Rings, in *Saturn from Cassini-Huygens*, (Ed.) Dougherty, M. K., Esposito, L. W., & Krimigis, S. M., p. 375, Springer Science+Business Media B.V., Heidelberg, Germany
- Connerney, J. E. P., Acuna, M. H., Ness, N. F., 1981, Saturn's ring current and inner magnetosphere, *Nature*, 292, 724–726

Bibliography

- Cooper, J. F., 1983, Nuclear cascades in Saturn's rings - Cosmic ray albedo neutron decay and origins of trapped protons in the inner magnetosphere, *J. Geophys. Res.*, 88, 3945–3954
- Cooper, J. F., Simpson, J. A., 1980, Sources of high-energy protons in Saturn's magnetosphere, *J. Geophys. Res.*, 85, 5793–5802
- Cowley, S., Bunce, E., Prangé, R., 2004, Saturn's polar ionospheric flows and their relation to the main auroral oval, *Ann. Geophys.*, 22, 1379–1394
- Cravens, T. E., Ozak, N., Richard, M. S., Campbell, M. E., Robertson, I. P., Perry, M., Rymer, A. M., 2011, Electron energetics in the Enceladus torus, *J. Geophys. Res.*, 116, A09205
- Cuzzi, J., Clark, R., Filacchione, G., French, R., Johnson, R., Marouf, E., Spilker, L., 2009, Ring Particle Composition and Size Distribution, in *Saturn from Cassini-Huygens*, (Eds.) M. K. Dougherty, L. W. Esposito, S. M. Krimigis, p. 459, Springer Science+Business Media B.V., Heidelberg, Germany
- Dagnac, R., Blanc, D., Molina, D., 1970, A study on the collision of hydrogen ions H_1^+ , H_2^+ and H_3^+ with a water-vapour target, *J. Phys. B*, 3, 1239–1251
- de Pater, I., Lissauer, J. J., 2011, *Planetary Sciences*, Cambridge University Press, Cambridge, UK, 2nd edn.
- de Pater, I., Martin, S. C., Showalter, M. R., 2004, Keck near-infrared observations of Saturn's E and G rings during Earth's ring plane crossing in August 1995, *Icarus*, 172, 446–454
- Dearnaley, G., 1966, *Semiconductor Counters for Nuclear Radiations*, E. & F. N. Spon Ltd., London, UK, 2nd edn.
- Dialynas, K., Krimigis, S. M., Mitchell, D. G., Hamilton, D. C., Krupp, N., Brandt, P. C., 2009, Energetic ion spectral characteristics in the Saturnian magnetosphere using Cassini/MIMI measurements, *J. Geophys. Res.*, 114, 1212
- Dialynas, K., Brandt, P. C., Krimigis, S. M., Mitchell, D. G., Hamilton, D. C., Krupp, N., Rymer, A. M., 2012, The extended Saturnian neutral cloud as revealed by global ENA simulations using Cassini/MIMI measurements, *J. Geophys. Res.*, to be submitted
- DiFabio, R. D., Hamilton, D. C., Krimigis, S. M., Mitchell, D. G., 2011, Long term time variations of the suprathermal ions in Saturn's magnetosphere, *Geophys. Res. Lett.*, 38, L18103
- Dougherty, M. K., Kellock, S., Southwood, D. J., Balogh, A., Smith, E. J., Tsurutani, B. T., Gerlach, B., Glassmeier, K., Gleim, F., Russell, C. T., Erdos, G., Neubauer, F. M., Cowley, S. W. H., 2004, The Cassini Magnetic Field Investigation, *Space Sci. Rev.*, 114, 331–383

- Dougherty, M. K., Achilleos, N., Andre, N., Arridge, C. S., Balogh, A., Bertucci, C., Burton, M. E., Cowley, S. W. H., Erdos, G., Giampieri, G., Glassmeier, K., Khurana, K. K., Leisner, J., Neubauer, F. M., Russell, C. T., Smith, E. J., Southwood, D. J., Tsurutani, B. T., 2005, Cassini Magnetometer Observations During Saturn Orbit Insertion, *Science*, 307, 1266–1270
- Dougherty, M. K., Khurana, K. K., Neubauer, F. M., Russell, C. T., Saur, J., Leisner, J. S., Burton, M. E., 2006, Identification of a Dynamic Atmosphere at Enceladus with the Cassini Magnetometer, *Science*, 311, 1406–1409
- Dragt, A. J., Austin, M. M., White, R. S., 1966, Cosmic Ray and Solar Proton Albedo Neutron Decay Injection, *J. Geophys. Res.*, 71, 1293
- Dungey, J. W., 1961, Interplanetary Magnetic Field and the Auroral Zones, *Phys. Rev. Lett.*, 6, 47–48
- Dungey, J. W., 1963, The structure of the exosphere or adventures in velocity space, in *Geophysique Exterieure – Geophysics: The Earth's Environment*, (Eds.) C. Dewitt, J. Hieblot, A. Lebeau, Gordon & Breach, New York
- Feibelman, W. A., 1967, Concerning the "D" Ring of Saturn, *Nature*, 214, 793–794
- Fok, M., Kozyra, J. U., Nagy, A. F., Cravens, T. E., 1991, Lifetime of ring current particles due to Coulomb collisions in the plasmasphere, *J. Geophys. Res.*, 96, 7861–7867
- Fouchet, T., Moses, J. I., Conrath, B. J., 2009, Saturn: Composition and Chemistry, in *Saturn from Cassini-Huygens*, (Ed.) Dougherty, M. K., Esposito, L. W., & Krimigis, S. M., p. 83, Springer Science+Business Media B.V., Heidelberg, Germany
- Furth, H. P., Killeen, J., Rosenbluth, M. N., 1963, Finite-Resistivity Instabilities of a Sheet Pinch, *Physics of Fluids*, 6, 459–484
- Geant4 Collaboration, 2011, Geant4, open software, <http://geant4.cern.ch>
- Glass, G., Jain, M., Evans, M. L., Hiebert, J. C., Northcliffe, L. C., Bonner, B. E., Simmons, J. E., Bjork, C., Riley, P., Cassapakis, C., 1977, Neutron spectra at 0° from proton-proton collisions between 647 and 805 MeV, *Phys. Rev. D*, 15, 36–46
- Gobet, F., Farizon, B., Farizon, M., Gaillard, M. J., Carré, M., Lezius, M., Scheier, P., Märk, T. D., 2001, Total, Partial, and Electron-Capture Cross Sections for Ionization of Water Vapor by 20–150 keV Protons, *Phys. Rev. Lett.*, 86, 3751–3754
- Goertz, C. K., 1983, Detached plasma in Saturn's front side magnetosphere, *Geophys. Res. Lett.*, 10, 455–458
- Goldhagen, P., Reginatto, M., Kniss, T., Wilson, J. W., Singleterry, R. C., Jones, I. W., Van Steveninck, W., 2002, Measurement of the energy spectrum of cosmic-ray induced neutrons aboard an ER-2 high-altitude airplane, *Nuc. Instr. Meth.*, 476, 42–51

Bibliography

- Goldhagen, P., Clem, J. M., Wilson, J. W., 2003, Recent results from measurements of the energy spectrum of cosmic-ray induced neutrons aboard an ER-2 airplane and on the ground, *Adv. Space Res.*, 32, 35–40
- Goldreich, P., Farmer, A. J., 2007, Spontaneous axisymmetry breaking of the external magnetic field at Saturn, *J. Geophys. Res.*, 112, A05225
- Gombosi, T. I., Armstrong, T. P., Arridge, C. S., Khurana, K. K., Krimigis, S. M., Krupp, N., Persoon, A., Thomsen, M. F., 2009, Saturn's Magnetospheric Configuration, in *Saturn from Cassini-Huygens*, (Eds.) M. K. Dougherty, L. W. Esposito, S. M. Krimigis, chap. 9, Springer Science+Business Media B.V., Heidelberg, Germany, 1st edn.
- Grodent, D., Radioti, A., Bonfond, B., Gérard, J., 2010, On the origin of Saturn's outer auroral emission, *J. Geophys. Res.*, 115, 8219
- Gubar, Y. I., 2004, A Diffusion Model of Radial Distributions of Energetic Protons in Saturn's Magnetosphere, *Cosmic Research*, 42, 370–373
- Gurnett, D. A., Kurth, W. S., Kirchner, D. L., Hospodarsky, G. B., Averkamp, T. F., Zarka, P., Lecacheux, A., Manning, R., Roux, A., Canu, P., Cornilleau-Wehrlin, N., Galopeau, P., Meyer, A., Boström, R., Gustafsson, G., Wahlund, J.-E., Åhlen, L., Rucker, H. O., Ladreiter, H. P., Macher, W., Woolliscroft, L. J. C., Alleyne, H., Kaiser, M. L., Desch, M. D., Farrell, W. M., Harvey, C. C., Louarn, P., Kellogg, P. J., Goetz, K., Pedersen, A., 2004, The Cassini Radio and Plasma Wave Investigation, *Space Sci. Rev.*, 114, 395–463
- Gusev, A. A., Pugacheva, G. I., Jayanthi, U. B., Schuch, N., 2003, Modeling of Low-altitude Quasi-trapped Proton Fluxes at the Equatorial Inner Magnetosphere, *Braz. J. Phys.*, 33, 775–781
- Haggerty, D. K., Livi, S., 2004, Monte Carlo simulations of CASSINI/LEMMS, *Adv. Space Res.*, 33, 2303–2308
- Haken, H., Wolf, H. C., 2004, *Atom- und Quantenphysik*, Springer Verlag, Heidelberg, Germany, 8th edn.
- Hartogh, P., Lellouch, E., Moreno, R., Bockelée-Morvan, D., Biver, N., Cassidy, T., Renngel, M., Jarchow, C., Cavalié, T., Crovisier, J., Helmich, F. P., Kidger, M., 2011, Direct detection of the Enceladus water torus with Herschel, *A&A*, 532, L2
- Hedman, M. M., Burns, J. A., Tiscareno, M. S., Porco, C. C., Jones, G. H., Roussos, E., Krupp, N., Paranicas, C., Kempf, S., 2007, The Source of Saturn's G Ring, *Science*, 317, 653
- Hess, W. N., Patterson, H. W., Wallace, R., Chupp, E. L., 1959, Cosmic-Ray Neutron Energy Spectrum, *Phys. Rev.*, 116, 445–457
- Hess, W. N., Canfield, E. H., Lingenfelter, R. E., 1961, Cosmic-Ray Neutron Demography, *J. Geophys. Res.*, 66, 665–677

- Hillier, J. K., Green, S. F., McBride, N., Schwanethal, J. P., Postberg, F., Srama, R., Kempf, S., Moragas-Klostermeyer, G., McDonnell, J. A. M., Grün, E., 2007, The composition of Saturn's E ring, *MNRAS*, 377, 1588–1596
- Hones, Jr., E. W., 1977, Substorm processes in the magnetotail - Comments on 'On hot tenuous plasmas, fireballs, and boundary layers in the earth's magnetotail' by L. A. Frank, K. L. Ackerson, and R. P. Lepping, *J. Geophys. Res.*, 82, 5633–5640
- Hood, L. L., 1983, Radial diffusion in Saturn's radiation belts - A modeling analysis assuming satellite and ring E absorption, *J. Geophys. Res.*, 88, 808–818
- Horányi, M., Juhász, A., Morfill, G. E., 2008, Large-scale structure of Saturn's E-ring, *Geophys. Res. Lett.*, 35, 4203
- Horányi, M., Burns, J. A., Hedman, M. M., Jones, G. H., Kempf, S., 2009, Diffuse Rings, in *Saturn from Cassini-Huygens*, (Ed.) Dougherty, M. K., Esposito, L. W., & Krimigis, S. M., p. 511, Springer Science+Business Media B.V., Heidelberg, Germany
- Houamer, S., Popov, Y. V., Cappello, C. D., 2009, Total cross sections for charge transfer reactions of protons with atomic and molecular targets at high projectile energies: The role of inner orbitals, *Phys. Lett. A*, 373, 4447–4452
- Hsu, H.-W., Postberg, F., Kempf, S., Trieloff, M., Burton, M., Roy, M., Moragas-Klostermeyer, G., Srama, R., 2011, Stream particles as the probe of the dust-plasma-magnetosphere interaction at Saturn, *J. Geophys. Res.*, 116, A09215
- Hubbard, W. B., Dougherty, M. K., Gautier, D., Jacobson, R., 2009, The Interior of Saturn, in *Saturn from Cassini-Huygens*, (Ed.) Dougherty, M. K., Esposito, L. W., & Krimigis, S. M., p. 75, Springer Science+Business Media B.V., Heidelberg, Germany
- ITT Visual Information Solutions, 2011, IDL 6-8, commerical software, <http://www.ittvis.com>
- Jackman, C. M., Russell, C. T., Southwood, D. J., Arridge, C. S., Achilleos, N., Dougherty, M. K., 2007, Strong rapid dipolarizations in Saturn's magnetotail: In situ evidence of reconnection, *Geophys. Res. Lett.*, 34, L11203
- Jackman, C. M., Arridge, C. S., Krupp, N., Bunce, E. J., Mitchell, D. G., McAndrews, H. J., Dougherty, M. K., Russell, C. T., Achilleos, N., Jones, G. H., Coates, A. J., 2008, A multi-instrument view of tail reconnection at Saturn, *J. Geophys. Res.*, 113, A11213
- Jackson, J. D., 1998, Classical Electrodynamics, John Wiley & Sons, Inc., New York, N.Y., 3rd edn.
- Johnson, R. E., 1990, Energetic charged-particle interactions with atmospheres and surfaces, Springer Verlag, Heidelberg, Germany, 1st edn.
- Jones, G. H., Roussos, E., Krupp, N., Beckmann, U., Coates, A. J., Crary, F., Dandouras, I., Dikarev, V., Dougherty, M. K., Garnier, P., Hansen, C. J., Hendrix, A. R., Hospodarsky, G. B., Johnson, R. E., Kempf, S., Khurana, K. K., Krimigis, S. M., Krüger,

Bibliography

- H., Kurth, W. S., Lagg, A., McAndrews, H. J., Mitchell, D. G., Paranicas, C., Postberg, F., Russell, C. T., Saur, J., Seiß, M., Spahn, F., Srama, R., Strobel, D. F., Tokar, R., Wahlund, J., Wilson, R. J., Woch, J., Young, D., 2008, The Dust Halo of Saturn's Largest Icy Moon, *Rhea*, *Science*, 319, 1380
- Jones, G. H., Arridge, C. S., Coates, A. J., Lewis, G. R., Kanani, S., Wellbrock, A., Young, D. T., Crary, F. J., Tokar, R. L., Wilson, R. J., Hill, T. W., Johnson, R. E., Mitchell, D. G., Schmidt, J., Kempf, S., Beckmann, U., Russell, C. T., Jia, Y. D., Dougherty, M. K., Waite, J. H., Magee, B. A., 2009, Fine jet structure of electrically charged grains in Enceladus' plume, *Geophys. Res. Lett.*, 36, 16 204
- Juhász, A., Horányi, M., 2004, Seasonal variations in Saturn's E-ring, *Geophys. Res. Lett.*, 31, 19 703
- Jurac, S., Richardson, J. D., 2005, A self-consistent model of plasma and neutrals at Saturn: Neutral cloud morphology, *J. Geophys. Res.*, 110, 9220
- Jurac, S., Johnson, R. E., Richardson, J. D., 2001a, Saturn's E Ring and Production of the Neutral Torus, *Icarus*, 149, 384–396
- Jurac, S., Johnson, R. E., Richardson, J. D., Paranicas, C., 2001b, Satellite sputtering in Saturn's magnetosphere, *Planet. Space Sci.*, 49, 319–326
- Kempf, S., Srama, R., Horányi, M., Burton, M., Helfert, S., Moragas-Klostermeyer, G., Roy, M., Grün, E., 2005, High-velocity streams of dust originating from Saturn, *Nature*, 433, 289–291
- Kempf, S., Beckmann, U., Srama, R., Horanyi, M., Auer, S., Grün, E., 2006, The electrostatic potential of E ring particles, *Planet. Space Sci.*, 54, 999–1006
- Kempf, S., Beckmann, U., Moragas-Klostermeyer, G., Postberg, F., Srama, R., Economou, T., Schmidt, J., Spahn, F., Grün, E., 2008, The E ring in the vicinity of Enceladus. I. Spatial distribution and properties of the ring particles, *Icarus*, 193, 420–437
- Kempf, S., Beckmann, U., Schmidt, J., 2010, How the Enceladus dust plume feeds Saturn's E ring, *Icarus*, 206, 446–457
- Kempf, S., Srama, R., Moragas-Klostermeyer, G., Postberg, F., Horanyi, M., Schmidt, J., Spahn, F., 2011, The Structure of Saturn's E ring as seen by Cassini CDA, EPSC Abstracts, EPSC-DPS2011, 1643
- Kennel, C. F., Petschek, H. E., 1966, Limit on Stably Trapped Particle Fluxes, *J. Geophys. Res.*, 71, 1
- Khurana, K. K., 2001, Influence of solar wind on Jupiter's magnetosphere deduced from currents in the equatorial plane, *J. Geophys. Res.*, 106, 25 999–26 016
- Khurana, K. K., Arridge, C. S., Schwarzl, H., Dougherty, M. K., 2006, A Model of Saturn's Magnetospheric Field Based on Latest Cassini Observations, AGU Spring Meeting Abstracts, p. A1

- Kivelson, M. G., Russell, C. T., 1995, *Introduction to Space Physics*, Cambridge University Press, Cambridge, UK, 3rd edn.
- Knoll, G. F., 2000, *Radiation detection and measurement*, John Wiley & Sons, New York, USA, 3rd edn.
- Kollmann, P., Roussos, E., Paranicas, C., Krupp, N., Haggerty, D., 2011a, Processes forming and sustaining Saturn's proton radiation belts, *Icarus*, submitted
- Kollmann, P., Roussos, E., Paranicas, C., Krupp, N., Jackman, C. M., Kirsch, E., Glassmeier, K.-H., 2011b, Energetic particle phase space densities at Saturn: Cassini observations and interpretations, *J. Geophys. Res.*, 116, A05 222
- Kreussler, S., Sizmann, R., 1982, Neutralization of 50-230-keV hydrogen ions which have penetrated Al, Au, C, and Cs films, *Phys. Rev. B*, 26, 520–529
- Krimigis, S. M., Armstrong, T. P., 1982, Two-component proton spectra in the inner Saturnian magnetosphere, *Geophys. Res. Lett.*, 9, 1143–1146
- Krimigis, S. M., Carbary, J. F., Keath, E. P., Armstrong, T. P., Lanzerotti, L. J., Gloeckler, G., 1983, General characteristics of hot plasma and energetic particles in the Saturnian magnetosphere: results from the Voyager spacecraft, *J. Geophys. Res.*, 88, 8633–8634
- Krimigis, S. M., Mitchell, D. G., Hamilton, D. C., Livi, S., Dandouras, J., Jaskulek, S., Armstrong, T. P., Boldt, J. D., Cheng, A. F., Gloeckler, G., Hayes, J. R., Hsieh, K. C., Ip, W.-H., Keath, E. P., Kirsch, E., Krupp, N., Lanzerotti, L. J., Lundgren, R., Mauk, B. H., McEntire, R. W., Roelof, E. C., Schlemm, C. E., Tossman, B. E., Wilken, B., Williams, D. J., 2004, Magnetosphere Imaging Instrument (MIMI) on the Cassini Mission to Saturn/Titan, *Space Sci. Rev.*, 114, 233–329
- Krimigis, S. M., Mitchell, D. G., Hamilton, D. C., Krupp, N., Livi, S., Roelof, E. C., Dandouras, J., Armstrong, T. P., Mauk, B. H., Paranicas, C., Brandt, P. C., Bolton, S., Cheng, A. F., Choo, T., Gloeckler, G., Hayes, J., Hsieh, K. C., Ip, W., Jaskulek, S., Keath, E. P., Kirsch, E., Kusterer, M., Lagg, A., Lanzerotti, L. J., LaVallee, D., Manweiler, J., McEntire, R. W., Rasmuss, W., Saur, J., Turner, F. S., Williams, D. J., Woch, J., 2005, Dynamics of Saturn's Magnetosphere from MIMI During Cassini's Orbital Insertion, *Science*, 307, 1270–1273
- Krimigis, S. M., Sergis, N., Mitchell, D. G., Hamilton, D. C., Krupp, N., 2007, A dynamic, rotating ring current around Saturn, *Nature*, 450, 1050–1053
- Krupp, N., Vasyliunas, V. M., Woch, J., Lagg, A., Khurana, K. K., Kivelson, M. G., Mauk, B. H., Roelof, E. C., Williams, D. J., Krimigis, S. M., Kurth, W. S., Frank, L. A., Paterson, W. R., 2004, Dynamics of the Jovian magnetosphere, in *Jupiter. The Planet, Satellites and Magnetosphere*, (Ed.) Bagenal, F., Dowling, T. E., & McKinnon, W. B., pp. 593–616, Cambridge University Press, Cambridge, U.K.
- Krupp, N., Roussos, E., Lagg, A., Woch, J., Müller, A. L., Krimigis, S. M., Mitchell, D. G., Roelof, E. C., Paranicas, C., Carbary, J., Jones, G. H., Hamilton, D. C., Livi, S., Armstrong, T. P., Dougherty, M. K., Sergis, N., 2009, Energetic particles

Bibliography

- in Saturn's magnetosphere during the Cassini nominal mission (July 2004-July 2008), *Planet. Space Sci.*, 57, 1754–1768
- Krupp, N., Roussos, E., Kollmann, P., Paranicas, C., Mitchell, D. G., Krimigis, S. M., Rymer, A., Jones, G. H., Arridge, C. S., Armstrong, T. P., Khurana, K. K., 2012, The Cassini Enceladus encounters 2005-2010 in the view of energetic electron measurements, *Icarus*, 218, 433–447
- Kurth, W. S., 1992, Comparative observations of plasma waves at the outer planets, *Adv. Space Res.*, 12, 83–90
- Landau, L. D., Lifschitz, E. M., 1975, Lehrbuch der theoretischen Physik V: statistische Physik, Akademie Verlag Berlin, Berlin, Germany, 4th edn.
- Lew, J. S., 1961, Drift Rate in a Dipole Field, *J. Geophys. Res.*, 66, 2681–2685
- Livadiotis, G., McComas, D. J., 2009, Beyond kappa distributions: Exploiting Tsallis statistical mechanics in space plasmas, *J. Geophys. Res.*, 114, A11105
- Lorenzato, L., Sicard-Piet, A., Bourdarie, S., 2011, A Physical Model of Electron Radiation Belts of Saturn, EPSC Abstracts, EPSC-DPS2011, 155
- Luna, H., de Barros, A. L. F., Wyer, J. A., Scully, S. W. J., Lecointre, J., Garcia, P. M. Y., Sigaud, G. M., Santos, A. C. F., Senthil, V., Shah, M. B., Latimer, C. J., Montenegro, E. C., 2007, Water-molecule dissociation by proton and hydrogen impact, *Phys. Rev. A*, 75, 042 711
- Matson, D. L., Castillo-Rogez, J. C., Schubert, G., Sotin, C., McKinnon, W. B., 2009, The Thermal Evolution and Internal Structure of Saturn's Mid-Sized Icy Satellites, in *Saturn from Cassini-Huygens*, (Ed.) Dougherty, M. K., Esposito, L. W., & Krimigis, S. M., p. 577, Springer Science+Business Media B.V., Heidelberg, Germany
- Mauk, B. H., Krimigis, S. M., Mitchell, D. G., Roelof, E. C., Keath, E. P., Dandouras, J., 1998, Imaging Saturns dust rings using energetic neutral atoms, *Planet. Space Sci.*, 46, 1349–1362
- Mauk, B. H., Saur, J., Mitchell, D. G., Roelof, E. C., Brandt, P. C., Armstrong, T. P., Hamilton, D. C., Krimigis, S. M., Krupp, N., Livi, S. A., Manweiler, J. W., Paranicas, C. P., 2005, Energetic particle injections in Saturn's magnetosphere, *Geophys. Res. Lett.*, 32, 14
- Mauk, B. H., Hamilton, D. C., Hill, T. W., Hospodarsky, G. B., Johnson, R. E., Paranicas, C., Roussos, E., Russell, C. T., Shemansky, D. E., Sittler, E. C., Thorne, R. M., 2009, Fundamental Plasma Processes in Saturn's Magnetosphere, in *Saturn from Cassini-Huygens*, (Eds.) M. K. Dougherty, L. W. Esposito, S. M. Krimigis, chap. 9, Springer Science+Business Media B.V., Heidelberg, Germany, 1st edn.
- McDonald, F. B., Schardt, A. W., Trainor, J. H., 1980, If you've seen one magnetosphere, you haven't seen them all - Energetic particle observations in the Saturn magnetosphere, *J. Geophys. Res.*, 85, 5813–5830

- McEntire, R. W., Mitchell, D. G., 1989, Instrumentation for global magnetospheric imaging via energetic neutral atoms, in Geophys. Monographs, vol. 54, pp. 69–80, AGU, Washington, D.C.
- McKinney, G. W., Lawrence, D. J., Prettyman, T. H., Elphic, R. C., Feldman, W. C., Hagerty, J. J., 2006, MCNPX benchmark for cosmic ray interactions with the Moon, *J. Geophys. Res.*, 111, E06004
- Melin, H., Shemansky, D. E., Liu, X., 2009, The distribution of atomic hydrogen and oxygen in the magnetosphere of Saturn, *Planet. Space Sci.*, 57, 1743–1753
- Milovanov, A. V., Zelenyi, L. M., 2000, Functional background of the Tsallis entropy: "coarse-grained" systems and "kappa" distribution functions, *Nonlin. Processes Geophys.*, 7, 211–221
- Mitchell, D. G., Carbary, J. F., Cowley, S. W. H., Hill, T. W., Zarka, P., 2009, The Dynamics of Saturn's Magnetosphere, in *Saturn from Cassini-Huygens*, (Ed.) Dougherty, M. K., Esposito, L. W., & Krimigis, S. M., chap. 9, Springer Science+Business Media B.V., Heidelberg, Germany, 1st edn.
- Müller, A. L., 2011, Energetic particle injection events in the Kronian magnetosphere: applications and properties, Ph.D. thesis, Universität zu Köln, 50923 Köln, Germany
- Moritz, J., 1972, Energetic Protons at Low Equatorial Altitudes, *Z. Geophys.*, 38, 701–717
- Morooka, M. W., Modolo, R., Wahlund, J.-E., André, M., Eriksson, A. I., Persoon, A. M., Gurnett, D. A., Kurth, W. S., Coates, A. J., Lewis, G. R., Khurana, K. K., Dougherty, M., 2009, The electron density of Saturn's magnetosphere, *Ann. Geophys.*, 27, 2971–2991
- Müller, A. L., Saur, J., Krupp, N., Roussos, E., Mauk, B. H., Rymer, A. M., Mitchell, D. G., Krimigis, S. M., 2010, Azimuthal plasma flow in the Kronian magnetosphere, *J. Geophys. Res.*, 115, 8203
- Nakamura, K., the Particle Data Group, 2010, Review of Particle Physics, *J. Phys. G*, 37, 075 021
- Ness, N. F., Acuna, M. H., Lepping, R. P., Connerney, J. E. P., Behannon, K. W., Burlaga, L. F., Neubauer, F. M., 1981, Magnetic field studies by Voyager 1 - Preliminary results at Saturn, *Science*, 212, 211–217
- Neufeld, J., Ritchie, R. H., 1955, Passage of Charged Particles through Plasma, *Phys. Rev.*, 98, 1632–1642
- Nicholson, P. D., Showalter, M. R., Dones, L., French, R. G., Larson, S. M., Lissauer, J. J., McGhee, C. A., Seitzer, P., Sicardy, B., Danielson, G. E., 1996, Observations of Saturn's Ring-Plane Crossings in August and November 1995, *Science*, 272, 509–515
- Nishida, A., 1976, Outward diffusion of energetic particles from the Jovian radiation belt, *J. Geophys. Res.*, 81, 1771–1773

Bibliography

- Oldekop, W., 1975, Einführung in die Kernreaktor- und Kernkraftwerkstechnik, Verlag Karl Thiemig, Munich, Germany, 1st edn.
- Ota, S., Kobayashi, S., Sihver, L., Yamashita, N., Hasebe, N., 2011, Neutron production in the lunar subsurface from alpha particles in galactic cosmic rays, *Earth, Planets, and Space*, 63, 25–35
- Paonessa, M., Cheng, A. F., 1985, A theory of satellite sweeping, *J. Geophys. Res.*, 90, 3428–3434
- Paranicas, C., Mitchell, D. G., Roelof, E. C., Brandt, P. C., Williams, D. J., Krimigis, S. M., Mauk, B. H., 2005, Periodic intensity variations in global ENA images of Saturn, *Geophys. Res. Lett.*, 32, L21 101
- Paranicas, C., Mitchell, D. G., Krimigis, S. M., Hamilton, D. C., Roussos, E., Krupp, N., Jones, G. H., Johnson, R. E., Cooper, J. F., Armstrong, T. P., 2008, Sources and losses of energetic protons in Saturn's magnetosphere, *Icarus*, 197, 519–525
- Paranicas, C., Mitchell, D. G., Krimigis, S. M., Carbary, J. F., Brandt, P. C., Turner, F. S., Roussos, E., Krupp, N., Kivelson, M. G., Khurana, K. K., Cooper, J. F., Armstrong, T. P., Burton, M., 2010, Asymmetries in Saturn's radiation belts, *J. Geophys. Res.*, 115, 7216
- Perry, M. E., Teolis, B., Smith, H. T., McNutt, R. L., Fletcher, G., Kasprzak, W., Magee, B., Mitchell, D. G., Waite, J. H., 2010, Cassini INMS observations of neutral molecules in Saturn's E-ring, *J. Geophys. Res.*, 115, A10206
- Persoon, A. M., Gurnett, D. A., Kurth, W. S., Hospodarsky, G. B., Groene, J. B., Canu, P., Dougherty, M. K., 2005, Equatorial electron density measurements in Saturn's inner magnetosphere, *Geophys. Res. Lett.*, 32, L23105
- Persoon, A. M., Gurnett, D. A., Santolik, O., Kurth, W. S., Faden, J. B., Groene, J. B., Lewis, G. R., Coates, A. J., Wilson, R. J., Tokar, R. L., Wahlund, J., Moncuquet, M., 2009, A diffusive equilibrium model for the plasma density in Saturn's magnetosphere, *J. Geophys. Res.*, 114, 4211
- Porco, C. C., Helfenstein, P., Thomas, P. C., Ingersoll, A. P., Wisdom, J., West, R., Neukum, G., Denk, T., Wagner, R., Roatsch, T., Kieffer, S., Turtle, E., McEwen, A., Johnson, T. V., Rathbun, J., Veverka, J., Wilson, D., Perry, J., Spitale, J., Brahic, A., Burns, J. A., Del Genio, A. D., Dones, L., Murray, C. D., Squyres, S., 2006, Cassini Observes the Active South Pole of Enceladus, *Science*, 311, 1393–1401
- Postberg, F., Kempf, S., Schmidt, J., Brilliantov, N., Beinsen, A., Abel, B., Buck, U., Srama, R., 2009, Sodium salts in E-ring ice grains from an ocean below the surface of Enceladus, *Nature*, 459, 1098–1101
- Pryor, W. R., Rymer, A. M., Mitchell, D. G., Hill, T. W., Young, D. T., Saur, J., Jones, G. H., Jacobsen, S., Cowley, S. W. H., Mauk, B. H., Coates, A. J., Gustin, J., Grodent, D., Gérard, J.-C., Lamy, L., Nichols, J. D., Krimigis, S. M., Esposito, L. W., Dougherty, M. K., Jouchoux, A. J., Stewart, A. I. F., McClintock, W. E., Holsclaw, G. M., Ajello,

- J. M., Colwell, J. E., Hendrix, A. R., Crary, F. J., Clarke, J. T., Zhou, X., 2011, The auroral footprint of Enceladus on Saturn, *Nature*, 472, 331–333
- Randall, B. A., 1994, Energetic electrons in the magnetosphere of Saturn, *J. Geophys. Res.*, 99, 8771–8785
- Richardson, J. D., Eviatar, A., McGrath, M. A., Vasyliūnas, V. M., 1998, OH in Saturn's magnetosphere: Observations and implications, *J. Geophys. Res.*, 103, 20 245–20 256
- Riessellmann, K., Anderson, L. W., Durand, L., Anderson, C. J., 1991, Classical impulse approximation for the electron loss from H(1s) or H⁻ projectiles passing through various gas targets, *Phys. Rev. A*, 43, 5934–5945
- Roederer, J. G., 1970, Dynamics of Geomagnetically Trapped Radiation, Springer Verlag, Heidelberg, Germany
- Roesler, S., Heinrich, W., Schraube, H., 1998, Neutron spectra in the atmosphere from interactions of primary cosmic rays, *Adv. Space Res.*, 21, 1717–1726
- Roussos, E., 2007, Interactions of weakly or non-magnetized bodies with solar system plasmas: Mars and the moons of Saturn, Ph.D. thesis, Technische Universität Carolo-Wilhelmina zu Braunschweig, 38106 Braunschweig, Germany
- Roussos, E., Krupp, N., Woch, J., Lagg, A., Jones, G. H., Paranicas, C., Mitchell, D. G., Livi, S., Krimigis, S. M., Dougherty, M. K., Armstrong, T., Ip, W.-H., Motschmann, U., 2005, Low energy electron microsignatures at the orbit of Tethys: Cassini MIMI/LEMMS observations, *Geophys. Res. Lett.*, 32, 24 107
- Roussos, E., Jones, G. H., Krupp, N., Paranicas, C., Mitchell, D. G., Lagg, A., Woch, J., Motschmann, U., Krimigis, S. M., Dougherty, M. K., 2007, Electron microdiffusion in the Saturnian radiation belts: Cassini MIMI/LEMMS observations of energetic electron absorption by the icy moons, *J. Geophys. Res.*, 112, 6214
- Roussos, E., Jones, G. H., Krupp, N., Paranicas, C., Mitchell, D. G., Krimigis, S. M., Woch, J., Lagg, A., Khurana, K., 2008a, Energetic electron signatures of Saturn's smaller moons: Evidence of an arc of material at Methone, *Icarus*, 193, 455–464
- Roussos, E., Krupp, N., Armstrong, T. P., Paranicas, C., Mitchell, D. G., Krimigis, S. M., Jones, G. H., Dialynas, K., Sergis, N., Hamilton, D. C., 2008b, Discovery of a transient radiation belt at Saturn, *Geophys. Res. Lett.*, 35, 22 106
- Roussos, E., Krupp, N., Paranicas, C. P., Mitchell, D. G., Müller, A. L., Kollmann, P., Bebesi, Z., Krimigis, S. M., Coates, A. J., 2010, Energetic electron microsignatures as tracers of radial flows and dynamics in Saturn's innermost magnetosphere, *J. Geophys. Res.*, 115, 3202
- Roussos, E., Krupp, N., Paranicas, C. P., Kollmann, P., Mitchell, D. G., Krimigis, S. M., Armstrong, T. P., Went, D. R., Dougherty, M. K., Jones, G. H., 2011, Long- and short-term variability of Saturn's ionic radiation belts, *J. Geophys. Res.*, 116, A02 217

Bibliography

- Rutherford, E., 1911, The Scattering of α and β Particles by Matter and the Structure of the Atom, *Philosophical Magazine*, 21, 669–688
- Rymer, A. M., Mauk, B. H., Hill, T. W., Paranicas, C., André, N., Sittler, E. C., Mitchell, D. G., Smith, H. T., Johnson, R. E., Coates, A. J., Young, D. T., Bolton, S. J., Thomsen, M. F., Dougherty, M. K., 2007, Electron sources in Saturn's magnetosphere, *J. Geophys. Res.*, 112, 2201
- Rymer, A. M., Mauk, B. H., Hill, T. W., Paranicas, C., Mitchell, D. G., Coates, A. J., Young, D. T., 2008, Electron circulation in Saturn's magnetosphere, *J. Geophys. Res.*, 113, 1201
- Santolík, O., Gurnett, D. A., Jones, G. H., Schippers, P., Crary, F. J., Leisner, J. S., Hospodarsky, G. B., Kurth, W. S., Russell, C. T., Dougherty, M. K., 2011, Intense plasma wave emissions associated with Saturn's moon Rhea, *Geophys. Res. Lett.*, 381, L19204
- Santos-Costa, D., Blanc, M., Maurice, S., Bolton, S. J., 2003, Modeling the electron and proton radiation belts of Saturn, *Geophys. Res. Lett.*, 30, 200 000–1
- Sauer, H. H., 1980, On Saturnian cosmic ray cutoff rigidities, *Geophys. Res. Lett.*, 7, 215–217
- Saur, J., 2004, Turbulent Heating of Jupiter's Middle Magnetosphere, *Astrophys. J.*, 602, L137–L140
- Saur, J., Schilling, N., Neubauer, F. M., Strobel, D. F., Simon, S., Dougherty, M. K., Russell, C. T., Pappalardo, R. T., 2008, Evidence for temporal variability of Enceladus' gas jets: Modeling of Cassini observations, *Geophys. Res. Lett.*, 352, L20105
- Schardt, A. W., McDonald, F. B., 1983, The flux and source of energetic protons in Saturn's inner magnetosphere, *J. Geophys. Res.*, 88, 8923–8935
- Schindler, K., 2006, Physics of Space Plasma Activity, Cambridge University Press, Cambridge, UK
- Schippers, P., Blanc, M., André, N., Dandouras, I., Lewis, G. R., Gilbert, L. K., Persoon, A. M., Krupp, N., Gurnett, D. A., Coates, A. J., Krimigis, S. M., Young, D. T., Dougherty, M. K., 2008, Multi-instrument analysis of electron populations in Saturn's magnetosphere, *J. Geophys. Res.*, 113, 7208
- Schlickeiser, R., 2002, Cosmic Ray Astrophysics, Springer Verlag, Berlin, Germany, 1st edn.
- Schulz, M., 1979, Jupiter's radiation belts, *Space Sci. Rev.*, 23, 277–318
- Schulz, M., Lanzerotti, L. J., 1974, Particle Diffusion in the Radiation Belts, in Physics and Chemistry in Space 7, (Ed.) J. G. Roederer, Springer Verlag, Heidelberg, Germany, 1st edn.

- Serber, R., 1947, The Production of High Energy Neutrons by Stripping, *Phys. Rev.*, 72, 1008–1016
- Sergis, N., Krimigis, S. M., Mitchell, D. G., Hamilton, D. C., Krupp, N., Mauk, B. H., Roelof, E. C., Dougherty, M. K., 2009, Energetic particle pressure in Saturn's magnetosphere measured with the Magnetospheric Imaging Instrument on Cassini, *J. Geophys. Res.*, 114, A02214
- Shemansky, D. E., Hall, D. T., 1992, The distribution of atomic hydrogen in the magnetosphere of Saturn, *J. Geophys. Res.*, 97, 4143–4161
- Shemansky, D. E., Matheson, P., Hall, D. T., Hu, H.-Y., Tripp, T. M., 1993, Detection of the hydroxyl radical in the Saturn magnetosphere, *Nature*, 363, 329–331
- Showalter, M. R., Cuzzi, J. N., Larson, S. M., 1991, Structure and particle properties of Saturn's E Ring, *Icarus*, 94, 451–473
- Simpson, J. A., Bastian, T. S., Chenette, D. L., McKibben, R. B., Pyle, K. R., 1980, The trapped radiations of Saturn and their absorption by satellites and rings, *J. Geophys. Res.*, 85, 5731–5762
- Singer, S. F., 1958, Trapped Albedo Theory of the Radiation Belt, *Phys. Rev. Lett.*, 1, 181–183
- Sittler, E. C., Thomsen, M., Johnson, R. E., Hartle, R. E., Burger, M., Chornay, D., Shapirio, M. D., Simpson, D., Smith, H. T., Coates, A. J., Rymer, A. M., McComas, D. J., Young, D. T., Reisenfeld, D., Dougherty, M., Andre, N., 2006, Cassini observations of Saturn's inner plasmasphere: Saturn orbit insertion results, *Planet. Space Sci.*, 54, 1197–1210
- Smith, E. J., Davis, L., Jones, D. E., Coleman, P. J., Colburn, D. S., Dyal, P., Sonett, C. P., 1980, Saturn's magnetic field and magnetosphere, *Science*, 207, 407–410
- Smith, E. J., Dougherty, M. K., Russell, C. T., Southwood, D. J., 2001, Scalar helium magnetometer observations at Cassini Earth swing-by, *J. Geophys. Res.*, 106, 30 129–30 140
- Smith, H. T., Johnson, R. E., Perry, M. E., Mitchell, D. G., McNutt, R. L., Young, D. T., 2010, Enceladus plume variability and the neutral gas densities in Saturn's magnetosphere, *J. Geophys. Res.*, 115, 10 252
- Southwood, D. J., Kivelson, M. G., 1987, Magnetospheric interchange instability, *J. Geophys. Res.*, 92, 109–116
- Spitzer, L., 1962, Physics of fully ionized gases, John Wiley & Sons, Inc., New York, N.Y., 2nd edn.
- Srama, R., Ahrens, T. J., Altobelli, N., Auer, S., Bradley, J. G., Burton, M., Dikarev, V. V., Economou, T., Fechtig, H., Görlich, M., Grande, M., Graps, A., Grün, E., Havnes, O., Helfert, S., Horanyi, M., Igenbergs, E., Jessberger, E. K., Johnson, T. V., Kempf, S.,

Bibliography

- Krivov, A. V., Krüger, H., Mocker-Ahreep, A., Moragas-Klostermeyer, G., Lamy, P., Landgraf, M., Linkert, D., Linkert, G., Lura, F., McDonnell, J. A. M., Möhlmann, D., Morfill, G. E., Müller, M., Roy, M., Schäfer, G., Schlotzhauer, G., Schwehm, G. H., Spahn, F., Stübig, M., Svestka, J., Tschernjawska, V., Tuzzolino, A. J., Wäsch, R., Zook, H. A., 2004, The Cassini Cosmic Dust Analyzer, *Space Sci. Rev.*, 114, 465–518
- Teolis, B. D., Perry, M. E., Magee, B. A., Westlake, J., Waite, J. H., 2010, Detection and measurement of ice grains and gas distribution in the Enceladus plume by Cassini's Ion Neutral Mass Spectrometer, *J. Geophys. Res.*, 115, A09222
- Thomas, P. C., 2010, Sizes, shapes, and derived properties of the saturnian satellites after the Cassini nominal mission, *Icarus*, 208, 395–401
- Thomsen, M. F., Van Allen, J. A., 1979, On the inference of properties of Saturn's Ring E from energetic charged particle observations, *Geophys. Res. Lett.*, 6, 893–896
- Thomsen, M. F., Goertz, C. K., Van Allen, J. A., 1977, On determining magnetospheric diffusion coefficients from the observed effects of Jupiter's satellite Io, *J. Geophys. Res.*, 82, 5541–5550
- Thomsen, M. F., Reisenfeld, D. B., Delapp, D. M., Tokar, R. L., Young, D. T., Crary, F. J., Sittler, E. C., McGraw, M. A., Williams, J. D., 2010, Survey of ion plasma parameters in Saturn's magnetosphere, *J. Geophys. Res.*, 115, A10 220
- Thomsen, M. F., Roussos, E., Andriopoulou, M., Kollmann, P., Arridge, C. S., Paranicas, C. P., Gurnett, D. A., Powell, R. L., Tokar, R. L., Young, D. T., 2011, Evidence at Saturn for an Inner Magnetospheric Convection Pattern, Fixed in Local Time, submitted
- Thorne, R. M., 2010, Radiation belt dynamics: The importance of wave-particle interactions, *Geophys. Res. Lett.*, 37, 22 107
- Toburen, L. H., Nakai, M. Y., Langley, R. A., 1968, Measurement of High-Energy Charge-Transfer Cross Sections for Incident Protons and Atomic Hydrogen in Various Gases, *Phys. Rev.*, 171, 114–122
- Tsallis, C., 2009, Nonadditive entropy and nonextensive statistical mechanics - An overview after 20 years, *Braz. J. Phys.*, 39, 337–356
- Van Allen, J. A., 1983, Absorption of energetic protons by Saturn's Ring G, *J. Geophys. Res.*, 88, 6911–6918
- Van Allen, J. A., 1984, Energetic particles in the inner magnetosphere of Saturn, in *Saturn*, (Eds.) T. Gerhels, M. S. Matthews, The University of Arizona Press, Tucson, Arizona
- Van Allen, J. A., Frank, L. A., 1959, Radiation Around the Earth to a Radial Distance of 107,400 km., *Nature*, 183, 430–434
- Van Allen, J. A., Randall, B. A., Thomsen, M. F., 1980a, Sources and sinks of energetic electrons and protons in Saturn's magnetosphere, *J. Geophys. Res.*, 85, 5679–5694

- Van Allen, J. A., Thomsen, M. F., Randall, B. A., 1980b, The energetic charged particle absorption signature of Mimas, *J. Geophys. Res.*, 85, 5709–5718
- van Milligen, B. P., Bons, P. D., Carreras, B. A., Sánchez, R., 2005, On the applicability of Fick's law to diffusion in inhomogeneous systems, *Europ. J. Phys.*, 26, 913–925
- Vasyliunas, V. M., 1968, A Survey of Low-Energy Electrons in the Evening Sector of the Magnetosphere with OGO 1 and OGO 3, *J. Geophys. Res.*, 73, 2839
- Vasyliūnas, V. M., 1983, Plasma distribution and flow, in Physics of the Jovian Magnetosphere, (Ed.) A. J. Dessler, chap. 11, Cambridge University Press, Cambridge, United Kingdom
- Vasyliūnas, V. M., 2009, Fundamentals of planetary magnetospheres, in Heliophysics: Plasma Physics of the Local Cosmos, (Eds.) C. J. Schrijver, G. L. Siscoe, Cambridge University Press
- Wahlund, J.-E., Boström, R., Gustafsson, G., Gurnett, D. A., Kurth, W. S., Averkamp, T., Hospodarsky, G. B., Persoon, A. M., Canu, P., Pedersen, A., Desch, M. D., Eriksson, A. I., Gill, R., Morooka, M. W., André, M., 2005, The inner magnetosphere of Saturn: Cassini RPWS cold plasma results from the first encounter, *Geophys. Res. Lett.*, 32, L20S09
- Waite, J. H., Lewis, W. S., Kasprzak, W. T., Anicich, V. G., Block, B. P., Cravens, T. E., Fletcher, G. G., Ip, W.-H., Luhmann, J. G., McNutt, R. L., Niemann, H. B., Parejko, J. K., Richards, J. E., Thorpe, R. L., Walter, E. M., Yelle, R. V., 2004, The Cassini Ion and Neutral Mass Spectrometer (INMS) Investigation, *Space Sci. Rev.*, 114, 113–231
- Waite, J. H., Combi, M. R., Ip, W.-H., Cravens, T. E., McNutt, R. L., Kasprzak, W., Yelle, R., Luhmann, J., Niemann, H., Gell, D., Magee, B., Fletcher, G., Lunine, J., Tseng, W.-L., 2006, Cassini Ion and Neutral Mass Spectrometer: Enceladus Plume Composition and Structure, *Science*, 311, 1419–1422
- Walt, M., 1971, Radial Diffusion of Trapped Particles and Some of Its Consequences, *Rev. Geophys.*, 9, 11–25
- Walt, M., 1994, Introduction to geomagnetically trapped radiation, Cambridge University Press, Cambridge, United Kingdom, 1st edn.
- Webber, W. R., Lockwood, J. A., 2001, Voyager and Pioneer spacecraft measurements of cosmic ray intensities in the outer heliosphere: Toward a new paradigm for understanding the global solar modulation process: 1. Minimum solar modulation (1987 and 1997), *J. Geophys. Res.*, 106, 29 323–29 332
- Williams, D. R., 2010, Planetary Fact Sheet, NASA Website, <http://nssdc.gsfc.nasa.gov/planetary/>
- Wilson, R. J., Tokar, R. L., Henderson, M. G., Hill, T. W., Thomsen, M. F., Pontius, D. H., 2008, Cassini plasma spectrometer thermal ion measurements in Saturn's inner magnetosphere, *J. Geophys. Res.*, 113, 12 218

Bibliography

- Wolfram Research, 2008, Mathematica, commerical software, <http://www.wolfram.com/>
- Wu, C. S., Lee, L. C., 1979, A theory of the terrestrial kilometric radiation, *Astrophys. J.*, 230, 621–626
- Yaroshenko, V. V., Ratynskaia, S., Olson, J., Brenning, N., Wahlund, J., Morooka, M., Kurth, W. S., Gurnett, D. A., Morfill, G. E., 2009, Characteristics of charged dust inferred from the Cassini RPWS measurements in the vicinity of Enceladus, *Planet. Space Sci.*, 57, 1807–1812
- Young, D. T., Berthelier, J. J., Blanc, M., Burch, J. L., Coates, A. J., Goldstein, R., Grande, M., Hill, T. W., Johnson, R. E., Kelha, V., McComas, D. J., Sittler, E. C., Svenes, K. R., Szegö, K., Tanskanen, P., Ahola, K., Anderson, D., Bakshi, S., Baragiola, R. A., Barracough, B. L., Black, R. K., Bolton, S., Booker, T., Bowman, R., Casey, P., Crary, F. J., Delapp, D., Dirks, G., Eaker, N., Funsten, H., Furman, J. D., Gosling, J. T., Hannula, H., Holmlund, C., Huomo, H., Illiano, J. M., Jensen, P., Johnson, M. A., Linder, D. R., Luntama, T., Maurice, S., McCabe, K. P., Mursula, K., Narheim, B. T., Nordholt, J. E., Preece, A., Rudzki, J., Ruitberg, A., Smith, K., Szalai, S., Thomsen, M. F., Viherkanto, K., Vilppola, J., Vollmer, T., Wahl, T. E., Wüest, M., Ylikorpi, T., Zinsmeyer, C., 2004, Cassini Plasma Spectrometer Investigation, *Space Sci. Rev.*, 114, 1–112
- Ziegler, J. F., 2008, SRIM 2008, free software, <http://www.srim.org>

Acknowledgements

There are many people that helped and supported me over the last three years. Without them, life would have been harder and this thesis would not have been possible in this form. I would like to thank all of them. In the following text, I will switch repeatedly between English and German, depending on whom I am referring to.

Als erstes möchte ich *Norbert Krupp* danken. Immer schon wollte ich etwas tun, was mit „Weltraum“ zu tun hat. Norbert hat mir diese Möglichkeit eröffnet, indem er diese Doktorandenstelle mit mir besetzt hat. Seit meinem Bewerbungsvortrag hat er großes Vertrauen in mich gesetzt. Bei der Wahl meines Themas hat er mich sehr unterstützt, aber die Entscheidung letztlich mir überlassen. Auch sonst hat er zwar darauf geachtet, dass ich voran und zum Abschluss komme, aber mir ansonsten viel Raum zur Entfaltung gelassen. Auch außerhalb des Büros hatten wir viel Spaß miteinander.

Since the focus during my studies and diploma thesis was on atomic physics and therefore totally different to what I am doing nowadays, I had to learn a lot of new stuff. I would not have come so far without *Elias Roussos*. Elias is a really good scientist who knows a lot and is able and patient enough to explain it. He was always available when I needed him and I got his attention the instance I entered his office. His calm nature made discussions with him easy, which I found always helpful or even enlightening.

Karl-Heinz Glaßmeier danke ich für seine Mentorenschaft. Diskussionen mit ihm brachten den Blick schnell zurück auf das große Ganze und steuerten neue, unvoreingenommene Ideen bei. Auch über Dinge, die nicht mit meiner unmittelbaren Arbeit zu tun hatten, habe ich eine Menge von ihm gelernt.

Sascha Kempf habe ich ursprünglich als Experten für den E-Ring herangezogen. Diskussionen mit ihm begeistern und machen Spaß, völlig egal, ob es dabei um Gebiete der Physik geht, mit denen ich mich vorher nie beschäftigt hatte, oder um ein beliebiges anderes Thema. Ich freue mich, dass er sich bereiterklärt hat, Zweitgutachter meiner Dissertation zu sein.

Auch *Uwe Motschmann* danke ich für seine schnelle Bereitschaft, meiner Prüfungskommission anzugehören.

Chris Paranicas is for me not just another name on the co-author lists of my papers. Discussions with him, either in person or via email, were always fruitful. I had lots of fun with him. I enjoyed visiting him at APL and our stay together in Washington.

Ein enormer Vorteil als ich mit meiner Arbeit anfing, war die Tatsache, dass nicht nur bereits Daten zur Auswertung vorlagen, sondern auch schon die Tools zur Verfügung standen, um die Daten zu handhaben. Ohne den IDL-Code xLemms von *Andreas Lagg* hätte ich es nicht so einfach gehabt. Obwohl er nicht mehr an LEMMS-Daten arbeitet, war Andreas dennoch flott darin, xLemms in jeder Hinsicht zu supporten.

Of course xLemms could not work without the data provided to us from APL. Thanks

to *Martha Kusterer* and *John Vandegriff* for data reduction and server support.

Es kostete mich einige Monate, bis ich das genaue Thema meiner Promotion gefunden hatte. Die grundsätzliche Frage, warum sich die Teilchen um einen Planeten so verteilen, wie sie es tun, stellte sich mir zwar von Anfang an, allerdings war *Erhard Kirsch* derjenige, der es mir ermöglichte, einen Fuß in dieses Thema zu setzen. Mit seiner Idee, dass man die Teilchenintensitäten benutzen könnte, um die Dichte des E-Rings zu bestimmen fand für mich die Arbeit an.

Mit *Daniel Verscharen* lassen sich gute Diskussionen insbesondere über theoretische Physik führen. Er weiß und versteht eine Menge davon. Sein angenehm kritischer Blick für Gleichungen kam mir öfters zugute.

Anne Angsmann und ich haben viel zusammen für ihre Doktorprüfung gelernt. Das lieferte mir einen Grund, mich mit den entsprechenden Themen noch einmal oder noch genauer zu beschäftigen, was gute Früchte bei uns beiden getragen hat. Die diversen Unternehmungen mit Anne waren vor allem während des Schreibens dieser Arbeit eine angenehme Abwechslung.

Anna Müller war die erste, die mich über Injection Events aufgeklärt hat und Diskussionen darüber waren hilfreich wie angenehm. Anna hat sehr dazu beigetragen, dass ich mich in der Arbeitsgruppe wohlgeföhlt habe, weshalb ich das Kompliment in der Dankesagung ihrer Dissertation, ihr moralische Unterstützung geliefert zu haben, mit Freuden zurückgeben kann.

I only met *Kostas Dialynas* once during my PhD, but at this time he gave me lots of support and a good start concerning the interaction of neutral and charged particles. The CE cross section tool from him and *Pontus Brandt* is a very useful compilation and helped me a lot.

In the past, I had major discussions with several people that provided valuable input for my work: *Vytenis Vasylunas* and *Ed Roeloff* supported me in the mathematical treatment of processes. *Uwe Beckmann* and *Peter Strub* further informed me about the E ring. *Bob Johnson* and *Todd Smith* helped me in the treatment of energy loss in matter.

After and during work it is good to have friends around and things to do. There is not enough space to name everybody of relevance here. However, a large fraction of people can be combined under the term "*coffee group*". Especially I thank *Sebastian Höfner* and *Borys Dabrowski* for providing their flats. Due to our gaming evenings, which I enjoyed very much, I never felt bored in Lindau.

Damit so eine Promotion funktioniert, muss natürlich auch alles drum herum funktionieren. Diese Dissertation entstand im Rahmen der International Max Planck Research School (IMPRS) on Physical Processes in the Solar System and Beyond at the Universities of Braunschweig and Göttingen. Der Koordinator unserer IMPRS ist *Dieter Schmitt*, der seinen Job so gut macht, dass ich gewöhnlich nur in seinem Büro vorbeischauen musste, um schnell eine Unterschrift zu holen.

Finanziert wurde diese Arbeit über die *IMPRS* und die *MPG*, sowie in weiten Teilen vom *DLR* unter den Verträgen 50 OH 0801, 50 OH 0802 und 50 OH 1101. Das DLR hat auch teilweise den Bau von LEMMS finanziert, dessen Daten in dieser Arbeit benutzt wurden.

Zum Abschluss möchte ich meinen Eltern *Karin* und *Helmut Kollmann* danken. Ihre Liebe und ihr steter Glaube an mich geben mir Halt und Geborgenheit.

Curriculum vitae

Persönliche Daten

Name	Peter Kollmann
Geburtsdatum	11. Oktober 1983
Geburtsort	Karlsruhe
Staatsangehörigkeit	deutsch

Schulausbildung

1990-1994	Spitalschule, Leonberg
1994-2003	Johannes Kepler Gymnasium, Leonberg

Studium

2003-2008	Universität Stuttgart, Stuttgart (Diplom in Physik)
2009-2012	MPI für Sonnensystemforschung, Katlenburg-Lindau TU Carolo-Wilhelmina zu Braunschweig, Braunschweig (Promotion über die Naturwissenschaften)